



TECHNISCHE
UNIVERSITÄT
WIEN
Vienna University of Technology

DISSERTATION

Characterization of local seismic events on the deep-seated gravitational slope deformation Gradenbach

Ausgeführt zum Zwecke der Erlangung des akademischen Grades eines Doktors der
Naturwissenschaften unter der Leitung von

Em.O.Univ.Prof. Dipl.-Ing. Dr.phil. Ewald Brückl
Department für Geodäsie und Geoinformation (E120)

eingereicht an der Technischen Universität Wien
Fakultät für Mathematik und Geoinformation

von

Mag. Stefan Mertl
Matrikelnummer 9405227
Reschgasse 17/11
1120 Wien

Wien, am 20. Oktober 2014

Assessors

Em.O.Univ.Prof. Dipl.-Ing. Dr.phil. Ewald Brückl

Department of Geodesy and Geoinformation
Faculty of Mathematics and Geoinformation
Vienna University of Technology
Vienna, Austria

Univ.Prof. Dr.rer.nat. Manfred Joswig

Institute for Geophysics
Faculty of Civil and Environmental Engineering
University of Stuttgart
Stuttgart, Germany

Deutsche Kurzfassung

Das Bewegungsmuster tiefgreifender Massenbewegungen ist häufig durch eine quasistationäre Basisaktivität mit langsamer Hanggeschwindigkeit, die durch Beschleunigungsphasen unterbrochen wird gekennzeichnet. Diese Variationen der Hangbewegung können nicht immer eindeutig mit externen Auslöse-Ereignissen in Verbindung gebracht werden.

Besonders der abrupte Übergang von einer Beschleunigungsphase in eine langsame, quasistationäre Bewegung zeigt, dass geodätische Messdaten alleine nicht ausreichen, um die zugrunde liegenden Prozesse zu verstehen und eine fundierte Prognose für den Bewegungsverlauf einer tiefgreifenden Massenbewegung zu treffen. Für aussagekräftige Prognosemodelle müssen noch weitere Parameter eingebunden werden. Die in dieser Dissertation untersuchte seismische Aktivität auf Massenbewegung bietet sich als ein solcher zusätzlicher Parameter an.

Für die Untersuchung der seismischen Aktivität von Massenbewegungen wurde nach mehreren Pilotstudien die Massenbewegung Gradenbach in Kärnten, Österreich ausgewählt. Die Zuordnung der Massenbewegung zur Rheologie des spröden Fels und die Annahme, dass die Bewegung der Hangrutschung einer Stik-Slip Bewegung entlang einer oder mehrerer Gleitzonen entspricht, lassen als Begleiterscheinung der Verschiebung seismische Massenbewegungen erwarten.

Im Jahr 2007 wurde auf der Massenbewegung Gradenbach ein permanentes seismisches Monitoringnetzwerk mit kontinuierlicher Datenerfassung installiert. Im Frühling 2009 wurde eine Beschleunigungsphase mit einer Dauer von ungefähr 3 Monaten beobachtet. Die Massenbewegung beschleunigte von der Basisaktivität $\sim 10\text{cm/a}$ auf eine Geschwindigkeit von $\sim 0.8\text{ cm/d}$ mit einer darauf folgenden Restabilisierung auf die Verschiebungsraten der Basisaktivität. Die während dieser Beschleunigungsphase aufgezeichneten seismischen Daten bildeten die Grundlage für die Charakterisierung der seismischen Aktivität der tiefgreifenden Massenbewegung Gradenbach.

Für die teilweise automatisierte Auswertung der seismischen Daten wurde eine Methode zur Detektion seismischer Signale entwickelt, die auf der Segmentierung der aus den Seismogrammen erzeugten Spektrogrammen unter Anwendung von Methoden der digitalen Bildverarbeitung basiert. Die Bewertung und Klassifizierung der Ereignisse erfolgte durch eine interaktive, computerunterstützte Durchsicht der Daten. Die Klassifizierung der Ereignisse basierte auf der Beurteilung unterschiedlicher Parameter wie der Wellenform, Muster im Zeit-Frequenzbereich, der Polarisierung des Wellenfeldes oder der Epizentren der seismischen Ereignisse. Um den Anforde-

rungen der Auswertung kontinuierlicher Daten und der Notwendigkeit der Entwicklung neuer Auswertemethoden gerecht zu werden, wurde eine MATLAB Software entwickelt, die einen schnellen Zugriff auf das vorhandene Datenmaterial sowie eine einfache Implementierung neuer Algorithmen und deren Test in einer großen Datenmenge ermöglicht.

Während der Beschleunigungsphase wurde eine Erhöhung der seismischen Aktivität registriert und es wurden Ereignisse identifiziert, die bereits einen Monat vor der mit dem Extensometer gemessenen Beschleunigung des Hangs auftraten. Für sechs unterschiedliche Ereignis-Typen wurde als Quelle die Verschiebung der Massenbewegung identifiziert. Die lokalen Magnituden der Ereignisse lagen zwischen -2.3 und -0.5. Ein Vergleich der Seismizität mit komplementären Daten wie der Hangverschiebung, meteorologischen- und hydrologischen Daten zeigte Zusammenhänge zwischen dem Auftreten unterschiedlicher Ereignistypen und der zunehmenden- oder abnehmenden Beschleunigung. Weiters konnte die empfindliche Reaktion der Massenbewegung auf versickerndes Schmelzwasser durch eine erhöhte seismische Aktivität während der Schneeschmelze nachgewiesen werden.

Diese Arbeit wurde von der Österreichischen Akademie der Wissenschaften im Rahmen des International Strategy for Disaster Reduction (ISDR) Programms finanziert.

Für Mutti und Papa,
die mir immer die Möglichkeit einer freien Entscheidung offen hielten.

Acknowledgements

I thank Ewald Brückl for his creative approach to geophysics, his exuberant mind full of new ideas and his flexibility which transformed my work at the Vienna University of Technology into a playground to explore many aspects of geophysical research. I thank Manfred Joswig for the motivating chats during our meetings in Vienna. I also thank Daniel and Uli for the countless escapes from geophysics-only talks and Eva for keeping me on track. Special thanks go to Walter for his neverending helpfulness. Moreover I'd like to thank all the colleagues at the research group Geophysics who supported me during my research with discussions and manual work.

Contents

1	Introduction	1
1.1	The development of seismic monitoring	1
1.2	Seismic monitoring of mass movements	3
2	Deep-seated gravitational slope deformation	5
2.1	Initiation of deep-seated gravitational slope deformations	9
2.2	Deformation behavior	10
2.3	Seismic activity	13
3	The deep-seated gravitational slope deformation Gradenbach	15
3.1	Location and morphology	15
3.2	Geology	18
3.3	Structure	19
3.4	A slope under observation	23
3.5	Kinematics	27
4	Seismic monitoring network Gradenbach	29
4.1	Instrumentation and station layout	29
4.2	Available data and data quality	32
4.3	Detection Threshold	36
4.4	Data handling	39
4.5	Processing software - Seismon	39
5	Event detection	41
5.1	Pattern extraction	43
5.2	Event binding	52
6	Event screening and classification	55
6.1	Candidates, earthquakes or noise?	57
6.2	The location of the candidates	61
6.3	Event amplitude distribution and amplitude correction	62
6.4	Event localization using NonLinLoc	65
6.5	Polarization analysis	70

CONTENTS

7	Seismic events recorded at Gradenbach	73
7.1	Events related to the movement of the slope	75
7.2	Source regions of the slope events	86
7.3	Earthquakes	90
7.4	Anthropogenic- and natural noise	93
8	Slope displacement and seismic events	97
	References	101
A	Seismon	109
A.1	Software design	110
A.2	Graphical user interface	113
A.3	Seismon usage within research projects	113
B	Slope candidate events	117
B.1	Type A	117
B.2	Type AA	124
B.3	Type B	131
B.4	Type D	138
B.5	Type rf	157
B.6	Type tremor	164

1

Introduction

When growing up in a small village in the Austrian Alps, I experienced the surrounding mountains as something solid, something that won't change with time. After my studies in Geophysics at the Vienna University and my work within the framework of my diploma thesis at the Vienna University of Technology, where I got in contact with mass movements, I have recognized the mountains as something that's far from stable. Everything seems to move, it's just the amount of time one needs to observe these changes. What fascinates me, are not the fast moving landslides like debris-flows or mud-flows with an immediate impact on human live, but mass-movements which deform at very low speed. It's the *hiding* of the slow moving landslide from human perception which I like. The effects of slow moving landslides are not noticed by the residents immediately and humans automatically adapt to the changes caused by the landslides. Slight damages of roads and buildings are repaired, land boundaries are changed, and so forth, but everyday live continues literally on the landslide. Only a long-term observation of the landslide reveals its massive and at times catastrophic effects.

While I was researching for my diploma thesis I encountered the huge potential of seismic monitoring to gain more knowledge of the subsurface processes involved in the slow displacement of large slopes. The field of seismic monitoring of deep-seated landslides has just started to evolve and many unknowns had to be resolved. Those that motivated me most where the application of state-of-the-art instrumentation in a not well explored research area, the necessity of developing new software to handle the long-term monitoring data and the uncertainty of what seismic signals the long-term monitoring will reveal.

1.1 The development of seismic monitoring

Passive seismic monitoring (PSM) is the recording and analysis of ground-motion created by elastic waves within the earth. The methods of PSM have developed slowly and at many different locations (Dewey & Byerly, 1969). The transition from seismoscopes, instruments built to indicate the occurrence of earthquakes, to seismographs which record the ground motion as a continuous function of time happened in the late 19th century. The first known recordings of an identified teleseismic earthquake were made in 1889 by Ernst von Rebeur-Paschwitz (von

1. INTRODUCTION

Rebeur-Pashwitz, 1889). With the improvement of seismic instrumentation, more sensitive seismographs were built and the deployment of seismic networks at local-, regional- and global scale was started. First prominent outcomes of global passive seismic monitoring were the description of the earth structure, the definition of the local magnitude scale by Richter or the discovery of the magnitude-frequency relation by Gutenberg and Richter.

The increase of the sensitivity of the seismic networks lowered the magnitude detection threshold. Lee & Stuart (1981) give a very good overview of the historical development of seismic monitoring from the 1930s to the 1980s with the main focus on microearthquake studies. They note, that the nowadays widely used term “*microearthquake*” was first introduced by Asada & Suzuki (1950) to describe a very small earthquake in an earthquake aftershock study. During the time, the term microearthquake was used to name earthquakes with magnitudes smaller than 3.

Like every other part of science and everyday life, passive seismic monitoring as well has profited by the revolutions of the digital age. The reduction of size, power-consumption and cost with an accompanying increase in performance of every electronic equipment has caused a significant improvement of seismological instruments. The change from analog to digital hardware together with the development of new technologies (e.g. GPS providing a worldwide available common time base for seismic stations, solar power supply, digital data storage or digital data transmission) has allowed a rapid increase of the effectiveness of passive seismic monitoring networks and has provided geoscientists with an almost unlimited flexibility of station placement. All of these gains have resulted in an increase of the sensitivity of seismographs, the possibility to install dense monitoring networks and the installation of seismic instruments near the source (e.g. boreholes). These improvements have made the seismic monitoring networks sensitive enough to detect earthquakes with magnitudes far below 0 at epicentral distances ≤ 1 km (Joswig, 2008).

Detecting such weak seismic signals, new terms similar to the definition of a microearthquake have been used by several authors in the literature. Earthquakes with magnitudes less than 0 have been named nanoearthquakes by Combs & Hadley (1977), Atkinson (1981) or Butler (2003). But nanoearthquakes are not the bottom-end of current detectable earthquakes. Nowadays, the detection threshold of some subsurface, near-source PSM networks is below $M = -3$. For example, the smallest earthquakes detected at the San Andreas Fault Observatory at Depth (SAFOD) network are below $M = -3.5$ (Bohnhoff *et al.*, 2009) and the JAGUARS network deployed at the Mponeng gold mine in South Africa detected earthquakes with magnitudes as small as $M_w = -4.4$ (Kwiątek *et al.*, 2010). Having this expansion of detectable magnitude ranges from $M = 9$ to $M = -4$, Bohnhoff *et al.* (2009) suggested a new labeling of earthquakes based on their seismic moment, which is a good way of conception to avoid overlapping and maybe misleading usage of the terms like micro- and nanoearthquake.

Reaching such a low detection threshold to record earthquake below a magnitude of -4 implies the deployment of a sophisticated PSM network near the expected source of the earthquakes. This usually requires drilling of boreholes or other methods of subsurface deployment (e.g. installation in mines). The subsurface deployment usually is accompanied with large financial and technical efforts which limits their frequent use in scientific studies. Usually, PSM networks involve the deployment of seismic stations at the surface of the earth. To overcome the disad-

vantages of higher noise level and signal disturbances at surface-based stations due to surface waves or near-surface inhomogeneities, more sophisticated signal processing techniques have to be used to lower the detection threshold of surface-based monitoring networks. Häge & Joswig (2009) used the deployment of surface based tripartite mini-arrays and special signal processing techniques to reach a detection threshold of local magnitude $ML = -2$ at an epidistance of 2.5km and $ML = -1$ at an epidistance of 10km at an active fault zone in Spain.

1.2 Seismic monitoring of mass movements

The development of sensitive seismic equipment and powerful processing methods has created the possibility to deploy low-cost, but highly sensitive PSM networks in remote and/or rugged areas. This has opened a completely new branch of passive seismic monitoring with the focus not only on tectonic earthquakes, but on other seismic wave generating processes. Monitoring of volcanoes (McNutt, 2002), icequakes (Rial *et al.*, 2009; Roux *et al.*, 2010), cliff collapses (Amitrano *et al.*, 2005; Got, 2010; Senfaute *et al.*, 2009), rock-falls (Occhiena *et al.*, 2012; Walter *et al.*, 2012) and avalanches (Bessason *et al.*, 2007; van Herwijnen & Schweizer, 2011) are only some examples of these new applications of PSM. Considering the potential hazard of slope instabilities it's not surprising, that the first PSM projects on mass movements have been related to catastrophic landslides. At the Vajont mass movement, a seismometer was installed to monitor the seismicity related to the acceleration of the slope in 1959 (Caloi, 1966). At the Frank Slide (Turtle Mountain), a PSM network was installed in the 1980s (Chen *et al.*, 2005; Froese *et al.*, 2009). Recent PSM projects on mass movements reported the existence of various kind of seismic events in brittle rock environment (e.g. Hochmais-Atenskopf mass movement (Brückl & Mertl, 2006; Mertl & Brückl, 2007b), Gradenbach mass movement (Brückl & Mertl, 2006; Brückl *et al.*, 2008b; Mertl & Brückl, 2007a,b), Randa rockslide (Spillmann *et al.*, 2007); Aknes rock-slide (Roth & Blikra, 2010, 2009); Sechilienne rockslide (Helmstetter & Garambois, 2010); Peschiera Springs slope (Lenti *et al.*, 2012)) as well as in plastic rheology like clay- or mudslides (Gomberg *et al.*, 1995, 2011; Walter & Joswig, 2008, 2009)).

1. INTRODUCTION

2

Deep-seated gravitational slope deformation

A landslide is defined as “*a movement of a mass of rock, earth or debris down a slope*” (Cruden, 1991). This definition is also used by the multilingual landslide glossary (WP/WLI, 1993). Several authors suggested to replace the term *landslide* with other expressions which don't already include the process. Varnes (1978) proposed the term *slope movement* to describe *a downward and outward movement of slope forming materials under the influence of gravity*. The even more general term *mass-movement* was introduced by Brunsten (1984) to describe the form of mass transport which doesn't require any transportation media like water, air or ice.

Depending on the process and the material involved, a landslide can be classified into several categories. In this thesis the terminology developed by Cruden & Varnes (1996) and the multilingual landslide glossary (WP/WLI, 1993) is used. The landslide classes and the landslide velocity scale proposed by Cruden & Varnes (1996) is given table 2.1 and figure 2.1 respectively. Dikau *et al.* (1996) describes the landslide classes in detail. As usual, any classification of a phenomena leads to some outliers which don't fit into this classification. In case of landslide classification these outliers are landslides of which the underlying mechanism is not clearly known. A prominent example of an unclassifiable landslide is the sagging (also named Sackung (Heim, 1932), Talzuschub (Zischinsky, 1969), deep seated gravitational creep, rock flow (Bisci *et al.*, 1996) or rock creep (Zischinsky, 1969) in the literature). Weidner (2000) and Piovano (2012) give good literature reviews of the historical evolution and the varying, sometimes confusing usage of the terms mentioned above. The confusion mainly arises by the changing association of the sagging to different landslide classes and by a non-conform use of the term sagging to describe different mechanisms within scientific literature (e.g. Bisci *et al.* (1996); Cruden & Varnes (1996); Heim (1932); Nemcok *et al.* (1972); Varnes (1978); Zischinsky (1969)). This is due to the definition of a sagging based on large-scale morphological features on the one hand, and on the mechanism or the phenomenon itself on the other hand.

To avoid a direct link between the observed landslide and the not yet clearly known, maybe complex and/or compound landslide mechanism, a more general name has been introduced by the Italian scientific community in the 1970s and 1980s. The expression *deep-seated gravitational*

2. DEEP-SEATED GRAVITATIONAL SLOPE DEFORMATION

slope deformation (DGSD) is used growingly to describe large-scale, deep-seated and slow moving landslide phenomena which can't be clearly assigned to any existing landslide class. Dramis & Sorriso-Valvo (1994) made a first approach to define the term DGSD using some general structural constraints but he also distinguished clearly three basic types of DGSDs: sagging, lateral spread of ridges and lateral spread of thrust fronts. This strict split-up into three basic types shouldn't be used. DGSDs should be only characterized using morphological, structural and kinematic features, but not specify any underlying mechanism. Based on the early observations made by Ampferer (1939), Stini (1941) and Zischinsky (1969), and slightly adapted from the good comprehensions given by Agliardi *et al.* (2001) and Dramis & Sorriso-Valvo (1994) the features characterizing a deep-seated gravitational slope deformation are:

- the size of the deforming mass covers almost the whole height of the slope;
- the volume of the deforming mass is of the order of several hundred thousands of cubic meters or more;
- the thickness of the deforming mass is several tens of meters or more;
- the present day velocity is extremely slow to very slow (in the range of mm/a to several cm/a in alpine areas);
- the deforming mass is not necessarily bound by a continuous sliding surface;
- several morphological structures like double ridges, scarps, counter-scarps, trenches or bulging are present;
- minor landslides inside the deformed mass and ancient collapses of the lower part of the slope are present.

I encourage to use the term DGSD as a kind of temporary container to label all landslides for which the mechanism or style of the landslide have not yet been clearly defined, but which show the features mentioned above (not all are mandatory). Once the mechanism(s) of a DGSD has/have been determined, it should be named according to the naming convention given by Cruden & Varnes (1996) and WP/WLI (1993) or if needed a new name based on a well defined and explained mechanism has to be introduced.

description	extremely slow	very slow	slow	moderate	rapid	very rapid	extremely rapid
velocity [mm/s]	5×10^{-7}	5×10^{-5}	5×10^{-3}	5×10^{-1}	50	5×10^3	
typ. velocity	16 mm/a	1.6 m/a	13 m/month	1.8 m/hr	3 m/min	5 m/s	

Figure 2.1: The classification of landslide velocities according to Cruden & Varnes (1996).

In general, the first identification of DGSDs is due to their morphological features. The schematic drawings in figure 2.2 and figure 2.3 illustrate the simplified structure of a DGSD and

type of movement	type of material		
	bedrock	engineering soil	
		predominantly coarse	predominantly fine
Fall	rockfall	debris fall	earth fall
Topple	rock topple	debris topple	earth topple
Slide	rock slide	debris slide	earth slide
Spread	rock spread	debris spread	earth spread
Flow	rock flow	debris flow	earth flow

Table 2.1: Classification of landslides according to Cruden & Varnes (1996).

its characteristic morphological features. Near the mountain crest, the outcome of the shear zone forms a scarp or a double ridge, depending if the shear zone cuts the mountain slope in front or behind the crest. The double ridge and the scarp are the most striking characteristics to be recognized in the field. Depending on the internal structure of the mass movement other morphological structures like minor scarps, counter scarps or trenches might develop in the upper part of the landslide (Agliardi *et al.*, 2001; Bisci *et al.*, 1996). The lower part of the slope shows compressional elements like bulging or minor landslides due to the over-steepening and erosion of the landslide toe (e.g. by rivers at the valley floor). The displacement usually takes place along one or more shear zones, which don't have to be fully developed from the top to the toe of the slope. The shear zone might be a clearly defined plane or a zone of several meters thickness in which the strain accumulates. Shear zones of DGSDs were observed in tunnels (Zangerl *et al.*, 2007, 2010) and in boreholes using core logs (Chigira *et al.*, 2013; Zangerl *et al.*, 2010) and inclinometer measurements (Bonzanigo *et al.*, 2007; Ferrucci *et al.*, 2000; Forlati *et al.*, 2001). The local structure of shear zones was described by geophysical surveys (Bonzanigo *et al.*, 2007; Brückl *et al.*, 2004, 2006; Zangerl *et al.*, 2012). The shear zones can be characterized as zones of intensive rock fragmentation, breccia, uncemented gouges, kakirites and pulverized rock (Chigira *et al.*, 2013; Zangerl *et al.*, 2010).

2. DEEP-SEATED GRAVITATIONAL SLOPE DEFORMATION

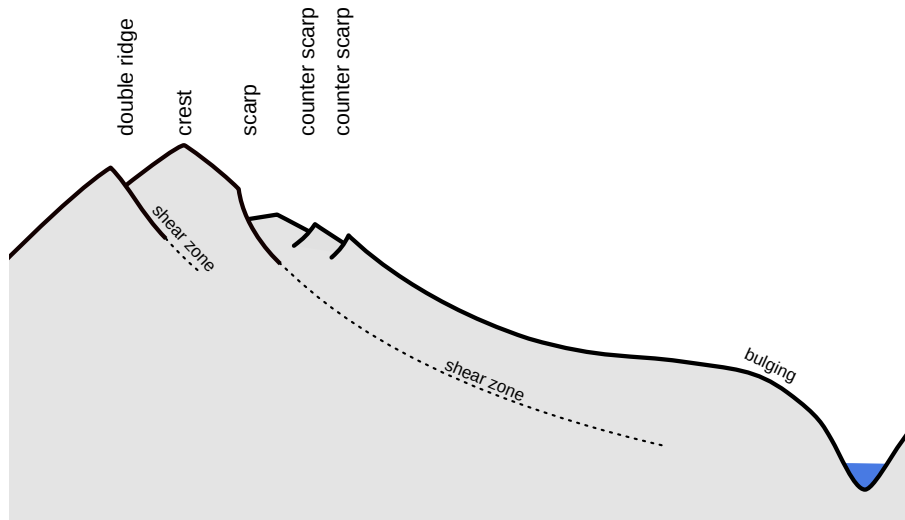


Figure 2.2: A schematic drawing of the structure of a DGSD. Not all structures have to be developed. The river at the toe of the slope is not considered as a feature of a DGSD, but in many cases, this river is present in the valley and usually plays an important role considering the erosion of the toe of the slope.

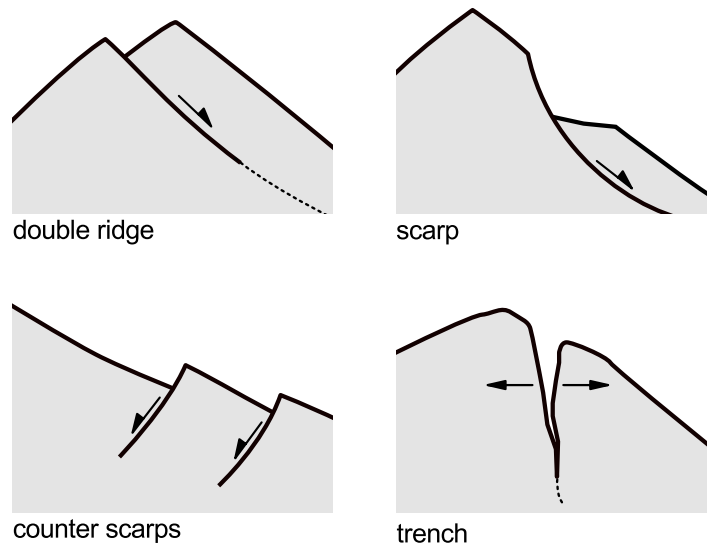


Figure 2.3: The morphological features characterizing a DGSD (according to Agliardi *et al.* (2001)). The arrows indicate the direction of motion.

2.1 Initiation of deep-seated gravitational slope deformations

Many authors related the initiation of DGSD more or less vaguely with the glaciation and deglaciation of alpine valleys (e.g. Abele, 1974; Zischinsky, 1969). The most obvious direct link between the development of slope instability and the glaciation-deglaciation process is given by the spatial and temporal distribution of DGSD. Worldwide, most DGSD in alpine area occur on glacially modified valley flanks (e.g. Crosta *et al.*, 2013; Pere, 2009) and Brückl *et al.* (2001) showed that the stress changes at the toe of the slope following glacial debuttressing is sufficient to initiate the mass movement. Glacial debuttressing is the removal of the support of adjacent glacier ice during periods of downstage (Ballantyne, 2002). Brückl & Parotidis (2001), Brückl (2001), Brückl & Parotidis (2005) and Agliardi *et al.* (2001) showed with numerical modeling, that after the glacial debuttressing, progressive damage starting at the toe of the slope causes the disintegration of compact rock forming a zone of softened rock corresponding to the landslide mass in its initial state.

Available datings of DGSDs also indicate an initiation after the last glacial maximum (Bedoui *et al.*, 2009; Cossart *et al.*, 2008; Hippolyte *et al.*, 2012; Sanchez *et al.*, 2010) but no direct triggering of the slope displacement caused by the glacial retreat. Bedoui *et al.* (2009) dated the earliest extensional structures at the La Clapiere slope to 10 ka BP, which is 3 ka after this area has been completely deglaciated. Bedoui *et al.* furthermore observed the evolution of structural features from the toe to the top of the slope over the range of 4.4 ka.

The delayed initiation of the DGSD after the last glacial maximum is further strengthened by the absolute dating of rock slope failures of the late-glacial to late Holocene time-period which revealed no immediate triggering of the rock slope failures by the glacial retreat (McColl, 2012; Prager *et al.*, 2008). The temporal distribution of the slope failures don't show any major accumulation correlating with the deglaciation process. In fact, it is a continuous distribution with moderate peaks between approximately 10 - 8 ka BP and 4 - 2 ka BP (see figure 2.4 and figure 2.5). Most of the slope failures took a preparation time of several thousand years after the ice withdrawal before the slopes collapsed, suggesting a preparatory phase with a progressive damaging of the slope before the actual triggering of the rock slope failure (Eberhardt *et al.*, 2004).

2. DEEP-SEATED GRAVITATIONAL SLOPE DEFORMATION

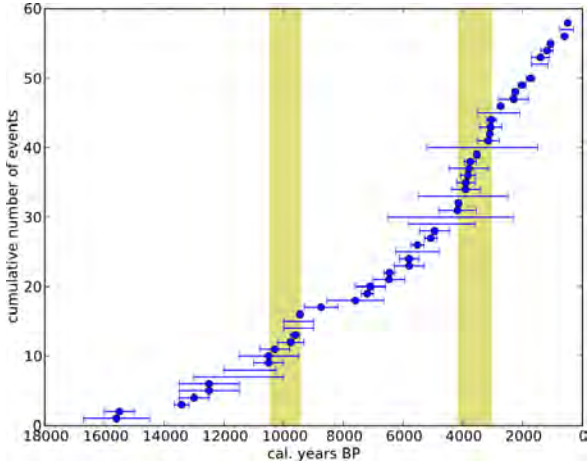


Figure 2.4: The temporal distribution of paraglacial slope failures using the dataset for the Tyrolean area compiled by Prager *et al.* (2008). Only rock-slope failures have been used. The beige vertical bars indicate the periods of accumulated landslide occurrence stated by Prager *et al.* (10.5 - 9.4 ka cal BP; 4.2 - 3 ka cal BP).

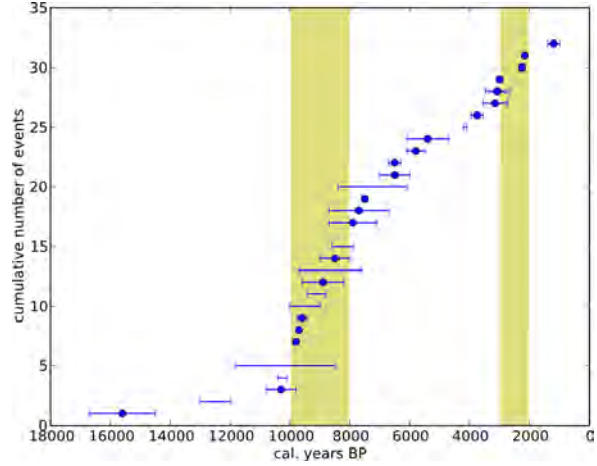


Figure 2.5: The temporal distribution of worldwide paraglacial slope failures using the dataset compiled by McColl (2012). Only events with an event- or range dating have been used. The beige vertical bars indicate the periods of accumulated landslide occurrence stated by McColl (10 - 8 ka; 3 - 2 ka).

2.2 Deformation behavior

Three deformation patterns can be used to describe the general deformation behavior of landslides (Petley & Allison, 1997; Zangerl *et al.*, 2008; Zischinsky, 1969): (A) a catastrophic failure with a very short-time or imperceptible preceding acceleration; (B) an accelerating slope deformation resulting in a catastrophic failure; (C) a slope deformation with increasing velocities at the beginning, leading to a successive decrease of the slope velocity and a stabilization of the slope. Sometimes, deformation types B and C show an overlain temporal variation of the slope velocity controlled by e.g. a changing pore-water pressure. The temporal variations usually can be characterized by a base activity with slow velocities which is interrupted by phases of acceleration with velocities raised by the factor of up to 1000 (Zangerl *et al.*, 2008). For DGSDs, the deformation type A can be neglected, but the long preparatory time from the debuttressing of the slope with the retreat of the glaciers after the last ice age and the initialization of the deformation of the slope has to be taken into account. The possible deformation patterns of DGSDs are outlined in figure 2.6. Based on the characterization of the deformation behavior by Brückl & Parotidis (2001) the following four phases can be used to describe these patterns:

Preparation phase corresponding to the initial phase of development of the mass movement. An originally compact rock will be transformed to a damaged or soft rock, including small-scale fractures, by concentrations of high stresses.

Quasi-stationary phase during which the softened rock exhibits a more or less spatially continuous deformation concentrated to the shear zone or shear plane. The deformation rate

is mainly controlled by pore pressure, and the motion may be continuous or show temporal variations.

Failure phase is the transition from a quasi-stationary phase to rapid and eventually catastrophic sliding.

Re-stabilization phase is the transition from the quasi-stationary phase to a re-stabilization of the slope leading to a slope showing no more deformation.

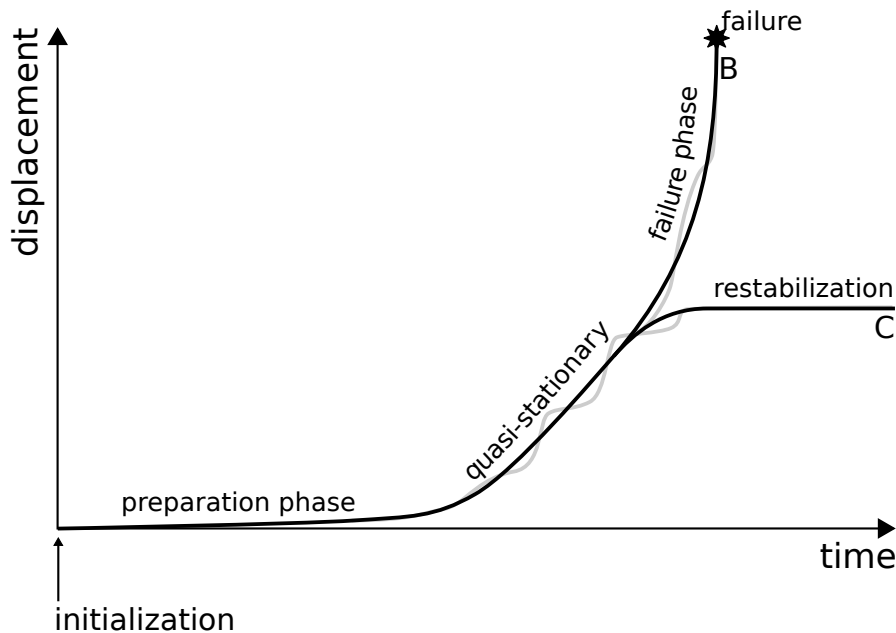


Figure 2.6: The two characteristic deformation patterns of DGSDs (black lines). After initialization of the disintegration of the slope (e.g. by debuttinging), it takes some time during the preparation phase until the deformation of the slope is triggered. Type B is a successive acceleration until the catastrophic failure of the slope. Type C is the re-stabilization of the slope after the acceleration. Both types can be overlain by temporal variations (gray lines).

For the re-stabilization-, failure- and quasi-stationary phases, representative examples of DGSDs can be found in the literature. No example for a slope currently in the preparation phase is available. Slopes that already have re-stabilized are Lesachriegel (Brückl *et al.*, 2006), Niedergallmigg (Zangerl *et al.*, 2012), Glunzerberg (Zischinsky, 1969) and Nassereiner Alm (Brückl & Scheidegger, 1972). DGSDs that developed to a catastrophic failure are Köfels (Brückl & Parotidis, 2001, 2005), La Clapiere (Hippolyte *et al.*, 2012), ValPola (Govi *et al.*, 2002) and Vajont (Genevois & Ghirotti, 2005), whereat it has to be noted, that the failure of Vajont has been triggered by the filling of a reservoir at the toe of the slope. Examples of DGSDs that are currently in the quasi-stationary phase are Campo Vallemaggia (Bonzanigo *et al.*, 2007), Gradenbach (Brückl *et al.*, 2013), Hochmais-Atemkopf (Zangerl *et al.*, 2010), Steinlehnen (Zangerl *et al.*, 2007) or Spriana (Crosta *et al.*, 2012b).

2. DEEP-SEATED GRAVITATIONAL SLOPE DEFORMATION

The deformation behavior of DGSDs can be reduced to 4 key features: (a) the transition from the preparatory phase to the quasi-stationary phase, (b) the mechanism of the deformation of the slope during the quasi-stationary phase, (c) the external factors causing the temporal variation of the slope velocity, and (d) the evolution to catastrophic failure or re-stabilization.

The factors and processes influencing these key features are an open field of discussion and many preconditioning (e.g. lithology, rock mass quality, joint characteristics, tectonic stress regime, structure), preparatory (e.g. deglaciation, change of the valley geometry, topographic stresses), triggering (e.g. climate change, seismicity, progressive damage) and sustaining factors (e.g. pore water pressure) have been proposed to influence the deformation behavior of DGSDs (see Agliardi *et al.* 2009 and Crosta *et al.* 2012a for reviews of case studies). Preconditioning factors are static and inherent acting as catalysts to allow other dynamic destabilization factors to operate more efficiently. Preparatory factors are dynamic and reduce the stability of a slope over time without actually initiating movement. Triggering factors initiate movement by changing the slope from a 'marginally stable' to 'actively unstable' state. Sustaining factors are factors that dictate the behavior of 'actively unstable' slopes, for example duration, rate and form of movement (Glade & Crozier, 2005).

As discussed in the section before, the deglaciation and the following stress-relief is thought as a major preparatory factor. Topographic stresses and structural constraints influencing the evolution of DGSDs have been reported by Radbruch-Hall (1978) and Agliardi *et al.* (2001). These factors lead to a progressive damage of the slope which initiates the slope deformation (Agliardi *et al.*, 2001; Brückl, 2001; Brückl & Parotidis, 2001, 2005; Parotidis, 2001) and the transition from the preparatory phase to the quasi-stationary phase. During the quasi-stationary phase, the most important sustaining factor is most likely the change of pore water pressure at the shear zones due to infiltrating water (Brückl & Parotidis, 2005; Brückl *et al.*, 2013) or by the change of the water-level of lakes or reservoirs at the toe of the slope (Genevois & Ghirotti, 2005; Zangerl *et al.*, 2010). Although caused by anthropogenic interaction, the Vajont rock slide showed, that these sustaining factors can also act as factors triggering the transition to the failure phase. An example with a non-anthropogenic triggering of the failure phase is the Val Pola rock slide which happened 1987 in Italy. This slope already had shown features of a DGSD before the catastrophic failure happened (Govi *et al.*, 2002). Massive erosion at the toe of the slope had caused a major stabilization of the slope which lead to an acceleration and finally to the catastrophic failure of the slope. Brückl & Parotidis (2005) modeled the evolution of DGSDs from the initiation to catastrophic failure or re-stabilization using sub-critical crack growth as the only active mechanism. Progressive damage of the slope after deglaciation creates a softened rock mass and a basal shear zone at which strain concentrates. This strain concentration causes a progressive smoothing of the asperities of the shear zone. The deformation along the basal shear zone has been modeled using a rotational slider block model. At three case studies (Köfels, Gradenbach and Hochmais-Atenskopf) transition from the quasi-stationary phase to dynamic rupture was modeled depending on the total displacement of the slopes. For one case study (Lesachriegel) the transition to the re-stabilization phase, which is mainly caused by a decrease of gravitational stresses due to the circular downslope movement of the rotational slider block, was modeled. The transition from quasi-stationary phase to dynamic rupture takes place, when the stress concentration at asperities caused by the progressive smoothing of the shear zone

was high enough to enable a dynamic rupture of all asperities. The Köfels landslide, which already failed ~9600 years BP was correctly modeled. The Gradenbach landslide with a current total displacement of ~40m and a modeled transition to dynamic rupture at ~100m shows the potential to reach this threshold displacement and initiate rapid sliding of the slope. The current total displacement of the Hochmais-Atenskopf landslide is ~10m. The modeled transition to rapid sliding is ~200m. Brückl & Parotidis note, that “*such a large displacement would change the gravitational stresses in a way not properly described by the model presented*”, and it is more likely, that the slope will stabilize before reaching the modeled deformation of ~200m.

2.3 Seismic activity

As shown in section 1.2 many seismic monitoring studies have been accomplished on various types of landslides and revealed seismic activity related to the displacement of slopes. Nevertheless not many information about the seismic activity related to the slow movement of DGSDs is available. To verify the existence and the detectability of seismic events related to the deformation of DGSDs using surface based deployment of seismic sensors, I have accomplished several pilot studies at 3 different DGSDs in the Austrian Alps within the framework of the IDNDR and ISDR programme of the Austrian Academy of Sciences. The study sites were Hochmais-Atenskopf in the Kaunertal, Tyrol, Niedergallmigg-Matekopf in the Inntal, Tyrol and Gradenbach in the Mölltal, Carinthia. Four short-term monitoring experiments were accomplished at these sites. The main goals of these studies were:

1. Get an overview of the seismic noise present in the area of the DGSD.
2. Proof of the detectability of weak signals on mass movements.
3. Verify the existence of seismic events related to the deformation of the slope.
4. Test and development of equipment suitable for permanent deployment in high alpine area.
5. Develop processing methods to detect and identify seismic events recorded on the DGSD.

Results of the pilot studies have already been published by Brückl & Brückl (2006) and Brückl *et al.* (2008b); Mertl & Brückl (2007a,b). Recently Lenti *et al.* (2012) described seismic events related to the displacement of a DGSD in karstified rock mass. Other examples of long term seismic monitoring studies at similar, but not completely comparable in terms of structure and kinematic, are the Aknes landslide (Roth & Blikra, 2010) or the Sechilienne rockslide (Helmstetter & Garambois, 2010; Lacroix & Helmstetter, 2011).

2. DEEP-SEATED GRAVITATIONAL SLOPE DEFORMATION

3

The deep-seated gravitational slope deformation Gradenbach

3.1 Location and morphology

The mass-movement Gradenbach (GB) is located in the Schober Group, a subrange of the Central Austrian Alps. It is located on a SSE facing slope in the Graden valley at its opening to the Möll valley near Putschall in Carinthia (see figure 3.1).

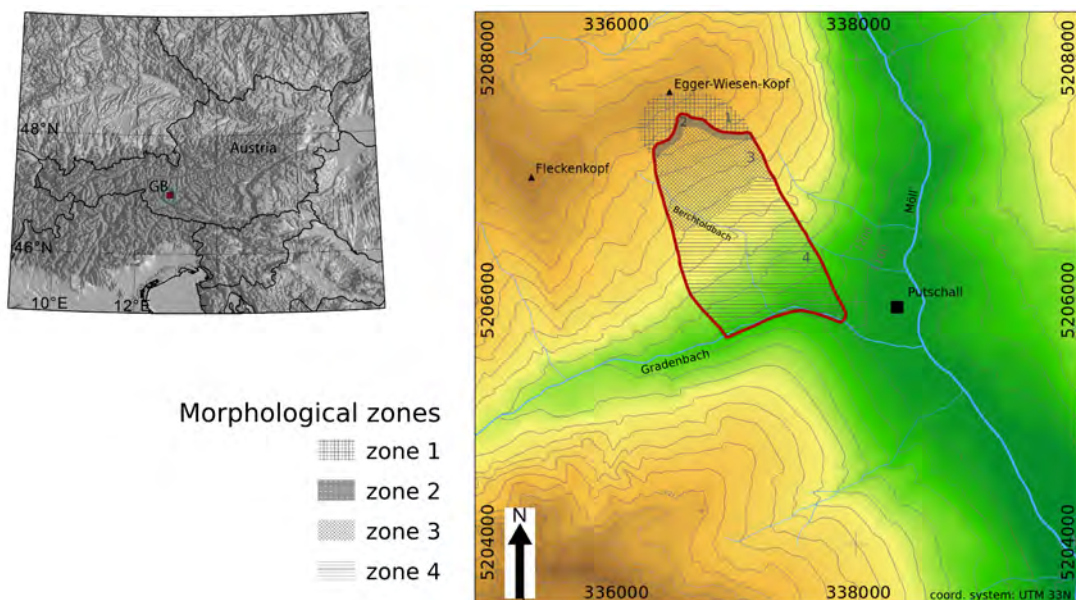


Figure 3.1: Location map of the mass-movement Gradenbach (GB). The red line in the detailed map outlines the boundary of the mass movement. The shaded morphological zones are reproduced after Moser & Glumac (1983). For a description of the zones see the text. The digital elevation model was provided by the Bundesamt für Eich- und Vermessungswesen (BEV).

3. THE DEEP-SEATED GRAVITATIONAL SLOPE DEFORMATION GRADENBACH

According to the diagnostic features given in chapter 2, the mass-movement can be categorized as a deep-seated gravitational slope deformation and it is easily recognized as such on aerial photos, digital elevation models and by field observations. The morphological features are illustrated in figures 3.2, 3.3 and 3.4. The main scarp with an extent of about 30-40m, the bulging at the zone of accumulation and the oversteepened valley flanks at the toe of the slope can be clearly identified. Following Moser & Glumac (1983), the mass movement Gradenbach can be divided into 5 morphological zones (see figure 3.1). Above the top scarp zone 1 extends to the crest of the Egger-Wiesen-Kopf. Minor deformation patterns like small scarps are visible in this zone, but the deformation is small tending to zero velocity. At the topmost part, from the top scarp (zone 2) several hundred meters down to a sea-level of about 1700m, the rock mass is heavily fractured into irregular large blocks forming talus structures (zone 3). In the adjacent part of the slope, the rock mass is heavily segmented showing large crevices as well as counter-scarps (zone 4). The toe of the slope shows strongly over-steepened valley flanks. Several small, surface based landslides and rockfalls at the toe of the slope and the top scarp area are visible (BFW, 2005, 2007).

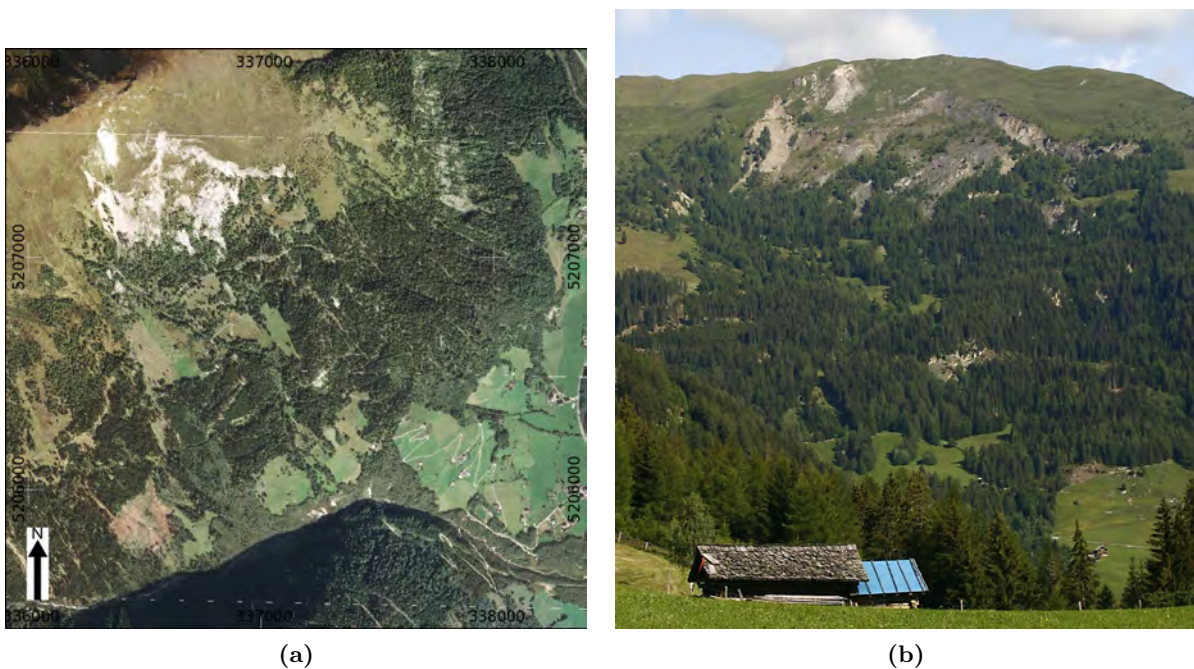


Figure 3.2: (a) Aerial photo from the year 2006 and (b) view from the opposite slope from the year 2011. The aerial photo was provided by the Bundesamt für Eich- und Vermessungswesen (BEV).



Figure 3.3: Detailed views of morphological features characterizing the Gradenbach mass movement. (a) The main scarp of the mass movement with a displacement of 40m can be clearly identified. Above the scarp, the crown with minor scarps can be seen. In the area below the main scarp talus structures of heavily fractured rocks are found as well as counter scarps shown in (b).



Figure 3.4: Minor landslides at the mass movement occur (a) at the top region and (b) at the toe of the slope (b).

3. THE DEEP-SEATED GRAVITATIONAL SLOPE DEFORMATION GRADENBACH

3.2 Geology

The slope deformation comprises almost the whole width of the Matriei-zone at the southern border of the Tauern-window (see figure 3.5). In the area of the Gradenbach landslide, the Matriei-zone dips to the SW below the Schober-crystalline and overlies the Glockner-nappe and the Venediger-nappe (see figure 3.6). The Matriei-zone is dominated by penninic metasediments and ophiolites as well as marginal east-alpine elements (phyllites, calcareous micaschists, dolomitic marbles, quartzite and gneisses). The eastern part of the landslide is aligned with the border of the Matriei-zone with the Glockner-nappe. The western border is mainly covered by loose sediments, outcrops are only visible at the top of the slope. The schistosity within the DGSD mainly dips at angles between 30° and 50° to SW - SSW, which corresponds to the regional settings of the Matriei-zone (Weidner, 2000).

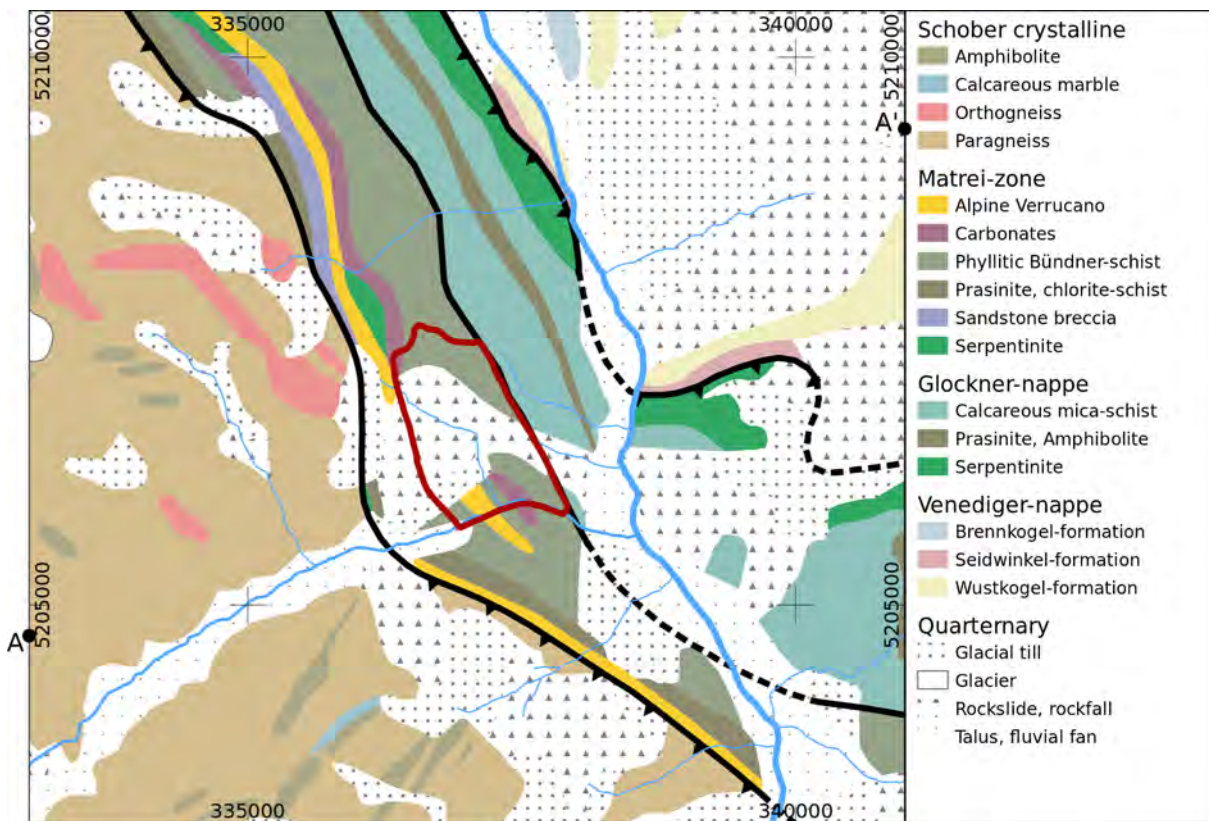


Figure 3.5: Overview map of the geological setting (reproduced after Brückl *et al.* (2013)). The points A and A' indicate the points of the cross section shown in figure 3.6.

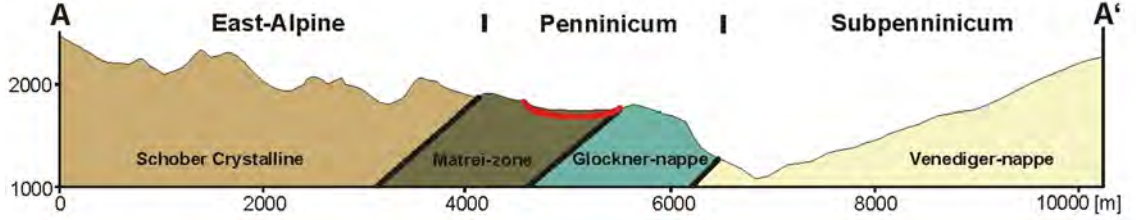


Figure 3.6: Cross section of the major geological nappes (reproduced after Brückl *et al.* (2013)).

3.3 Structure

The boundary of the slope deformation has been delineated by Moser & Glumac (1983) based on geomorphological and geodetic studies. Brückl & Brückl (2006) have used this boundary, the results of 5 seismic refraction profiles and the information from two boreholes to construct a model of the basal zone of the deep-seated gravitational creep Gradenbach (see figure 3.7).

The basal zone, which may be a discontinuity or a transition zone, defines the base of the moving rock mass. The maximum vertical depth of the basal zone is 130m and the computed volume of the sagging rock mass is $120 \cdot 10^6 \text{ m}^3$. The average P-wave velocity of the compact rock beneath the basal zone is 4740 m/s. Additionally to the refraction analysis of the seismic profiles, Brückl & Brückl (2006) have generated a 1D P-wave velocity model of the landslide rock mass by diving wave tomography using the first arrival travel time (see figure 3.8). Using a power law fitting to the data of the diving wave tomography the 1D P-wave velocity versus depth relationship has been computed:

$$V_p = 455D^{0.4}. \quad (3.1)$$

V_p is the P-wave velocity and D is the depth measured as a vertical to the surface. Similar relations exist for the deep-seated gravitational slope deformations Köfels, Lesachriegel (both Brückl, 2001) and Hochmais-Atemkopf (Brückl *et al.*, 2004). A combined review of all four 1D P-wave velocity relationships is given in Brückl & Parotidis (2005).

I have used the structural information and the velocity-depth relationship to create a 3D velocity model of the mass-movement (see figure 3.9) which was used for seismic event localization. Because equation 3.1 is defined for vertical depths, all computations of the velocity model were done in a rotated coordinate system. The x-y plane of the rotated, right handed coordinate system represents a reference datum which is a linear best fit to the digital elevation model within the boundary of the slope deformation. The y-axis is along the strike of the adjustment plane and the x-axis along its dip. Positive x points in the direction of the dip, positive z points downwards. The creation of the velocity model involved the following steps:

1. Rotation of the coordinate system (see figure 3.10).
2. Application of reduction values to the x-y-z coordinates so that the x-y plane aligns with the reference datum plane.
3. Creation of a regular xyz grid with equal grid-spacing of 10m, containing the boundary of the slope deformation. This grid will be used to compute the 3D velocity model.

3. THE DEEP-SEATED GRAVITATIONAL SLOPE DEFORMATION GRADENBACH

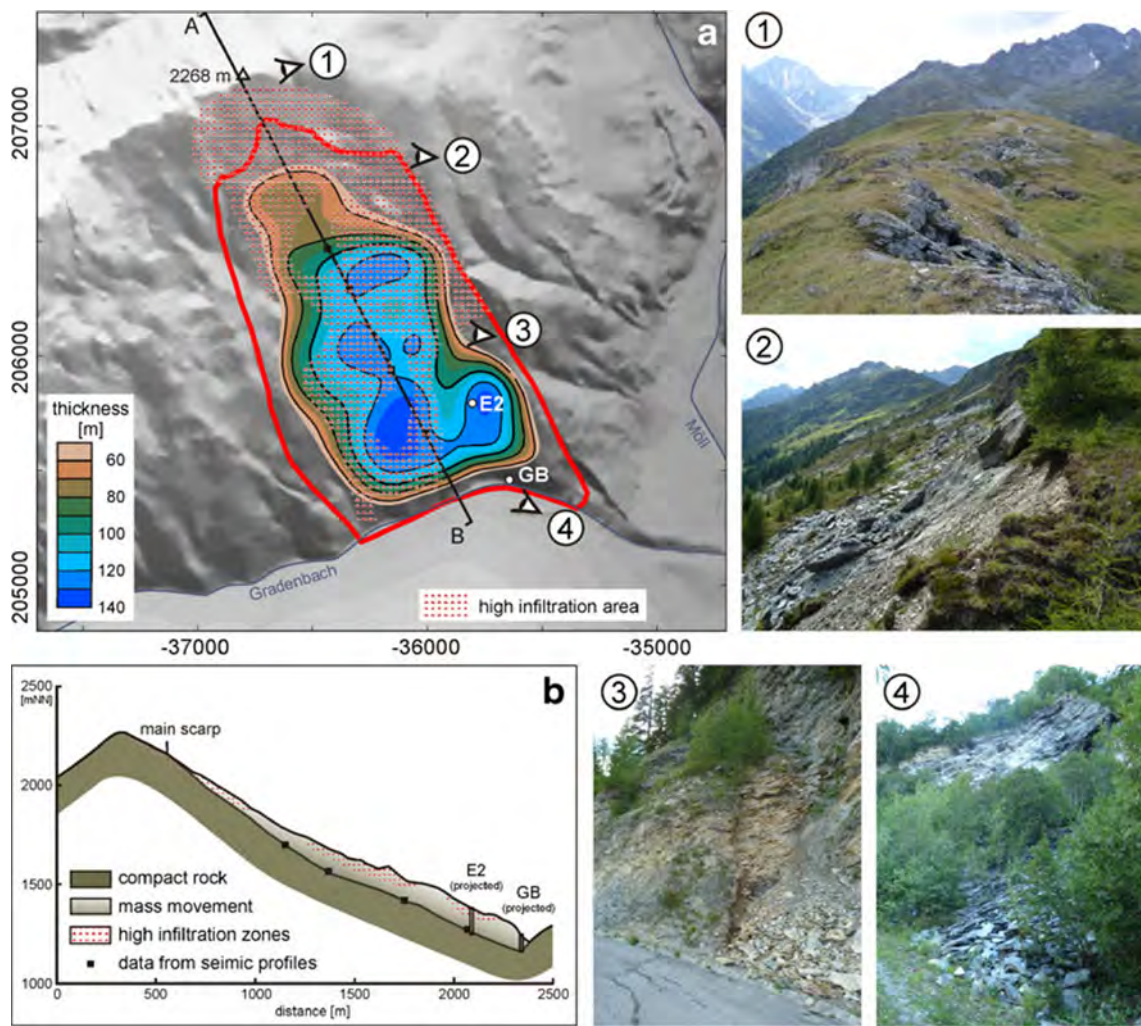


Figure 3.7: Structural model and morphology of the DGSD Gradenbach. (a) Boundary (red solid line) and the area of high infiltration of the mass movement (Moser & Glumac, 1983) are shown on top of a high resolution digital elevation model (DEM) (courtesy Bundesamt für Eich- und Vermessungswesen); contours and a color code show the thickness of the creeping mass according to Brückl *et al.* (2006); the boreholes GB and E2 mark boreholes with evidence of the basal zone; viewpoints of photos 1–4 are marked in the DEM. (b) Cross section through the slope along the profile A–B marked in (a). (source: Brückl *et al.* (2013))

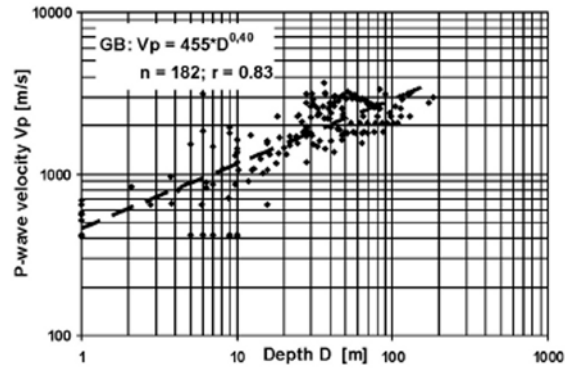


Figure 3.8: The 1D P-wave velocity relationship used for the construction of the 3D velocity model. The longitudinal seismic p-wave velocity is plotted against the the depth of the landslide mass (black squares). The dashed line is the exponential trend line given on the top left together with the number of data points (n) and the correlation coefficient (r) (reproduced after Brückl & Parotidis (2005)).

4. Creation of an landslide mass layer based on the boundary, the basal zone and the smoothed topography.
5. Creation of a P-wave velocity model of the landslide layer based on the 1D velocity-depth relation.
6. Below the landslide mass layer the velocity model is computed with a linear gradient of 1m/s per meter starting with the P-wave velocity 4000 m/s determined by refraction analysis of the seismic profiles for shallow depths of the landslide.

3. THE DEEP-SEATED GRAVITATIONAL SLOPE DEFORMATION GRADENBACH

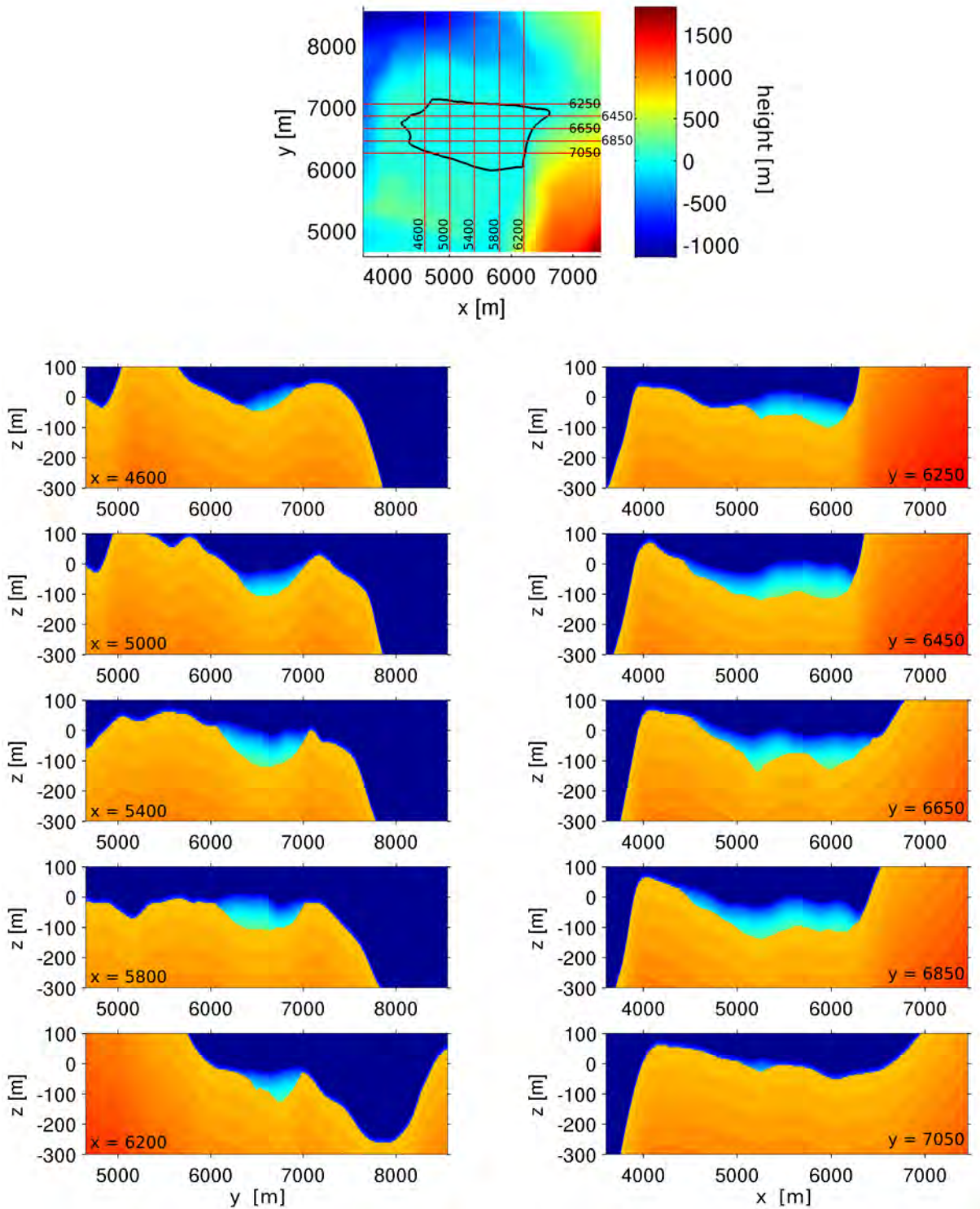


Figure 3.9: Slices along the x- and y axes of the 3D P-wave velocity model. The topmost image shows the rotated coordinate system with the boundary of the mass movement (black polygon) and the x- and y-slices of the velocity model (red lines).

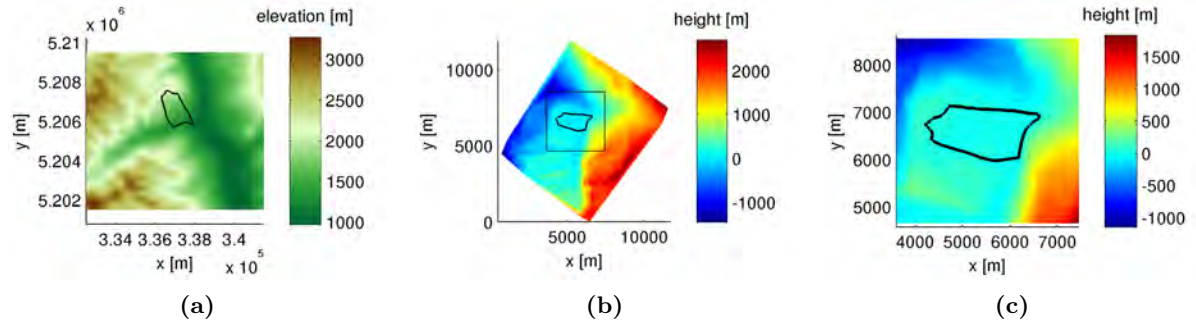


Figure 3.10: Creation of the rotated coordinate system. (a) is the digital elevation model (DEM) in the original coordinate system (epsg:32633), (b) is the DEM of (a) in the rotated coordinate system and (c) is a cropped version of (b) to create a DEM in the rotated coordinate system without missing values. The black polygon is the boundary of the mass movement, the black rectangle in (b) marks the area to which the DEM is cropped in (c). The DEM was provided by the Bundesamt für Eich- und Vermessungswesen (BEV).

3.4 A slope under observation

Similar to the start of passive seismic monitoring of mass-movements, a catastrophic event has initiated the monitoring of the slope deformation at Gradenbach. In 1965 and 1966, an acceleration of the Gradenbach landslide with a displacement of several meters induced rock-falls and debris flows at the toe of the slope which caused devastating flooding of the village Putschall. Due to this catastrophe, several monitoring projects on the slope have started in 1969 with geodetic-, geotechnical-, hydrological- and meteorological monitoring systems. Gottschling (1999) and literature therein give a good overview of the studies at Gradenbach.

In 1999, within the scope of the International Strategy of Disaster Reduction (ISDR) of the Austrian Academy of Sciences (OEAW), the existing monitoring systems have been extended by a GPS network (Brunner *et al.*, 2003) and in 2004, also as a part of the ISDR program, I have started the installation of a seismic monitoring network at Gradenbach.

Additionally to the permanent monitoring of the slope, several studies like active geophysics experiments and geological field mapping have been accomplished to better understand the structure of the DGSD Gradenbach. Table 3.1 summarizes all studies that have been accomplished at Gradenbach including references to existing literature, and the time line in figure 3.11 summarize the studies in a visual overview. The table and the time line list all studies accomplished at the mass movement, including those that are no longer running. The currently operating monitoring studies are outlined in the map in figure 3.12. A combined treatment of the continuous monitoring data has been published by Brückl *et al.* (2013). Most of the data recorded by the monitoring stations in figure 3.12 are transmitted in near real-time to a central data server and visualized online at the public website of the Gradenbach Observatory <http://gbonline.tugraz.at>.

The studies and monitoring projects mentioned above, some of them have been operating continuously up to now, have collected a huge data set covering the slope deformation for al-

3. THE DEEP-SEATED GRAVITATIONAL SLOPE DEFORMATION GRADENBACH

Organization	Description	Begin	End	Literature
Geotechnical				
BFW	Rock pressure in barrages	1971	1987	Kronfellner-Kraus (1980) Kronfellner-Kraus (1990)
WLV	Steel-band measurements	1972	1996	Weidner <i>et al.</i> (1998) Weidner (2000)
Fa. Interfels	Core drilling and inclinometer measurements Drilling of 3 boreholes (Gradenbach 1, Egg 1, Egg 2). Inclinometer measurements provided no usable results.	1978	1978	Gottschling (1999)
BFW	Wire extensometer at the toe of the slope. ET-1 (July 1979) ET-2 (June 1980)	1979	running	Kronfellner-Kraus (1980)
Moser	Geological, geotechnical and hydrological studies	1983	1986	Moser & Glumac (1983) Moser & Kiefer (1988)
Graz University of Technology	Strainmeter	2007	running	Lienhart & Brunner (2013) Brückl <i>et al.</i> (2013)
Geodetic				
BFW	Traverses Annual measurement of up to 5 traverses on the slope.	1968	1973	Kronfellner-Kraus (1980)
BFW	Geodetic measurement of 150 markers.	1968	1991	
University Karlsruhe University Erlangen	Geodetic measurement of 20 markers. Reduced in 1999	1979	unknown	Moser & Kiefer (1988) Weidner (2000)
Graz University of Technology	GPS Several GPS measurements per year. Since summer 2009 all-season monitoring	1999	running	Brückl <i>et al.</i> (2006) Brunner <i>et al.</i> (2003)
Vienna University of Technology	Photogrammetry study covering the period from 1962 to 1996	2006	2006	Brückl <i>et al.</i> (2006)
Hydrological & Meteorological				
BFW	Air temperature, precipitation and wind measured at 5 stations.	1968	running	Weidner (2000)
unknown	Combined tracer-experiment and hydrochemical analysis	1971	1972	Zojer & Zötl (1975)
University Karlsruhe	Combined tracer-experiment and hydrochemical analysis	1981	1982	Moser & Kiefer (1988)
BFW	Slope water level at borehole gauges. 22 gauges at the beginning, since 1999 13 gauges.	1979	running	Moser & Kiefer (1988) Weidner (2000)
BFW	Discharge measurements (3 springs) Graben-Quellmesswehr (started 1975) Berchtoldgraben (started 1975) Weidenbachl (started 1977/78)	1975	running	Kronfellner-Kraus (1980) Gao <i>et al.</i> (1997)
BFW	Water equivalent of snow cover. Measured at snow courses at altitudes between 1400m and 2100m in an interval of 100m	1985	running	Hagen & Lang (2000)
Geophysical				
Vienna University of Technology	Seismic monitoring	2004	running	Mertl & Brückl (2007b) Brückl <i>et al.</i> (2008b)
Brückl	Active seismics. 3 seismic profiles.	1978	1978	Brückl & Brückl (2006)
Vienna University of Technology	Active seismics. 2 seismic profiles.	1998	1998	Brückl & Brückl (2006)

Table 3.1: A list of all studies accomplished or currently running at the mass-movement Gradenbach. The literature reference give a starting point where to find information about the studies or where the study is explained best, they don't represent a comprehensive bibliography.

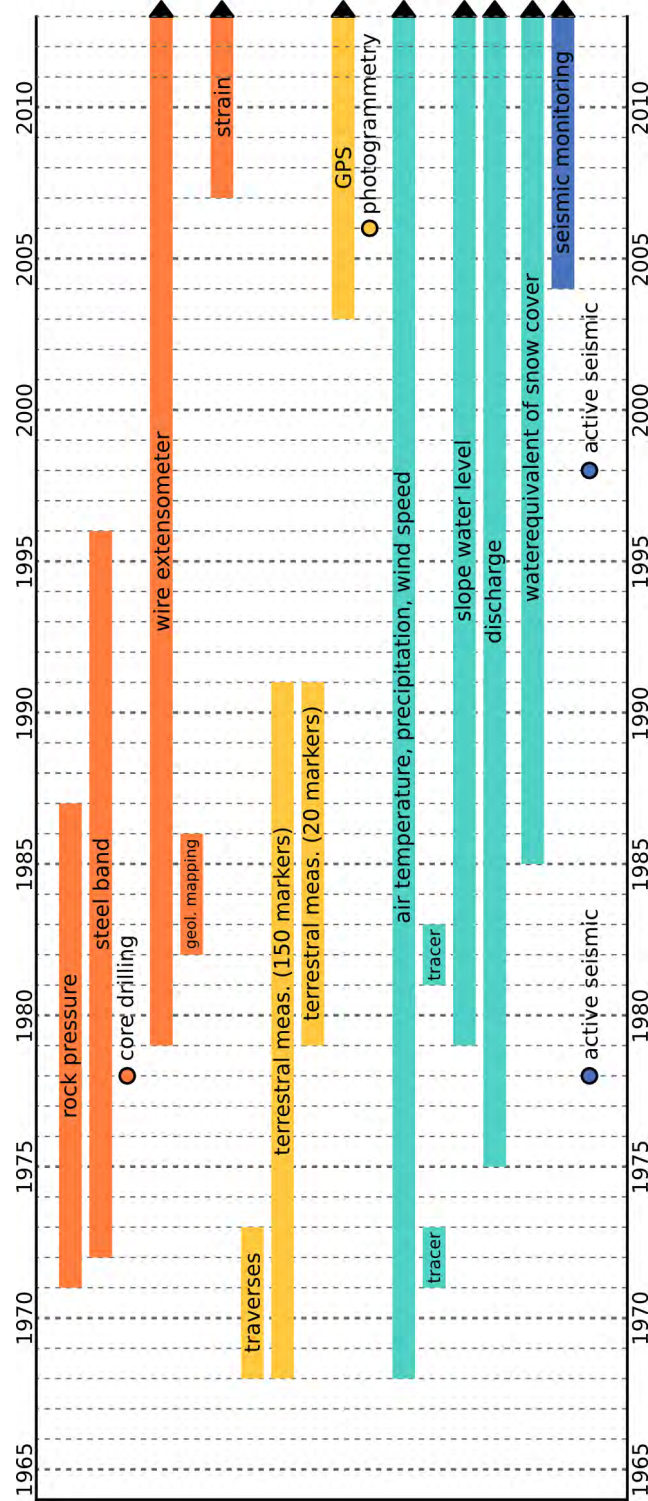


Figure 3.11: This time line gives an overview of the scientific studies accomplished at the mass movement Gradenbach. The bars with an arrow on the right side mark those monitoring studies that are still active. The colors of the time line bars highlight the four categories of table 3.1: geotechnical (orange), geodetic (yellow), hydrological & meteorological (light blue), seismic (dark blue).

3. THE DEEP-SEATED GRAVITATIONAL SLOPE DEFORMATION GRADENBACH

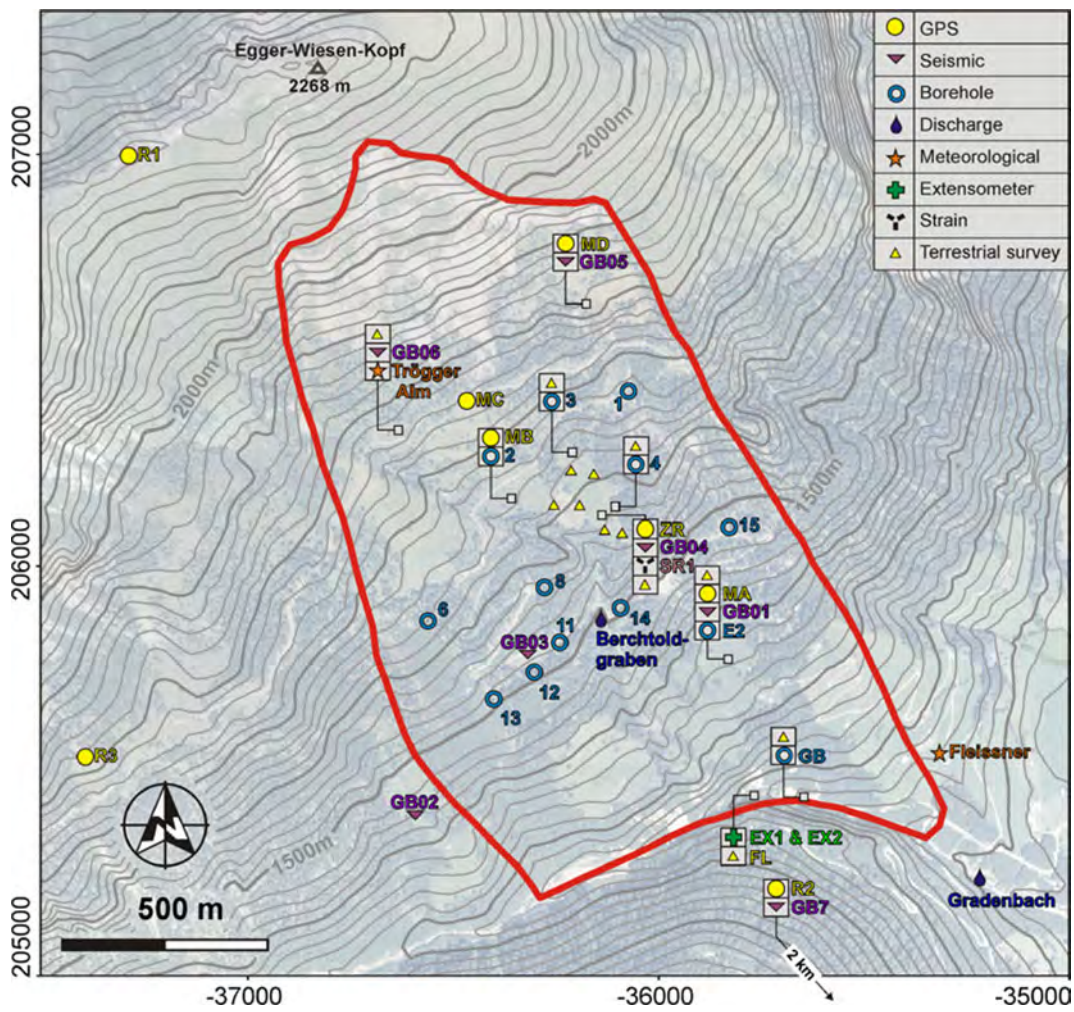


Figure 3.12: The map shows all currently active monitoring stations at the DGSD Gradenbach (Brückl *et al.*, 2013).

most half a century. The still ongoing, multidisciplinary monitoring of the mass-movement Gradenbach provides an outstanding opportunity to better understand the processes controlling the slope deformation. The data set covering the last decades gives valuable insights about the long-term behavior of the deep-seated gravitational slope deformation. Especially when regarding the on the average low velocity of the base activity, with eventually occurring accelerations of the slope, a long lasting and continuous monitoring is inevitable. The long duration of the continuous monitoring provides an in-depth knowledge of the long-time behavior of the slope and the continuous monitoring moreover guarantees to fully catch the sporadic occurring accelerations of the slope.

3.5 Kinematics

The historic summary given by Weidner (2000) mentioned first signs of a deformation of the Gradenbach mass movement visible on historic photographs in the second half of the 19th century. First reports of deformations of the slope are present from 1917 (Weidner, 2000). The instrumental, multidisciplinary monitoring of the slope has started in 1968 and produced a long-term observation of the slope deformation. Brückl *et al.* (2013) have reconstructed the deformation history of the slope from 1962 to 2011 using the data of various displacement observations (see figure 3.13). The deformation behavior clearly shows a base activity overlain by temporal variations of the slope velocity as described in section 2.2.

Brückl & Parotidis (2005) have used a rotational slider block model and the principle of progressive failure due to subcritical crack growth to predict the displacement of the Gradenbach mass-movement. The prediction has shown, that the Gradenbach mass-movement will continue accelerating and after a total slip of $\sim 100\text{m}$, a transition to rapid sliding is very likely (deformation type B). Only additional stabilization at the toe of the slope can stop this development. The assumption of a block movement of the landslide and the main deformation along a basal deformation zone made by Brückl & Parotidis (2005) is supported by the kinematics of the Gradenbach landslide derived from photogrammetric, GPS and geophysical data (Brückl *et al.*, 2006). Although, the long-term assumption of a block displacement of the slope is valid, short-term surface displacements of the slope measured by GPS showed lateral variations (Müller *et al.*, 2011) and a compressional behavior (Lienhart & Brunner, 2013). Most prominent is an earlier start of the surface displacement at the top of the slope compared to the toe of the slope (Müller *et al.*, 2011).

Derived from GPS- and extensometer measurements, the current base activity of the slope is $\sim 10\text{ cm/a}$ and the recent acceleration phase in 2009 has reached a maximum velocity of $\sim 0.8\text{cm/d}$. The comparison of the slope deformation with hydrological- and meteorological data indicate a seasonal influence of the snowmelt on the velocity of the Gradenbach mass-movement (see chapter 8). The relation between the hydrological parameters and the slope velocity has also been successfully modeled by Brückl *et al.* (2013).

3. THE DEEP-SEATED GRAVITATIONAL SLOPE DEFORMATION GRADENBACH

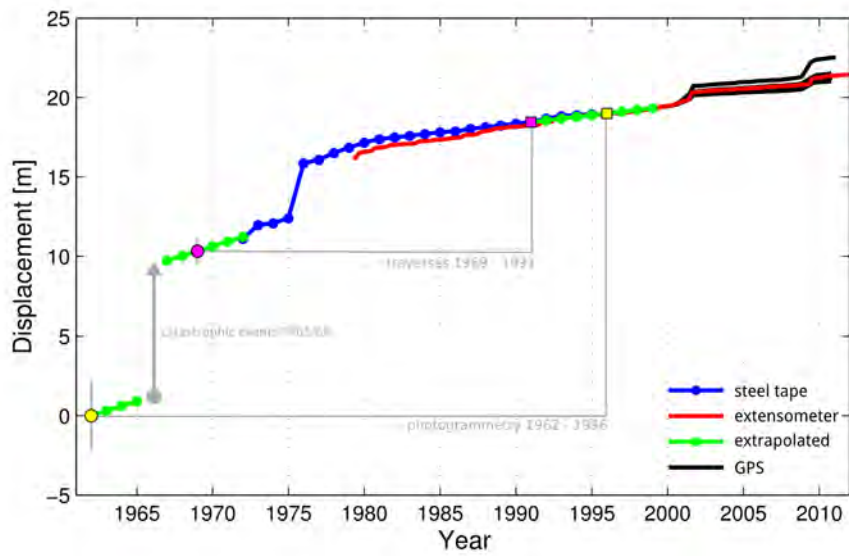


Figure 3.13: Reconstruction of the deformation history of the Gradenbach landslide for the period 1962 - 2011 (Brückl *et al.*, 2013).

4

Seismic monitoring network Gradenbach

Seismic monitoring at Gradenbach has started on September 7, 2004 with the installation of a single 3-component broadband station to get an overview of the seismicity present at the Gradenbach landslide. After the evaluation of this data and several short-term monitoring experiments (Brückl & Mertl, 2006; Brückl *et al.*, 2008b; Mertl & Brückl, 2007a,b) at the landslide, a permanent monitoring network consisting of 6 stations has been deployed at the Gradenbach mass-movement in May 2007. This network has been extended with a 7th station in August 2009. This research focuses on the data recorded during the year 2009, therefore the layout of the network is described for this period only.

4.1 Instrumentation and station layout

The station layout of the seismic monitoring network is given in figure 4.1. Six stations have been deployed on the mass-movement. The seventh station (GB07), which has been installed in August 2009, is located at a distance of approx. 3km from the slope and acts as a reference station at a stable location. The stations have been equipped with Reftek 130 data loggers, 4.5Hz or 1Hz 3-component geophones and solar power supply. Station GB05 additionally records the data of a standard microphone. A detailed listing of the used equipment can be found in table 4.1. The power supply of all stations consists of one 70W solar panel and a 12V 75Ah gel battery. The data is sampled with a sampling rate of 200 samples per second (sps) and stored locally on CF storage cards.

The electronic equipment is housed in a metal box (see figure 4.2b) and the geophones are buried at a depth of approx. 80cm. Figure 4.2a shows station GB02 as an example of the station's final look.

The microphone, which has been installed at station GB05 is used to identify sonic signals and the circuit design followed the J1-basic¹ circuit. The microphone circuit is powered by 2

¹http://volcanomodels.sr.unh.edu/jbj/MICROPHONES/microphone_list.html, accessed November 2013

4. SEISMIC MONITORING NETWORK GRADENBACH

alkaline batteries and the sensor output is digitized and recorded by the Reftek 130 data logger with 200 sps.

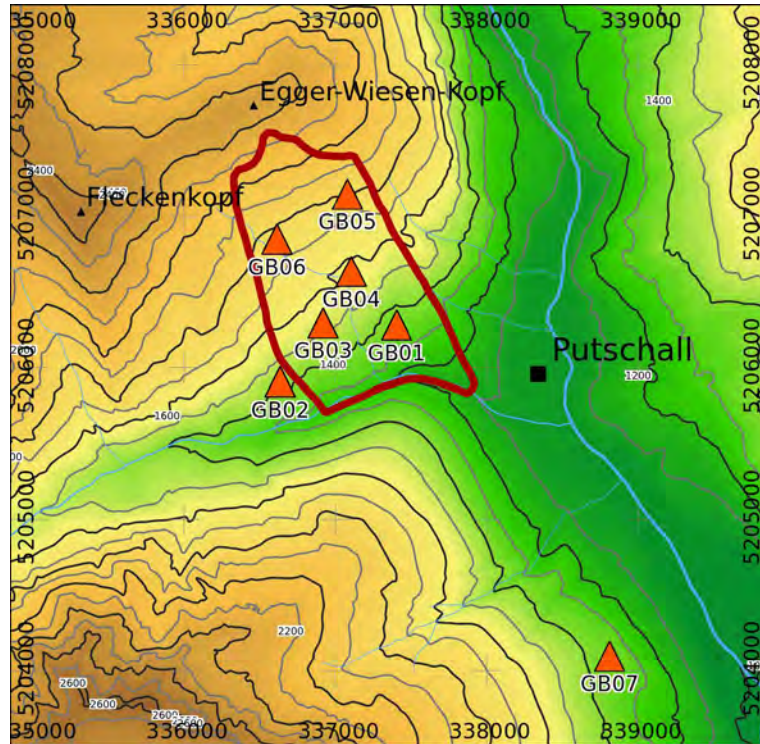


Figure 4.1: The station locations of the seismic monitoring network during the year 2009. Six stations (GB01 - GB06) have been operating on the slope. The seventh station (GB07) was installed in autumn 2009. The digital elevation model was provided by the Bundesamt für Eich- und Vermessungswesen (BEV).

4.1 Instrumentation and station layout

Stations	datalogger	Sensor
GB01, GB02, GB03, GB06 and GB07	Reftek 130	Geospace GS-11D 4.5Hz, 3C, shunt 18200, dc res. 4000
GB04	Reftek 130	Geospace Seismonitor 1Hz, 3C Microphone (11.6.2009 - 7.9.2009)
GB05	Reftek 130	Geospace GS-11D 4.5Hz, 3C, shunt 18200, dc res. 4000 Microphone (from 7.9.2009)

Table 4.1: Equipment used at the seismic monitoring network Gradenbach.



(a)



(b)

Figure 4.2: Station GB02 (a) and the metal box containing the Reftek data logger, the solar regulator and the battery (b).

4.2 Available data and data quality

Figure 4.3 gives an overview of the available data for the year 2009. The missing data at the beginning of the year was caused by the strong winter 2008/2009 with a lot of snowfall, which completely covered the solar panels. From May on, an average of 5 stations have been operating.

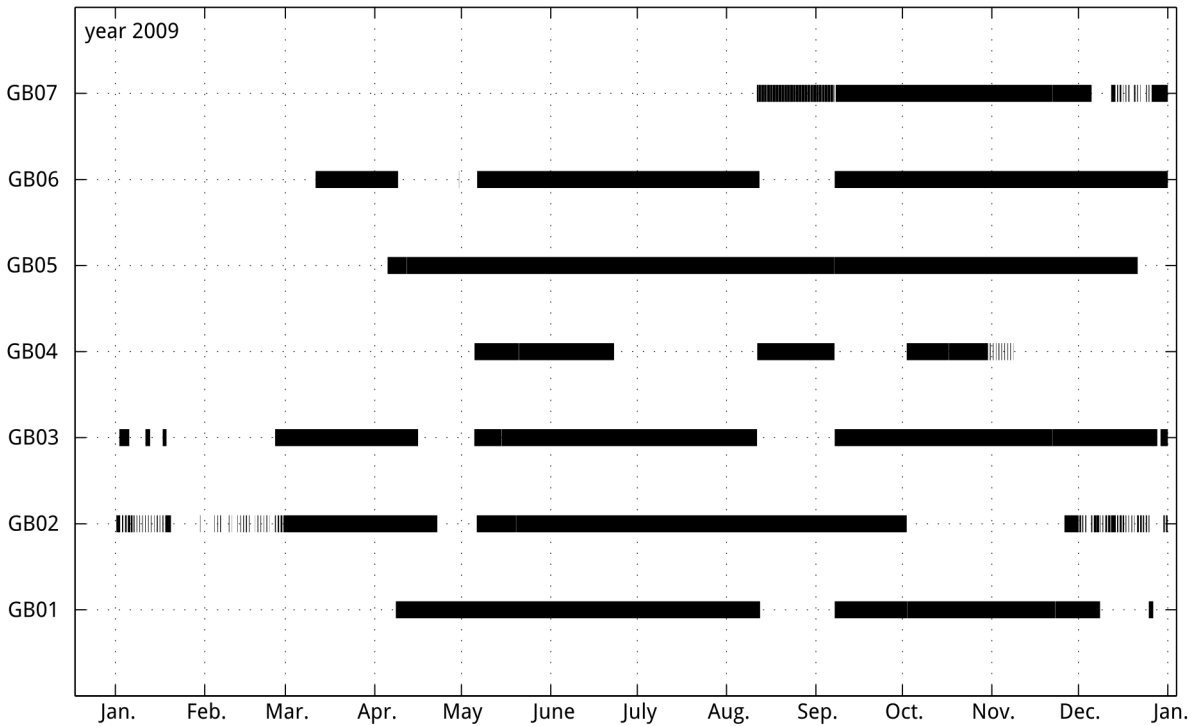


Figure 4.3: The available data of the monitoring network Gradenbach for the year 2009. The black, horizontal bars mark the timespan for which data is available.

The data recorded at Gradenbach is of high quality. The remote location results in a low background noise level. Figures 4.4 and 4.5 show the probability density function (PDF) of the seismic noise computed for the year 2009. The computation of the PDFs follows McNamara & Buland (2004), but no averaging of the frequency bins has been done to conserve the full information contained in the high frequency range of the spectra.

To compute the power spectrum density (PSD), and thereafter the PDFs, the data to be analyzed was split into 1 hour long time series with an overlap of 75%. For each of the hourly segments, a PSD was computed (Havskov & Alguacil, 2004). Each segment was again split into parts of 8192 samples length. These parts were windowed with a 10% Tukey window and the PSDs of the individual parts were computed. The scaling effect due to the windowing of the data was removed by multiplying the amplitude spectrum with the inverse coherent gain of the window (Harris, 1978) before computing the PSD. The coherent gain g of a window w of the length N was computed by:

$$g = \frac{\sum_{n=0}^{N-1} w_n}{N} \quad (4.1)$$

. Finally, the instrument response was removed from the PSDs by multiplication with the inverse amplitude spectrum of the frequency response of the seismometer. To compute the frequency response of the geophones, the seismometer frequency response with a damping of $h = 0.707$ was used. The transfer function $T(s)$ of a velocity-transducer in the Laplace domain is

$$T(s) = \frac{-s^2}{s^2 + 2h\omega_0 s + \omega_0^2} \quad (4.2)$$

, where h is the damping and ω_0 the corner frequency. To compute the one-hour PSDs, all 8192 samples long segments contained in one hour were averaged.

The PDFs presented in figures 4.4 and 4.5 have been computed using the available data from 1. April 2009 to 1. October 2009. They give a general overview of the seismic background noise frequency characteristic at Gradenbach. The seismic background noise is bound to the lower part of the new noise models introduced by Peterson (1993). It can be seen, that after removing the instrument response, the 4.5Hz geophones have a reasonable signal content down to periods between 2 and 5 seconds. Below this period non-seismic (e.g. electronic) noise is amplified by the inverse filtering with the frequency response of the seismometer and the seismogram in this frequency range does not reflect the ground-motion anymore. The 1Hz geophone located at station GB04 can be extended down to 10 seconds. When comparing the median lines of the day- and nighttime data (light- and dark purple lines in the plots), a clear difference between the day- and nighttime is visible. The change of the seismic background noise with the time of day implies anthropogenic sources being the cause for raising the noise level within this frequency range. One can also see quite large differences between the stations themselves. Station GB01 shows a generally higher amplitude over the whole frequency range which can be caused by local soil amplification effects. Moreover, the spectrum PDFs reveal several modes between 1Hz and 2Hz which are present at all stations except the reference station GB07 during the whole day. Overall it can be said, that the spectrum PDFs not only proof the high quality - low noise of the recorded seismic data, but reveal interesting signal content, that might be connected to the Gradenbach mass-movement. A detailed study of the seismic background noise to analyze the seismic sources contributing to the background noise level has been carried out by Andrea Draxler within the framework of her master thesis “Seismic Noise Analysis at the Gradenbach Landslide” (Draxler, 2013).

4. SEISMIC MONITORING NETWORK GRADENBACH

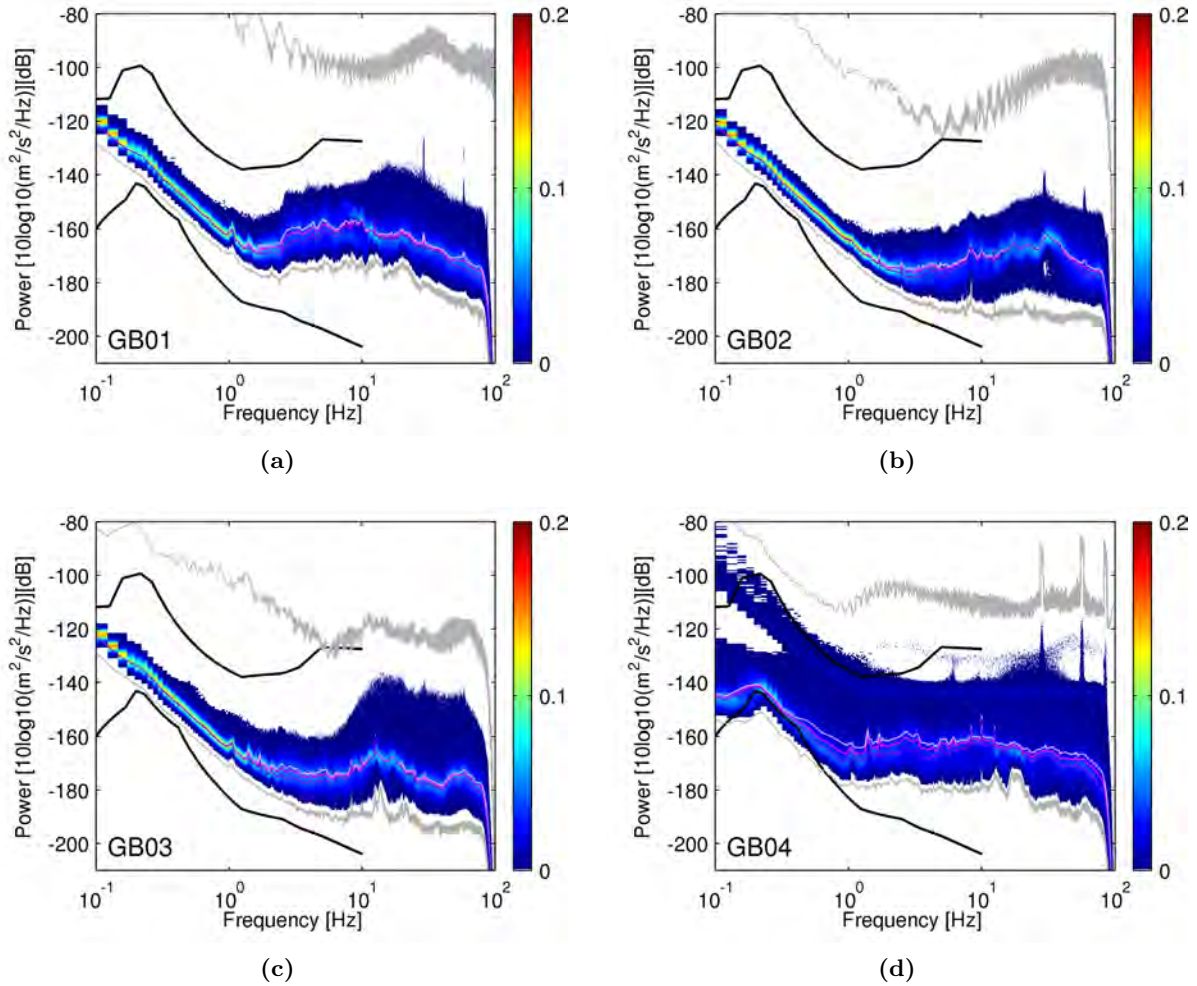


Figure 4.4: The images a to d show the PDF of the stations GB01 to GB04 respectively. All available data of the year 2009 has been used for the computation of the spectra. black lines: new low noise model (NLNM) and new high noise model (NHNM); gray lines: minimum and maximum values; magenta line: median; dark purple line: median using the night-time data only; light purple line: median using the day-time (between 4:00 and 20:00 UTC) data only;

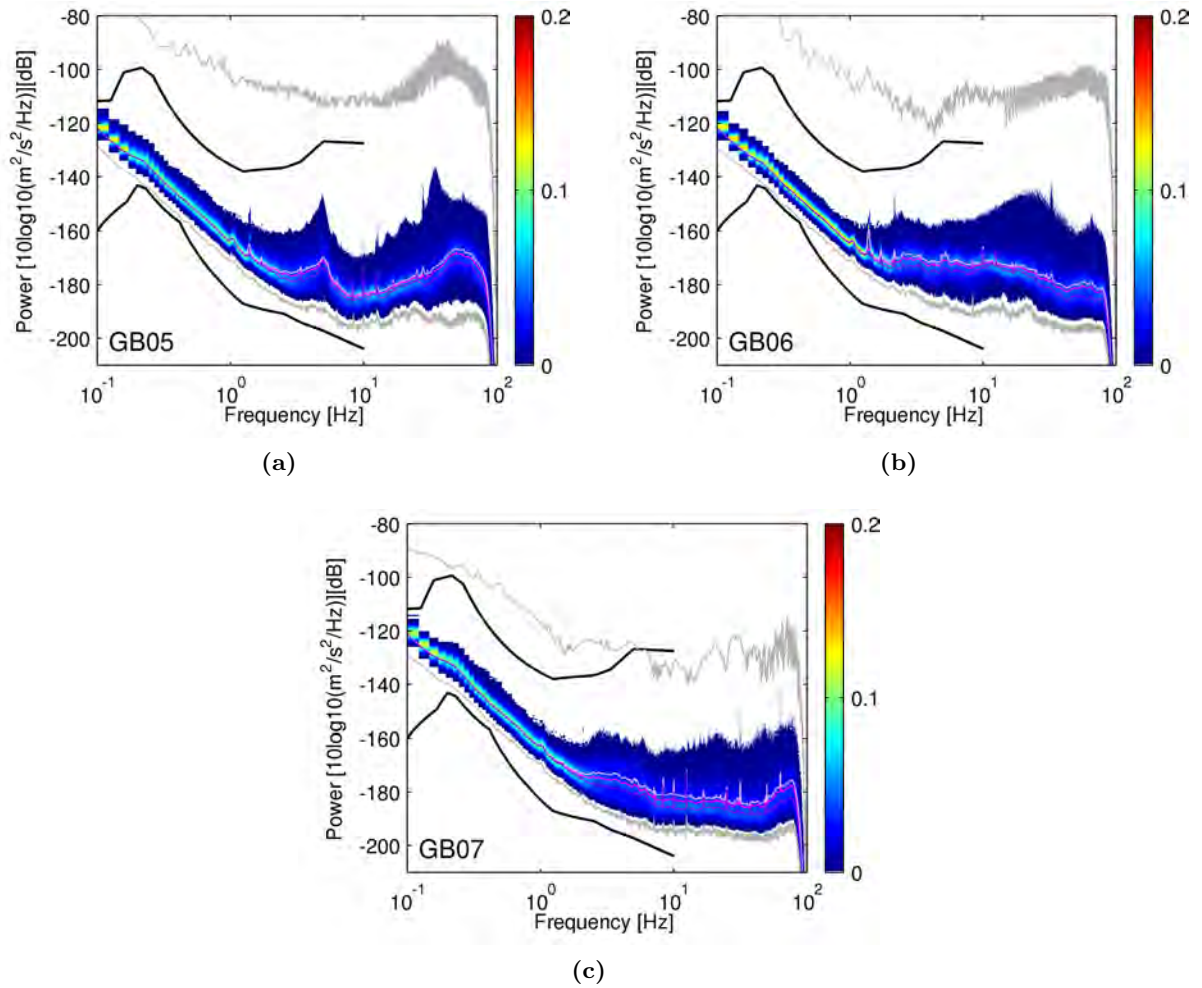


Figure 4.5: The images a to d show the PDF of the stations GB05 to GB07 respectively. All available data of the year 2009 has been used for the computation of the spectra. black lines: new low noise model (NLNM) and new high noise model (NNNM); gray lines: minimum and maximum values; magenta line: median; dark purple line: median using the night-time data only; light purple line: median using the day-time (between 4:00 and 20:00 UTC) data only;

4.3 Detection Threshold

The detection threshold magnitude was empirically determined comparing the earthquake catalog compiled by the Central Institute for Meteorology and Geodynamics (ZAMG) with the earthquakes recorded with the Gradenbach seismic network. The magnitude was computed by scaling the measured amplitude of an earthquake at a station with a given epidistance with an empirically determined distance-dependent amplification factor and a constant regional correction factor. The general form of the magnitude formula is

$$M = \log_{10} \left(\frac{A_d}{T} \right)_{max} + Q(\Delta, h) + C \quad (4.3)$$

, where A_d is the displacement amplitude, T the corresponding period, Q the calibration function dependent of epidistance Δ and focal depth h and C a regional- and station dependent correction term. Keeping the max. amplitude term and the focal depth in equation 4.3 constant and varying the epidistance results in a straight line in the semilogarithmic magnitude-distance plot (see figure 4.6), that is, the same measured amplitude at a station can be produced by events with various magnitudes increasing with the epidistance. The amplitude dependency used in figure 4.6 is

$$Q(\Delta) = 1.66 \log_{10}(\Delta) \quad (4.4)$$

. This amplitude dependency is used in the local magnitude formula used by the ZAMG:

$$M_L = -0.304 + \log_{10}(A_{vel}^{max}) + 1.66 \log_{10}(\Delta) \quad (4.5)$$

, where A_{vel}^{max} is the max. velocity in nanometer/s and Δ is the epidistance in degree.

For example, as illustrated in figure 4.6, at a fixed station S_1 , an earthquake E_1 at epidistance R_1 with magnitude M_1 creates the same amplitude as an earthquake E_2 at a larger epidistance R_2 with a larger magnitude M_2 . In reverse, one can assume, that if the large event at R_2 is recorded at station S with a sufficient signal-to-noise ratio, the weaker event at R_1 , producing the same amplitude, must be detected as well. This converse argument was used to determine the detection threshold magnitude of the Gradenbach seismic network. The lowest detectable magnitude was determined for earthquakes with large epicentral distances for which reliable hypocenters and magnitudes were determined by the ZAMG. This detection threshold magnitude at large epicentral distances and the amplitude-distance relation were used to extrapolate the threshold magnitude at smaller epicentral distances.

First, all earthquakes recorded at the Gradenbach seismic network and listed in the ZAMG earthquake catalog were plotted on a magnitude-distance plot (figure 4.7). Local earthquakes with epicentral distances between up to 150 km were used. Next, the lower limit of detectable magnitudes was visually determined and a line representing the amplitude-distance relation $1.66 \log_{10}(R)$ was fitted to this limit. Along this line, the detection threshold magnitude was extrapolated to an epidistance of 500m, which is the mean station spacing of the network.

This method gave a detection threshold of the monitoring network Gradenbach $M_L = -2.3$ at an epidistance of 500m.

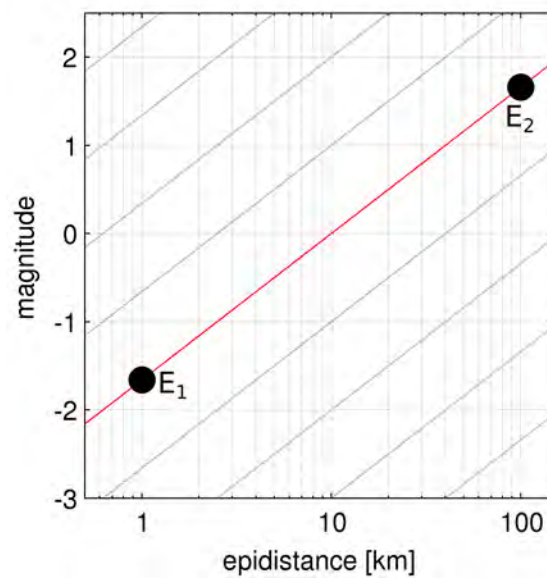


Figure 4.6: Plot of the amplitude distance relation $1.66 \log_{10}(R)$ used in the local magnitude equation of the ZAMG. Each gray line represents all possible magnitude-epidistance combinations with a constant recording amplitude. The red line highlights one of these magnitude-epidistance combinations, which connects the two earthquakes E_1 and E_2 having the same recording amplitudes at a common station.

4. SEISMIC MONITORING NETWORK GRADENBACH

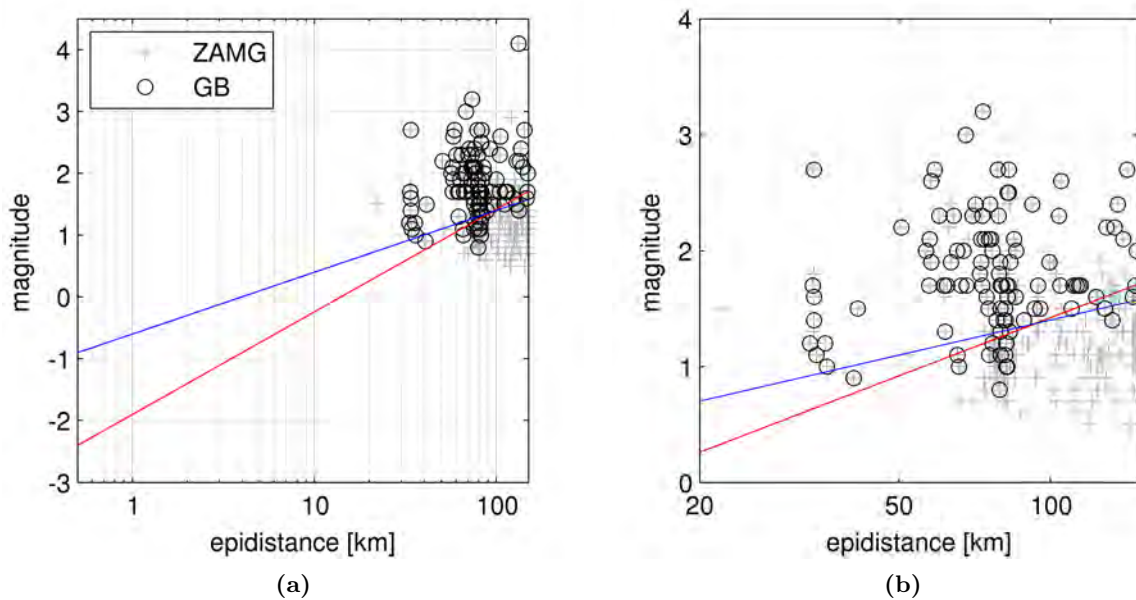


Figure 4.7: Comparison of the magnitude-epidistance relation of the earthquakes listed in the ZAMG catalog (gray plus) and the earthquakes detected at the monitoring network Gradenbach (black circles). The detection threshold magnitude is determined by extrapolating the lower limit of the detected local earthquakes using the amplitude-distance relation $1.66 \log_{10}(R)$ (red line). For comparison, the blue line shows the amplitude-distance relation $\log_{10}(R)$ to highlight the sensitivity of the detection threshold to the amplitude-distance relation.

4.4 Data handling

The recorded data were stored locally by the Reftek 130 data loggers on CF storage card (2x4GB or 2x8GB cards are used). With the total storage capacity of 8GB, 3.5 months of 3-channel data sampled at 200sps can be stored (16GB allow up to 7 months of recording). In frequent intervals of 3 to 4 months a trip (so-called service-run) to Gradenbach was done to download the data from the stations by swapping the CF storage cards with empty ones. The service-runs were also used for a general inspection of the equipment and maintenance work at the stations.

The data was recorded in the Program for Array Seismic Studies of the Continental Lithosphere (PASSCAL) recording format (RefTek, 2011). The raw data was archived using the Reftek arcutils tools. The arcutils tools create a raw data archive which can be inspected for available data and from which the data for specified time periods can be extracted. From this archive, hourly miniseed files were created using the programs arcfetch and rt_mseed, which are both provided by Reftek. The miniseed archive was the data source for all further data processing.

4.5 Processing software - Seismon

The data processing was done using the software *Seismon* (see Appendix A) which has been developed within the framework of this study. *Seismon* has been started to support the data processing of non-standard seismological monitoring studies working with continuously data. It's main focus is to provide an easy-to-use graphical user interface (GUI) for data visualization and to provide a framework to develop new algorithms and to test them on real-world data. To fulfill these goals, MATLAB has been chosen as the programming language. *Seismon* is licensed under the Gnu General Public License (GPL).

Seismon is based on a modular approach. That is, by following a few interface design rules new code can be integrated into *Seismon* without changing the source code of the main program. This makes it very easy to quickly add new algorithms for experimenting and testing. More details about the software design can be found in Appendix A.1. The main features provided by *Seismon* are:

data import

The import of miniseed, GSE2.1, SAC and SEG-Y file formats is supported.

station inventory

Editing and visualization of the station layout and the sensor deployment.

data visualization

Visualization of continuous time series, time- and amplitude picks, event markers (e.g. bulletin earthquakes).

processing tools

Various processing tools like frequency filtering, time- and amplitude picking, time-frequency analysis, frequency spectrum, instrument response removal, integration and differentiation, ...

event management

Database driven management of event markers. Events can be searched and the data

4. SEISMIC MONITORING NETWORK GRADENBACH

of selected events can be visualized.

batch processing

A list of events can be processed with user-defined processing tools.

5

Event detection

Event detection in seismology is usually a variation of the STA/LTA detection introduced by Allen (1978). The STA/LTA algorithm is based on the comparison of a long time average (LTA) and a short time average (STA) of one or more features computed from the seismological data. The derived features are named characteristic function (CF) by Allen. The most simple examples of a CF are the absolute value or the square of the amplitude of a time series. The LTA of the characteristic function models the seismic noise. Seismic noise is regarded as “*that part of the data that we chose not to explain*” (Scales & Snieder, 1998). Short-term variations of the seismic data, which are regarded as events (e.g. earthquakes), is represented by the STA of the characteristic function. Whenever the STA exceeds the LTA by a given ratio (the threshold value) an event is declared. The STA/LTA detector is a fast and easy to implement event detector which makes it still the detector of choice in near real-time data processing. Routine earthquake processing tools like Earthworm¹ use the original algorithm by Allen (1978) (Johnson *et al.*, 1995) and digitizer/data logger running in event-triggered mode also rely on the STA/LTA event detection to record only the signal of interest and withdraw the non-relevant noise.

Besides the standard STA/LTA detector (Allen, 1978) of course many detection algorithms have evolved over time. Some of these are a variation of Allen’s algorithm using more sophisticated CFs (Wagner & Owens, 1996, e.g.), others pursue a completely different approach for example using pattern matching (Joswig, 1995, 1996, e.g.). Reviews of the detection algorithms used in seismology have been given by Allen (1982), Joswig (1990), Withers *et al.* (1998) and Ohrnberger (2001, chap.4). Withers *et al.* (1998) has categorized the previous works done on the topic of event detection into time domain, frequency domain, particle motion processing, and pattern matching methods. This categorization has been based on the features computed from the seismological data which are used as an input of the detection algorithm. Ohrnberger (2001, chap.4) have defined a similar categorization based on the computed features: a) single station single component recordings (SSSC), b) single station three component seismograms (SS3C), and c) multi-station single/three component data (MSS/3C).

When monitoring the seismic activity on landslides using small-scale, surface based networks

¹<http://www.earthwormcentral.org/>

5. EVENT DETECTION

several challenges have to be accepted. Although the noise level in alpine area can be expected to be low, it may vary heavily from station to station and with the time of the day. In contradiction to the unpredictable and sometimes bad noise condition, usually it is desired to lower the detection threshold as much as possible to catch even the weakest signals. This may result in searching for events (e.g. earthquakes) which lie within the noise-level and can only be identified in certain frequency bands and using information from multiple features (e.g. 3-component recordings on multiple stations) and the knowledge of a human operator to connect the different features with each other. This human knowledge is of special value if the seismic data is searched for events which might not have been registered before and therefore are hard to be recognized by an automatic detection method. Besides the goal of detecting events as weak as possible, reasonable statements about the seismic activity demand a long term monitoring. This results in a large dataset which has to be studied. This is done easiest with an automated detection method, which is in obvious discrepancy to the desired human operator mentioned before.

Although there are some approaches for automatic event detection and classification using multiple features and/or multiple stations (e.g. Köhler *et al.* (2009); Ohrnberger (2001)), I think that currently, in the field of weak event detection, the knowledge and intuition of a human operator has to be part of the detection and classification process. Therefore a semi-automatic event detection has been used to detect and classify the seismic events of this research. Manfred Joswig, who has done a lot of work in exploring the possibilities of using pattern recognition methods for seismic event detection (e.g. Joswig (1990, 1996)), has developed the nanoseismic monitoring method (Joswig, 2008). This method is using data from tripartite sparse arrays for detecting and locating event. The NanoSeismicSuite¹ software provides tools for visual event screening (Sick *et al.*, 2012) which allows the processing of the data similar to computer aided diagnostics as it is widely used in medicine (e.g. tumor diagnostics). There, an easy to read representation (most often an image) of a dataset containing as much information as possible and highlighting the most important features is presented to the human operator. Based on this representation the operator then decides about the importance of the shown data. In the case of the seismic event detection this would be the question: Is the presented signal a seismic event relevant to the monitoring project or not?

To answer this question image processing techniques applied to the time-frequency transformation of the seismogram have been used in this research to extract signal patterns which stand out against the general noise. The time-frequency transformation is the most intuitive way to get a lot of information at one sight about the signal content of the seismogram. For visual screening of the seismic data, the time-frequency transformation with the highlighted extracted patterns of all seismic stations have been presented to the user who has decided which pattern to consider as a seismic event of further interest. The three major steps of the presented event detection method are:

Pattern extraction

Using seeded region growing applied to the spectrograms, the patterns representing any variation from the general seismic noise are extracted.

Event binding

Cluster analysis is used to connect related patterns on multiple stations to each other

¹NanoSeismicSuite available from <http://www.nanoseismic.net>, accessed June 2012

to form an event.

Event screening

The seismic data (seismograms and spectrogram of all stations) is screened by an operator guided by the information provided by the two steps above.

With these steps, the detection method used for this research can be classified as a multiple station, single component (MSSC) algorithm using multiple features from the time-frequency domain as the characteristic function.

5.1 Pattern extraction

The basis for the pattern extraction method is the spectrogram of the seismogram. It is computed as the short time Fourier transformation of the seismogram. The advantage of the spectrogram is that it visualizes the signal in a way that is very easy to understand for humans. Humans are very well trained to handle visual information and when taking a look at the spectrogram in figure 5.1 it is an easy task to identify the interesting signals even in a noisy seismogram. It's even more easy to mark them using a pen by drawing a border around the patterns as shown in figure 5.2. This simple example shows the incredible power of human visual examination. Just by taking a look at the image, several partly overlapping events can be recognized. Also some classification has already been done when identifying the horizontal lines as electronic noise. The process illustrated in figure 5.2 seems to take almost no time but it includes many sophisticated and also knowledge based decisions. The challenge is to simplify these decisions and to translate them into processing steps which a computer can run in an automated way to process a large amount of monitoring data.

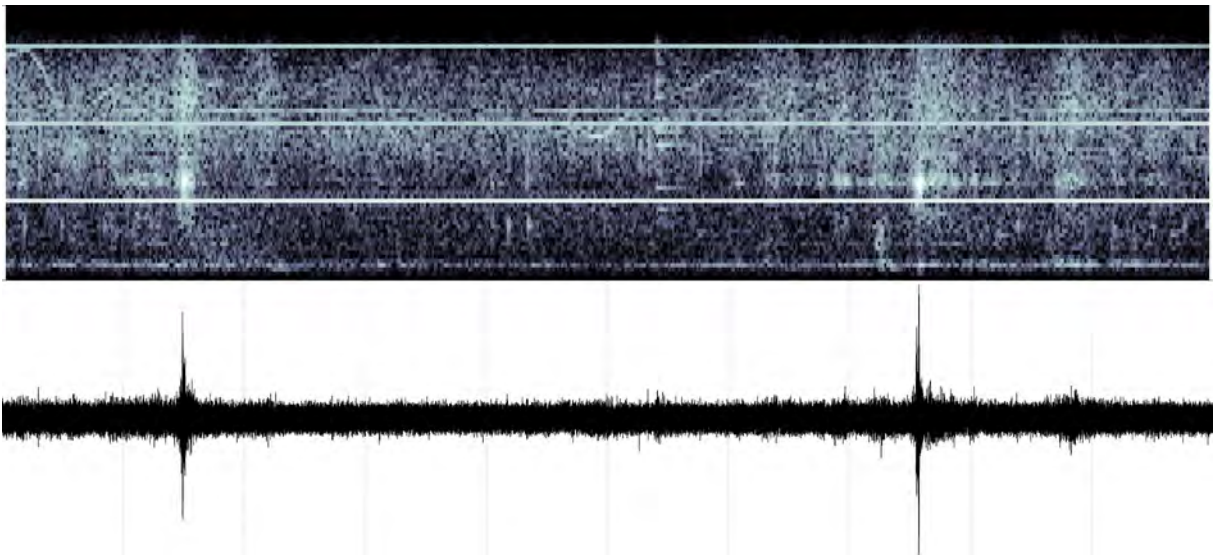


Figure 5.1: Seismogram (bottom) and spectrogram (top) of a 5 minutes recording at Gradenbach. The axes of the seismogram and spectrogram are omitted on purpose because for the detection process, which treats the spectrogram as an image, these values are not of interest.

5. EVENT DETECTION



Figure 5.2: Simple detection of event patterns using a printout and a pen. For humans it is very easy to quickly outline connected patterns in the spectrogram, even if they are overlapping. With some background knowledge and experience characteristic events can also be classified (e.g. electronic noise).

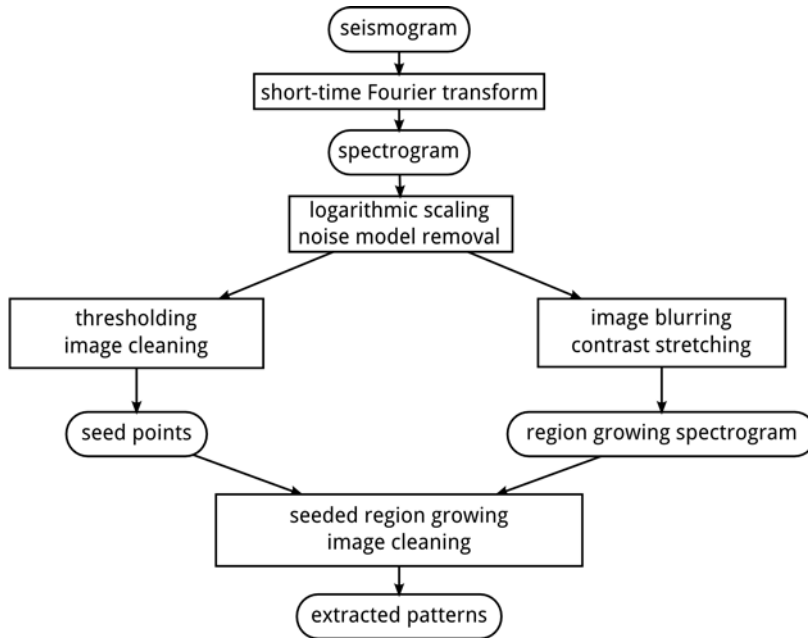


Figure 5.3: The flowchart of the pattern extraction processing steps.

The major steps of the pattern extraction are (a) compute the spectrogram of a seismogram (b) find all signals in the spectrogram and (c) extract these signals from the spectrogram image. The flowchart in figure 5.3 outlines the processing steps used to extract the patterns from the spectrogram. The processing starts with the computation of the spectrogram as a short-time Fourier transformation (SFT) using the spectrogram function of MATLAB. During the whole processing, the spectrogram is treated as an image without any physical background. For both processing tracks, the seed point generation and the region growing spectrogram, the logarithmic transformation

$$g_{ij} = \log_{10}(1 + f_{ij}) \quad (5.1)$$

, where f_{ij} is the input image and g_{ij} is the output (processed) image, is applied to the spec-

trogram. The indexes i and j represent the x- and y-axes, respectively. The logarithmic transformation enhances the image by compressing the dynamic range of the spectrogram. This is important when visualizing the image on a computer screen using a color-map with limited amount of colors.

Next, to find all the signals in the spectrogram a definition of “the signal“ is needed. Without any a priori knowledge of the events which can be expected, the most general definition of a signal is used. The definition of seismic noise given by Scales & Snieder (1998) is: Seismic noise is regarded as *“that part of the data that we chose not to explain“*. Therefore, a signal is that part of the data that is not noise. If it is not possible to directly define what a signal is, it is much easier to go the other way round and define what is noise, remove the noise from the spectrogram and treat the remaining part as the signals.

When taking a look at the spectrogram image and how a human searches for signals, it’s obvious, that a human interprets a signal as something that shows an unusual variation from the average value of the parameter under observation. In other words: a person searches for patterns that are not noise. Using the spectrogram as an example, the parameter under observation is the amplitude of the spectrogram represented by the gray-value of the spectrogram image. The signals are the bright spots with high amplitudes that vary over time from the average gray-level of the frequency bins.

To compute a representation of the noise model of the spectrogram, the average value of the image along the time-axis can be used. This noise model represents the general seismic background noise as well as any other signal disturbances (e.g. electronic noise) that don’t change with time over the processed timespan. The noise model h_j is given by the median value of the spectrogram along the time-axis, and the variation of the noise from the mean value which is given by the standard deviation:

$$h_j = \text{median}_i(g_{ij}) + C * \text{std}_i(f_{ij}) \quad (5.2)$$

where median_i the median of the image g_{ij} for frequency bin j (along the time axis i), C a constant (usually between 1 and 2), std_i the standard deviation of the image g_{ij} for frequency bin j . Figure 5.4 shows the spectrogram with logarithmic transform and the computed noise model. The standard deviation is added to the median to raise the noise-level with a parameter, that dynamically adapts to the noise situation of the processed time-span, thus avoiding the usage of fixed threshold values to describe the noise variation. According to Joswig (1995), the correct choice of the noise-level is important in classic detection theory to lower the false-alarm rate, but for pattern recognition, as well as pattern extraction, the influence of the noise-model is less crucial. False detections are accepted and eliminated in later steps by event classification. The raise of the noise-model by the standard deviation multiplied with a constant ensures a more robust extraction of the signal patterns with a drawback of less exact determination of signal limits.

To remove the noise model from the spectrogram image g_{ij} , the noise model h_j is subtracted from the spectrogram to compute the denoised spectrogram g_{ij}^d :

$$g_{ij}^d = g_{ij} - h_j. \quad (5.3)$$

All pixel values smaller than zero are set to zero and the denoised image g_{ij}^d is converted to a

5. EVENT DETECTION

gray scale image with intensity values between 0 and 1 for further processing. The noise removal eliminates the stationary transients (e.g. electronic hum) and highlights any variation from the seismic background noise (see figure 5.5).

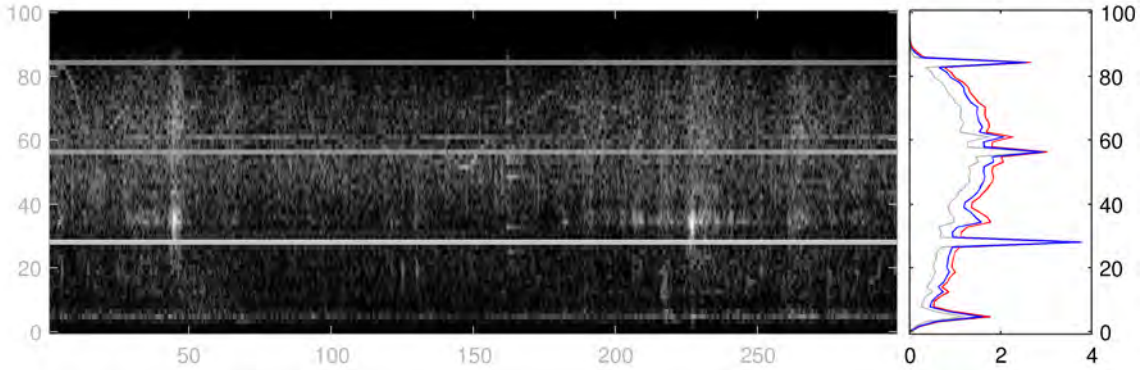


Figure 5.4: Computation of the noise model. The logarithmic scaled spectrogram is shown on the left. The noise-model is computed using the median (M50 percentile, gray line on the left) of each frequency bin and adding a representation of the noise variation. This variation can be represented by the differences of the M75 - M50 percentiles or the standard deviation (each computed along the frequency bins). The blue line on the left shows the M75-M50 difference added to the median and the red line is the standard deviation added to the median. (x-axis: time [s]; y-axis: frequency [Hz])

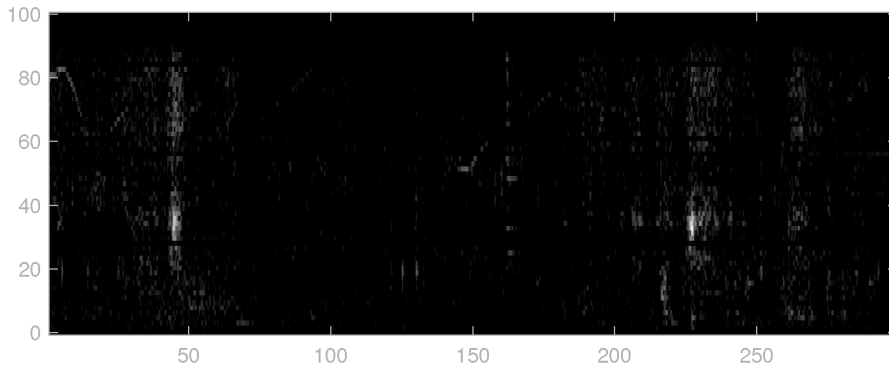


Figure 5.5: The spectrogram after logarithmic scaling and removal of the noise model. (x-axis: time [s]; y-axis: frequency [Hz])

It has to be emphasized, that the noise model and thereafter the pattern extraction result strongly depends on the length of the processed time-span. Scales & Snieder (1998) has given a nice example of the influence of the displayed time-span when distinguishing between noise and event. This example is reproduced in figure 5.6, which shows a seismogram at two different zoom levels. When taking a look at figure 5.6a only, the data would be considered as noise and no event would be declared. This changes dramatically when zooming out as shown in figure 5.6b. An earthquake can be clearly recognized and the zoomed part from figure 5.6a is now part

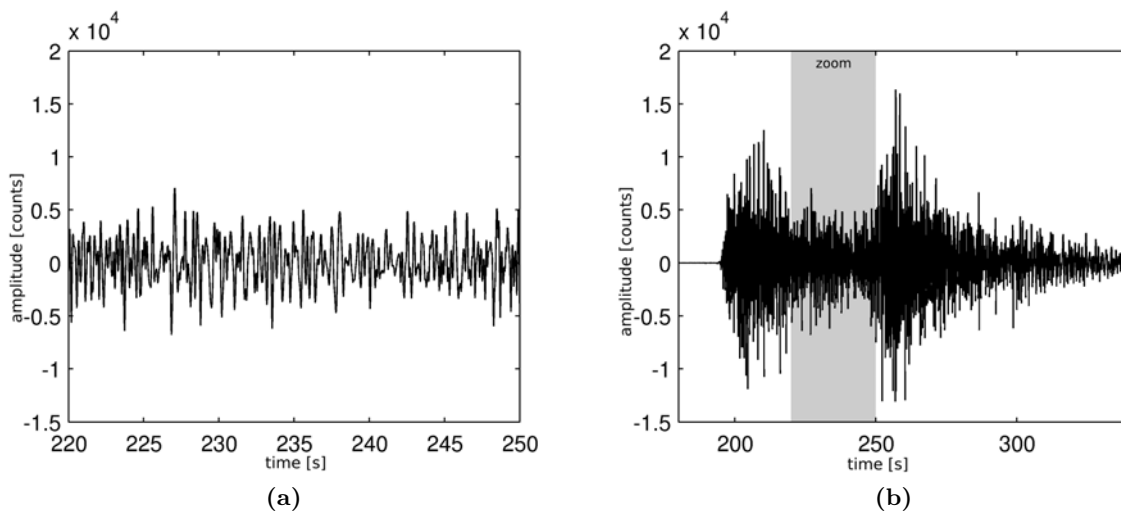


Figure 5.6: The decision whether the viewed seismogram is noise or signal depends on the zoom-level at which the seismogram is viewed. (a) shows a time-period of 30 s of a seismogram. (b) shows a longer time-period containing the time-period of (a).

of the event. The same effect occurs when computing the noise model of a selected timespan. Computing the noise model based on the processed time span ensures, that the model quickly adapts to short-time variations but it makes the detector 'blind' for events that are longer than the time-span for which the noise model is computed. In other words, by selecting the length of the time chunks which are used for the computation, the user adds an a priori knowledge to the detector: the length of the events which should be detected.

After the noise model is removed from the image and only the signal patterns are left, the next step is to extract the signal patterns from the spectrogram image. In figure 5.2 the patterns were highlighted by drawing the borders around the patterns using a red pen. To accomplish this task using a computer, a region growing algorithm (Gonzalez *et al.*, 2004, chap. 10) is used. The region growing procedure starts with a set of seed points from which the regions are grown by appending neighboring pixels based on some predefined rules (e.g. similar intensity values). As shown in the flowchart in figure 5.3 two images are needed for the region growing: the seed points and the region growing spectrogram.

Figure 5.7 visualizes the steps done to compute the seed points. First, the denoised spectrogram is thresholded using the threshold value

$$thr = \bar{g}^d + 2 * s \quad (5.4)$$

where \bar{g}^d is the mean value of the denoised spectrogram g_{ij}^d and s is the standard deviation of g_{ij}^d . The result is a black and white image containing the high intensity parts of the image (see 5.7a). This image contains a lot of speckle noise which would result in many false detections and would lead to an unstable detection algorithm. To remove the speckle noise the morphological image processing methods *opening* and *closing* of the image (Gonzalez *et al.*, 2004, chap. 9) are

5. EVENT DETECTION

applied (see figure 5.7b). Both methods use a structuring element (e.g. a small disk) to alter the original image. Opening an image removes image content into which the structuring element doesn't fit. Closing an image fills holes in the image which are smaller than the structuring element.

The last step in the seed point computation is to shrink the seed point objects using the `bwmorph` function of MATLAB. Shrinking the objects converts objects with no holes to points and objects with holes to rings. The final seed point image after shrinking the objects is shown in figure 5.7c.

To compute the region growing spectrogram g_{ij}^r two processing steps are applied: blurring of the image and contrast stretching. To blur the image spatial image filtering (Gonzalez *et al.*, 2004, chap. 3.4) with an averaging filter element is used. Spatial filtering is performed by correlating a filter mask with an image:

$$g_{ij}^b = \sum_{k=-A}^A \sum_{m=-B}^B w_{km} g_{i+k, j+m}^d \quad (5.5)$$

where g_{ij}^b is the filtered image, w is the filter mask of size $O \times P$ and g_{ij}^d the image of size $M \times N$, $A = (O - 1)/2$ and $B = (P - 1)/2$. The size of the filter mask is restricted to odd sizes with $O = 2A + 1$ and $P = 2B + 1$, where A and B are nonnegative integers.

Blurring the image acts as a lowpass filter and removes high frequency noise from the image. The drawback is the loss of high intensity information of small patterns and exact pattern boundaries. The small patterns and boundaries are smeared out and seem to vanish in the spectrogram images (see figure 5.8a). To undo this 'smearing', intensity contrast stretching (Gonzalez *et al.*, 2004, chap. 3.2) is used. Contrast stretching sharpens the borders between high intensity (signal) and low intensity (noise) areas and, depending on the threshold value, raises the low intensity values (see figure 5.8b).

The intensity contrast stretching can be compared to a 'soft thresholding' where the output image is not black and white, but still has grayscale values which are mapped from the original to the output image using the formula:

$$g_{ij}^r = \frac{1}{1 + (m/g_{ij}^b)^E} \quad (5.6)$$

where g_{ij}^r is the intensity stretched image, m is a threshold value and E a constant controlling the slope of the transformation function. The threshold value m is computed by

$$m = \bar{g}^d + 2s \quad (5.7)$$

where \bar{g}^d is the mean value of the denoised spectrogram g_{ij}^d and s is the standard deviation of g_{ij}^d . An example of the transformation function with $m=0.125$ and $E=2$ is plotted in figure 5.9a. For comparison, the transform function of a simple thresholding is given in figure 5.9b.

The seed points (figure 5.7c) and the region growing spectrogram (figure 5.8b) are taken as the input of the region growing algorithm to extract the patterns in the region growing spectrogram. The seed points define the starting points of the region growing algorithm. Pixels neighboring the seed points are joined to the region until the intensity difference between the

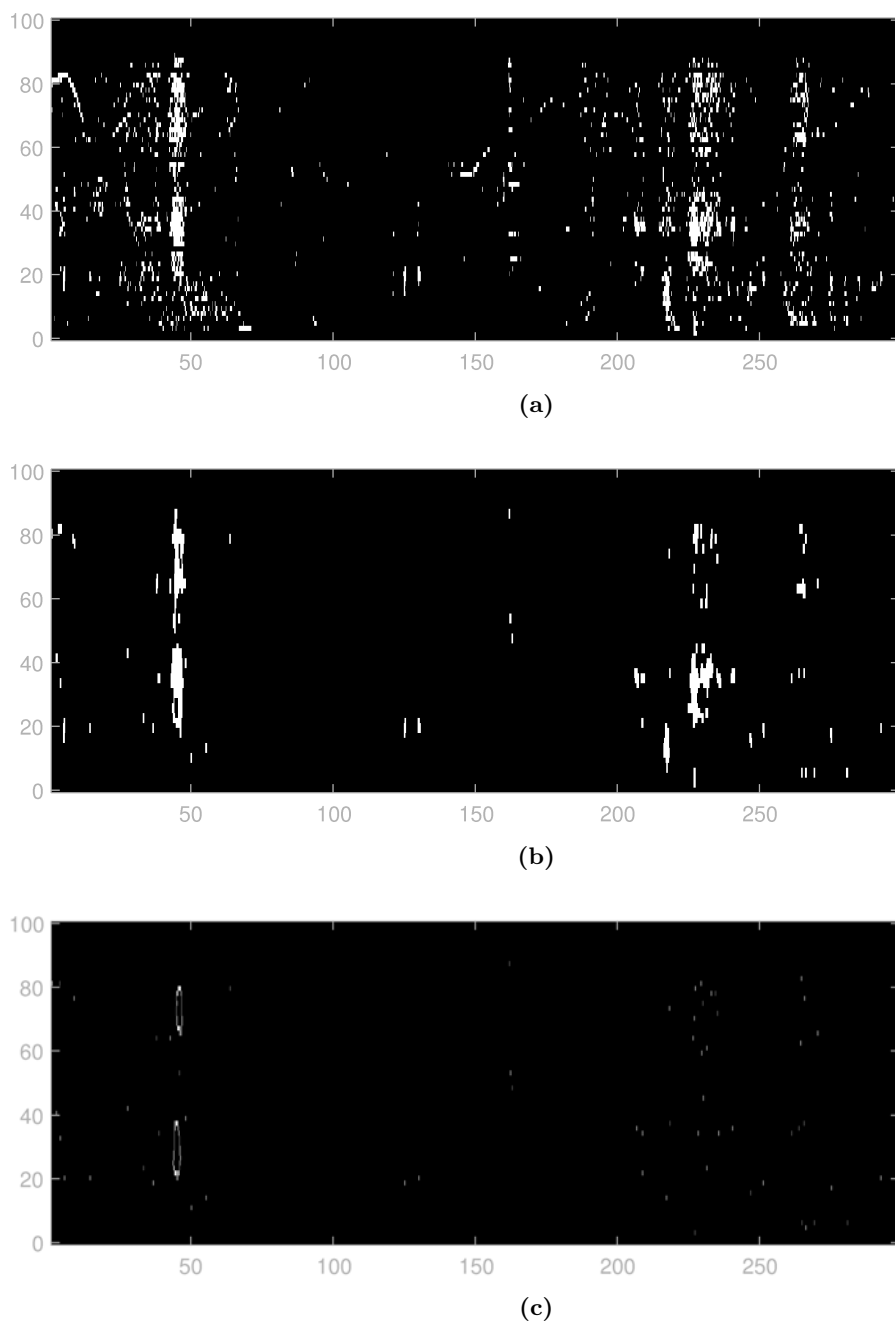


Figure 5.7: The three major steps included in the seed point computation of the spectrogram image. (a) thresholding of the spectrogram image, (b) removal of speckle noise by opening and closing of the image, (c) shrinking of the objects to reduce the seed point patterns to single points or rings. (x-axis: time [s]; y-axis: frequency [Hz])

5. EVENT DETECTION

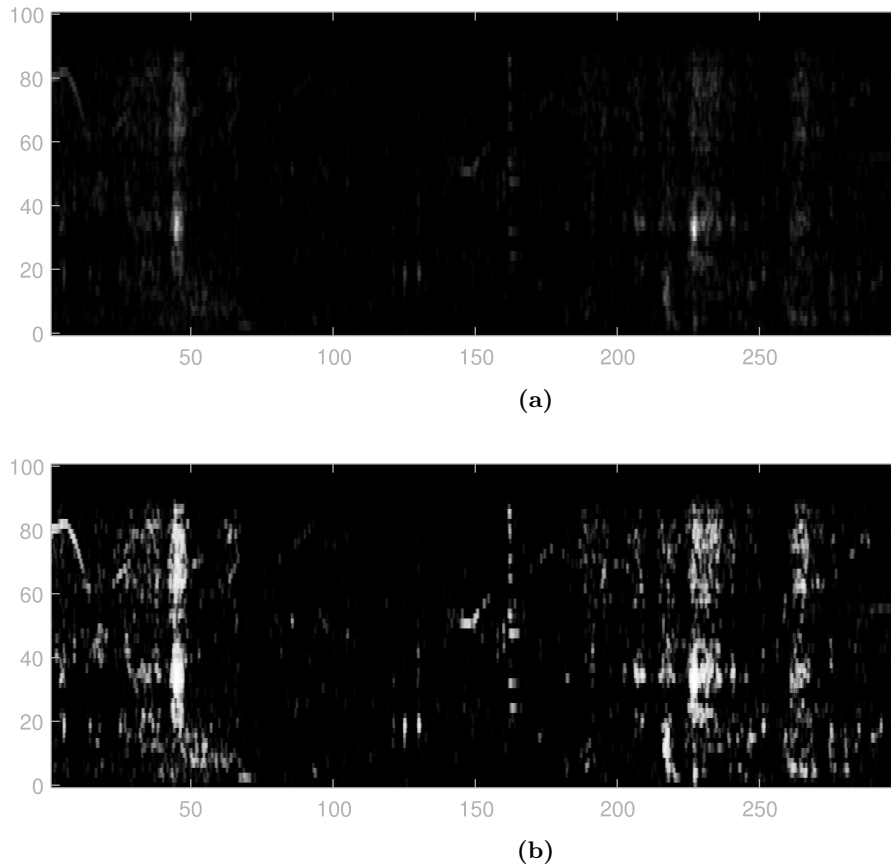


Figure 5.8: Blurring (a) and contrast stretching (b) to compute the region growing spectrogram. (x-axis: time [s]; y-axis: frequency [Hz])

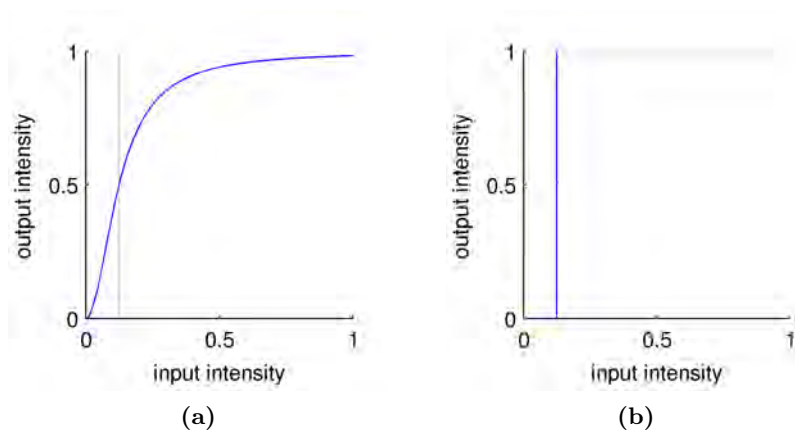


Figure 5.9: (a) Transformation function (blue line) used for contrast stretching. The threshold value $m=0.125$ is marked by the vertical gray line. (b) A threshold function at $m=0.125$ for comparison.

seed point pixel and the neighboring pixel drops below a threshold value. The resulting binary image is further cleaned using image opening and closing. This removes sparkle noise and closes holes in the regions. Figure 5.10 shows the extracted patterns after region growing (5.10a) and the cleaned patterns after the closing and opening of the image (5.10b).

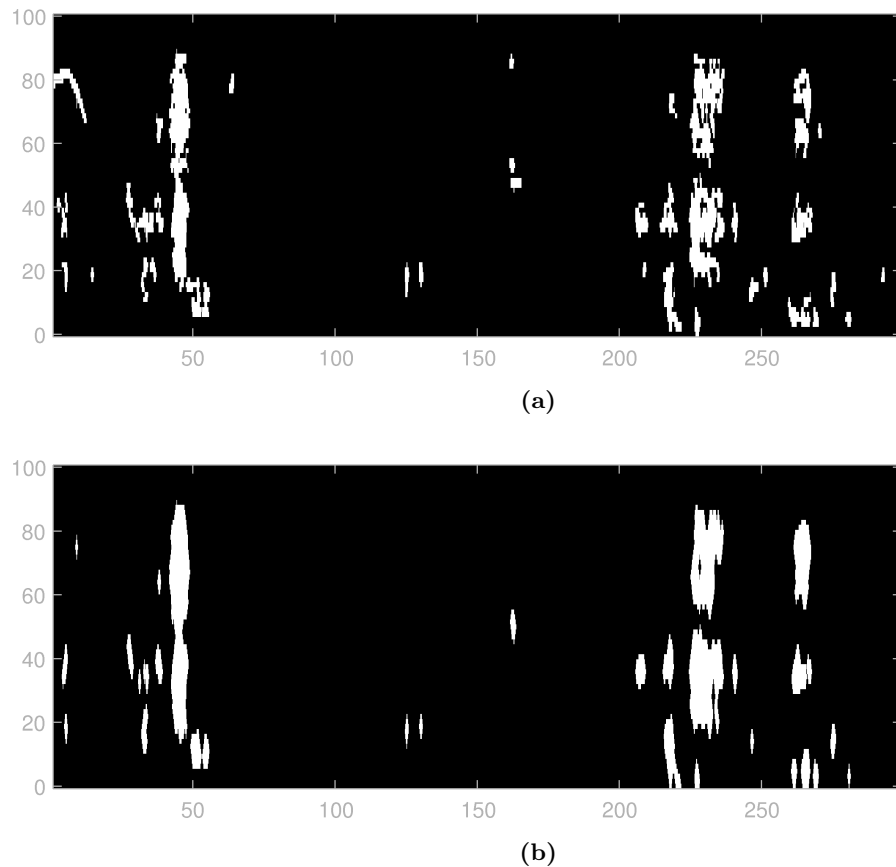


Figure 5.10: (a) the extracted patterns after regiongrowing, and (b) after cleaning the patterns by closing and opening of the image. (x-axis: time [s]; y-axis: frequency [Hz])

5. EVENT DETECTION

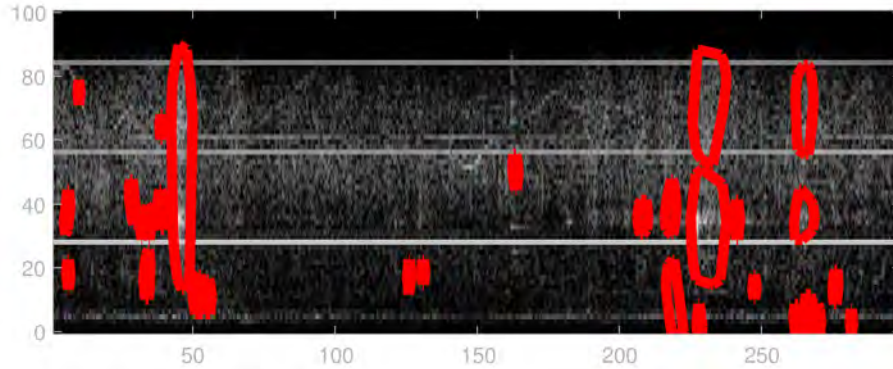


Figure 5.11: The extracted patterns on top of the original spectrogram. (x-axis: time [s]; y-axis: frequency [Hz])

5.2 Event binding

The pattern extraction is a single station process and, depending on the analyzed time-span, usually results in a huge amount of patterns without any relation to each other. The most important point in declaring a seismic event is the occurrence of related seismic signals on multiple stations with travel time differences that reasonably reflect the local velocity structure. In local- and regional earthquake analysis, the event-binding usually requires a sophisticated algorithm. This includes the localizations of possible hypocenters to compute theoretical travel-times to which the first onsets of the detected patterns are compared to. Because for many weak events reliable first onsets can't be determined, a simplified algorithm using the begin times of the extracted patterns to bind the single-station events has been used. This simplification adds the drawback of a larger amount of false positive event declarations. The comparison of the event begin times is done using a complete linkage cluster analysis of the travel-time differences. The result of the event binding process is a list of events with a quality factor. The quality factor is the number of stations on which a pattern contributing to the event has been extracted. The higher the quality factor, the more likely the detected event is a seismic event of special interest. Figure 5.12 gives an example of a detected event with contributing patterns on six stations.

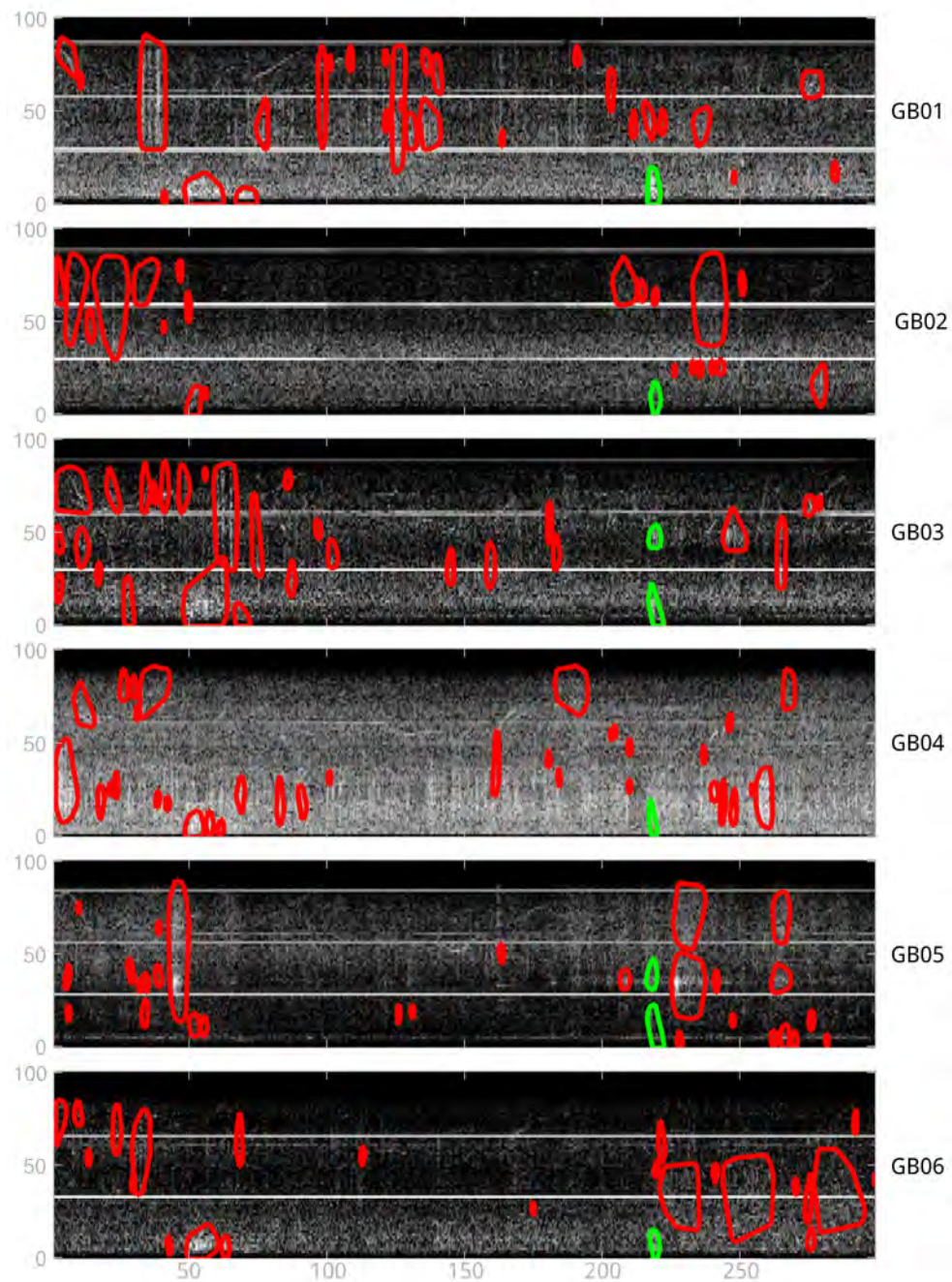


Figure 5.12: This example demonstrates the event binding based on cluster analysis of the begin times of the single station events. The red polygons mark the extracted patterns on each station. The green polygons highlight the patterns which have been linked to a common event recorded on 6 stations. (x-axis: time [s]; y-axis: frequency [Hz])

5. EVENT DETECTION

6

Event screening and classification

To classify the detected events, the dataset was screened by me using the results from the pattern extraction and event binding presented in an intuitive way along with the seismic data. The spectrogram with the signal enhancement, the detected events including their quality factor and additional information (e.g. bulletin earthquakes, observatory waveform data) was displayed on the computer screen using the Seismon software (see figure 6.1 and Appendix A).

The event screening and classification can be divided into the following major steps:

1. Eliminate seismic events of known sources (e.g. earthquakes).
2. Eliminate events that are not related to a natural seismic source (e.g. man-made noise, sonic signals)
3. Find similarities in features (e.g. frequency content) to divide the remaining events into classes.
4. Determine if the events of the individual event classes can be related to a seismic source originating from the displacement of the mass movement.

6. EVENT SCREENING AND CLASSIFICATION

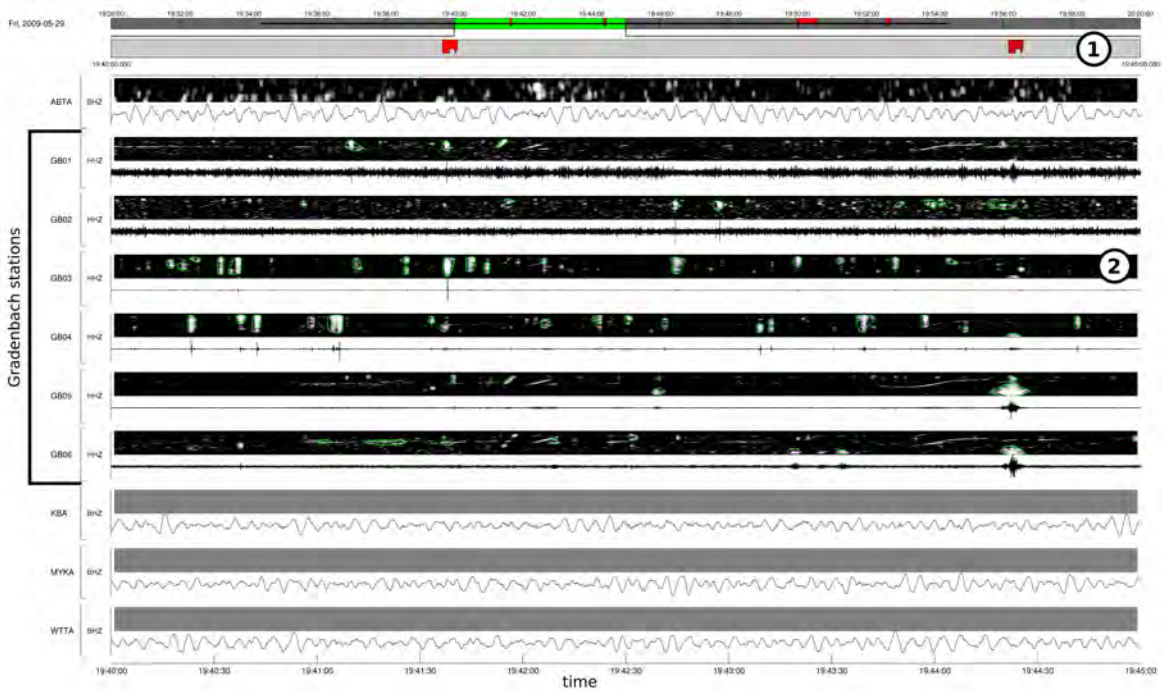


Figure 6.1: Example of a dataset displayed for event screening in Seismon. (1) is the area showing the event markers of the events detected by the pattern extraction. (2) are the vertical component seismograms with the extracted patterns of the stations located at the mass movement (GB01 - GB06). The other stations show the waveform data from nearby observatory stations for better identification of earthquakes.

6.1 Candidates, earthquakes or noise?

The elimination of known seismic sources, mainly local, regional and teleseismic earthquakes, was done using the earthquake catalog of the Central Institute for Meteorology and Geodynamics (ZAMG) as well as the waveform data of surrounding observatory stations (see figure 6.2). The observatory stations ABTA, KBA, MYKA and WTTA were used. The earthquake bulletins were requested from the ZAMG using the AutoDRM service¹ and imported into the Seismon database. The waveform data was downloaded from the ORFEUS data center. The earthquake event markers were displayed on top of the screen of the Seismon tracedisplay window along with the waveform data for an easy identification of the earthquakes (see figure 6.3). Not all earthquakes, mainly very local or weak regional events, were listed in the earthquake bulletin. To avoid a misinterpretation of these events, the waveform data of nearby observatory stations was searched for correlating signals. If a correlating earthquake signal was found on one of the observatory stations, the event was classified as an earthquake.

Another strong indicator to identify seismic signals with a source outside the mass-movement boundary is the reference station GB07. This station is located at a distance of about 3 km from the mass-movement. An event, which is recorded at all stations including station GB07 was most likely not created by the mass movement. According to the arrival time of a signal at the stations located on the mass-movement and the reference station as well as the amplitude distribution, signals with sources from outside the mass-movement boundary can be easily identified. It has to be noted, that the station GB07 has been installed in August 2009. Therefore, the most important resource for identifying events from outside the landslide boundary during the acceleration of the landslide were the observatory stations.

After all known earthquakes had been identified, the next step was the elimination of signals not related to a natural, underground seismic source (e.g. man-made noise, airborne sound, weather effects). The airborne sound made up a large amount of the seismic noise in the data recorded at Gradenbach. A microphone has been installed at one of the stations (see section 4.1 Instrumentation and station layout) to better identify these signals. The signal of the microphone is recorded with the same recorder and sampled with the same sampling frequency as the geophone signal to avoid any ambiguity due to imprecise time stamping of the data. The comparison of the microphone- and the geophone data showed that the geophone very often picks up signals that were induced into the ground directly at the station location by the sound wave. In this case, the microphone- and geophone waveform correlated very well in the time- as well as in the time-frequency domain. Examples of such airborne sound events can be found in figure 6.4 and section 7.4. All detected events with correlating microphone recordings were classified as airborne sound and removed from the further processing.

The remaining events were considered as being possible candidates of events related to the displacement of the mass movement. They were classified according to the following criteria:

- The shape of the waveform in the seismogram.
- The shape of the pattern in the time-frequency domain (spectrogram).
- The number of stations on which the event was detected.

¹http://www.seismo.ethz.ch/prod/autodrm/manual/index_EN, accessed October 2014

6. EVENT SCREENING AND CLASSIFICATION

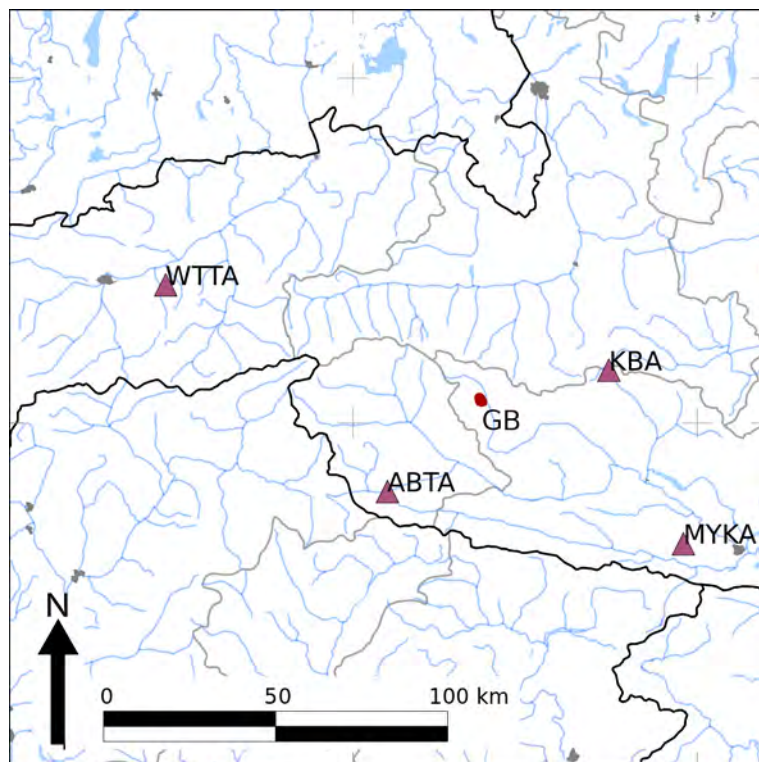


Figure 6.2: The observatory stations surrounding the Gradenbach mass-movement. The waveform data of these observatories was used for identifying earthquakes in the Gradenbach dataset.

6.1 Candidates, earthquakes or noise?

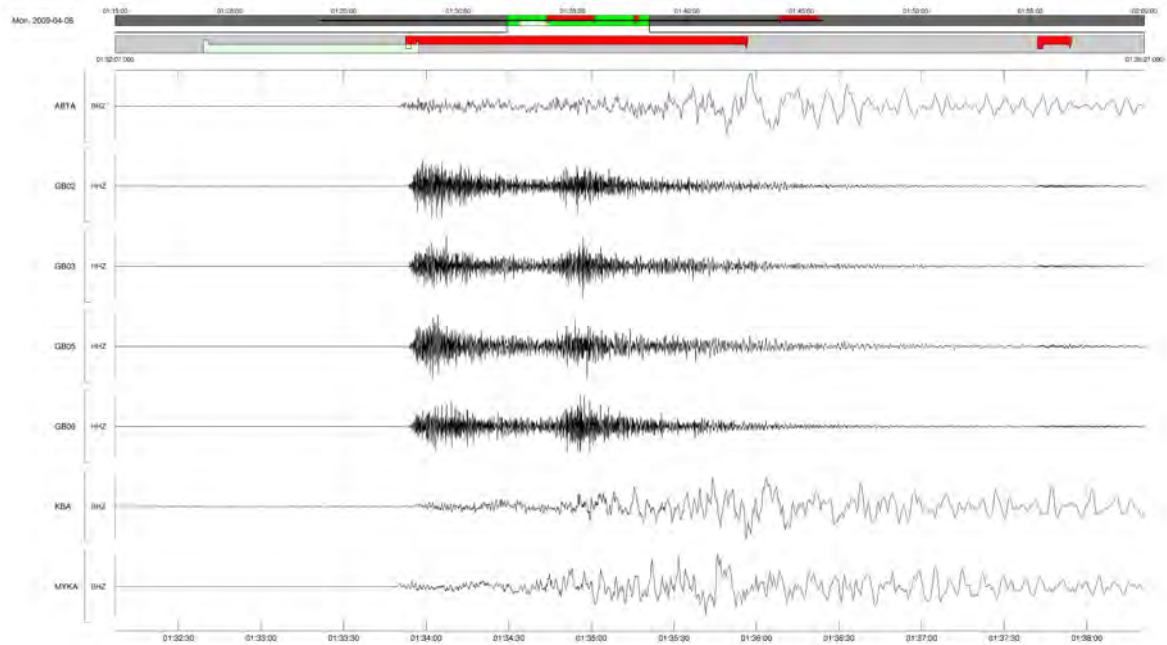


Figure 6.3: The Seismon tracedisplay with the bulletin earthquake markers and the waveform data of the seismic monitoring network and the nearby observatory stations.

- The correlation of the waveform and the time-frequency content among the stations of the network.
- The travel-time differences and the apparent velocity.

The features of all five criteria create a certain *event shape*. Reoccurring events with similar event shape were grouped into event types. The event types were numbered alphabetically (e.g. type A, type B, ...). The criteria to assign certain event shapes to event types didn't have any fixed threshold values. They rather acted as a guideline for me when classifying the candidate events. The decision to which event type a candidate was assigned to was a subjective process with my experience as a very important factor.

6. EVENT SCREENING AND CLASSIFICATION

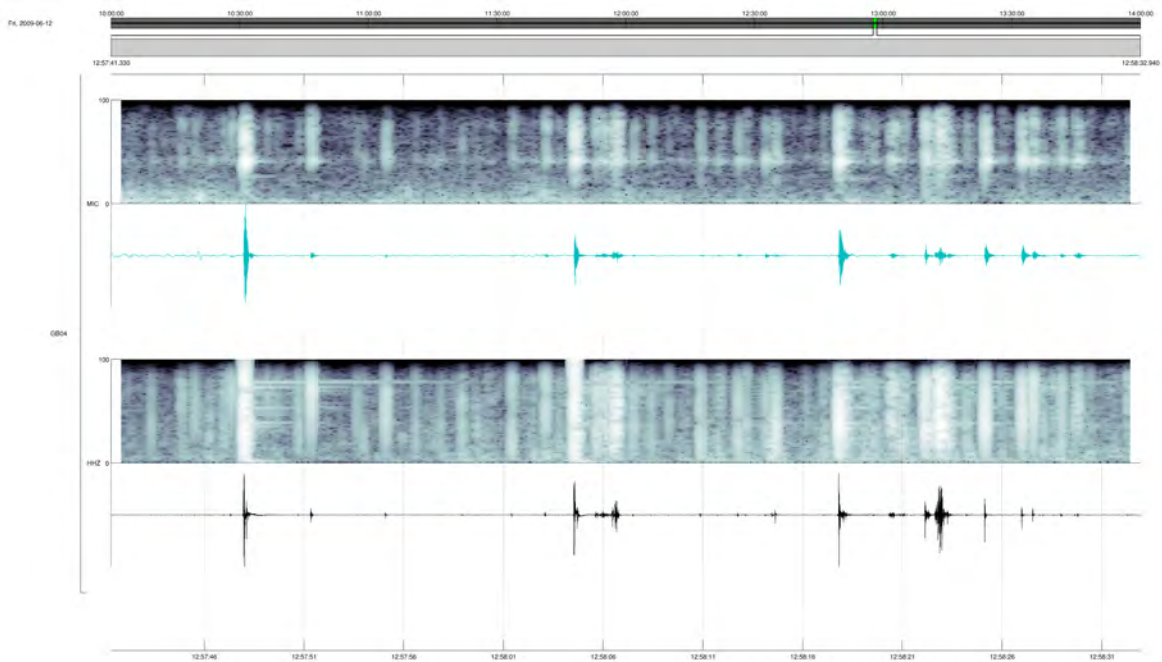


Figure 6.4: An example of local airborne sound generated nearby the station GB04. The spectrogram and the waveform of the geophone- (black line) and the microphone recording (turquoise line) are shown. The source of the signals was most likely wood works.

6.2 The location of the candidates

Once a list of seismic events categorized into event types had been available, the next step was to verify the association of the event types to the mass-movement. The key question was: Is the seismic source of the events related to the displacement of the mass-movement?

The location of the hypocenter of the source was the most important information to answer this question. Several methods have already been used on various mass movements: at the Randa rock-slide, a non-linearized grid-search algorithm implemented in the software NonLinLoc was used (Spillmann *et al.*, 2007), the intersection of hypolines implemented in the software Hypoline (Joswig, 2008) was used at the Heumös mass-movement (Walter & Joswig, 2008) and the Supersauze mud-slide (Walter *et al.*, 2012), a beam-forming using stacked cross-correlation of seismograms and waveform envelopes was used at the Sechilienne rock-slide (Lacroix & Helmstetter, 2011) and the Slumgullion mud-slide (Gomberg *et al.*, 2011), where a grid-search of travel-time differences using a layered velocity model was applied additionally to the beam-forming.

For this thesis, the following methods have been used to identify the source regions of the seismic events:

- the event amplitude distribution;
- the localization of events with recognizable first onsets using an non-linearized localization method (NonLinLoc);
- and polarization analysis of the incoming wavefield.

The source region of an event was estimated by the distribution of the peak ground velocity of the event over the seismic network. This is a simple but reliable method which can be compared to the isoseisal maps used in macroseismical studies. To ensure comparable amplitudes among the individual stations of the seismic network, amplitude correction factors have been computed using distant earthquakes recorded at the monitoring network.

For events with a good signal-to-noise ratio (SNR) and clearly visible first onsets, a non-linearized localization method (NonLinLoc) was used to determine the epicenters of the events. The information of the source depth was not used, because the layout of the seismic network with surface-based stations only didn't allow a reliable resolution of the hypocenter with depth.

Further information on the source region could be determined from the polarization analysis of the 3-component data. A master thesis (Doblhoff-Dier, 2011) analyzing the polarization of the data recorded at Gradenbach showed, that although the incoming wave field is heavily distorted by near-surface heterogeneities it still can be used for an estimation of the direction of the source from polarization analysis for certain events.

Furthermore, the correlation of the occurrence of the seismic events with other monitored parameters of the landslide (e.g. the displacement of the landslide) was an important indicator of an existing relationship between the seismic activity and the landslide. Seismic events which occurred during the acceleration phase of the landslide only are very likely linked to the processes underlying the displacement of the slope.

A detailed description of the methods outlined above is given in the following sections.

6.3 Event amplitude distribution and amplitude correction

Before using the amplitude distribution to estimate the source region of a seismic event, the local amplification or attenuation of the incoming seismic waves at each station has to be considered. This modification of the recorded amplitude of the ground-shaking is influenced by the coupling of the seismic sensor to the ground as well as the site-effects. Site effects are the usually frequency dependent changes of the ground motion due to local variations of the physical parameters and irregularly shaped earth structures formed by weathering, erosion, deposition and other geological processes near the surface of the earth (Aki, 1993).

To determine the relative attenuation among the stations deployed on the mass movement (stations GB01 to GB06) the local, regional and teleseismic earthquakes recorded during the processed time period from March 1 to September 31, 2013 were used. It was assumed, that the amplitude of earthquakes with a large epidistance from the Gradenbach mass-movement didn't vary much over the spread of the seismic monitoring network. Assuming only geometric spreading attenuating the amplitudes of the seismic waves, the amplitude decay is

$$A = \frac{A_0}{d} \quad (6.1)$$

, where A is the attenuated amplitude at epidistance d with a source amplitude A_0 . Using this assumption, the change of the amplitude per kilometer reduces below 0.001 at an epidistance of approx. 31.6 kilometers. Considering this variation as negligible small, the recorded amplitudes of earthquakes with an epidistance larger than 30 kilometers should be equal on all stations of the Gradenbach mass-movement.

To compute the amplitude correction factor for each station, the earthquakes described in section 7.3 Earthquakes were used. The earthquakes were classified according to Bormann *et al.* (2002) into local (epidistance $d \leq 150$ km), regional ($150 \text{ km} < d \leq 1668$ km) and teleseismic ($d > 1668$ km) earthquakes. The waveform data was corrected for the instrument response of the recording sensor and the data was filtered with a 1 Hz to 20 Hz Butterworth bandpass filter. For each earthquake i , the maximal value M_{ij} of the envelope e_{ij} of each station j was computed and referenced to the maximal value M_{i5} of the station GB05:

$$r_{ij} = \frac{M_{ij}}{M_{i5}} \quad (6.2)$$

. The relative maximal amplitudes r_{ij} of the three earthquake classes are given in figure 6.5. The station-wise median MED_j of r_{ij} is plotted in red on top of the r_{ij} of each earthquake. The general shape of the relative maximal value curves is similar for most of the earthquakes and also stays the same over the individual earthquake classes. The drop of the general size of the amplification of the teleseismic earthquakes, most likely reflects stronger attenuation of high frequent waves by the surface-near low velocity layers.

For the further analysis of the event amplitudes, the seismograms were corrected using the amplitude correction factors (which is the inverse of the station amplification) computed from the data of the local earthquakes. The correction factors computed from the local earthquakes have been chosen, because the local earthquakes cover the frequency range of the seismic events originating from the mass-movement and are not dominated by low-frequency signal content

6.3 Event amplitude distribution and amplitude correction

type	channel	GB01	GB02	GB03	GB04	GB05	GB06
local	HHZ	5.24	1.48	1.84	4.23	1	1.62
local	HHN	4.10	1.74	1.31	3.94	1	1.07
local	HHE	6.51	2.89	2.23	4.96	1	1.84
regional	HHZ	3.51	1.32	1.50	3.75	1	1.57
regional	HHN	3.51	1.55	1.27	3.45	1	1.22
regional	HHE	5.29	1.87	1.84	3.80	1	1.63
teleseismic	HHZ	2.22	0.93	1.17	2.26	1	0.94
teleseismic	HHN	2.58	1.31	1.29	2.44	1	1.11
teleseismic	HHE	3.82	1.56	1.84	3.28	1	1.36

Table 6.1: The station amplification computed from local-, regional- and teleseismic earthquakes for the channels HHZ, HHN and HHE of the stations GB01 to GB06. The site amplification is referenced to station GB05.

like the regional- and teleseismic earthquakes. Nevertheless it has to be kept in mind, that the wave-types of the local earthquakes and those originating from the mass-movement may not be the same and the computed amplitude attenuation doesn't represent a perfect solution of the real wave attenuation. The seismograms with the amplitude corrections applied allowed a more reliable relative comparison of the amplitudes. It was assumed, that the station-wise amplification or attenuation is related to near-surface variations in the velocity structure or the coupling of the geophone to the ground. Site-effects like the edge effect (Kawase, 1996) or geometric effects (Bonney-Claudet *et al.*, 2006; Semblat *et al.*, 2005, e.g.) which have been observed in sediment filled valleys have not been taken into account or investigated in detail. A more dense network and a reference station installed on solid rock would be necessary for studying these effects.

6. EVENT SCREENING AND CLASSIFICATION

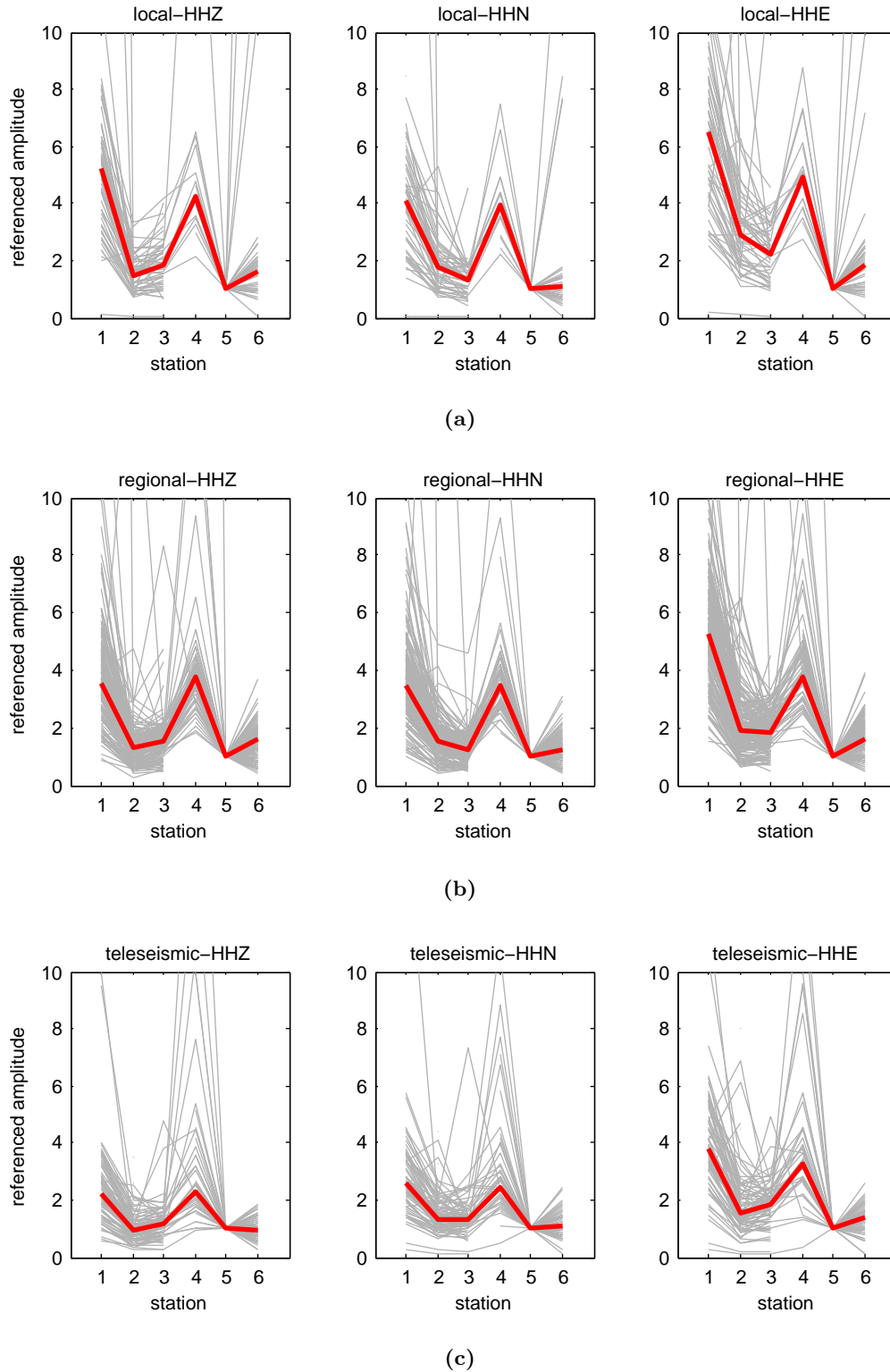


Figure 6.5: The relative maximal amplitudes of the seismogram envelope of local-, regional- and teleseismic earthquakes. The gray lines represent the maximal amplitudes of individual earthquakes referenced to station GB05. The red line is the median of all earthquakes.

6.4 Event localization using NonLinLoc

The earthquake localization usually requires the solving of an inverse problem. Based on observed arrival times of seismic phases and predicted travel times computed using a seismic velocity model, the earthquake hypocenter is determined by finding the location in space and time which best describes the observed arrival times. Even in the most simple example of a seismic velocity model, a homogeneous medium with wave speed v , the calculated travel time t_{calc} at an observing location $x_{obs}, y_{obs}, z_{obs}$ of a signal emitted at location x_h, y_h, z_h at origin time t_0 is a nonlinear function:

$$t_{calc} = t_0 + \frac{1}{v} [(x_{obs} - x_h)^2 + (y_{obs} - y_h)^2 + (z_{obs} - z_h)^2]^{1/2}. \quad (6.3)$$

This clearly highlights the nonlinear behavior of the travel time calculation and it shows, that the earthquake localization, which maps the observed travel times into spatial location and origin time is a nonlinear problem.

Generally, earthquake localization methods can be divided into two groups depending how they treat the nonlinearity of the localization problem: linearized- and nonlinearized or direct-search methods. As Lomax *et al.* (2009) has mentioned, the term nonlinear is used ambiguously in geophysics to refer to iterated-linearized as well as nonlinearized methods, therefore the term direct-search method is preferred to name non-linearized methods.

Linearized methods are characterized by approximating the nonlinear problem using linearization. This is usually done by expanding the travel time computation (the model function $f(m)$ with $m = (x, y, z, t)$) into a Taylor series around a prior estimation of the model solution $\mathbf{m}_0 = (x_0, y_0, z_0, t_0)$ and using only the first two terms of the Taylor series expansion

$$f(m) = f(m_0) + (m - m_0)f'(m_0). \quad (6.4)$$

Using this linearization, the inverse problem can be formulated as a set of linear equations which can be solved using linear algebraic methods. This solution is the linearized earthquake localization method. To get the best fit solution of the inverse problem, the linearization is iterated with the computed, new solution until a certain convergence criteria is reached. By this approach of iterated-linearization, the linearized methods takes into account the nonlinear behavior of the problem. Description of the iterated-linearized method can be found in (Havskov *et al.*, 2002, e.g.). Examples of implementations of the iterated-linearized method, which are mainly based on Geiger's method (Geiger, 1910), are Hypo71 (Lee & Lahr, 1975) or HypoEllipse (Lahr, 1989).

The result of the linearized and iterated-linearized methods is a single-point location with some statistical error estimates (e.g. the error ellipsoid). The methods are computationally fast and are therefore still the method of choice for routine earthquake localization in seismological observatory operation. The drawback of this localization methods is that the single-point location is dependent on the first estimate of the model solution and that it might not represent the true, optimum solution. If local minima are present, the single-point solution might get trapped in one of them. To get a better representation of the complete solution space, direct-search methods can be used.

6. EVENT SCREENING AND CLASSIFICATION

Direct-search localization methods explore the whole space of possible locations (the possible model space) by some type of grid-search algorithm (see Bormann (2002)). The arrival times from each point in the possible model space to each station is computed and the point in the possible model space with the best agreement between the observed and the calculated arrival times is searched. To perform this search, a representation of this *best agreement* has to be used. The root mean squared (RMS) or the L1 norm of the arrival time residuals are two well known ways to quantify the best agreement. The grid-search to find the point with the best agreement can be performed by various methods: for example by graphical analysis (e.g. plotting the contour lines of the best agreement representation), regular search, directed search or importance sampling (Lomax *et al.*, 2009). Lomax *et al.* (2009) has outlined the advantages of direct-search methods compared to linearized methods: “*Direct-search earthquake location is important because, relative to linearized methods, it is easy to apply with realistic earth models which may have abrupt and complicated velocity variations in three-dimensions, it places little restriction on the form of the measure of misfit, it is stable (i.e., does not suffer numerical convergence problems) when the observations are insufficient to fully constrain the spatial location or origin time, and it can produce comprehensive, probabilistic solutions which indicate the full location uncertainty, often a complex function of space and time.*”

The seismic event localization of this research was done using a direct-search method. The probabilistic approach to inverse problems implemented in the localization program NonLinLoc Lomax *et al.* (2000, 2001, 2009) was used. A good introduction to the probabilistic approach to inverse problems with an emphasis on earthquake localization is given in Tarantola (2005), Mosegaard & Tarantola (2002) and Tarantola & Valette (1982). To formulate the statement of inverse problems using probabilistic methods, a physical system Φ to study is needed. In the case of earthquake localization, this system would be the earth. To describe the system Φ , it is parameterized using a minimal set of parameters forming the parameter space \mathbf{X} which fully describes the system. The parameter space \mathbf{X} can be divided into the model space \mathbf{M} and the data space \mathbf{D} . The model space \mathbf{M} contains all possible models \mathbf{m} of the system Φ . The data space \mathbf{D} describes the observations \mathbf{d}_{obs} of a physical experiment which are the measurements of observable parameters. The model- and data space usually is related by a physical theory which can be used to formulate the *forward problem*. The forward problem

$$\mathbf{d}_{calc} = \mathbf{g}(\mathbf{m}) \quad (6.5)$$

predicts the outcome (the observations in the data space) of a physical experiment based on a certain model which is a point in the model space.

The *a priori* (prior to the experiment) information on the model parameters \mathbf{m} , the observations \mathbf{d}_{obs} and the predicted data \mathbf{d}_{calc} can be formulated as probability density functions (*pdf*). A *pdf* $f(\mathbf{x})$ is a function in one or more dimensional space S (where \mathbf{x} represents a point in S) that when integrated over some region A in S gives a probability $P(A)$ of occurrence of any event within region A . Moreover, the integral of $f(\mathbf{x})$ over the whole space S is one. If the integral over the whole space S is not normalized to one, the probability density is called a *measure density*. The probability $P(A)$ expressed in term of the pdf $f(\mathbf{x})$ is

$$P(A) = \int_A f(\mathbf{x}) \, d\mathbf{x}. \quad (6.6)$$

The *pdf* $p(\mathbf{d})$ over \mathbf{D} describes the data uncertainty in \mathbf{d}_{obs} . This can be due to recording, measurement and processing uncertainties. The *pdf* $p(\mathbf{m})$ over \mathbf{M} describes the prior information available on the model \mathbf{m} before the physical experiment. With respect to earthquake localization, this prior information could include knowledge about possible hypocenter locations due to the knowledge of the fault system, or it might define an area restricted due to the knowledge from shakemaps, or in the most basic sense, it could include the bounds of the seismic network which recorded the earthquake. The forward problem can be described as the theoretical probability density function $F(\mathbf{d}, \mathbf{m})$. Combining these three states of information produces the *a posteriori state of information*

$$Q(\mathbf{d}, \mathbf{m}) = k \frac{p(\mathbf{d})F(\mathbf{d}, \mathbf{m})p(\mathbf{m})}{\mu(\mathbf{d}, \mathbf{m})} \quad (6.7)$$

where the constant k normalizes Q to unit integral over $\mathbf{D} \times \mathbf{M}$ and $\mu(\mathbf{d}, \mathbf{m})$ is the homogeneous distribution over data \mathbf{d} and model parameters \mathbf{m} . The homogeneous distribution (also called the *null information*) is the probability distribution that assigns to each region of the space a probability proportional to the volume of the region. It therefore is the distribution, that provides the least information on the region. In cartesian coordinates, the homogeneous distribution is a constant.

To get information from the formulation of the probabilistic inverse problem in equation (6.7) on the *a posteriori* (the post experimental) state of information about the model \mathbf{m} , the integrating over the data \mathbf{d} is needed:

$$Q(\mathbf{m}) = kp(\mathbf{m}) \int_{\mathbf{D}} \frac{p(\mathbf{d})F(\mathbf{d}, \mathbf{m})}{\mu(\mathbf{d}, \mathbf{m})} d\mathbf{d} \quad (6.8)$$

which can also be written as

$$Q(\mathbf{d}, \mathbf{m}) = kp(\mathbf{m})L(\mathbf{m}) \quad (6.9)$$

where k is a constant.

The term

$$L(\mathbf{m}) = \int_{\mathbf{D}} \frac{p(\mathbf{d})F(\mathbf{d}, \mathbf{m})}{\mu(\mathbf{d}, \mathbf{m})} d\mathbf{d} \quad (6.10)$$

in equation (6.9) is named the *likelihood function* and describes the measure of how good a model \mathbf{m} explains the observed data.

Equation (6.8) describes the general solution of the inverse problem using the probabilistic approach. For earthquake localization with NonLinLoc some assumptions are made to achieve a simplification of the solution given in (6.8):

1. The error of the observed data \mathbf{d}_{obs} is assumed to be Gaussian and it is described by a Gauss distribution with mean \mathbf{d}_0 and covariance matrix \mathbf{C}_d ;
2. The uncertainties in the forward model problem relating \mathbf{d} and \mathbf{m} is assumed to be negligible small;
3. It is assumed that the data \mathbf{d} and the model \mathbf{m} are independent and therefore the homogeneous distribution $\mu(\mathbf{d}, \mathbf{m})$ can be written as $\mu(\mathbf{d})\mu(\mathbf{m})$.

6. EVENT SCREENING AND CLASSIFICATION

With these three simplifications, the likelihood function is given by

$$L(\mathbf{m}) = \exp \left\{ -\frac{1}{2} [\mathbf{d}_0 - \mathbf{f}(\mathbf{m})]^T \mathbf{C}_d^{-1} [\mathbf{d}_0 - \mathbf{f}(\mathbf{m})] \right\}. \quad (6.11)$$

Using the computation of the maximum likelihood origin time t_0 using weighted means of the observed arrival times and the predicted travel times (see Moser *et al.* (1992); Tarantola & Valette (1982)) and if the observed and predicted travel times are uncorrelated the likelihood function in equation (6.11) can be rewritten to

$$L(\mathbf{m}) = \exp \left\{ -\frac{1}{2} \sum_i \frac{[t_i^{obs} - t_i^{calc}(\mathbf{x})]^2}{\sigma_i^2} \right\}, \quad (6.12)$$

where \mathbf{x} is the spatial part of \mathbf{m} , t_i^{obs} are observed travel times, t_i^{calc} are calculated travel times for observation i , and σ_i summarizes the associated standard deviation of uncertainty in t_i^{obs} and t_i^{calc} .

The likelihood function in equation (6.11) and (6.12) is not normalized and therefore doesn't represent a true probability density function. It nevertheless describes the relative probability of any location \mathbf{m} in the model space \mathbf{M} being the best estimate of the true earthquake location given the observations t_i^{obs} from a measurement. Because of the high computational cost of computing the integral over \mathbf{D} and \mathbf{M} , the product of the prior, spatial location information $p(\mathbf{x})$ with the likelihood function $L(\mathbf{x})$ (named location pdf hereafter) is used as the objective function for inversion and direct search localization algorithm. This has the drawback, that the values of the pdf of two different event localizations are not comparable. The likelihood function introduced in equation (6.11) is based on the exponential of the L2-norm misfit function. Other methods to describe the misfit can be used, for example the L1-norm or the equal differential-time (EDT) formulation (Font *et al.*, 2004; Lomax, 2005).

Once an objective function is defined, regular search, directed search or importance sampling methods can be used to explore the objective function. A good overview of various search methods has been given by Lomax *et al.* (2009). Regular search methods (e.g. grid-search, stochastic, 'crude' Monte-Carlo) perform a global and well-distributed sampling of the objective function and therefore can produce an estimation of the complete location pdf. On the other hand, the regular search methods require time-consuming computations and are therefore not suitable for a rapid earthquake hypocenter determination. Directed search methods are very efficient techniques, but they don't explore the whole location pdf and might get trapped in local maxima. Importance sampling is a variation of the Monte Carlo algorithm with the modification, that the sampling density follows the objective function as closely as possible. The importance sampling method implemented in NonLinLoc is the oct-tree importance-sampling method ¹ (Lomax & Curtis, 2001; Lomax *et al.*, 2009). The oct-tree algorithm explores the original location pdf by a recursive subdivision and sampling of the 3D grid containing the location pdf into nested cells. One cell in 3-dimensional space is split into 8 new cells (see figure 6.6). For each cell, the probability that the cell contains the hypocenter of the earthquake is approximately

$$P_i = V_i L(x_i), \quad (6.13)$$

¹<http://alomax.free.fr/nllloc/octtree>, accessed October 2012

where V_i is the volume of the cell and $L(x_i)$ is the location pdf evaluated at the cell center x_i . Based on these probabilities, the most likely cell is chosen for another subdivision and computation of the probabilities of the cells. After that, the probabilities of all available cells are evaluated again, and the most likely cell is taken for another subdivision. This process is repeated until a certain stop criterion is reached. The resulting structure of cells follows the shape of the location pdf. Areas with higher probability contain a large number of small cells, whereas lower probable areas are more coarsely subdivided (see figure 6.7). For a better representation of the cell structure, the cells are randomly sampled depending on the probability of the cells. This sampling produces a 3D scatter plot describing the structure of the location pdf (see figure 6.8). The scatter plot is suited to represent complex shapes of the location pdf (e.g. multiple local maxima, irregular probability distribution) which might arise for example due to the network configuration or the pick quality. A good demonstration of the impacts of these frame conditions on the complexity and the quality of the localization result has been given by Lomax *et al.* (2009).

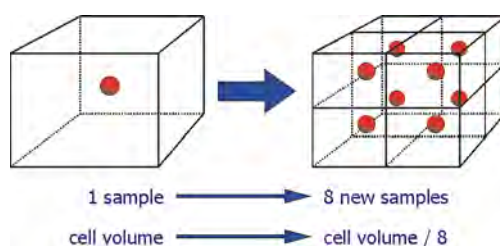


Figure 6.6: One cell in 3D space is subdivided into 8 cells. The cell centers (red dots) are used to evaluate the location pdf to compute the cell probability. (source: <http://alomax.free.fr/nlloc/octtree>)

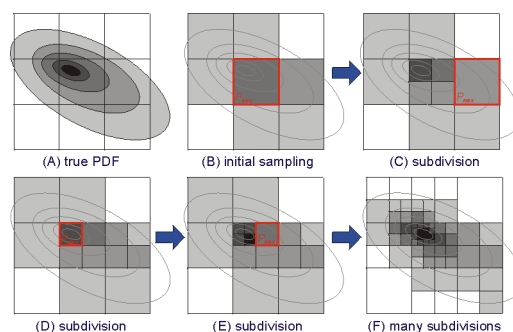


Figure 6.7: The subdivision of the cells is repeated to produce a cell structure representing the structure of the location pdf. MISSING: description of the plotted features. (source: <http://alomax.free.fr/nlloc/octtree>)

6. EVENT SCREENING AND CLASSIFICATION

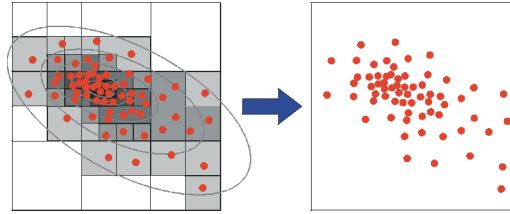


Figure 6.8: For a better visualization of the cell structure, the cells are randomly sampled depending on their probability. (source: <http://alomax.free.fr/nlloc/octtree>)

6.5 Polarization analysis

Katharina Doblhoff-Dier evaluated in her master thesis (Doblhoff-Dier, 2011) various methods of polarization analysis. She tested them on global- and regional earthquake data recorded at the monitoring network Gradenbach and applied selected methods to the high-frequent data of the event types recorded during the acceleration of the slope. Doblhoff-Dier (2010) has implemented state-of-the-art polarization analysis methods in Seismon, and tested them on global earthquake data recorded by the ZAMG observatory station CONA (see figure 6.9 for an example). The application of the covariance matrix - and the complex covariance matrix method to local earthquake data recorded with the seismic network Gradenbach was tested and the results were compared with those computed using broadband observatory stations of ZAMG. Doblhoff-Dier (2011) has drawn the conclusion, that polarization of the seismic wave field can be observed at the surface-based station of the Gradenbach network, but with a less quality compared to observatory stations. A summary of the observations made by Doblhoff-Dier is: (a) it is possible to obtain meaningful results from a polarization analysis at Gradenbach in the sense that the P-wave onset of events located close to each other typically show the same main direction of motion; (b) the polarization is weaker at Gradenbach compared to neighboring observatory stations; (c) the polarization at the Gradenbach stations could be measured less frequently with a sufficient quality; and (d) for some earthquakes with epicenters in the same region, the measured direction of motion at the Gradenbach stations showed a common bias. An example of the computed apparent azimuths at the Gradenbach stations compared with Austrian broadband observatory stations is given in figure 6.10.

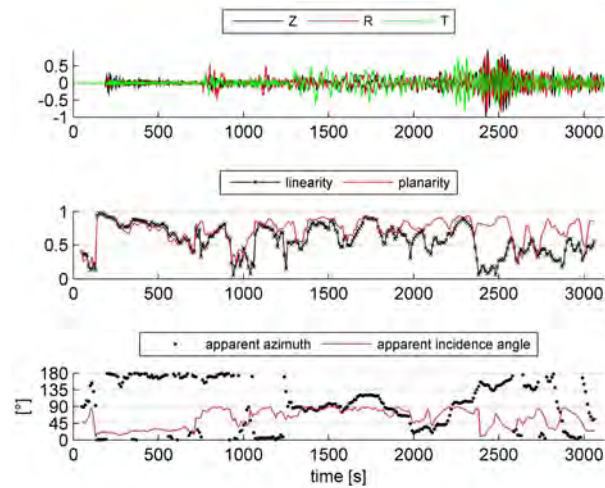


Figure 6.9: Example of the analysis of a global earthquake recorded at CONA using the covariance matrix method. source: Doblhoff-Dier (2011)

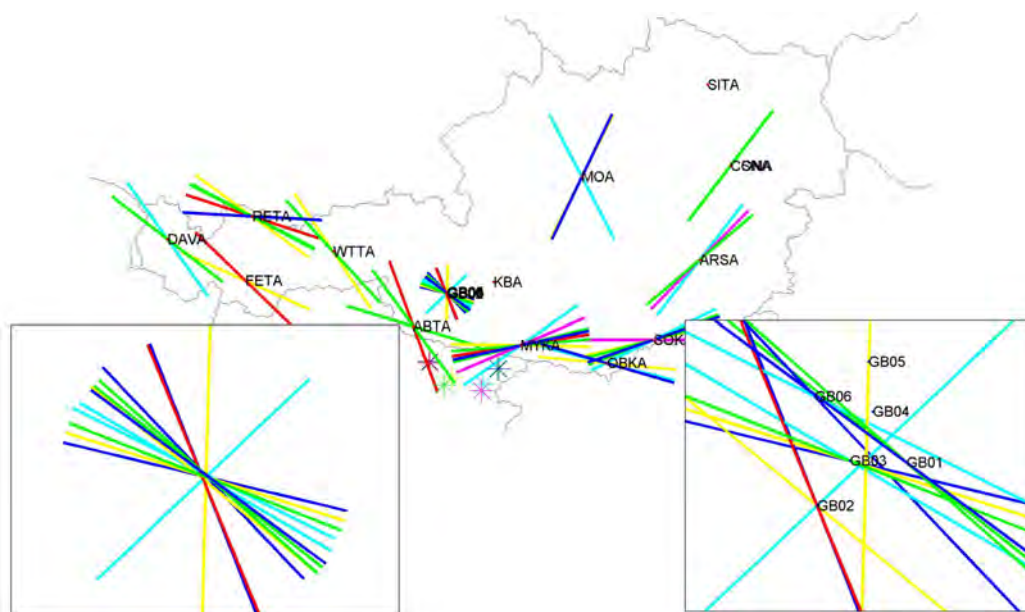


Figure 6.10: Example of the apparent azimuths (colored lines) obtained from P-wave polarization analysis of local earthquake data. P-wave polarization for several earthquakes (colored stars) located in the Friul region. The insets are zoomed-in views of the stations at Gradenbach (lower left: 20x20km; lower right: 2.5x2.5km). Each color depicts the results for one earthquake whose epicenter is represented by a star in the same color. source: Doblhoff-Dier (2011)

6. EVENT SCREENING AND CLASSIFICATION

7

Seismic events recorded at Gradenbach

The seismic data from March 1, 2009 to October 1, 2009, containing the acceleration phase 2009, was studied in detail using the methods described in chapters 5 and 6. A first screening of the data resulted in a separation into the three categories: (a) candidates, (b) earthquakes and (c) other events (see section 6.1). Figure 7.1a shows the cumulative number of all detected events and the subdivision into candidates, earthquakes and other events. In total, 2005 events have been classified. 815 events have been identified as earthquakes, 408 as candidates and 782 as other events.

The cumulative sum of all detected events showed a strong increase at the beginning of April. This increase was caused by the L'Aquila earthquake on April 6, 2009, 01:32 UTC and the subsequent aftershocks. Another minor increase of the candidate- and slope events occurred during the same time. This increase doesn't coincide exactly with the L'Aquila earthquake and it was mainly caused by the occurrence of a special type of events from April 2 to April 6, 2009 (see section 7.1). The increase of other events from the middle of May on was mainly caused by an increased thunderstorm activity in the mountains during summer.

The three main categories were further subdivided into different event types (see section 7.1). Following the description given in chapter 6 the candidates were classified according to their similarity of selected criteria (e.g. spectral content or waveform shape). Furthermore, for each event type, it was evaluated whether the events were related to the displacement of the slope or not. Those candidate events with a relation to the displacement of the slope were labeled as *slope events*. 159 of the 408 candidates were identified as slope events (see figure 7.1b). Earthquakes were split into local, regional and teleseismic earthquakes. Also for frequently reoccurring other events, the sources of the events was determined (e.g. thunderstorms, air traffic or car traffic).

7. SEISMIC EVENTS RECORDED AT GRADENBACH

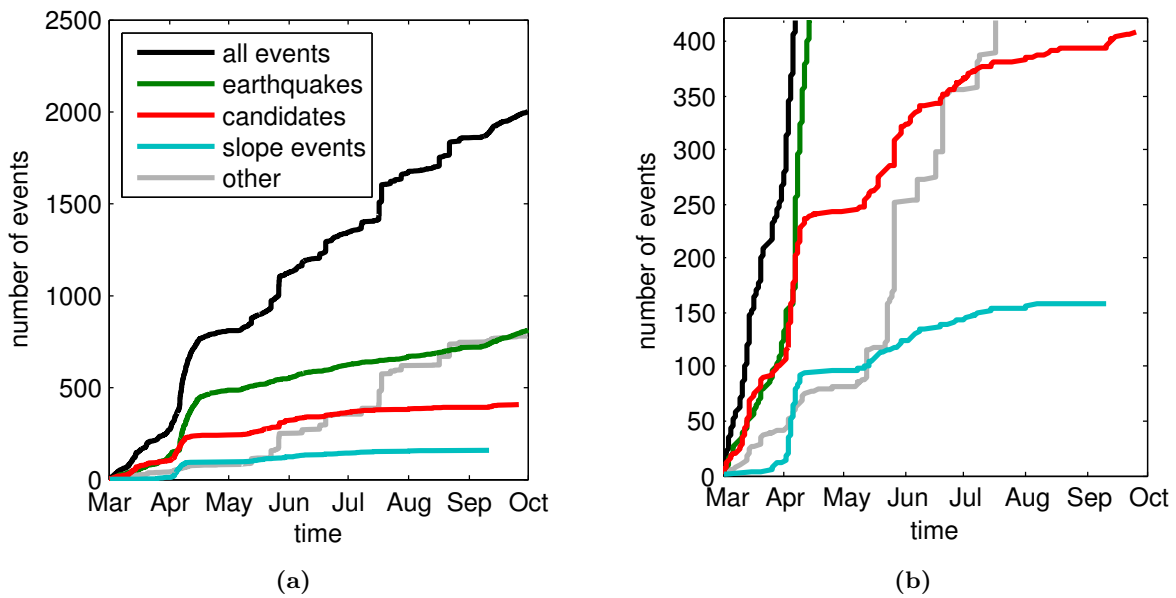


Figure 7.1: The cumulative number of events recorded during the period from March 1, 2009 to October 1, 2009 at Gradenbach. The cumulative number of all events and the identified event classes is shown in (a). To better visualize the detected events related to the slope displacement, (b) shows a zoomed version of (a). The strong increase of earthquakes beginning on 6. April was caused by the L'Aquila earthquake sequence.

7.1 Events related to the movement of the slope

During the period of the acceleration phase 2009, 6 event types of the candidate events have been identified as slope events. These event types are the type A, AA, B, D, RF and tremor (see table 7.1 and figure 7.2). Representative waveforms and spectrograms of each event type are shown in figure 7.3, highlighting the difference between the event types, both in waveform and spectral content. A complete list of waveforms and spectrograms of all events can be found in appendix B.

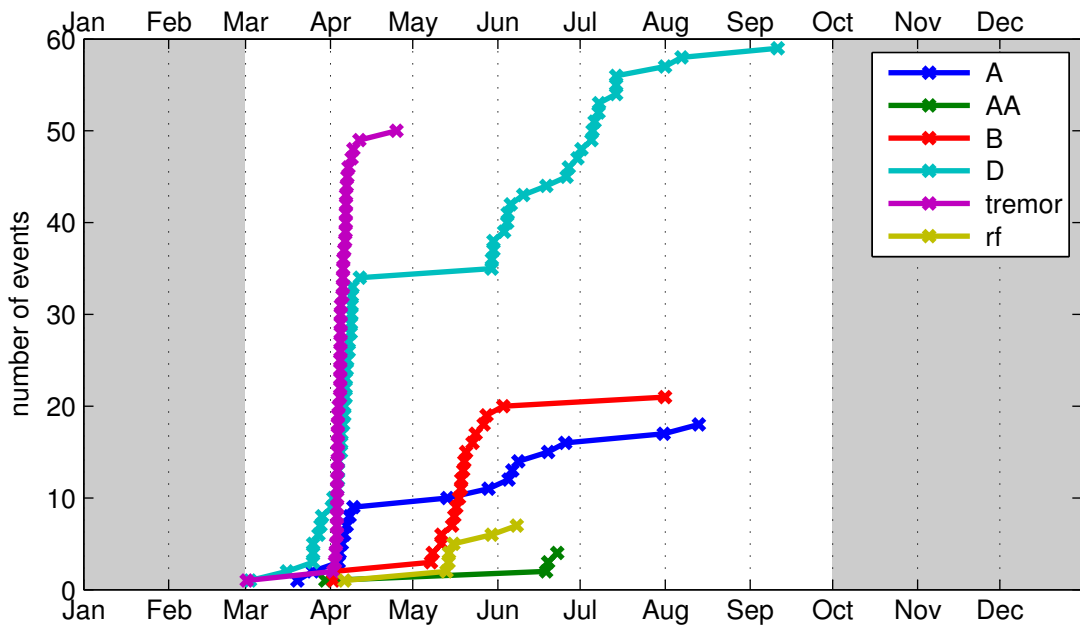


Figure 7.2: The cumulative sum of the slope events.

Boxplots of the event lengths and the signal to noise ratio (SNR) are shown in figure 7.5 and figure 7.6. The event lengths were visually determined using the spectrograms of the events. The SNR was computed in the spectral domain using the power spectral density (PSD) described below. For each event i and station j , the PSDs were divided into 5 frequency bands: 2-4, 4-8, 8-16, 16-32, 32-64 (all values in Hertz). For each frequency band k , the median PSD values M_{ijk}^{event} of the event-PSD and M_{ijk}^{noise} of the noise-PSD were computed. The SNR of the frequency bins is

$$SNR_{ijk} = \frac{M_{ijk}^{event}}{M_{ijk}^{noise}} \quad (7.1)$$

. The median of SNR_{ijk} taken first over the frequency bands k and then over the stations j is the signal to noise ratio SNR_i of the event i .

The local time of day (CET) of the occurrence of the events is given in figure 7.7. Except for the type tremor and the type rf events, no significant pattern in the distribution of the events over the time of the day was observed. The type tremor showed an accumulation in the daytime

7. SEISMIC EVENTS RECORDED AT GRADENBACH

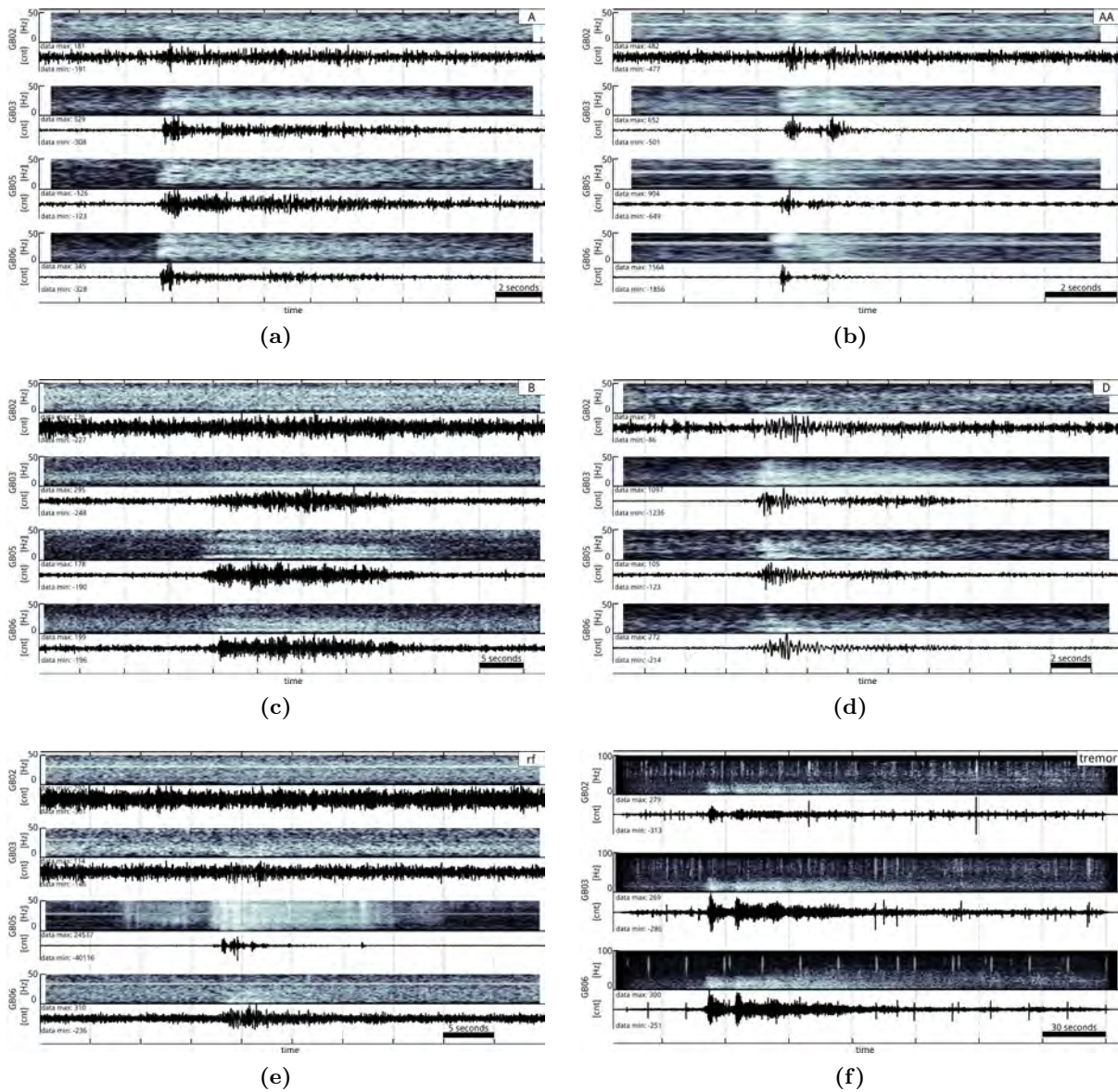


Figure 7.3: Representative waveforms and spectrograms of the candidate event types.

7.1 Events related to the movement of the slope

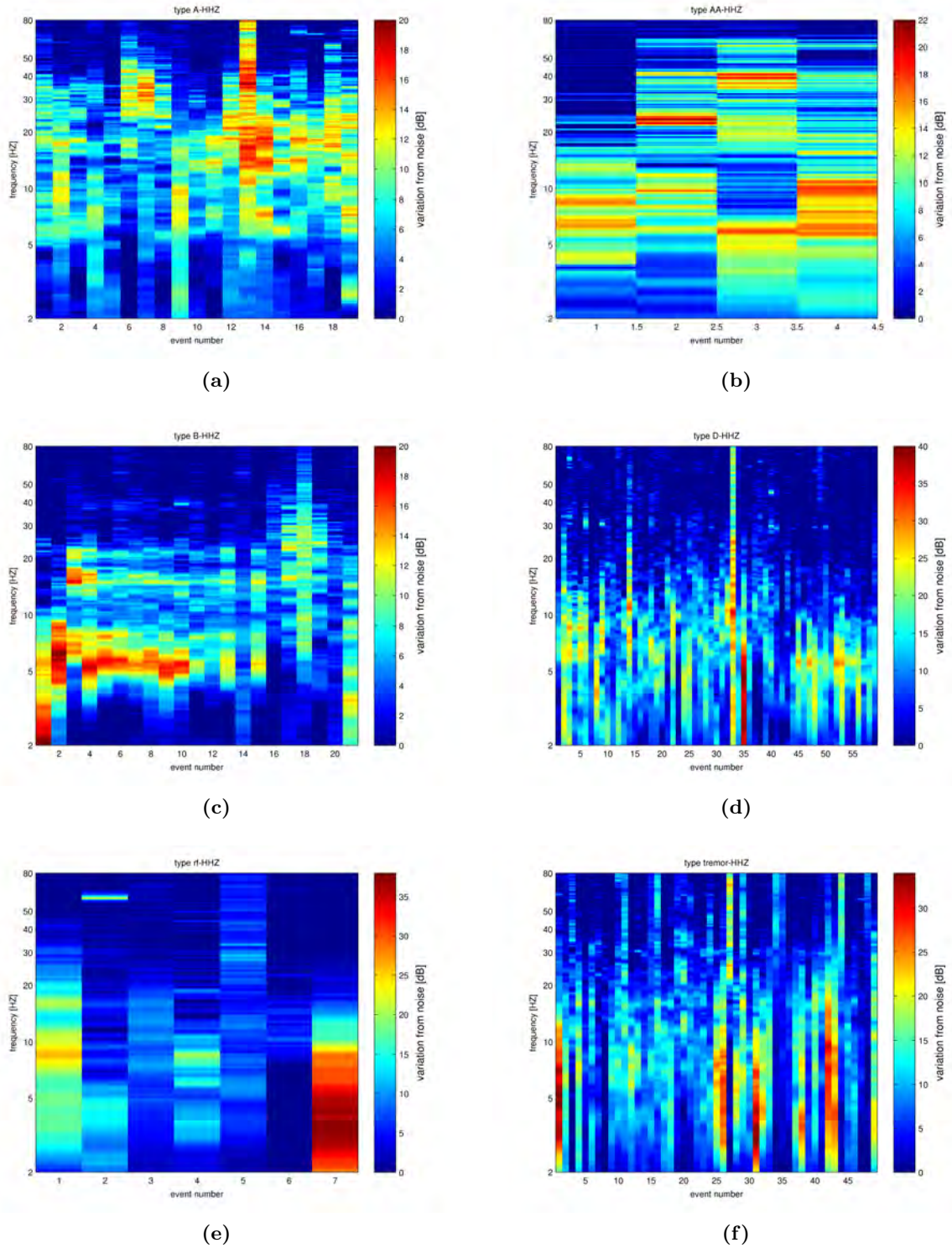


Figure 7.4: The spectral variation from noise of the slope-events. Each vertical bar represents the variation of the event power spectral density from the noise power spectral density. The noise power spectral density has been computed using a 300 seconds long time window before the event. The event numbers are sorted by ascending date.

7. SEISMIC EVENTS RECORDED AT GRADENBACH

event type	number of events	length [s]	length range [s]	snr	snr range [s]
A	19	14.1	4.6	3.6	2.7
AA	4	3.1	0.3	5.2	1.0
B	21	24.1	11.8	2.4	1.1
D	59	5.6	5.6	3.4	3.8
tremor	49	50.4	38.3	4.9	11.5
rf	7	32.1	31.3	3.6	32.3

Table 7.1: 159 events of the 408 candidate events have been related to the acceleration phase of the slope. They have been classified into six event type groups: A, AA, B, D, tremor and rf. The median values of the event length and the signal to noise ratio (snr) is given along with the number of events of the individual event types. The range of the event length and the snr is the interquartile range.

with most of the events happening between 10:00 and 20:00 CET. The type rf events mainly occurred during the night-time.

To better characterize the spectral shape of the event types, the mean spectral variation from the general background noise of each event was computed (figure 7.4). First the power spectral density (PSD) of the event (event-PSD) and the PSD of the noise (noise-PSD) was computed. The event-PSD was computed using a time-window with the length of the event. The noise-PSD was determined using a 300 seconds long time-window before the start of the event. The end-time of the noise-PSD window was 20 seconds before the start-time of the event. Both PSDs were corrected for the instrument response. The spectral variation is the difference between the event-PSD and the noise-PSD. The spectral variation was computed for each station with a recording of the event. To compute the mean spectral variation of each event, the median of all available station-wise computed spectral variations was taken.

The local magnitude of the events was computed with the magnitude formula used by the Central Institute for Meteorology and Geodynamics:

$$M_L = -0.304 + \log_{10}(A_{vel}^{max}) + 1.66 \log_{10}(\Delta) \quad (7.2)$$

, where A_{vel}^{max} is the max. velocity in nanometer/s and Δ is the epidistance in degree. The max. velocity of the event was measured using bandpass filtered data. Cutoff frequencies of 1 Hz and 30 Hz were used for all events except the type B events, for which cutoff frequencies of 1 Hz and 15 Hz were used. The absolute maximum value of the two horizontal components was used for A_{vel}^{max} . For events which were localized with the NonLinLoc software (see section 6.4), the local magnitudes were computed based on the epicenters computed with NonLinLoc and a fixed depth of 100m. For events with no available localization, the epicenter were set to the center of gravity of the mass movement boundary and a fixed depth of 100m. A fixed depth was used because of the poor depth resolution of the localizations. The fixed depth was chosen

7.1 Events related to the movement of the slope

to represent the general depth of the basal zone of the landslide. All magnitudes referring to this estimated hypocenter are labeled as *estimated local magnitudes* further in this thesis. Local magnitudes between -2.3 and -0.5 were computed for the events localized with NonLinLoc (see figure 7.8). The estimated local magnitudes of all events were in the range of $-2.8 \leq M \leq -0.6$ (see figure 7.9). A comparison of the magnitudes computed with the NonLinLoc hypocenters and the estimated local magnitudes showed, that the estimated local magnitudes are systematically smaller than the magnitudes computed for the NonLinLoc hypocenter. The median difference was 0.2 with the 25% percentile of 0.1 and the 75% percentile of 0.47. The magnitude distribution of the individual event types is given in figure 7.10. The rockfall events (type rf) showed the largest estimated local magnitudes with a maximum value of -0.6. The type tremor and type D events also had maximum estimated local magnitudes above -1, although the median estimated local magnitude of these event types was below -2.

The frequency-magnitude plot is shown in figure 7.11. The rockfall events (type rf) were not included in the frequency-magnitude plot because these events were not directly related to the internal displacement of the landslide. The estimated local magnitudes computed with the epicenter fixed to the center of gravity of the boundary of the mass movement were used for frequency-magnitude plot. The Gutenberg-Richter relation $\log_{10}(N) = a - bM$, where N is the number of events with a magnitude greater than M occurring in a given time and a and b are constants, was fitted to the data between $-2 \leq M \leq -0.9$. The b-value of this relation is 1.73. From figure 7.11 the magnitude of completeness $M_c \approx -2$ can be determined. This fits well to the detection threshold of $M_L = -2.3$ computed in section 4.3. M_c was determined as the magnitude in figure 7.11 where the data points don't follow the computed Gutenberg-Richter relation anymore.

The amplitude values for the magnitude determination were corrected using the amplitude correction values described in section 6.3. All amplitudes were referenced to the station GB05, which generally showed the lowest amplitudes. Therefore the given magnitudes represent the lowest magnitudes of the events. Using station GB01, which usually had the largest amplitude readings, as a reference station, the magnitudes were about 0.7 higher.

Type A

Type A events have an abrupt first motion and a median signal duration of 14.1 seconds. The interquartile range (IQR), which is the difference between the upper and lower quartile, is 4.6 seconds. The recordings of the type A events have a SNR with a median of 3.6 and an IQR of 2.7. In general the signal is visible on all stations. The frequency content of the event is between 5 Hz and 40 Hz. The onset of the event is usually more broadband than the trailing. The energy of the event weakens with its duration and sometimes the energy is bound to a frequency band between 10 Hz and 20 Hz.

Type AA

Type AA events are short events with an abrupt first motion and a median signal duration of 3.1 seconds. The IQR is 0.3 seconds. The recordings of the type AA events have a high SNR with a median of 5.2 and an IQR of 1. In general the signal is visible on all stations. The events

7. SEISMIC EVENTS RECORDED AT GRADENBACH

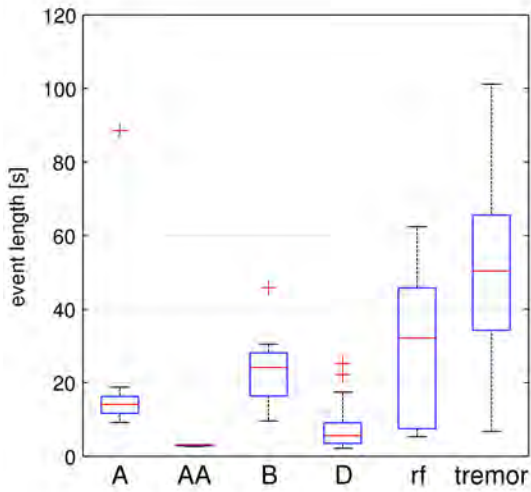


Figure 7.5: Boxplot of the event lengths of the individual event types. The red line marks the median, the lower and upper limit of the blue box is the 25% and 75% percentile, respectively, the top and bottom whiskers mark the minimum and maximum data and the red crosses indicate the outliers.

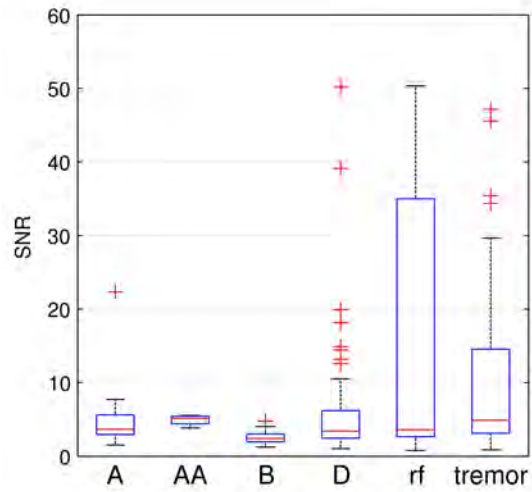


Figure 7.6: Boxplot of the event SNR of the individual event types. The red line marks the median, the lower and upper limit of the blue box is the 25% and 75% percentile, respectively, the top and bottom whiskers mark the minimum and maximum data and the red crosses indicate the outliers.

7.1 Events related to the movement of the slope

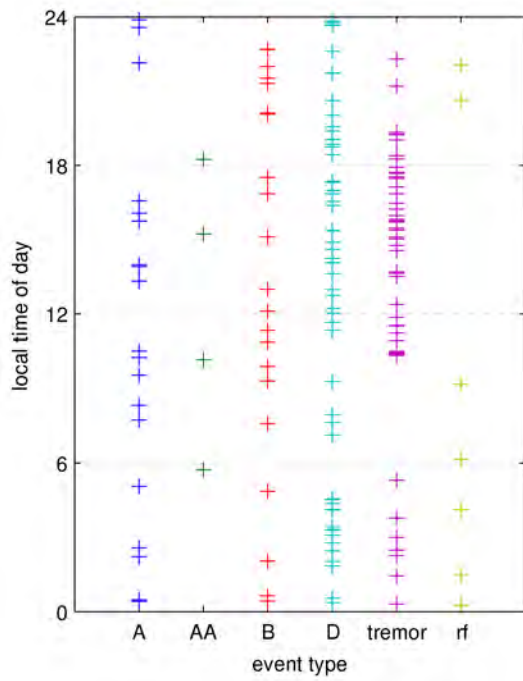


Figure 7.7: The temporal distribution of events.

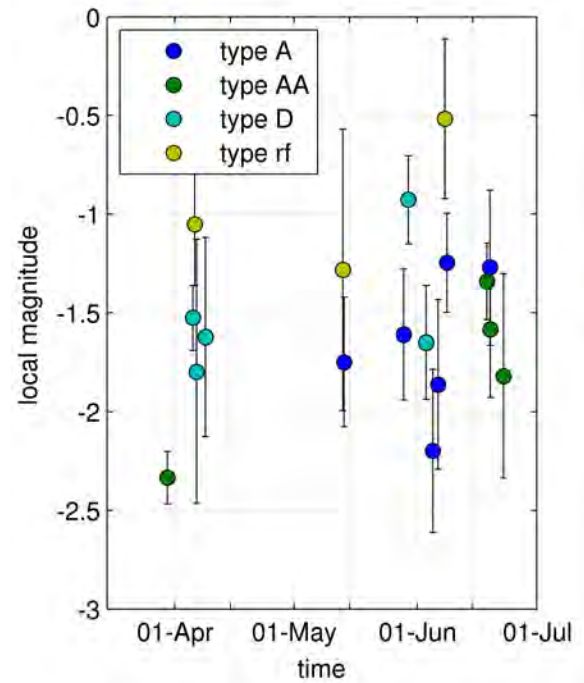


Figure 7.8: The magnitudes of the events localized with NonLinLoc.

7. SEISMIC EVENTS RECORDED AT GRADENBACH

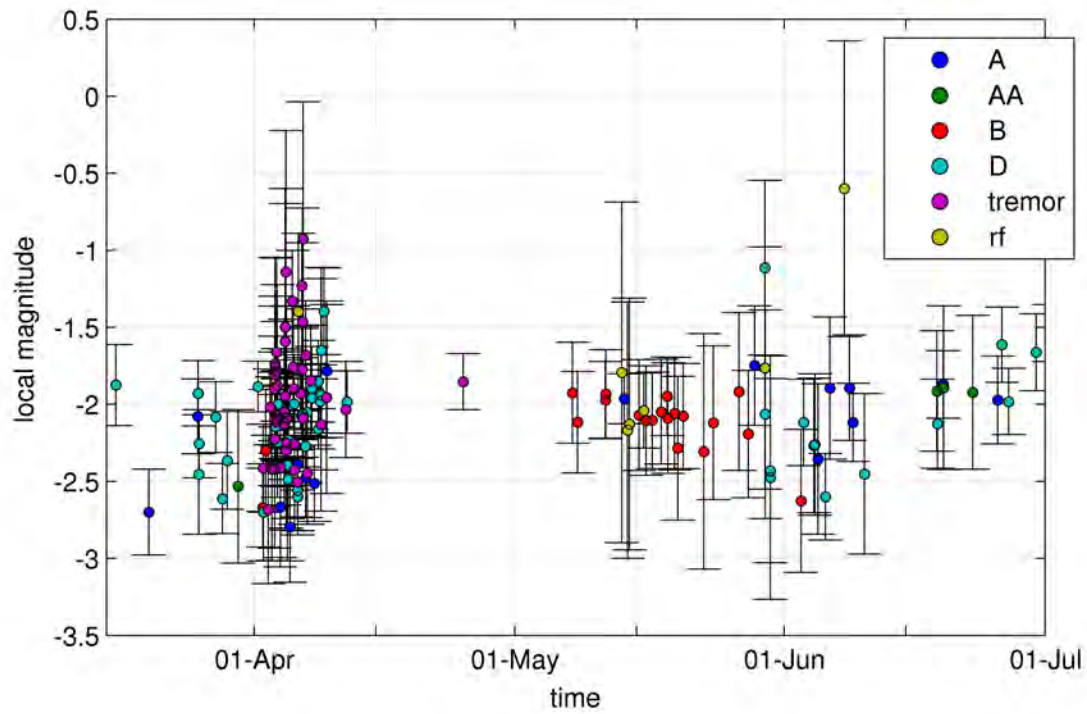


Figure 7.9: The estimated local magnitude using a fixed epicenter at the center of gravity of the mass movement boundary and a fixed depth of 100m.

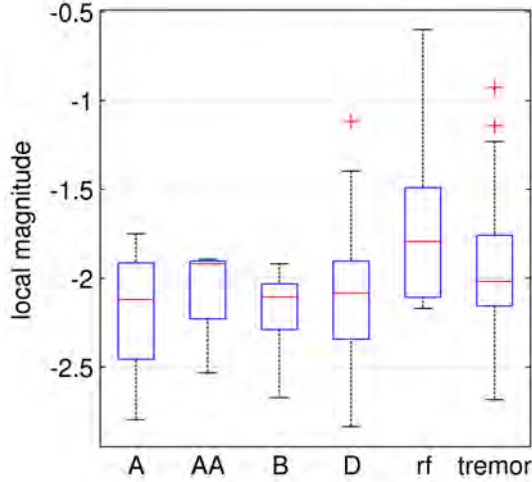


Figure 7.10: The magnitude distribution of the event types.

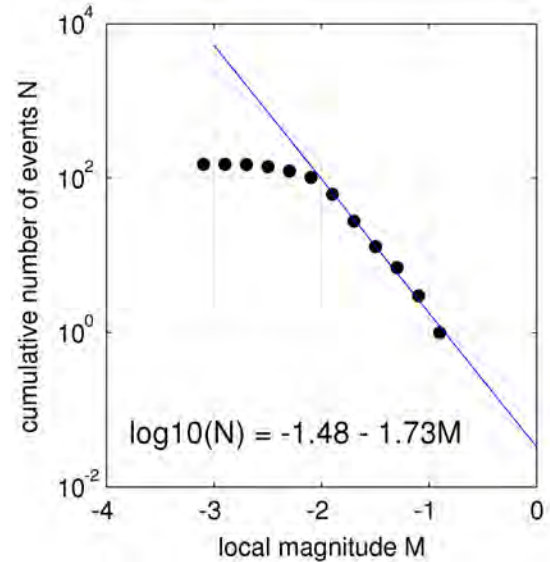


Figure 7.11: The frequency-magnitude plots of all events types except type rf events during the acceleration phase of the slope.

show a high frequency onset between 3 Hz and 100 Hz. The onset is followed by a low frequent waveform with frequencies between 3 Hz and 30 Hz. Only 4 of these events have been recorded during the acceleration phase 2009. 3 events occurred with 5 days in June.

Type B

Type B events have an emergent onset and a long duration with a median of 24.1 seconds and an IQR of 11.8 seconds. The events have a low SNR (median = 2.4, IQR = 1.1) and are sometimes not visible in an unfiltered seismogram. Mostly, the events are not visible at the station GB02. Most of the energy is present in a low frequency band between 3 Hz and 10 Hz. Some of the events have energy in a second frequency band between 15 Hz and 25 Hz. All of the events show a similar frequency spectrum and a decreasing energy with time (see figure 7.4d). The later type B events (beginning with event number 14 in figure 7.4d) have a different spectrum than the events happening earlier.

Type D

Type D events are short events with a weak first onset, that is sometimes hidden in the background noise. The median event length is 5.6 seconds (IQR = 5.6 s) and the median SNR is 3.4 (IQR = 3.8). The onset of the events shows frequencies above 10 Hz whereas the later part of the events is dominated by frequencies below 10 Hz. The separation between the high frequent onset and the low frequent ending of the events is clearly visible in the waveform. The

7. SEISMIC EVENTS RECORDED AT GRADENBACH

low frequent part sometimes shows quite a monotone characteristic. Sometimes two or three successive type D events have been recorded.

Type RF

The type RF events have a long duration (median = 32.1 s, IQR = 38.3 s) and a SNR that varies strongly among the stations. The median SNR is 3.6 with an IQR of 32.3. It was possible to link one of these events to a rockfall happening on June 7, 2009 at 22:15:35 UTC (see figure 7.12). The waveform of the type RF events generally shows a series of short impulsive events with large amplitudes on one of the topmost stations GB05 and GB06. The amplitudes are attenuated strongly with distance and sometimes the waveform is not visible on the stations deployed at the toe of the slope. The daytime distribution of the events given in figure 7.7 shows, that the type RF events occurred mainly during the nighttime.

The observed rockfall with a known source location was used to verify the localization using NonLinLoc (see figure 7.13).

Type tremor

The type tremor events have the longest duration (median = 50.4 s, IQR = 38.2 s) among the slope event types. The events have a high SNR (median = 4.9) with large variations (IQR = 11.5) among the individual events. The bandwidth of the events generally is quite broad with maximum frequencies of up to 100 Hz. The dominant energy is located in the frequency bands around 10 Hz. The waveform and time-frequency patterns correlate well among the individual stations and the amplitudes show noticeable attenuation over the seismic network. The main occurrence of the type tremor events is bound to a narrow time-span of 5 days from April 2, 2009 to April 6, 2009. 42 of the 49 tremor events occurred during this period.

7.1 Events related to the movement of the slope



Figure 7.12: Photo of a rockfall observed at Gradenbach. The top photo shows the impact on a road of the rock shown in the bottom photo.

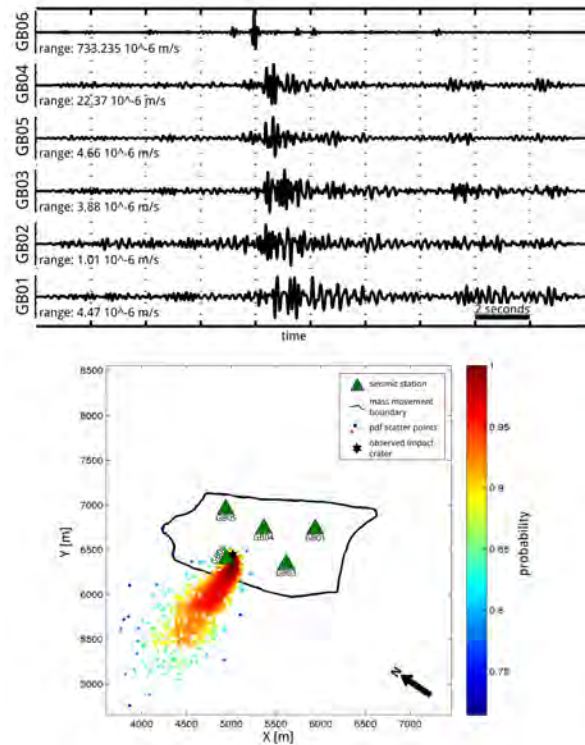


Figure 7.13: Location of the impact by a rock fall; (top) seismic recordings at the stations GB01–GB06, (bottom) location using NonLinLoc, seismic stations used for the localization are marked by green triangles; probability density function (PDF) scatter points of trial epicenters are color coded (color bar); the most probable epicenter (red star) corresponds to the highest PDF and density of the trial epicenters.

7.2 Source regions of the slope events

The result of the localization with NonLinLoc of events with a clear onset (see section 6.4) is given in figure 7.14. It shows the spatial frequency of possible epicenters, the best fit epicenters given by NonLinLoc and observed morphological changes caused by the displacement of the slope. 18 events (6 A, 4 AA, 5 D, 3 rf) were localized using NonLinLoc. The scatter points of the event localizations created with NonLinLoc have been used to create a cell-hit matrix of the possible epicenters. The cell-hit matrix is computed by counting the number of scatter points within a grid-cell of a regular grid. The cell-hit matrix highlights the zones of the seismic activity taking into account the uncertainty of the localization of each individual event. Figure 7.14 indicates a limitation of the source region of the localized events to the western and upper part of the slope. Morphological changes like scarps or bulging were observed in this area during the acceleration phase as well. In the eastern part and at the toe of the slope no similar morphological features were found.

Because only a small number of events were localized using NonLinLoc, the station-wise distribution of the peak ground velocity (PGV) was used to estimate the source region of the events (see figure 7.16). Before measuring the PGV, the instrument response was removed from the data, the amplitude correction was applied and the data was filtered with a bandpass filter (1-15Hz for type B events, all other events: 1-30Hz). The PGV was measured using the envelope of the waveform. For each event the PGV of all three channels at each station was determined. The station-wise PGV value was computed by taking the mean value of the three channels. The PGV was normalized to the absolute maximum of the event. The median of the normalized PGV values per station for all events of a common event type was determined and plotted on a map. If a certain event type was bound to a common source region it is reflected in the distribution of the normalized PGV values. Stations with a high PGV value are located closer to the epicenter than those with low PGV values. Type A events showed a quite uniform distribution with an emphasis to the western and upper part of the slope. The source region of type AA events was also located in the western and upper part of the slope. Type B events showed increased PGV values at the eastern part of the slope, whereas the highest PGV values of type D events were situated at the western part. The source regions of type rf and type tremor events were at the top of the slope.

The polarization of the slope events was analyzed using the complex covariance method (Vidale, 1986). The polarization analysis was based on the work done by Doblhoff-Dier (2010, 2011). The aims of the polarization analysis were to use the backazimuth for a determination of the source region of the events and to reveal the wave-types of the events. The polarization analysis of many events lead to no usable data. No clear pattern in the polarization attributes (strength of polarization, ellipticity, apparent azimuth and apparent incidence angle) were observed. Only for type B events a high strength of polarization together with a low ellipticity and a consistent apparent azimuth was observed (see figure 7.17). Doblhoff-Dier moreover showed, that the apparent azimuth of type B events between May 15 and May 20, 2009 show a similar direction of motion as shown in figure 7.18. This supports the assumption of a common, maybe small source region of type B events which could be drawn from the similar waveform, the similar frequency spectrum and the PGV distribution of the type B events.

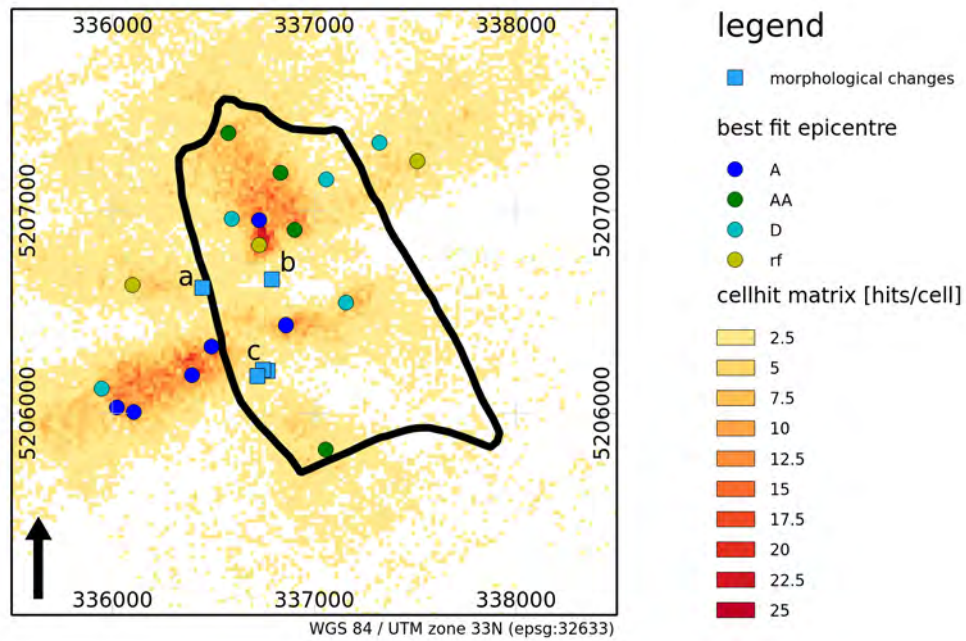


Figure 7.14: Cell-hit matrix of the scatterplots of the NonLinLoc localizations of 18 slope events. The best-fit epicenters of the events are colored according to the related event type. The labels (a,b,c) of the locations of the observed morphological changes reference the photos in figure 7.15.



Figure 7.15: Morphological changes observed during the acceleration phase 2009. The photos a, b and c correspond with the labeled markers in figure 7.14.

7. SEISMIC EVENTS RECORDED AT GRADENBACH

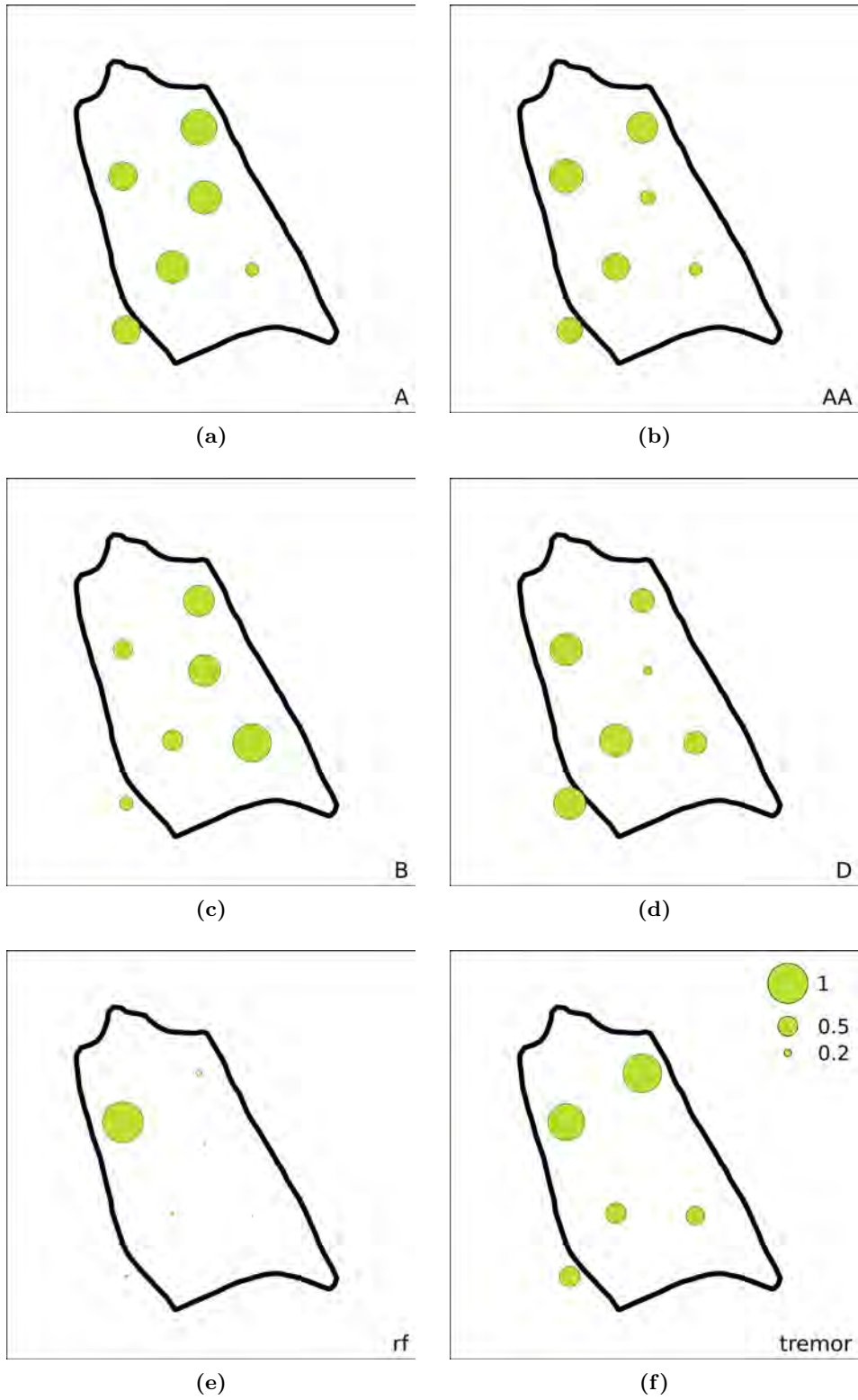


Figure 7.16: Distribution of the mean normalized peak ground velocity (PGV) of the event types.

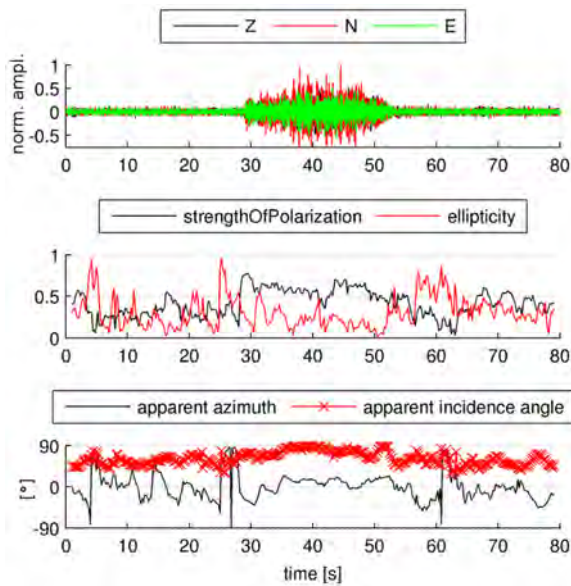


Figure 7.17: Example of the polarization of a type B event. The data is taken from the type B event on May 16, 2009 19:31:40 recorded at station GB04.

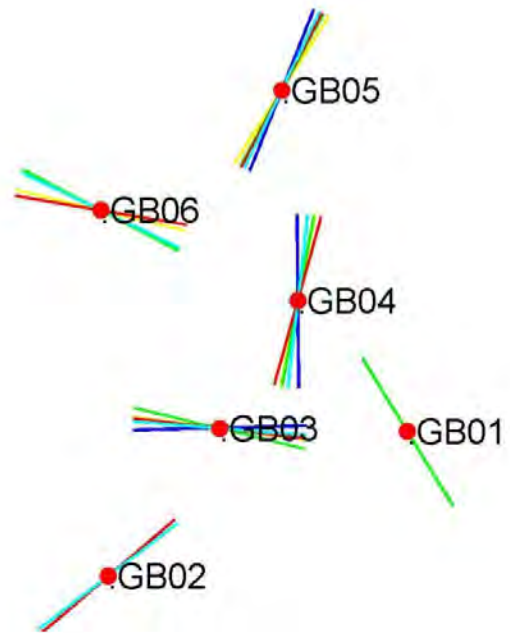


Figure 7.18: The mean apparent azimuth of type B events recorded between May 15 and May 20, 2009. source: Doblhoff-Dier (2011)

7.3 Earthquakes

The data processing of the acceleration phase 2009 also included the identification of earthquakes not related to the displacement of the landslide. A significant increase of the recorded earthquakes was observed during the beginning of April which was caused by the L'Aquila earthquake on April 6th at 01:32 UTC (epidistance to the Gradenbach landslide: 518km). This co-occurrence of increased earthquakes with the acceleration phase led to a more detailed investigation of the earthquakes recorded at the Gradenbach monitoring network. As will be shown in chapter 8, the acceleration of the slope was not directly linked to the increase of the earthquakes recorded at the Gradenbach mass movement. Nevertheless some single events were observed directly during - or shortly after an earthquake. These events can be thought of triggered events caused by changing the stress regime of a system near the point of equilibrium by the ground motion of weak earthquakes. Further investigation of these triggered events has to be done to strengthen this hypothesis.

During the processed time period 812 earthquakes were recorded at the Gradenbach landslide. 530 of these earthquakes were listed in the earthquake bulletin of the Central Institute for Meteorology and Geodynamics Austria (ZAMG) provided by their AutoDRM service. The remaining 282 earthquakes were not listed in the AutoDRM earthquake bulletin of the ZAMG. These events were identified as earthquakes using the waveform data of nearby observatory stations (ABTA, KBA, MYKA, WTTA). The earthquakes listed in the bulletin (B-earthquakes) were categorized depending on their epidistance d into local ($d \leq 150$ km), regional ($150 \text{ km} < d \leq 1668$ km) and teleseismic ($d > 1668$ km) (Bormann, 2002). For the classification of the earthquakes not listed in the bulletin (NB-earthquakes), the S-P difference was used to estimate the epidistance. For earthquakes with no recognizable P and S onsets, the epidistance category was estimated based on the waveform recordings on nearby observatories and the length of the earthquake. Table 7.2 lists the number of recorded earthquakes for each category and figure 7.19 shows the epicenter distribution of the local and regional earthquakes. A map of the epicenters of the bulletin-earthquakes is given in figure 7.20. The number of recorded earthquakes highlights the good data quality of the Gradenbach monitoring network.

category	B-earthquakes	NB-earthquakes
local	105	70
regional	293	204
teleseismic	132	0

Table 7.2: Earthquakes recorded at the Gradenbach seismic monitoring network between March and October 2012. Earthquakes listed in the ZAMG bulletin catalog (B-earthquakes) and earthquakes not listed in the ZAMG earthquake catalog (NB-earthquakes) are categorized into local, regional, teleseismic and undefined earthquakes. The categorization is done according to the epidistance (see text).

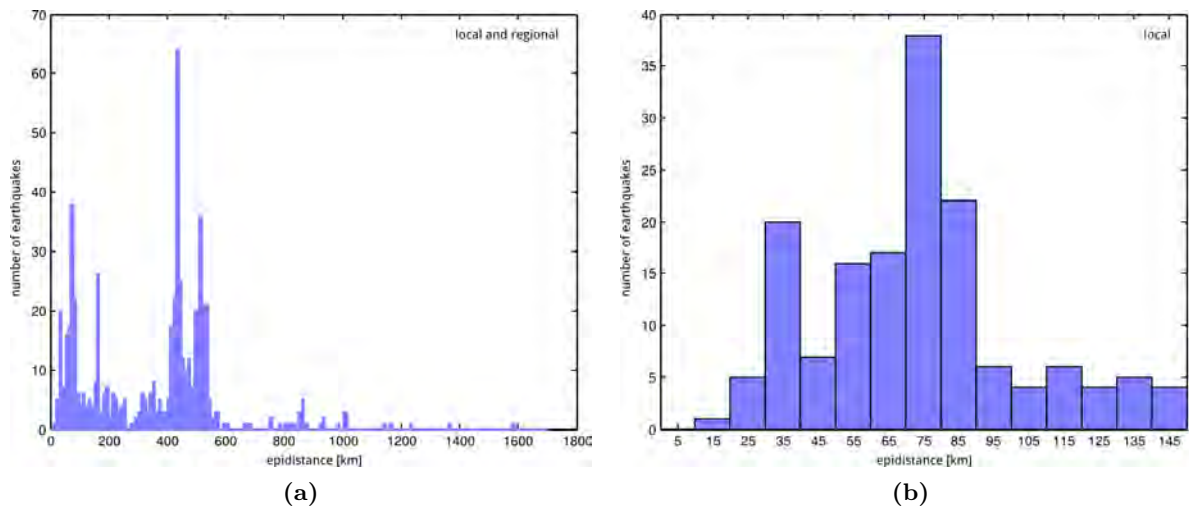


Figure 7.19: Histogram of the epicentral distances of local and regional earthquakes recorded at the seismic monitoring network Gradenbach. A detailed view of the local earthquakes only is given in b

7. SEISMIC EVENTS RECORDED AT GRADENBACH

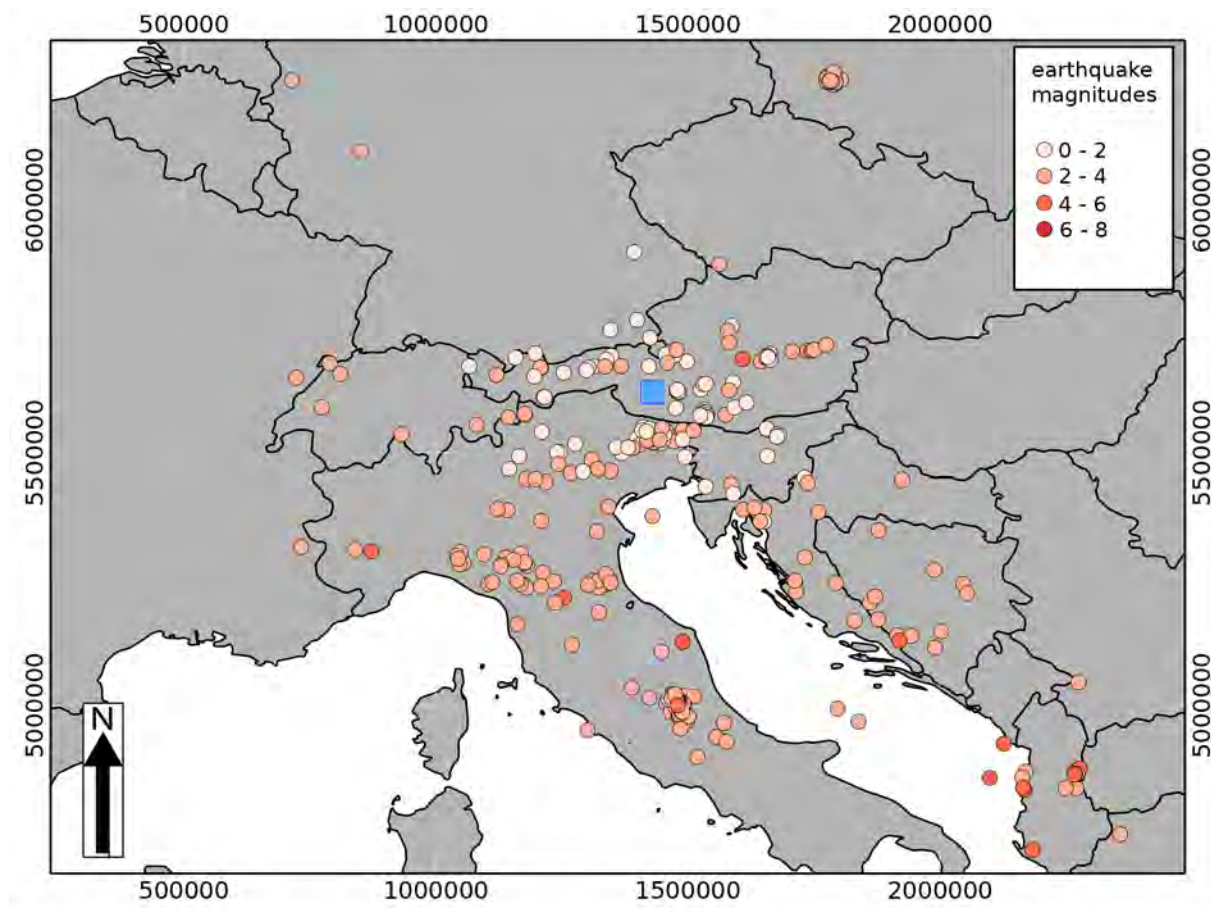


Figure 7.20: Map of the epicenters of the earthquakes recorded at the seismic monitoring network at the Gradenbach landslide in the period from 1.3.2009 to 1.10.2009. Only the known epicenters from the ZAMG bulletin are plotted.

7.4 Anthropogenic- and natural noise

Besides the slope events and the earthquakes described above, many other signals were recorded at the seismic network Gradenbach. They were classified as noise. Some of these noise signals which reoccurred with similar signatures were identified and related to anthropogenic or natural sources. As examples the recordings of a jet plane passing the seismic network at high altitude (figure 7.21), a helicopter (figure 7.22), a motorcycle (figure 7.23) and a thunderstorm (figure 7.24) are given. The comparison of the microphone and geophone spectrograms show almost identical patterns. Thus it can be concluded, that the signal recorded with the geophone was created by a coupling of the acoustic wave with the ground at the station location. I didn't expect such a high direct impact of airborne sound on the ground motion.

I mainly focused on discrete seismic events in this thesis. The microseismic activity might also be reflected in the ambient seismic noise (e.g. Got, 2010). Draxler (2013) showed in her master thesis, that patterns in the ambient seismic noise related to the displacement of the slope were recorded. An interesting finding was the correlation of the occurrence of seismic signals with peaks in the precipitation measured at the Gradenbach mass movement. The patterns were bound to the period of the acceleration of the slope and Draxler proposed infiltrating water as a possible source of the noise patterns.

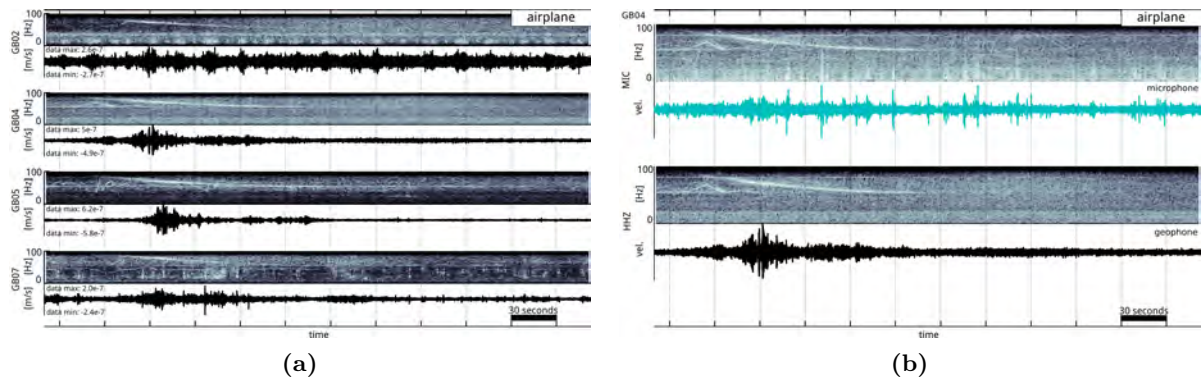


Figure 7.21: Example recording of a jet plane passing the seismic network at high altitude. (a) shows the seismograms and related spectrograms of the vertical component of 4 stations of the seismic network and (b) shows the microphone recording (turquoise) and the geophone recording at station GB04.

7. SEISMIC EVENTS RECORDED AT GRADENBACH

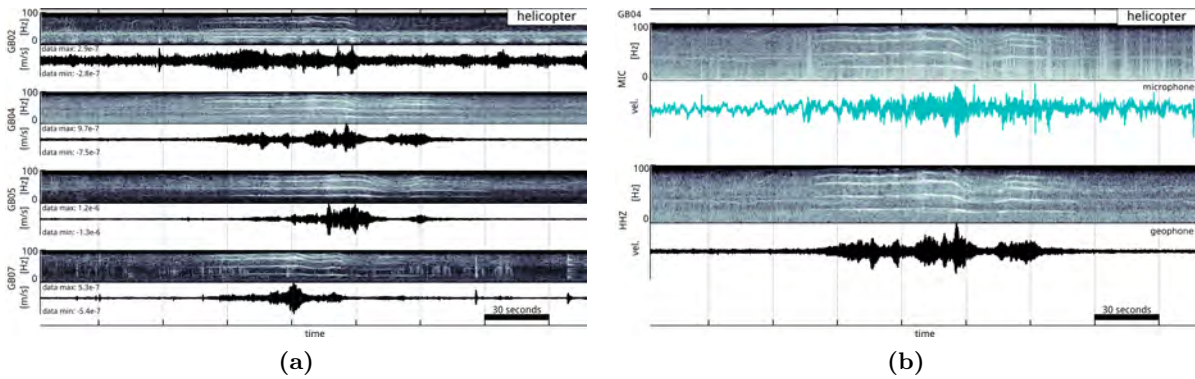


Figure 7.22: Example recording of a helicopter passing the seismic network. (a) shows the seismograms and related spectrograms of the vertical component of 4 stations of the seismic network and (b) shows the microphone recording (turquoise) and the geophone recording at station GB04.

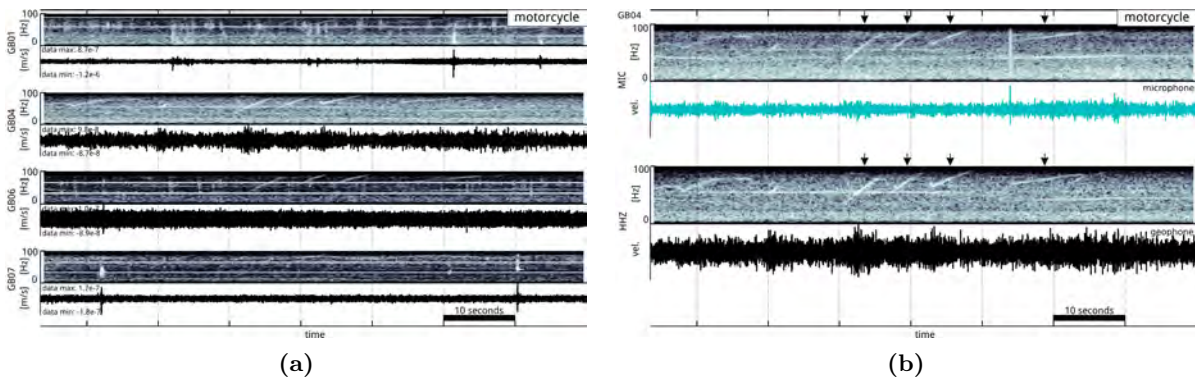


Figure 7.23: Example recording of a motorcycle passing the seismic network at the main road in the valley. The changing of the gears is visible in the seismic- and acoustic recordings. (a) shows the seismograms and related spectrograms of the vertical component of 4 stations of the seismic network and (b) shows the microphone recording (turquoise) and the geophone recording at station GB04.

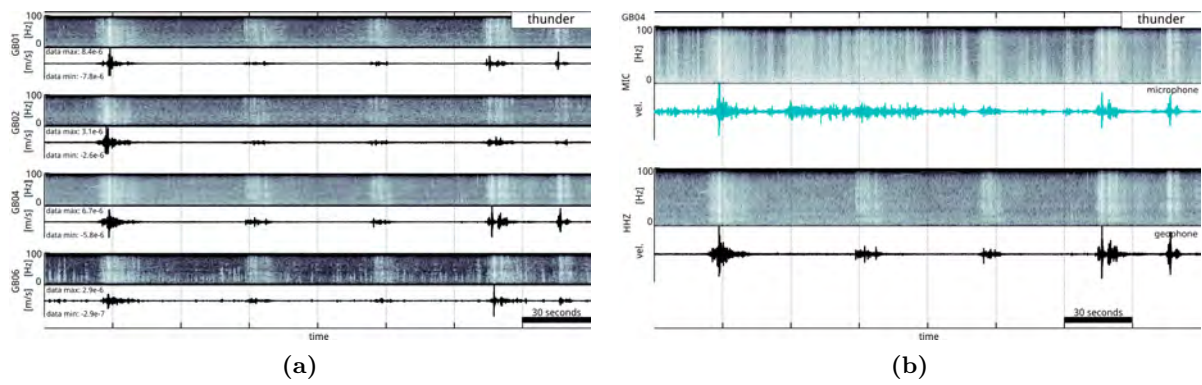


Figure 7.24: Example recording of a thunder recorded at the seismic network. (a) shows the seismograms and related spectrograms of the vertical component of 4 stations of the seismic network and (b) shows the microphone recording (turquoise) and the geophone recording at station GB04.

7. SEISMIC EVENTS RECORDED AT GRADENBACH

8

Slope displacement and seismic events

In figure 8.1 the seismic events recorded during the period from March 1 to October 1, 2009 are presented along with geodetic, hydrological, and meteorological data. The temporal distribution of the various seismic event types shows significant patterns and correlation with geodetic and hydrological parameters of the slope.

The type tremor events occurred during a period of 1 week at the beginning of April only. As can be seen from the data of the water-equivalent of the snow-cover, the type tremor coincided clearly with the time of the snow-melt indicated by the decrease of the water-equivalent and an increase of the Berchtoldgraben stream discharge. During this time, also a slight increase of the extensometer displacement was observed. However, this increase measured by the extensometer might contain some errors due to the influence of the changing weather conditions on the wire extensometer and is not significant. Recordings of type A and type D events accompanied the increase of tremor events. After this major increase of recorded events during the first week of April, the seismic activity of the slope ceased completely for the duration of about 1 month.

The next significant increase of events correlates with the start of the main acceleration of the slope at the beginning of May. During the period of the acceleration of the slope up to the beginning of June, mainly type B and type rf events were recorded. With the change of the slope from acceleration to re-stabilization the type B events vanished more or less abruptly and type D events dominated the seismic records from this time on. Type A events were recorded during both, the acceleration and the deceleration phase.

The separation of the event types in time as well as the different source regions of the event types (see section 7.2) indicate that various processes caused the individual event types.

The type tremor events were bound to a very narrow time period and coincided with the snow-melt. Brückl *et al.* (2013) have shown that the infiltration of water into the slope and the accompanied change of the pore-water pressure is a major triggering factor of the slope acceleration. The fast response of the occurrence of type tremor events to the beginning and the end of the snow-melt supports the assumption, that the infiltrating water triggered the type tremor events. Their source region was located at the top of the slope. This area below the

8. SLOPE DISPLACEMENT AND SEISMIC EVENTS

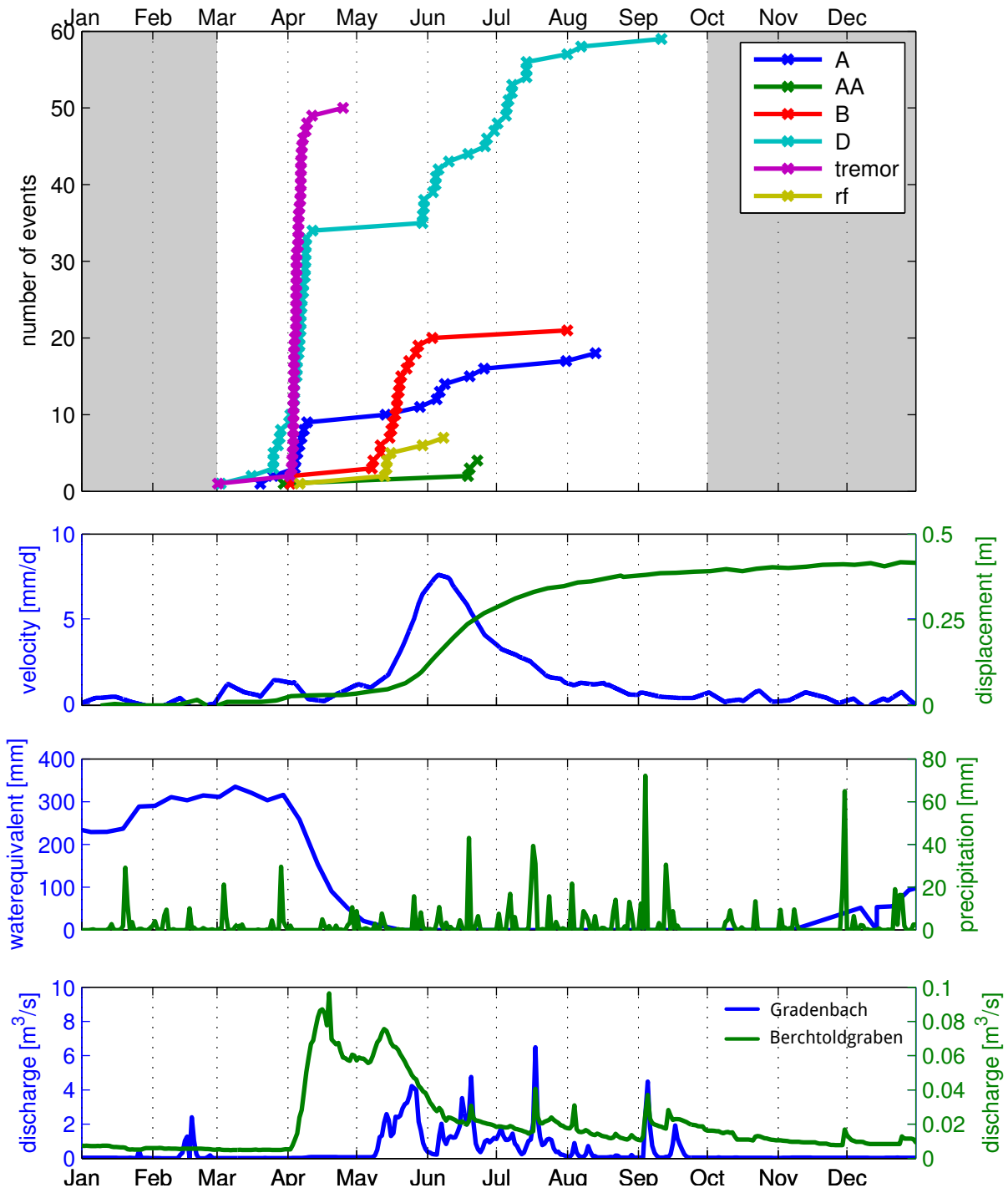


Figure 8.1: The seismic activity of the landslide together with complementary environmental data recorded at the Gradenbach landslide. The complementary data was provided by the Federal Research and Training Centre for Forests, Natural Hazards and Landscape (BFW).

main scarp is a zone of high infiltration and possible fissure water ways. This would enable a quick infiltration of the melt-water to trigger the seismic events in shallow depth. The quick infiltration of water and shallow source depths could also explain the temporal distribution of type tremor events with a cumulated occurrence during the daytime. The accumulation of tremor events during the daytime could be caused by the day- and nighttime variation of the snow-melt due to the thaw-freeze cycle during day and night.

The source region of the type B events was in the eastern part of the slope. Their occurrence was limited to the period of the acceleration of the slope only. Moreover, during this time, no type D events were recorded. Brückl & Parotidis (2005) and Brückl *et al.* (2006) have proposed a description of the displacement of the DGSD Gradenbach with a rotational slider-block model. If a block-displacement of the whole slope along the basal sliding zone was assumed, the concentration of the type B epicenters to the eastern part of the slope implies an aseismic slip of the slope in the western part or the release of seismic energy with events below the detection threshold of the network during the acceleration of the slope. Kilburn & Petley (2003) estimated a similar creation of low magnitude events below the detection range of a seismometer for the Vajont landslide. Therefore, the accumulation of the type B events in the eastern part would require the creation of stronger events in this area to overcome the detection threshold of the seismograph. This increased event magnitude could be created by irregularities of the topography of the sliding zone (see figure 3.7). The topography of the sliding zone shows a nose-shaped ridge in the eastern part which could have acted as a barrier blocking the downslope movement (Müller *et al.* (2011) draw a similar conclusion based on GPS measurements). Higher shear stress caused by this barrier could have caused the type B events with a magnitude large enough to be detected by the seismic network. The similarity of the spectra of the type B events as well as the polarization analysis further strengthen the assumption of a common source region and mechanism of these events.

A sensitive response of the upper part of the slope to changes in the hydrological regime was observed in 2012 during a minor acceleration of the slope in autumn following a period of heavy rainfall. In figure 8.2 it can be seen, that the onset of the base activity of the slope correlates with the snow-melt (decreasing snow water equivalent). The GPS station MC, which is located in the upper part of the slope, immediately reacted to the rise of the hydraulic head measured in borehole 3b (also located in the upper part of the slope) at the end of July. The GPS station MA, located in the lower part of the slope, showed no increased displacement rate during this time. In mid November, both GPS stations, MA and MC, showed an acceleration of the slope. This acceleration followed a period of heavy rainfall and in both boreholes, 3b and 15, a rise of the hydraulic head was observed.

It is assumed, that for long term observations, the slope behaves according to the slider block model introduced by Brückl & Parotidis (2005). For short-term observations, the landslide doesn't deform as a rigid body in a block-like manner. The main deformation is concentrated to a basal sliding zone. Nevertheless, deformation can occur throughout the entire body of the landslide and it can vary with the location on the slope. The deformation in the basal sliding zone can be caused by sub-critical crack growth (Brückl *et al.*, 2013), although other mechanisms might be related to the deformation at small depths within the sliding mass.

The observations of the recorded seismic events, the geodetic- and the geotechnical measure-

8. SLOPE DISPLACEMENT AND SEISMIC EVENTS

ments can be described with the hypothesis, that the deformation behavior of the landslide is mainly controlled by a 'wave' of infiltrating groundwater. The upper part of the slope consists of heavily fractured material and allows a quick infiltration of the water (see section 3.1). The infiltrating water of the snow-melt triggers a minor displacement of the upper, shallow part of the slope inducing the type tremor events as well as type D events. The main acceleration of the slope is triggered by a change of the pore-pressure at the basal sliding zone caused by infiltrating water reaching larger depths and the lower part of the slope. Brückl *et al.* (2013) has shown the possibility of modeling the acceleration of the slope by infiltrating water raising the pore-pressure at the basal sliding plane. The deformation of the main acceleration phase comprises the entire slope and mainly takes part within the sliding zone. This deformation creates seismic events below the detection threshold of the seismic network. Only a barrier at the eastern part of the slope causes an increase of the shear stress and therefore the type B events with magnitudes large enough to be detected by the seismic network are created. When the infiltrating groundwater starts to leave the area of the landslide, the pore-pressure decreases leading to a re-stabilization of the slope. This causes the disappearance of the type B events from the seismic records.

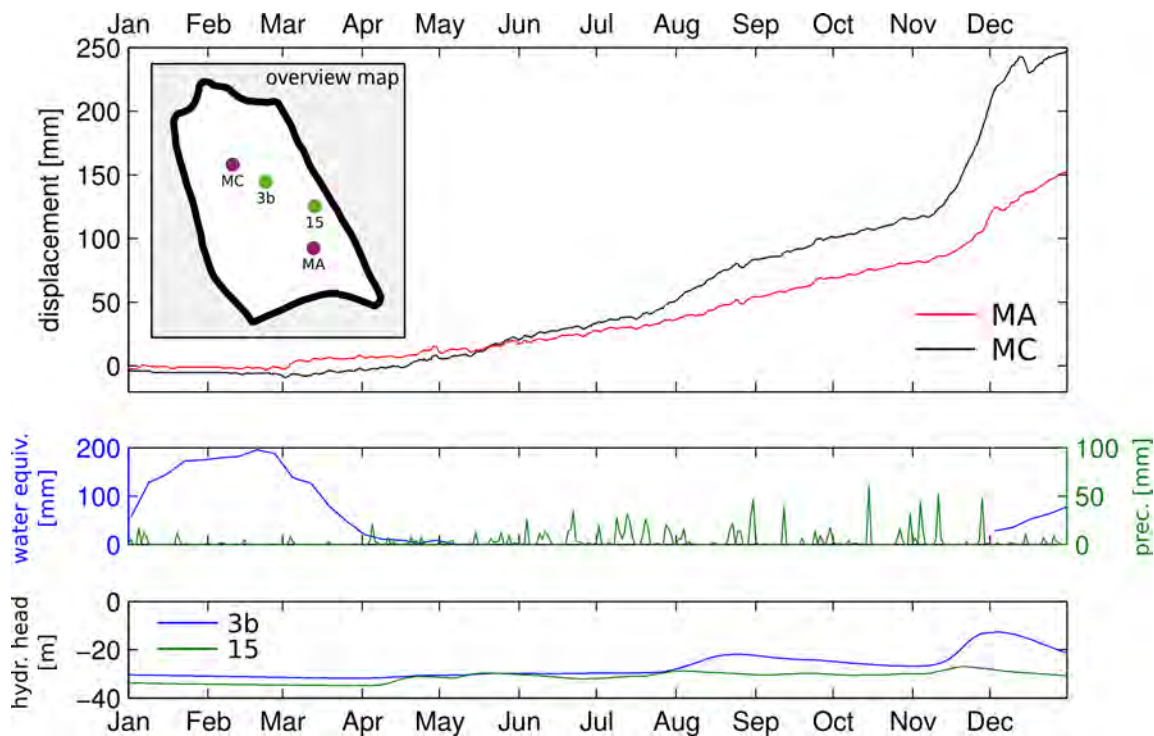


Figure 8.2: A plot of the GPS displacement and the precipitation during the year 2012. The overview map highlights the locations of the GPS stations MA and MC and the wells 3b and 15. The data was provided by the Federal Research and Training Centre for Forests, Natural Hazards and Landscape (BFW). The GPS data was provided by the Graz University of Technology.

References

- ABELE, G. (1974). *Bergstürze in den Alpen - ihre Verbreitung, Morphologie und Folgeerscheinungen*, vol. 25. Wissenschaftliche alpenvereinshefte edn. 9
- AGLIARDI, F., CROSTA, G.B., ZANCHI, A. & RAVAZZI, C. (2009). Onset and timing of deep-seated gravitational slope deformations in the eastern alps, italy. *Geomorphology*, **103**, 113–129-. 12
- AGLIARDI, R., CROSTA, G. & ZANCHI, A. (2001). Structural constraints on deep-seated slope deformation kinematics. *Engineering Geology*, **59**, 83–102-. 6, 7, 8, 9, 12
- AKI, K. (1993). Local site effects on weak and strong ground motion. *Tectonophysics*, **218**, 93–111. 62
- ALLEN, R. (1978). Automatic earthquake recognition and timing from single traces. *Bulletin of the Seismological Society of America*, **68**, 1521–1532-. 41
- ALLEN, R. (1982). Automatic phase pickers: their present use and future prospects. *Bulletin of the Seismological Society of America*, **72**, S225–S242-. 41
- AMITRANO, D., GRASSO, J.R. & SENFAUTE, G. (2005). Seismic precursory patterns before a cliff collapse and critical point phenomena. *Geophys. Res. Lett.*, **32**, L08314-. 3
- AMPFERER, O. (1939). *Über einige Formen der Bergzerreißung. - Wien & Leipzig: Hölder-Pichler-Tempsky in Komm. 1939. 14 S. 8Å° [Umschlagt.] Aus: Sitzungsberichte d. Akad. d. Wiss. in Wien. Math. -nat. Kl. 1, 148. Hölder-Pichler-Tempsky in Komm. 6*
- ASADA, T. & SUZUKI, Z. (1950). On micro-earthquakes observed after the imaichi earthquake, dec. 26, 1949. *Bulletin of the Earthquake Research Institute, University of Tokyo*, **28**, 414–420. 2
- ATKINSON, B. (1981). Earthquake prediction. *Physics in Technology*, **12**, 60–68. 2
- BALLANTYNE, C.K. (2002). Paraglacial geomorphology. *Quaternary Science Reviews*, **21**, 1935 – 2017. 9
- BEDOUI, S.E., GUGLIELMI, Y., LEBOURG, T. & PEREZ, J.L. (2009). Deep-seated failure propagation in a fractured rock slope over 10,000 years: The la clapiere slope, the south-eastern french alps. *Geomorphology*, **105**, 232 – 238. 9
- BEHM, M. & SNIEDER, R. (2013). Love waves from local traffic noise interferometry. *The Leading Edge*, **32**, 628–632. 115
- BESSASON, B., EIRIKSSON, G., THORARINSSON, O., THORARINSSON, A. & EINARSSON, S. (2007). Automatic detection of avalanches and debris flows by seismic methods. *Journal of Glaciology*, **53**, 461–472-. 3
- BFW (2005). Gradenbach, sackung und steinschlag 2005. <http://bfw.ac.at/rz/bfwcms.window?dok=7143>, accessed December 2010. 16
- BFW (2007). Gradenbach, felssturz 2007. <http://bfw.ac.at/rz/bfwcms.window?dok=7146>, accessed December 2010. 16
- BISCI, C., DRAMIS, F. & SORRISO-VALVO, M. (1996). Rock flow (sackung). In R. Dikau, D. Brunsten, L. Schrott & M.L. Ibsen, eds., *Landslide Recognition*, chap. 7.2, 150–160, Jon Wiley & Sons. 5, 7
- BOHNHOFF, M., DRESEN, G., ELLSWORTH, W.L. & ITO, H. (2009). *Passive Seismic Monitoring of Natural and Induced Earthquakes: Case Studies, Future Directions and Socio-Economic Relevance*, 261–285. Springer Netherlands. 2
- BONNEFOY-CLAUDET, S., COTTON, F. & BARD, P.Y. (2006). The nature of noise wavefield and its applications for site effects studies: A literature review. *Earth-Science Reviews*, **79**, 205 – 227. 63
- BONZANIGO, L., EBERHARDT, E. & LOEW, S. (2007). Long-term investigation of a deep-seated creeping landslide in crystalline rock. part i. geological and hydromechanical factors controlling the campo vallemaggia landslide. *Canadian Geotechnical Journal*, **44**, 1157–1180(24). 7, 11
- BORMANN, P. (2002). *IASPEI New Manual of Seismological Observatory Practice (NMSOP)*. GeoForschungsZentrum Potsdam. 66, 90

REFERENCES

- BORMANN, P., ENGDAHL, B. & KIND, R. (2002). Seismic wave propagation and earth models. In P. Bormann, ed., *IASPEI New Manual of Seismological Observatory Practice*, chap. 2, 1–70, GeoForschungsZentrum Potsdam. 62
- BRUNNER, F.K., ZOBL, F. & GASSNER, G. (2003). On the capability of gps for landslide monitoring. *Felsbau*, **21**, 51 – 55. 23, 24
- BRUNSDEN, D. (1984). Mudslides. In D. Brunsten & D. Prior, eds., *Slope Stability*, 363–418, Wiley, Chichester. 5
- BRÜCKL, E. (2001). Cause-effect models of large landslides. *Natural Hazards*, **23**, 291–314. 9, 12, 19
- BRÜCKL, E. & BRÜCKL, J. (2006). Geophysical models of the lesachriegel and gradenbach deep-seated mass-movements (schober range, austria). *Engineering Geology*, **83**, 254–272-. 13, 19, 24
- BRÜCKL, E. & MERTL, S. (2006). Seismic monitoring of deep-seated mass movements. -. 3, 29
- BRÜCKL, E. & PAROTIDIS, M. (2001). Estimation of large-scale mechanical properties of a large landslide on the basis of seismic results. *International Journal of Rock Mechanics & Mining Sciences*, **38**, 877–883-. 9, 10, 11, 12
- BRÜCKL, E. & PAROTIDIS, M. (2005). Prediction of slope instabilities due to deep-seated gravitational creep. *Natural hazards and earth system sciences*, **5**, 155–172-. 9, 11, 12, 13, 19, 21, 27, 99
- BRÜCKL, E. & SCHEIDEGGER, A. (1972). The rheology of spacially continuous mass creep in rock. *Rock mechanics*, **4**, 237–250. 11
- BRÜCKL, E., BRÜCKL, J. & HEUBERGER, H. (2001). Present structure and prefailure topography of the giant rockslide of köfels. *Zeitschrift für Gletscherkunde und Glazilogie*, **37**, 49–79. 9
- BRÜCKL, E., ZANGERL, C. & TENTSCHERT, E. (2004). Geometry and deformation mechanisms of a deep-seated gravitational creep in crystalline rocks. In *Proceedings of the ISRM Regional Symposium EUROCK*, 229–232. 7, 19
- BRÜCKL, E., BRUNNER, F. & KRAUS, K. (2006). Kinematics of a deep-seated landslide derived from photogrammetric, gps and geophysical data. *Engineering Geology*, **88**, 149 – 159. 7, 11, 20, 24, 27, 99
- BRÜCKL, E., CHWATAL, W., MERTL, S. & RADINGER, A. (2008a). Exploration ahead of a tunnel face by tswd-tunnel seismic white drilling. *Geomechanics and Tunneling*, **5**, 460–465. 114
- BRÜCKL, E., MERTL, S., BINDER, D. & HAUSMANN, H. (2008b). Hazard estimation of deep seated mass movements by microseismic monitoring, final report 2004 - 2008. In *International Strategy for Disaster Reduction (ISDR)*, self published, online available: <http://epub.oew.ac.at/?arp=0x001b7169> - Last access:3.3.2014. 3, 13, 24, 29
- BRÜCKL, E., BRUNNER, F., LANG, E., MERTL, S., MÜLLER, M. & STARY, U. (2013). The gradenbach observatory - monitoring deep-seated gravitational slope deformation by geodetic, hydrological, and seismological methods. *Landslides*, 1–15. 11, 12, 18, 19, 20, 23, 24, 26, 27, 28, 97, 99, 100
- BUTLER, R. (2003). Nanoearthquakes at the hawaii-2 observatory. *Seismological Reserach Letters*, **74**, 290 – 297. 2
- CALOI, P. (1966). L'evento del vajont nei suoi aspetti geodinamici. *Annals of Geophysics*, **19**. 3
- CHEN, Z., STEWART, R., BLAND, H. & THURSTON, J. (2005). Microseismic activity and location at turtle mountain, alberta. In *Proceedings of the Canadian Society of Exploration Geophysics National Convention, Calgary, Alta., 17–19 May 2005*, -. 3
- CHIGIRA, M., HARIYAMA, T. & YAMASAKI, S. (2013). Development of deep-seated gravitational slope deformation on a shale dip-slope: Observations from high-quality drill cores. *Tectonophysics*, -. 7
- COMBS, J. & HADLEY, D. (1977). Microearthquake investigation of the mesa geothermal anomaly, imperial valley, california. *Geophysics*, **42**, 17–33. 2
- COSSART, E., BRAUCHER, R., FORT, M., BOURLES, D. & CARCAILLET, J. (2008). Slope instability in relation to glacial debuitressing in alpine areas (upper durance catchment, southeastern france): Evidence from field data and 10be cosmic ray exposure ages. *Geomorphology*, **95**, 3 – 26, jce:title;Paraglacial Geomorphology: Processes and Paraglacial Context|ce:title;. 9
- CROSTA, G., FRATTINI, P. & AGLIARDI, F. (2013). Deep seated gravitational slope deformations in the european alps. *Tectonophysics*, -. 9
- CROSTA, G.B., AGLIARDI, F., FRATTINI, P. & SOSIO, R. (2012a). Landslide triggering by deglaciation. In G.B. Crosta, F. Agliardi, P. Frattini & R. Sosio, eds., *Deliverable 1.1 - Landslide triggering mechanisms in Europe – Overview and State of the Art - Work Package 1.1 – Identification of mechanisms and triggers*, chap. 7, 249–270, SafeLand FP-7. 12
- CROSTA, G.B., AGLIARDI, F., FRATTINI, P. & SOSIO, R. (2012b). Landslide triggering by rainfalls and changes in slope hydrology. In G.B. Crosta, F. Agliardi, P. Frattini & R. Sosio, eds., *Deliverable 1.1 - Landslide triggering mechanisms in Europe – Overview and State of the Art - Work Package 1.1 – Identification of mechanisms and triggers*, chap. 3, 84–143, SafeLand FP-7. 11
- CRUDEN, D. (1991). A simple definition of a landslide. *Bulletin International Association for Engineering Geology*, **43**, 27–29. 5
- CRUDEN, D.M. & VARNES, D.J. (1996). Landslide types and processes. In A.K. Turner & R.L. Schuster, eds., *Landslides - investigation and mitigation*, chap. 3, 36–75, National Academic Press, Washington D.C. 5, 6, 7

REFERENCES

- DEWEY, J. & BYERLY, P. (1969). The early history of seismometry (to 1900). *Bulletin of the Seismological Society of America*, **59**, 183–227. 1
- DIKAU, R., BRUNSDEN, D., SCHROTT, L. & IBSEN, M.L., eds. (1996). *Landslide recognition - identification, movement and causes*. John Wiley & Sons, Ltd. 5
- DOBLHOFF-DIER, K. (2010). Implementation of a polarization analysis for seismon. 70, 86
- DOBLHOFF-DIER, K. (2011). *Seismic signal analysis using polarization attributes and its applications*. Master's thesis, Vienna University of Technology. 61, 70, 71, 86, 89
- DRAMIS, F. & SORRISO-VALVO, M. (1994). Deep-seated gravitational slope deformations, related landslides and tectonics. *Engineering Geology*, **38**, 231–243, das pdf noch besorgen und kontrollieren ob mit DSGSD wirklich eine Sackung gemeint ist. 6
- DRAXLER, A. (2013). *Seismic Noise Analysis at the Gradenbach Landslide*. Master's thesis, Vienna University of Technology. 33, 93
- EBERHARDT, E., STEAD, D. & COGGAN, J. (2004). Numerical analysis of initiation and progressive failure in natural rock slopes - the 1991 randa rockslide. *International Journal of Rock Mechanics & Mining Sciences*, **41**, 69–87-. 9
- FERRUCCI, F., AMELIO, M., SORRISO-VALVO, M. & TANSI, C. (2000). Seismic prospecting of a slope affected by deep-seated gravitational slope deformation: the lago sackung, calabria, italy. *Engineering Geology*, **57**, 23–64-. 7
- FONT, Y., KAO, H., LALLEMAND, S., LIU, C.S. & CHIAO, L.Y. (2004). Hypocentre determination offshore of eastern taiwan using the maximum intersection method. *Geophysical Journal International*, **158**, 655–675. 68
- FORLATI, F., GIODA, G. & SCAVIA, C. (2001). Finite element analysis of a deep-seated slope deformation. *Rock Mechanics and Rock Engineering*, **34**, 135–159. 7
- FROESE, C.R., MORENO, F., JABOYEDOFF, M. & CRUDEN, D.M. (2009). 25 years of movement monitoring on south peak, turtle mountain: understanding the hazard. *Canadian Geotechnical Journal*, **46**, 256–269. 3
- GAO, J., WEINMEISTER, W. & LANG, E. (1997). Bewertung der entwässerungsmaßnahmen im talzuschub des gradenbaches aus hydrologischer sicht. *Journal of torrent, avalanche, landslide and rock fall engineering*, **133**, 23–37. 24
- GEIGER, L.C. (1910). Herdbestimmung bei erdbeben aus den ankunftszeiten. *Nachrichten von der Königlichen Gesellschaft der Wissenschaften zu Göttingen, Mathematisch-Physikalische Klasse*, 331–349. 65
- GENEVOIS, R. & GHIROTTI, M. (2005). The 1963 vaiont landslide. *Giornale di Geologia Applicata*, **1**, 41–52. 11, 12
- GLADE, T. & CROZIER, M. (2005). The nature of landslide hazard impact. In T. Glade, M. Anderson & M. Crozier, eds., *Landslide Hazard and Risk*, 43 – 74, John Wiley & Sons, Ltd. 12
- GOMBERG, J., BODIN, P., SAVAGE, W. & JACKSON, M. (1995). Landslide faults and tectonic faults, analogs?: The slumgullion earthflow, colorado. *Geology*, **23**, 41–44-. 3
- GOMBERG, J., SCHULZ, W., BODIN, P. & KEAN, J. (2011). Seismic and geodetic signatures of fault slip at the slumgullion landslide natural laboratory. *J. Geophys. Res.*, **116**, B09404-. 3, 61
- GONZALEZ, R.C., WOODS, R.E. & EDDINS, S.L. (2004). *Digital Image Processing Using Matlab*. Pearson Prentice Hall. 47, 48
- GOT, P.G.J., JEAN-LUC MOUROT (2010). Pre-failure behaviour of an unstable limestone cliff from displacement and seismic data. *Natural hazards and earth system sciences*, **10**, 819–829. 3, 93
- GOTTSCHLING, H. (1999). Der talzuschub gradenbach - ein geologisch-geotechnischer Überblick. *Jahrbuch der Geologischen Bundesanstalt*, **141**, 345–367. 23, 24
- GOVI, M., GULLA, G. & NICOLETTI, P.G. (2002). Val pola rock avalanche of july 28, 1987, in valtellina (central italian alps). In S. Evans & J.V. DeGraff, eds., *Catastrophic landslides: Effects, occurrence, and mechanisms*, vol. XV, 71–89, Geological Society of America, reviews in engineering geology edn. 11, 12
- HAGEN, K. & LANG, E. (2000). Schneehydrologische untersuchungen im einzugsgebiet des gradenbaches (kärnten). *FBVA-Berichte*, 116–168. 24
- HARRIS, F.J. (1978). On the use of windows for harmonic analysis with the discrete fourier transform. *Proceedings IEEE*, **66**, 51–83. 32
- HART, D.M., MERCHANT, B.J., HARRIS, J.M. & YOUNG, C.J. (2005). The 2005 matseis and nnsa seismic regional analysis tools. In *27th Seismic Research Review*, -. 109
- HAUSMANN, H., KRAINER, K., STAUDINGER, M. & BRÜCKL, E. (2009). Continuous recording of seismic signals in alpine permafrost. In *EGU General Assembly Conference Abstracts*, vol. 11, 10330. 114
- HAUSMANN, H., HOYER, S., SCHURR, B., BRUECKL, E., HOUSEMAN, G. & STUART, G. (2010). New seismic data improve earthquake location in the vienna basin area, austria.. *Austrian Journal of Earth Sciences*, **103**, 2–14. 114
- HAVSKOV, J. & ALGUACIL, G. (2004). *Instrumentation in Earthquake Seismology*. Springer. 32

REFERENCES

- HAVSKOV, J., BORMANN, P. & SCHWEITZER, J. (2002). Earthquake location. In *New Manual of Seismological Observatory Practice (NMSOP)*, chap. IS 11.1, 1–28, GeoForschungsZentrum Potsdam. 65
- HAVSKOV, J., OTTEMOLLER, L., WILLIAM H.K. LEE, H.K.P.C.J. & KISSLINGER, C. (2003). Seisan earthquake analysis and seisnet network automation software. In *International Geophysics*, 1615–1616–, Academic Press. 109
- HEIM, A. (1932). *Bergsturz und Menschenleben*. Fretz & Wasmuth Verlag A.G. 5
- HELMSTETTER, A. & GARAMBOIS, S. (2010). Seismic monitoring of séchilienne rockslide (french alps): Analysis of seismic signals and their correlation with rainfalls. *Journal of Geophysical Research*, **115**, F03016–. 3, 13
- HIPPOLYTE, J.C., BOURLAËs, D., LÄ©ANNI, L., BRAUCHER, R., CHAUVET, F. & LEBATARD, A.E. (2012). 10be ages reveal ç 12 ka of gravitational movement in a major sackung of the western alps (france). *Geomorphology*, **171**â[U+0080][U+0093]**172**, 139 – 153. 9, 11
- HÄGE, M. & JOSWIG, M. (2009). Microseismic feasibility study: detection of small magnitude events (mlç0.0) for mapping active faults in the betic cordillera (spain). *Annals of geophysics*, **52**, 117–126. 3
- JOHNSON, C., BITTENBINDER, A., BOGAERT, B., DIETZ, L. & KOHLER, W. (1995). Earthworm : A flexible approach to seismic network processing. *IRIS Newsletter*, **14**, 1–4. 41
- JOSWIG, M. (1990). Pattern recognition for earthquake detection. *Bulletin of the Seismological Society of America*, **80**, 170–186–. 41, 42
- JOSWIG, M. (1995). Automated classification of local earthquake data in the bug small array. *Geophysical Journal International*, **120**, 262–268–. 41, 45
- JOSWIG, M. (1996). Pattern recognition techniques in seismic signal processing. *Cahiers du Centre Europeen de Geodynamique et de Seismologie*, **12**, –. 41, 42
- JOSWIG, M. (2008). Nanoseismic monitoring fills the gap between microseismic networks and passive seismic. *first break*, **26**, 121–128–. 2, 42, 61
- KAWASE, H. (1996). The cause of the damage belt in kobe: â[U+0080][U+009C]the basin-edge effect,â[U+0080][U+009D] constructive interference of the direct s-wave with the basin-induced diffracted/rayleigh waves. *Seismological Research Letters*, **67**, 25–34. 63
- KILBURN, C.R. & PETLEY, D.N. (2003). Forecasting giant, catastrophic slope collapse: lessons from vajont, northern italy. *Geomorphology*, **54**, 21 – 32, çe:titileçStudies on Large Volume Landslidesç/ce:titileç. 99
- KRONFELLNER-KRAUS, G. (1980). Neue untersuchungsergebnisse in wildbächen - der talzuschub in abhängigkeit von niederschlägen. In *IP 1980, Hochwasser-Abwehr (Sonderband des Landes Oberösterreich)*, vol. 1, 179.182. 24
- KRONFELLNER-KRAUS, G. (1990). Einige aktuelle probleme und ergebnisse der wildbachforschung in Österreich. *Berichte der Forstlichen Bundesversuchsanstalt*, **9**, 7–24. 24
- KWIATEK, G., PLENKERS, K., NAKATANI, M., YABE, Y., DRESEN, G. & JAGUARS-GROUP (2010). Frequency-magnitude characteristics down to magnitude -4.4 for induced seismicity recorded at mponeng gold mine, south africa. *BULLETIN OF THE SEISMOLOGICAL SOCIETY OF AMERICA*, **100**, 1165–1173. 2
- KÖHLER, A., OHNRBERGER, M. & SCHERBAUM, F. (2009). Unsupervised feature selection and general pattern discovery using self-organizing maps for gaining insights into the nature of seismic wavefields. *Computers & Geosciences*, **35**, 1757–1767. 42
- LACROIX, P. & HELMSTETTER, A. (2011). Location of seismic signals associated with microearthquakes and rockfalls on the séchilienne landslide, french alps. *Bulletin of the Seismological Society of America*, **101**, 341–353. 13, 61
- LAHR, J.C. (1989). Hypoellipse/version 2.0; a computer program for determining local earthquake hydrocentral parameters, magnitude, and first motion pattern. Tech. rep., U.S. Geological Survey Open-File Report 89-116. 65
- LEE, W. & STUART, S. (1981). *Principles and applications of microearthquake networks*. Academic Press. 2
- LEE, W.H.K. & LAHR, J. (1975). Hyp071 (revised): A computer program for determining hypocenter, magnitude, and first motion pattern of local earthquakes. Tech. rep., U. S. Geological Survey Open File Report 75-311. 65
- LENTI, L., MARTINO, S., PACIELLO, A., PRESTININZI, A. & RIVELLINO, S. (2012). Microseismicity within a karstified rock mass due to cracks and collapses as a tool for risk management. *Natural Hazards*, **64**, 359–379. 3, 13
- LIENHART, W. & BRUNNER, F.K. (2013). Geodätische Überwachung von gravitativen massenbewegungen am beispiel des gradenbach-observatoriums. *Zeitschrift für Geodäsie, Geoinformation und Landmanagement (zfv)*, **138**, 64–74. 24, 27
- LOMAX, A. (2005). A reanalysis of the hypocentral location and related observations for the great 1906 california earthquake. *Bulletin of the Seismological Society of America*, **95**, 861–877. 68
- LOMAX, A. & CURTIS, A. (2001). Fast, probabilistic earthquake location iin 3d models using oct-tree importance sampling. *Geophysical Research Abstracts*, **3**, 955. 68

REFERENCES

- LOMAX, A., VIRIEUX, J., VOANT, P. & BERGE, C. (2000). *Probabilistic earthquake location in 3D and layered models: Introduction of a Metropolis-Gibbs method and comparison with linear locations.*, chap. Chapter 5, 101 – 134. Kluwer Academic Publishers. 66
- LOMAX, A., ZOLLO, A., CAPUANO, P. & VIRIEUX, J. (2001). Precise, absolute earthquake location under somma-vesuvius volcano using a new three-dimensional velocity model. *Geophysical Journal International*, **146**, 313–331–. 66
- LOMAX, A., MICHELINI, A. & CURTIS, A. (2009). Earthquake location, direct, global-search methods. In R.A. Meyers, ed., *Encyclopedia of Complexity and Systems Science*, 2449–2473, Springer New York. 65, 66, 68, 69
- MCCOLL, S.T. (2012). Paraglacial rock-slope stability. *Geomorphology*, **153–154**, 1 – 16. 9, 10
- MCMANARA, D.E. & BULAND, R.P. (2004). Ambient noise levels in the continental united states. *Bulletin of the Seismological Society of America*, **94**, 1517–1527. 32
- MCMUTT, S.R. (2002). Volcano seismology and monitoring for eruptions. In H.K.P.C.J. William H.K. Lee & C. Kisslinger, eds., *International Geophysics*, vol. A, chap. 25, 383–406, V–, Academic Press, international handbook of earthquake & engineering seismology edn. 3
- MERTL, S. & BRÜCKL, E. (2007a). Detection and localization of micro-earthquakes on deep-seated mass movements. In *Geophysical Research Abstracts*, vol. 9, 07187. 3, 13, 29
- MERTL, S. & BRÜCKL, E. (2007b). Observation of fracture processes in creeping rock masses by seismic monitoring. *Proceedings of 11th congress of the international society for rock mechanics, Lisbon, Portugal 9-13 July 2007*, –. 3, 13, 24, 29
- MITTERBAUER, U., BEHM, M., BRÄ $\frac{1}{4}$ CKL, E., LIPPITSCH, R., GUTERCH, A., KELLER, G.R., KOSLOVSKAYA, E., RUMPFHUBER, E.M. & Å UMANOVAC, F. (2011). Shape and origin of the east-alpine slab constrained by the {ALPASS} teleseismic model. *Tectonophysics*, **510**, 195 – 206. 114
- MOSEGAARD, K. & TARANTOLA, A. (2002). Probabilistic approach to inverse problems. In *International Handbook of Earthquake and Engineering Seismology*, chap. Appendix B9 16, 237–265, Academic Press. 66
- MOSER, M. & GLUMAC, S. (1983). Geotechnische untersuchungen zum massenkriechen in fels am beispiel des talzuschubes gradenbach (kärnten). *Verh. Geol. B.-A.*, **3**, 209–241. 15, 16, 19, 20, 24
- MOSER, M. & KIEFER, J. (1988). Die hydrogeologischen verhältnisse und ihre beziehungen zur kinematik im bereich der talzuschubsmasse gradenbach, kärnten. *Beiträge zur Hydrogeologie*, **39**, 0. 24
- MOSER, T., ECK, T.V. & NOLET, G. (1992). Hypocenter determination in strongly heterogeneous earth model using the shortest path method. *Journal of Geophysical Research*, **97**, 6563–6572–. 68
- MÜLLER, M., BRUNNER, F.K. & LANG, E. (2011). Long term measurement and analysis of a deep-seated mass movement. In *5th Int. Conf. on Engineering Surveying - INGENO, Brijuni, Croatia*. 27, 99
- NEMCOK, A., PASEK, J. & RYBAR, J. (1972). Classification of landslides and other mass movements. *Rock Mechanics and Rock Engineering*, **4**, 71–78. 5
- OCCHIANA, C., COVIELLO, V., ARATTANO, M., CHIARLE, M., MORRA DI CELLA, U., PIRULLI, M., POGLIOTTI, P. & SCAVIA, C. (2012). Analysis of microseismic signals and temperature recordings for rock slope stability investigations in high mountain areas. *Natural Hazards and Earth System Science*, **12**, 2283–2298. 3
- OHRNBERGER, M. (2001). *Continuous automatic classification of seismic signals of volcanic origin at Mt. Merapi, Java, Indonesiano journal*. Ph.D. thesis. 41, 42
- PAROTIDIS, M. (2001). *Geomechanische Modellierung von Massenbewegungen*. Ph.D. thesis, Vienna University of Technology, wien, Techn. Univ., Diss., 2001. 12
- PERE, V.H. (2009). *Antiscarp initiation and evolution*. Ph.D. thesis, University of Canterbury. Geological Sciences. 9
- PETERSON, J. (1993). Observation and modeling of seismic background noise. 33
- PETLEY, D.N. & ALLISON, R.J. (1997). The mechanics of deep-seated landslides. *Earth Surf. Process. Landforms*, **22**, 747–758. 10
- PIOVANO, G. (2012). *Combined finite-discrete element modelling of key instabilities which characterise deep-seated landslides from massive rock slope failure*. Ph.D. thesis, Politecnico di Torino. 5
- PRAGER, C., ZANGERL, C., PATZELT, G. & BRANDNER, R. (2008). Age distribution of fossil landslides in the tyrol (austria) and its surrounding areas. *Nat. Hazards Earth Syst. Sci.*, **8**, 377–407. 9, 10
- RADBRUCH-HALL, D.H. (1978). Gravitational creep of rock masses on slopes. In B. Voight, ed., *Rockslides and Avalanches, 1. Developments in Geotechnical Engineering*, Elsevier, Amsterdam. 12
- REFTEK (2011). *130 Recording Format*. Refraction Technology, 1600 Tenth Street Suite A Plano, Texas 75074, rev 3.3.1 document revision g 2011.07.26 edn. 39
- RIAL, J., TANG, C. & STEFFEN, K. (2009). Glacial rumblings of jakobshavn ice stream, greenland. *Journal of glaciology*, **55**, 389 –399. 3

REFERENCES

- ROTH, M. & BLIKRA, L. (2010). Seismic monitoring of the unstable rock slope at Åknes, norway. *Berichte der Geologischen Bundesanstalt*, **82**, 67–68. 3, 13
- ROTH, M. & BLIKRA, L.H. (2009). Seismic monitoring of the unstable rock slope at aaknes, norway. *Geophysical Research Abstracts*, **11**, 3680. 3
- ROUX, P.F., WALTER, F., RIESEN, P., SUGIYAMA, S. & FUNK, M. (2010). Observation of surface seismic activity changes of an alpine glacier during a glacier[U+2010]dammed lake outburst. *Journal of geophysical research*, **115**, F03014. 3
- SANCHEZ, G., ROLLAND, Y., CORSINI, M., BRAUCHER, R., BOURLES, D., ARNOLD, M. & AUMAITRE, G. (2010). Relationships between tectonics, slope instability and climate change: Cosmic ray exposure dating of active faults, landslides and glacial surfaces in the {SW} alps. *Geomorphology*, **117**, 1 – 13. 9
- SCALES, J.A. & SNIEDER, R. (1998). What is noise? *Geophysics*, **63**, 1122–1124. 41, 45, 46
- SEMBLAT, J., KHAM, M., PARARA, E., BARD, P., PTILAKIS, K., MAKRA, K. & RAPTAKIS, D. (2005). Seismic wave amplification: Basin geometry vs soil layering. *Soil Dynamics and Earthquake Engineering*, **25**, 529 – 538, |ce:title|11th International Conference on Soil Dynamics and Earthquake Engineering (ICSDEE): Part 1;|ce:title|. 63
- SENAUTE, G., DUPERRET, A. & LAWRENCE, J. (2009). Micro-seismic precursory cracks prior to rock-fall on coastal chalk cliffs: a case study at mesnil-val, normandie, nw france. *Natural Hazards and Earth System Sciences*, **9**, 1625–1641. 3
- SICK, B., WALTER, M. & JOSWIG, M. (2012). Visual event screening of continuous seismic data by superonograms. *Pure and Applied Geophysics*, 1–11. 42
- SPILLMANN, T., MAURER, H., GREEN, A., HEINCKE, B., WILLENBERG, H. & HUSEN, S. (2007). Microseismic investigation of an unstable mountain slope in the swiss alps. *Journal of Geophysical Research*, **112**, B07301, -. 3, 61
- STINI, J. (1941). Unsere taler wachsen zu. *Geologie und Bauwesen*, **13**, 71–79. 6
- TARANTOLA, A. (2005). *Inverse problem theory and methods for model parameter estimation*. SIAM. 66
- TARANTOLA, A. & VALETTE, B. (1982). Inverse problems = quest for information. *Journal of Geophysics*, **50**, 159–170-. 66, 68
- VAN HERWIJNEN, A. & SCHWEIZER, J. (2011). Monitoring avalanche activity using a seismic sensor. *Cold Regions Science and Technology*, **69**, 165 – 176, |ce:title|International Snow Science Workshop 2010 Lake Tahoe;|ce:title|. 3
- VARNES, D. (1978). Slope movement types and processes. In R.L. Schuster & R. Krizek, eds., *Special Report 176: Landslides: Analysis and Control*, 11–33, National Research Council, Washington, D.C. 5
- VIDALE, J.E. (1986). Complex polarization analy sis of particle motion. *Bulletin of the Seismological Society of America*, **76**, 1393–1405. 86
- VON REBEUR-PASHWITZ, E. (1889). The earthquake of tokiro, april 18, 1889. *Nature*, **40**, 294–295. 1
- WAGNER, G. & OWENS, T. (1996). Signal detection using multi-channel seismic data. *Bulletin of the Seismological Society of America*, **86**, 221–231-. 41
- WALTER, M. & JOSWIG, M. (2008). Seismic monitoring of fracture processes generated by a creeping landslide in the vorarlberg alps. *first break*, **26**, 131–135-. 3, 61
- WALTER, M. & JOSWIG, M. (2009). Seismic characterization of slope dynamics caused by softrock-landslides: The super-sauze case study. -. 3
- WALTER, M., ARNHARDT, C. & JOSWIG, M. (2012). Seismic monitoring of rockfalls, slide quakes, and fissure development at the super-sauze mudslide, french alps. *Engineering Geology*, **128**, 12–22. 3, 61
- WEIDNER, S. (2000). *Kinematik und Mechanismus tiefgreifender alpiner Hangdeformationen unter besonderer Berucksichtigung der hydrologischen Verhaltnisse*. Ph.D. thesis, Friedrich-Alexander Universitat Erlangen - Nurnberg. 5, 18, 24, 27
- WEIDNER, S., MOSER, M. & LANG, E. (1998). Influence of hydrology on sagging of mountain slopes ("talzuschube") - new results of time series analysis. In D. Moore & O. Hungr, eds., *Proceedings eighths international congress International Association for Engineering Geology and Environment*, 1259 – 1266, A.A. Balkema / Rotterdam / Brookfield. 24
- WITHERS, M., ASTER, R., YOUNG, C., BEIRIGER, J., HARRIS, M., MOORE, S. & TRUJILLO, J. (1998). A comparison of select trigger algorithms for automated global seismic phase and event detection. *Bulletin of the Seismological Society of America*, **88**, 95–106. 41
- WP/WLI (1993). *Multilingual Landslide Glossary*. BiTech Publishers Ltd. Richmond, Canada. 5, 6
- ZANGERL, C., EBERHARDT, E., SCHONLAUB, H. & ANEGG, J. (2007). *Deformation behavior of deep-seated rockslides in crystalline rock*, -. Tylor & Francis Group, London. 7, 11
- ZANGERL, C., PRAGER, C., RAINER BRANDNER, R., BRUCKL, E., EDER, S., FELLIN, W., TENTSCHERT, E., POSCHER, G. & SCHONLAUB, H. (2008). Methodischer leitfaden zur prozessorientierten bearbeitung von massenbewegungen. *Geo.Alp*, **5**, 1 – 51. 10

REFERENCES

- ZANGERL, C., EBERHARDT, E. & PERZLMAIER, S. (2010). Kinematic behaviour and velocity characteristics of a complex deep-seated crystalline rockslide system in relation to its interaction with a dam reservoir. *Engineering Geology*, **112**, 53 – 67. 7, 11, 12
- ZANGERL, C., PRAGER, C., CHWATAL, W., BRÜCKL, E., KIRSCHNER, H. & BRANDNER, R. (2012). Kinematics and internal deformation of a slow deep-seated rock slide in metamorphic rock (niedergallmigg, austria). In E. Eberhardt, C. Froese, K. Turner & S. Leroueil, eds., *Landslides and Engineered Slopes - Protecting Society through Improved Understanding*, 653 – 658, CRC Press. 7, 11
- ZISCHINSKY, U. (1969). Über sackungen. *Rock Mechanics*, **1**, 30–52-. 5, 6, 9, 10, 11
- ZOJER, H. & ZÖTL, J. (1975). Hydrogeologische untersuchungen im bereich der großrutschung des gradenbachtals bei döllach / kärnten. *Steirische Beiträge zur Hydrogeologie*, **27**, 65–84. 24

REFERENCES

Appendix A

Seismon

Usually, scientific work in seismology involves new approaches for data collection, unconventional instrumentation and the development of new algorithms to process the data. The combination of these needs limits the usage of routine software packages. Moreover small research projects running on low-budget might not be able to afford the license fees for proprietary software and the services needed to adapt the software to special needs. Therefore Seismon started as an open source software project using the GNU General Public License (GPL). To enable a quick development workflow, Seismon is written in MATLAB which is widely used at Universities.

Compareable software like MatSeis (Hart *et al.*, 2005), Seisan (Havskov *et al.*, 2003) or SeismicHandler¹ are great tools if you are working within standard seismological projects, but for small scale or unconventional seismic projects you quickly reach the limits of usability and adaptability. Therefore I started to program Seismon with the background of making it as flexible and as easy expandable as possible. The goal was not to replace the above mentioned programs for standard seismological analysis, but to create a seismic development tool for small scale and unconventional research projects. It moreover was intended to create a software development tool which is widely used at our research group and which should act as a kind of *repository* for all the code developed within the many master thesis, dissertations and project works accomplished at our research group.

Seismon started as a simple tool for the import of various seismic data formats, but rapidly grew to a processing tool used within many research projects accomplished at the Department of Geodesy and Geoinformation like the seismic monitoring of landslides, local earthquake monitoring, tunnel seismic while drilling, seismic interferometry and active seismic experiments in alpine areas. Currently I'm working on porting the MATLAB software Seismon to the Python programming language. The ported version is named *psysmon* and the progress of this work is documented at <http://psysmon.mertl-research.at>.

¹<http://www.seismic-handler.org/> - accessed 8.11.2013

A.1 Software design

To fulfill the goal of a flexible software, Seismon was coded in a modular approach. The main program (named Seismon-core within this thesis) acts as a front-end to a MySQL database and manages a set of packages, which provide the functionality (modules) to Seismon (see figure A.1). Moreover, the packages can add tools to already existing modules. This comes in handy if one wants to customize big modules (e.g. adding some special filter algorithm to the waveform display module) without changing the code of the module itself. Most important, the division into packages and modules guarantees a maintainable code.

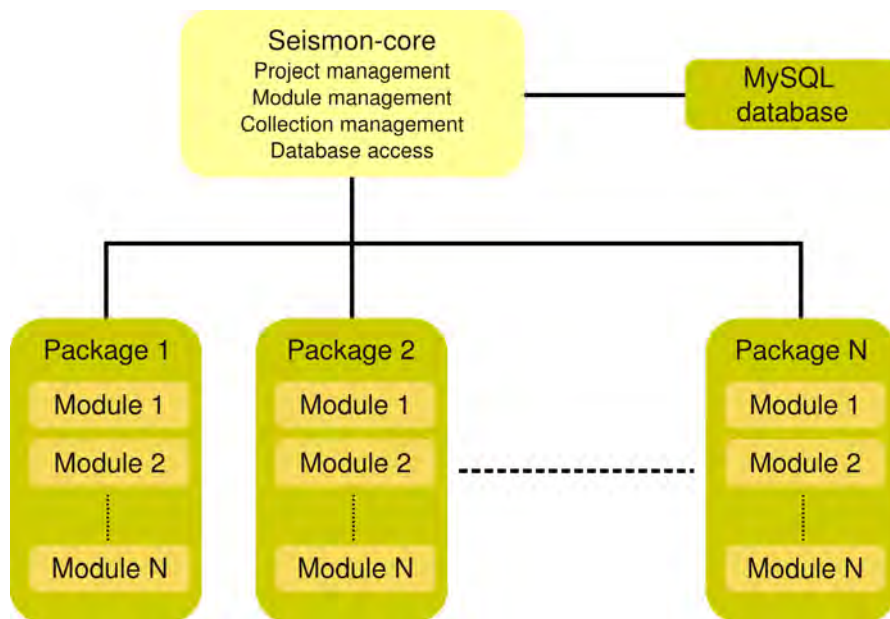


Figure A.1: The modular design approach of Seismon. The Seismon-core manages the database communication and the packages and modules. A package is a collection of modules which provide the functionality (e.g. waveform display, event management,..) to Seismon.

The Seismon packages are loaded by Seismon-core during the start of the program. Each package contains one or more modules which provide various functionality to the user (see figure A.2). During Seismon startup, two package interface functions, *prefix_installation.m* and *prefix_init.m* (*prefix* is a packages specific unique string) are called to register the modules within Seismon-core and perform some installation tasks (e.g. compile files, install documentation,...). The *prefix_database.m* function is called only once when Seismon-core recognizes a new package. The *prefix_database.m* function can be used to add additional database tables to the Seismon database structure. A module is a set of MATLAB functions which can be accessed by Seismon using two interface functions (the module functions). The module functions (*edit-function* and *command-function*) have to be coded following given guidelines. The edit-function is called by Seismon-core to edit the configuration parameters of the related module. The command-function is called by Seismon-core when the module is executed. The module functions may call several

subfunctions which don't have to follow any coding directive.

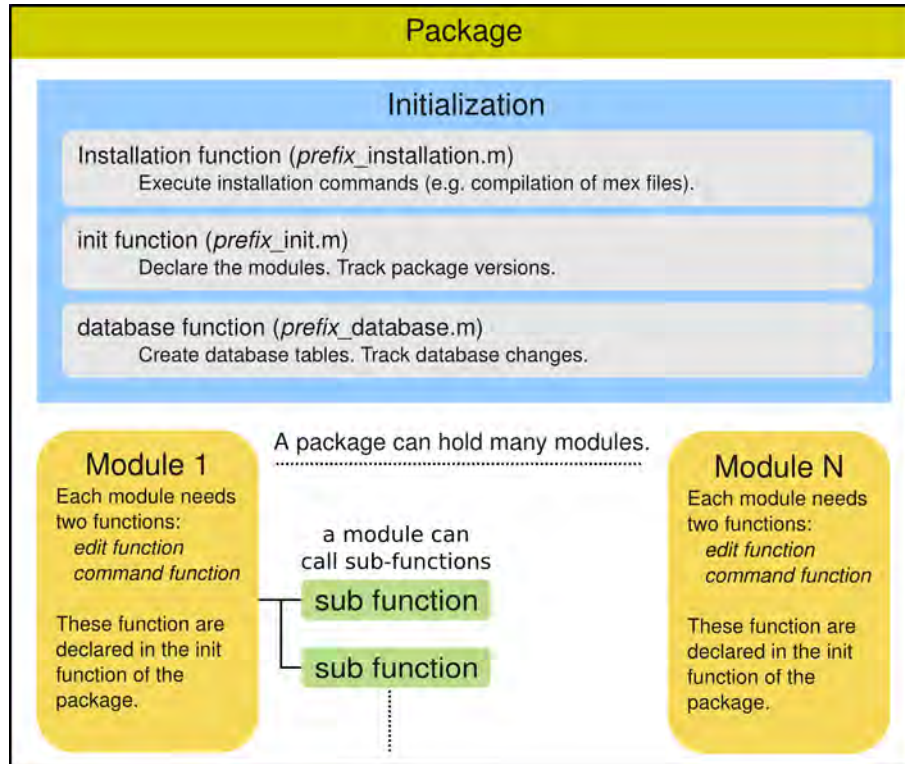


Figure A.2: The general structure of a Seismon package.

The handling of the modules and their configuration parameters is organized in Seismon using projects and collections. Before working with Seismon modules, a project has to be created. This also initializes all needed database tables which is done by calling the package interface function `prefix_database.m`. Within a project, one or several collections can be created. A collection can hold a set of modules and their related configuration parameters. Figure A.3 gives an overview of the structure of a collection and the possible data flows within the modules of the collection. For each module, there are two data flows. The edit data flow (green in figure A.3) is used to change the configuration parameters of a module using the edit function. The execution data flow (purple in figure A.3) runs when a collection is executed by the user. This flow passes the configuration data of each module to according command function. The command function executes it's algorithms using the configuration data as an input and returns some output values. These output parameters are passed to the next module in the collection as an input data. This enables a flow-like behavior of the collection.

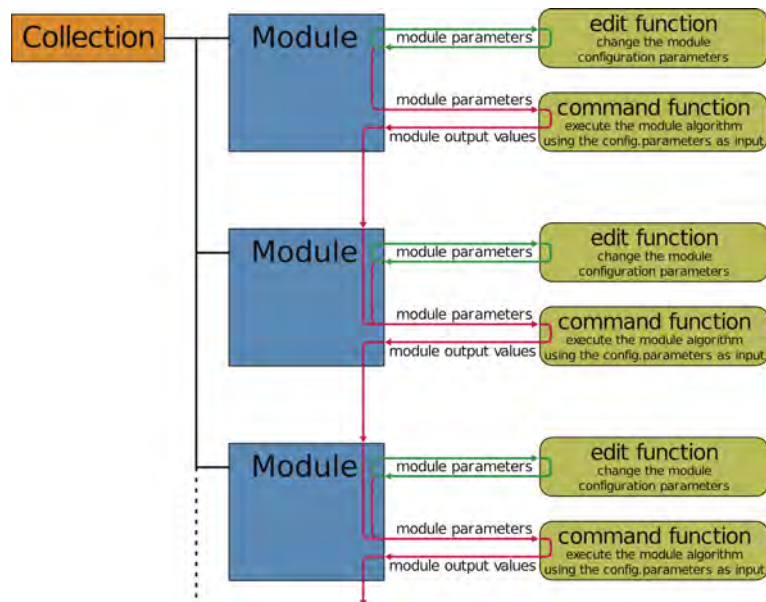


Figure A.3: A collection is used to combine one or more modules for editing and execution. The parameters of a module can be edited using the `edit_function`. The `command_function` is called when the collection is executed. The module parameters are passed to the `command_function` which returns some output values. These output values are passed to the next module in the collection and can be used by the related `command_function`.

A.2 Graphical user interface

To interact with the Seismon-core and the modules, a graphical user interface (GUI) is provided. The Seismon main window (see figure A.4) provides the basic functionality for the project-, collection- and modules management. The main window is divided into a collection listbox, which shows the modules of the currently used collection, the modules category selector and the modules listbox, which holds the available modules. A standard work-flow of a Seismon session is:

1. Create a new collection;
2. Add the needed modules from the module listbox to the collection;
3. Edit the parameters of the modules in the collection;
4. Execute the collection.

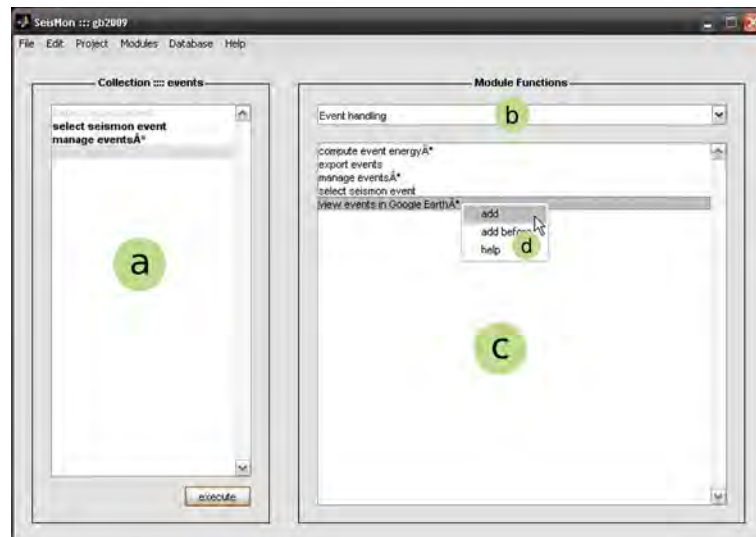


Figure A.4: The main parts of the Seismon main window are (a) the collection listbox, (b) the module category selector, and (c) the module listbox. Usually context menus (d) are used to control the GUI.

A.3 Seismon usage within research projects

Seismon is intended to act as a tool supporting the work within scientific research projects. Seismon can be used to easily integrate new processing algorithms into a quasi-routine work flow. The following application examples show different projects which used or are still using Seismon, demonstrating the wide field of its possible application. The application to seismic monitoring of landslides has been extensively described in this thesis and therefore is not included in the following list.

A. SEISMON

Local earthquake monitoring

Within the project ALPAACT¹, funded by the Austrian Academy of Sciences (OeAW), Seismon is used for data management and earthquake analysis. Seismon is used as a post-processing tool after an automatic event detection done with the Earthworm software. Seismon also was used for local earthquake analysis within the CBP (Hausmann *et al.*, 2010) and ALPASS (Mitterbauer *et al.*, 2011) projects. An example screenshot is given in figure A.5.

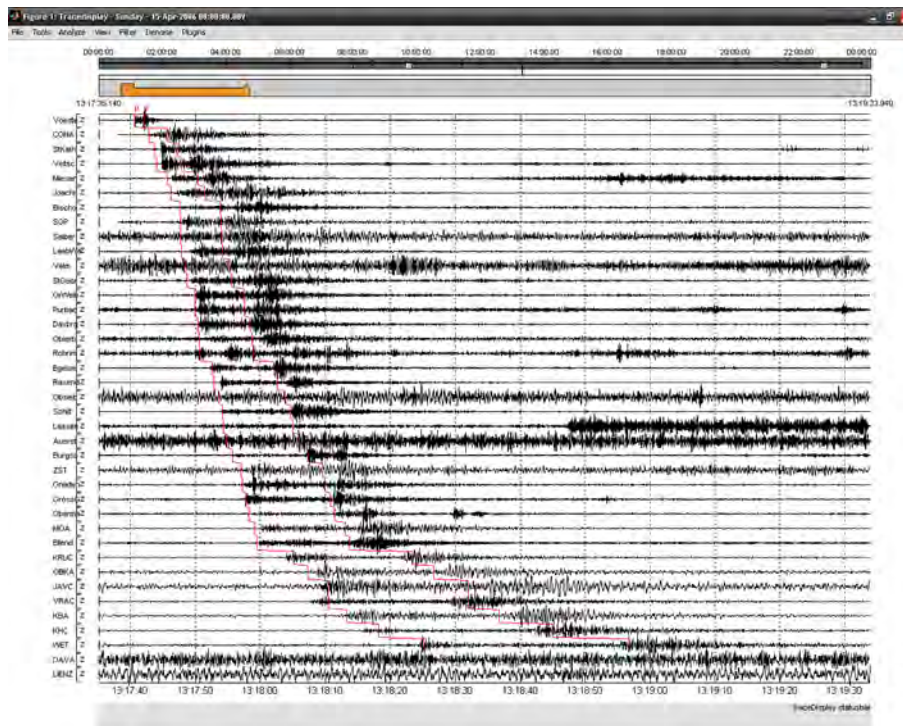


Figure A.5: Example screenshot of Seismon used for the analysis of local earthquake data.

Permafrost mapping

Small scale active seismic experiments to map the permafrost in alpine valleys were processed using Seismon (Hausmann *et al.*, 2009). For this purpose, newly developed algorithms were integrated into Seismon. Figure A.6 gives an example of the usage of Seismon for the processing of active seismic data for the characterization of permafrost sites.

Tunnel seismic while drilling

Seismon was used to manage and analyze the data of a tunnel seismic while drilling (TSWD) pilot study in cooperation with Pöyry Infrastructure. New algorithms were developed and tested using Seismon (Brückl *et al.*, 2008a).

¹<http://info.tuwien.ac.at/geophysik/research/alpdynamics/alpaact.htm>

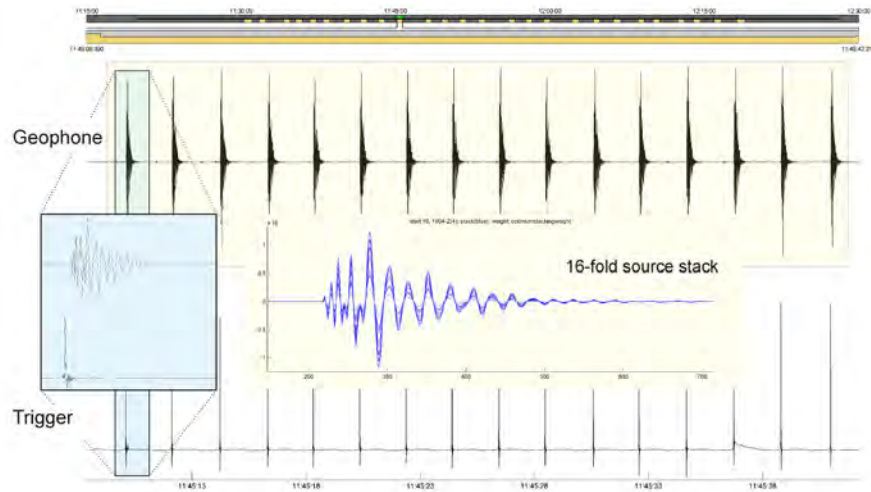


Figure A.6: Example usage of Seismon for the processing of active seismic data used for the characterization of permafrost sites.

Seismic noise interferometry

Seismon was used by Behm & Snieder (2013) as the base-software to develop methods for seismic noise interferometric analysis. Seismon provided the tools for data management, data visualization and quality control. The event processing tools were extended and a complete work-flow for seismic noise interferometry was developed and added to Seismon as a Seismon package.

Appendix B

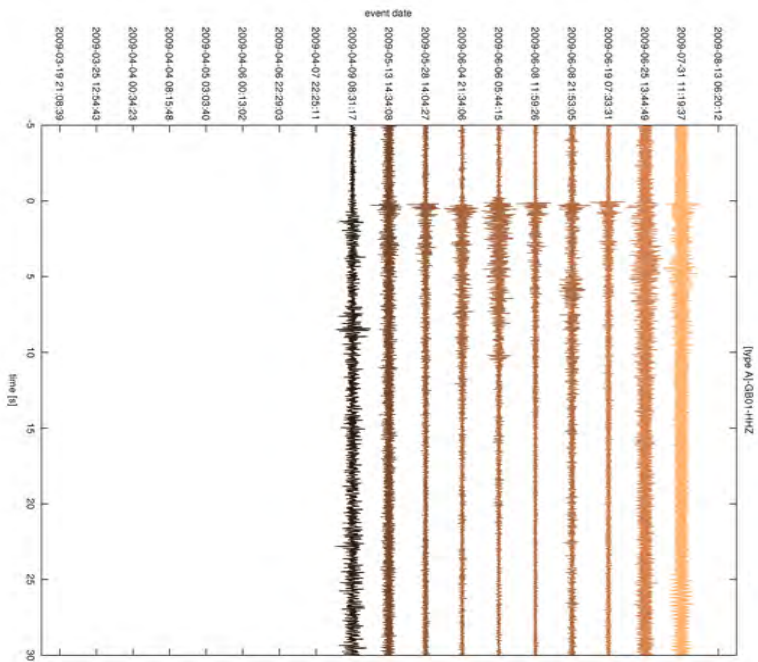
Slope candidate events

The following sections give a complete list of the slope events recorded at the seismic network Gradenbach from March 1 to September 30, 2009. For each event type, the seismograms and spectrograms of the vertical component are plotted. For the seismograms, the data has been filtered depending on the event type: type A: 1 - 30 Hz; type AA: 1 - 80 Hz; type B: 1 - 15 Hz; type D: 1 - 30 Hz; type tremor: 1 - 30 Hz; type rf: 1 - 30 Hz. The spectrograms have been created using the unfiltered data.

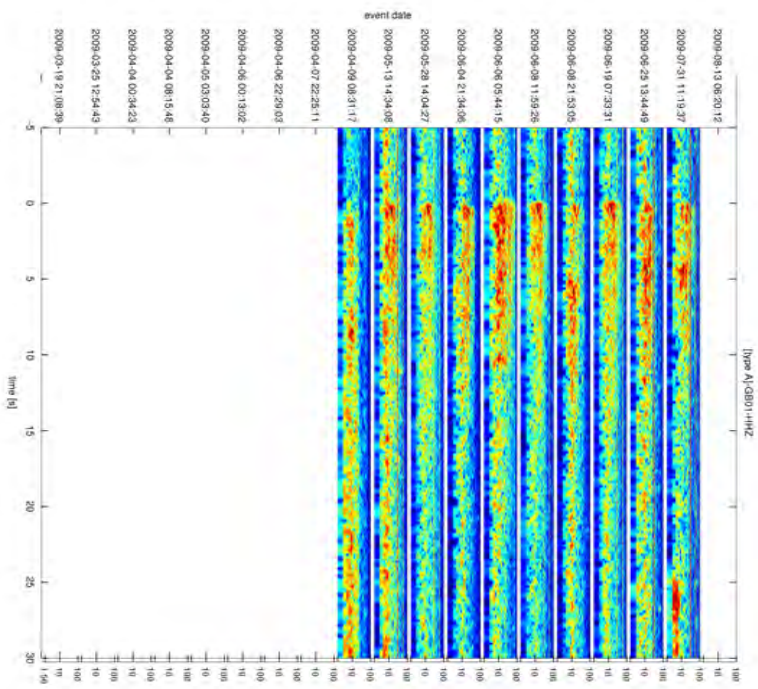
B.1 Type A

Type A events have an abrupt first motion and a median signal duration of 14.1 seconds. The interquartile range (IQR), which is the difference between the upper and lower quartile, is 4.6 seconds. The recordings of the type A events have a SNR with a median of 3.6 and an IQR of 2.7. In general the signal is visible on all stations. The frequency content of the event is between 5 Hz and 40 Hz. The onset of the event is usually more broadband than the trailing. The energy of the event weakens with its duration and sometimes the energy is bound to a frequency band between 10 Hz and 20 Hz.

B. SLOPE CANDIDATE EVENTS

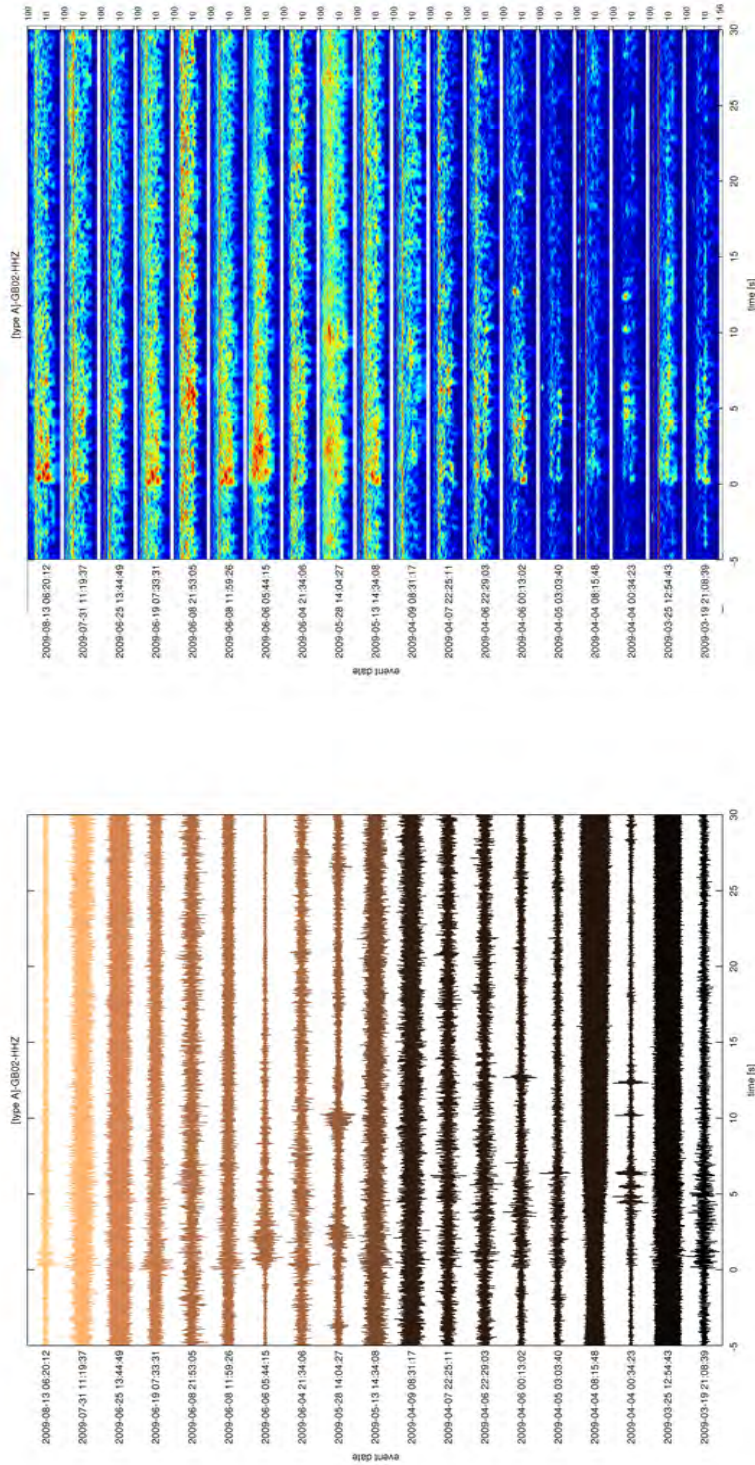


(a)



(b)

Figure B.1: Type A - GB01 - HHZ. The seismograms are colored according to the event date in UTC (black: first; light brown: last). In the spectrogram, blue colors indicate low energy, red colors high energy. The units of the frequency scale on the right side of the seismograms is Hz.

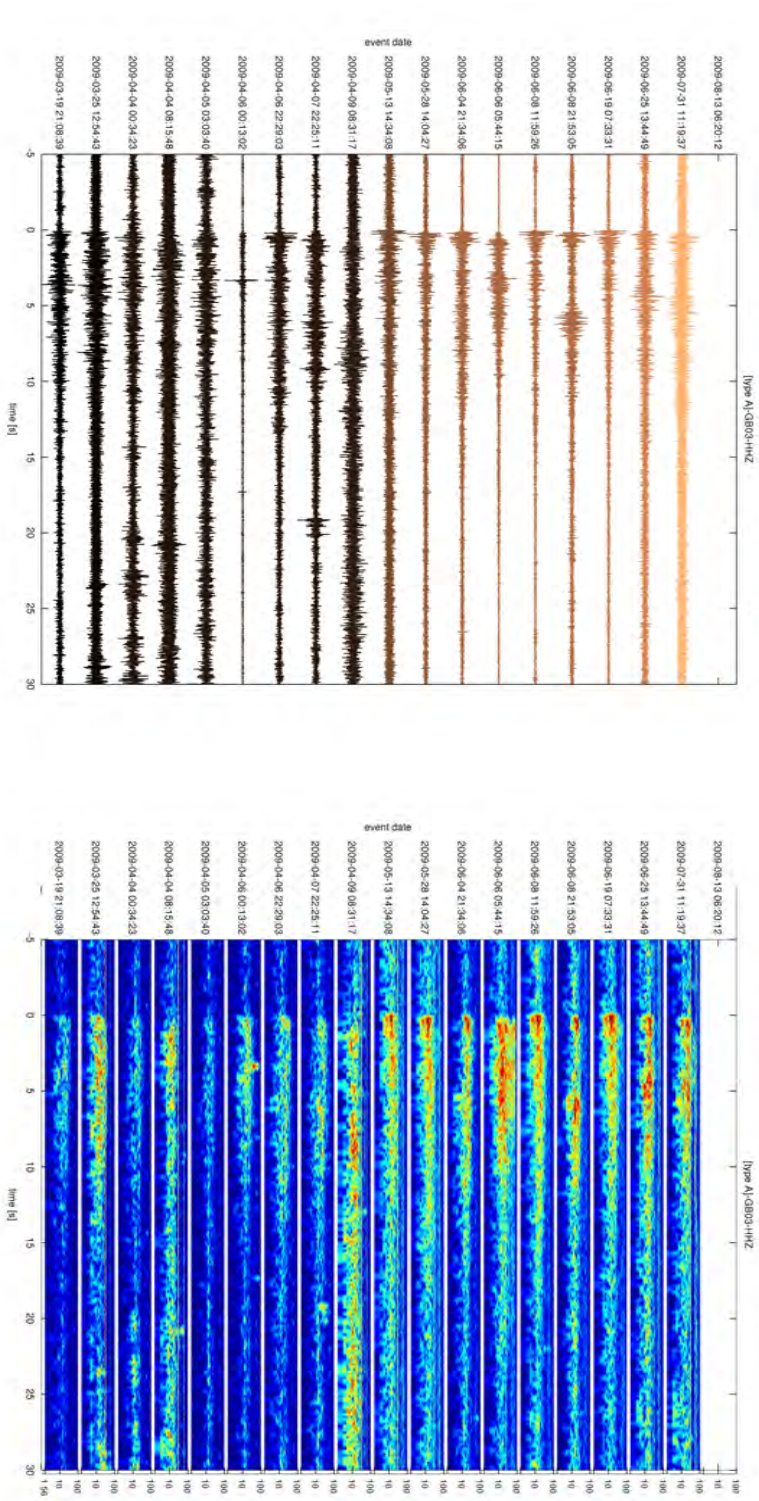


(b)

(a)

Figure B.2: Type A - GB02 - HHZ. The seismograms are colored according to the event date in UTC (black: first; light brown: last). In the spectrogram, blue colors indicate low energy, red colors high energy. The units of the frequency scale on the right side of the spectrograms is Hz.

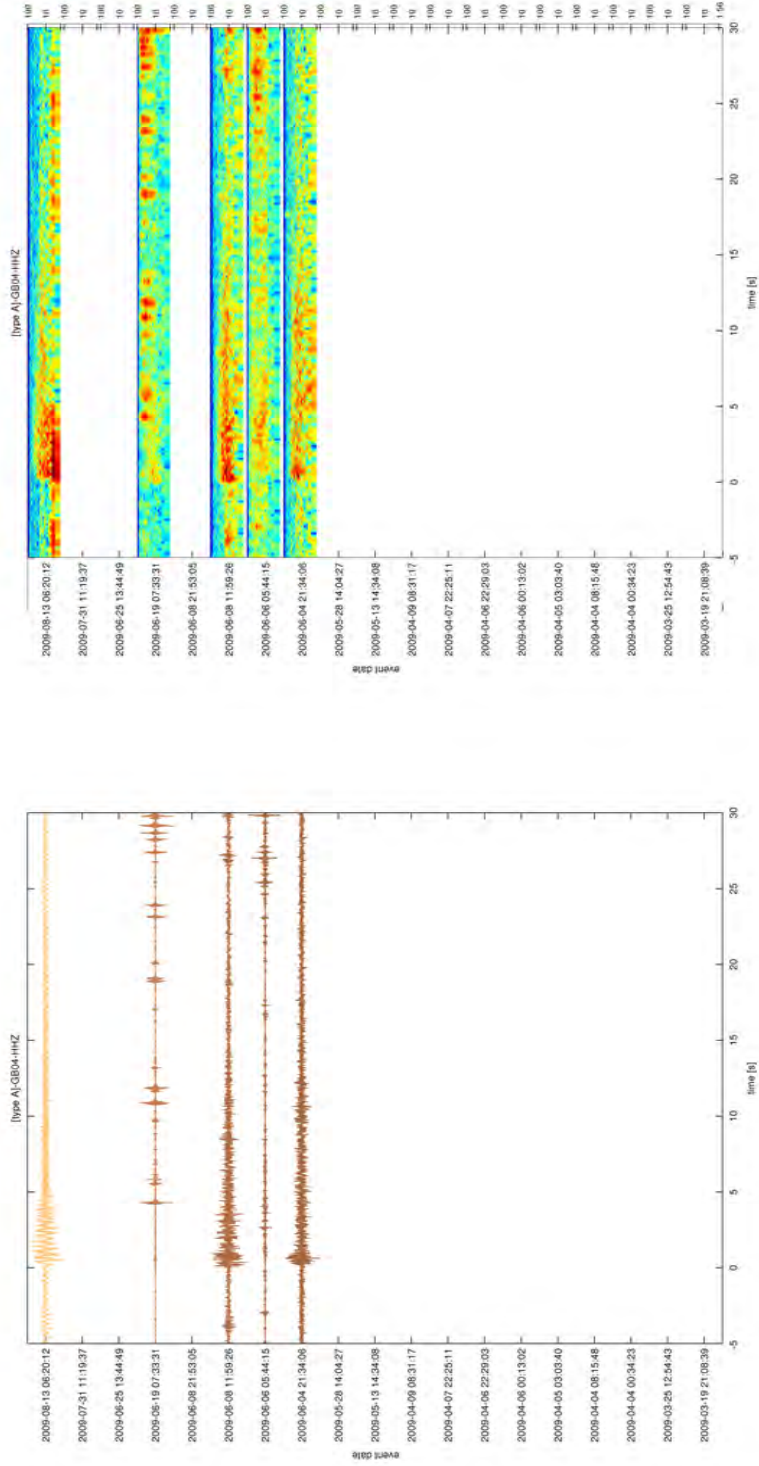
B. SLOPE CANDIDATE EVENTS



(a)

(b)

Figure B.3: Type A - GB03 - HHZ. The seismograms are colored according to the event date in UTC (black: first; light brown: last). In the spectrogram, blue colors indicate low energy, red colors high energy. The units of the frequency scale on the right side of the seismograms is Hz.

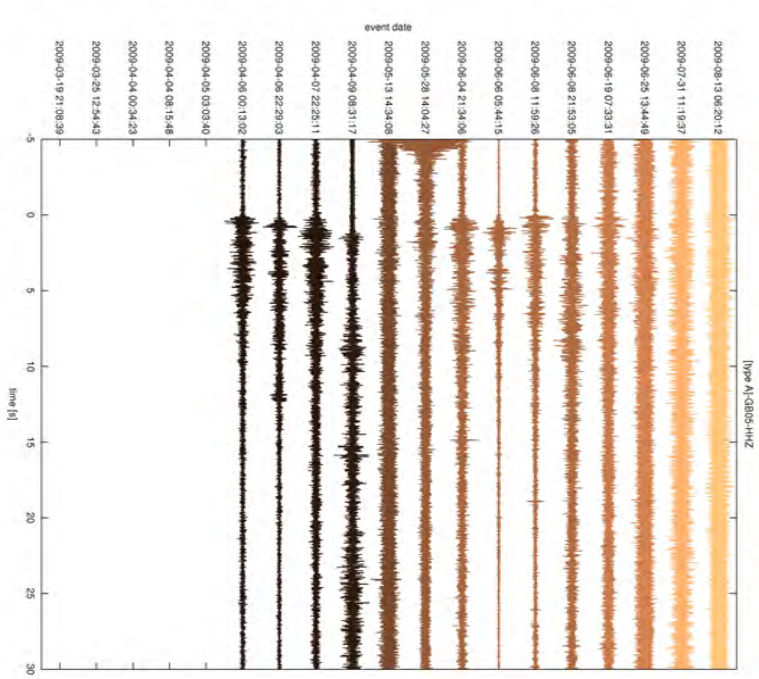


(b)

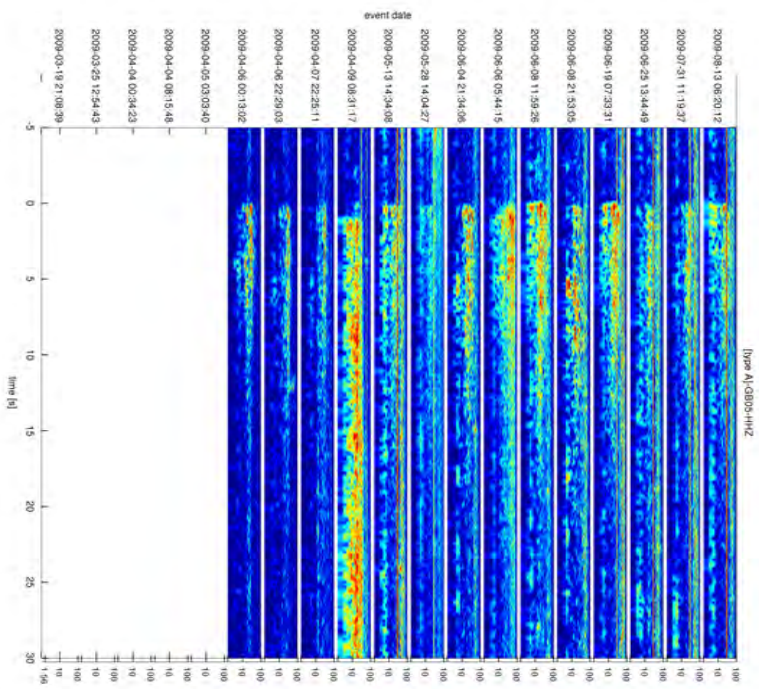
(a)

Figure B.4: Type A - GB04 - HHZ. The seismograms are colored according to the event date in UTC (black: first; light brown: last). In the spectrogram, blue colors indicate low energy, red colors high energy. The units of the frequency scale on the right side of the spectrograms is Hz.

B. SLOPE CANDIDATE EVENTS

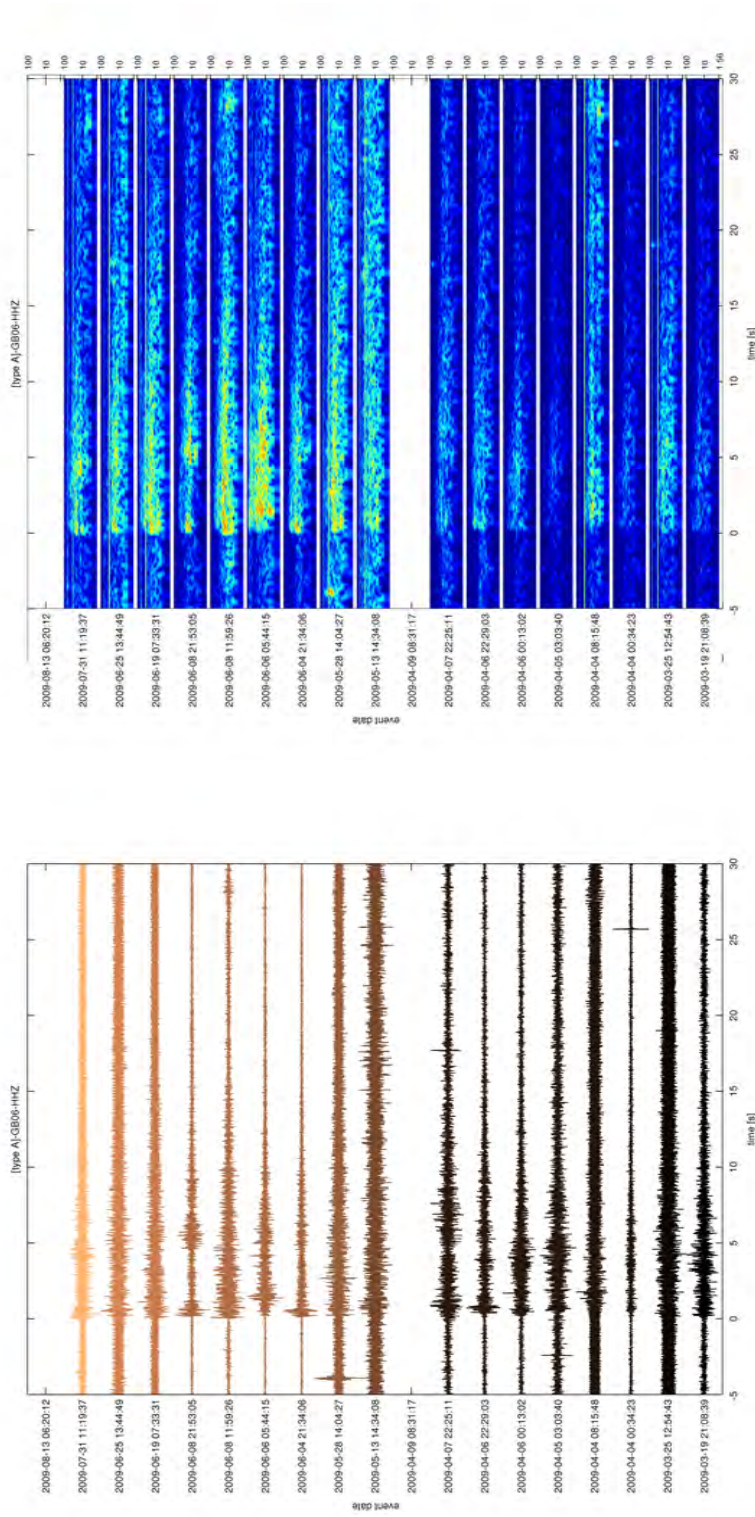


(a)



(b)

Figure B.5: Type A - GB05 - HHZ. The seismograms are colored according to the event date in UTC (black: first; light brown: last). In the spectrogram, blue colors indicate low energy, red colors high energy. The units of the frequency scale on the right side of the seismograms is Hz.



(a)

(b)

Figure B.6: Type A - GB06 - HHZ. The seismograms are colored according to the event date in UTC (black: first; light brown: last). In the spectrogram, blue colors indicate low energy, red colors high energy. The units of the frequency scale on the right side of the seismograms is Hz.

B. SLOPE CANDIDATE EVENTS

B.2 Type AA

Type AA events are short events with an abrupt first motion and a median signal duration of 3.1 seconds. The IQR is 0.3 seconds. The recordings of the type AA events have a high SNR with a median of 5.2 and an IQR of 1. In general the signal is visible on all stations. The events show a high frequency onset between 3 Hz and 100 Hz. The onset is followed by a low frequent waveform with frequencies between 3 Hz and 30 Hz. Only 4 of these events have been recorded during the acceleration phase 2009. 3 events occurred with 5 days in June.

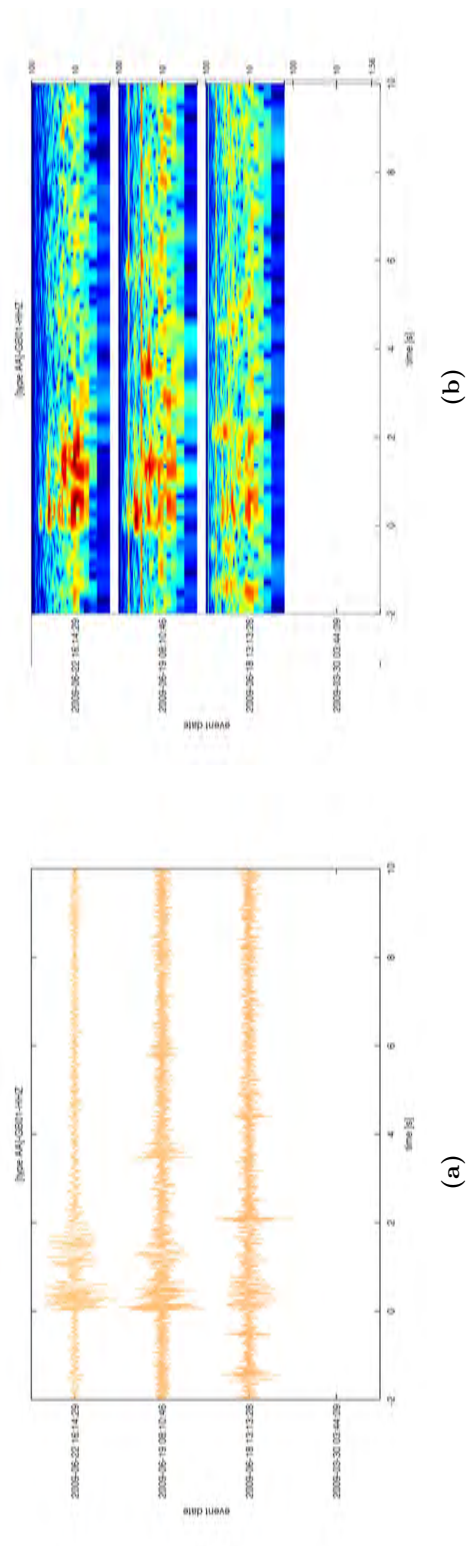


Figure B.7: Type AA - GB01 - HHZ. The seismograms are colored according to the event date in UTC (black: first; light brown: last). In the spectrogram, blue colors indicate low energy, red colors indicate high energy. The units of the frequency scale on the right side of the seismograms is Hz.

B. SLOPE CANDIDATE EVENTS

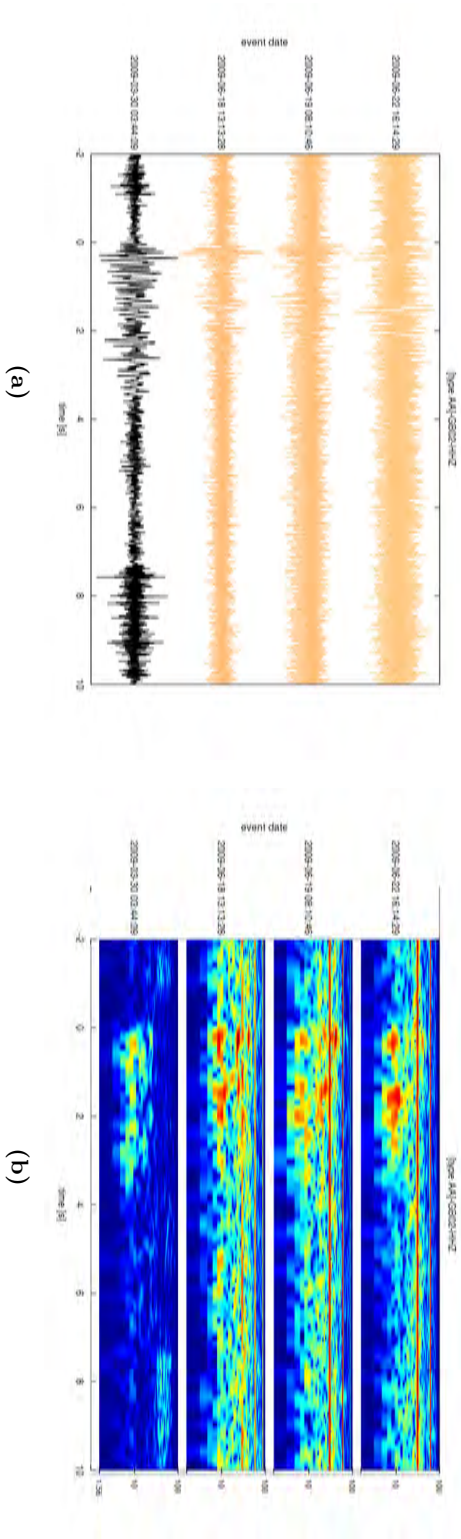


Figure B.8: Type AA - GB02-HHZ. The seismograms are colored according to the event date in UTC (black: first; light brown: last). In the spectrogram, blue colors indicate low energy, red colors high energy. The units of the frequency scale on the right side of the seismograms is Hz.

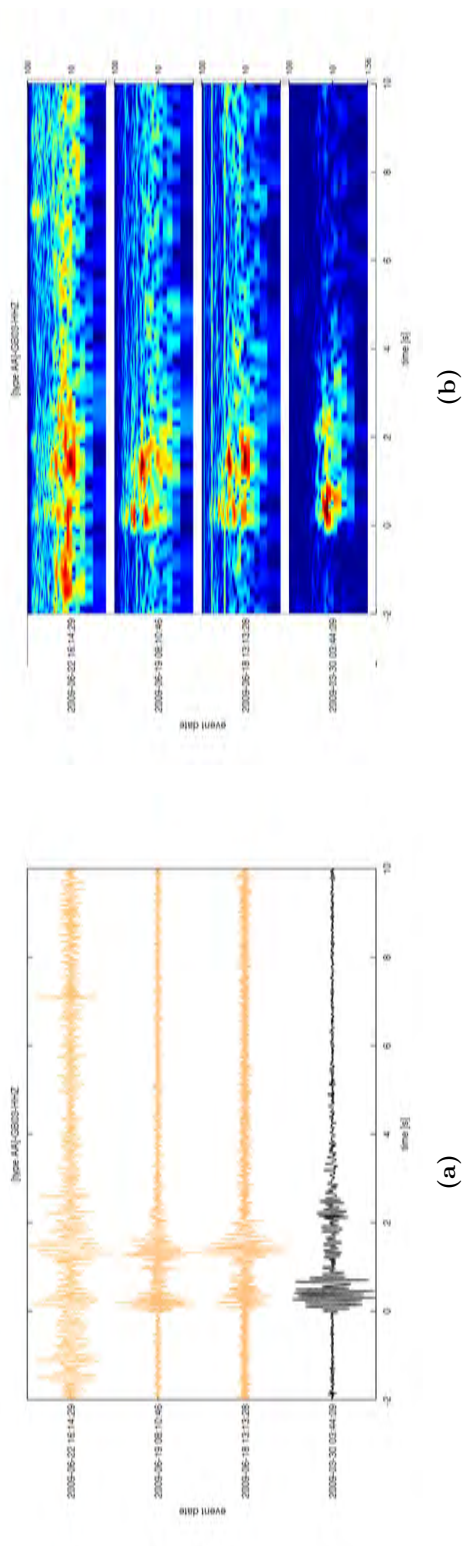


Figure B.9: Type AA - GB03 - HHZ. The seismograms are colored according to the event date in UTC (black: first; light brown: last). In the spectrogram, blue colors indicate low energy, red colors high energy. The units of the frequency scale on the right side of the seismograms is Hz.

B. SLOPE CANDIDATE EVENTS

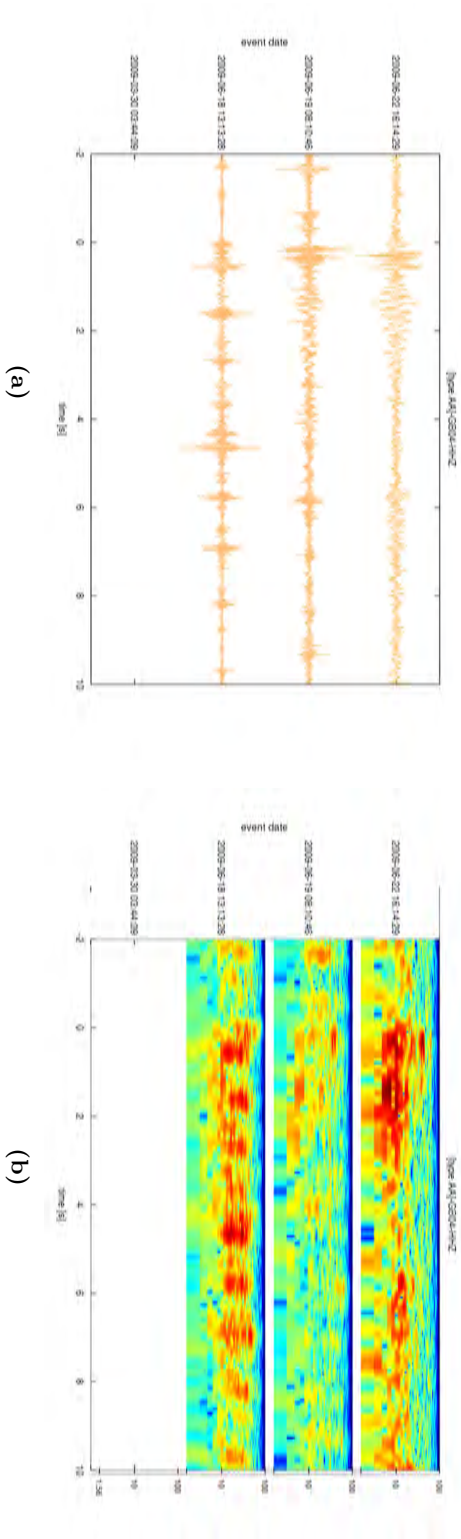


Figure B.10: Type AA - GB04 - HHZ. The seismograms are colored according to the event date in UTC (black: first; light brown: last). In the spectrogram, blue colors indicate low energy, red colors high energy. The units of the frequency scale on the right side of the seismograms is Hz.

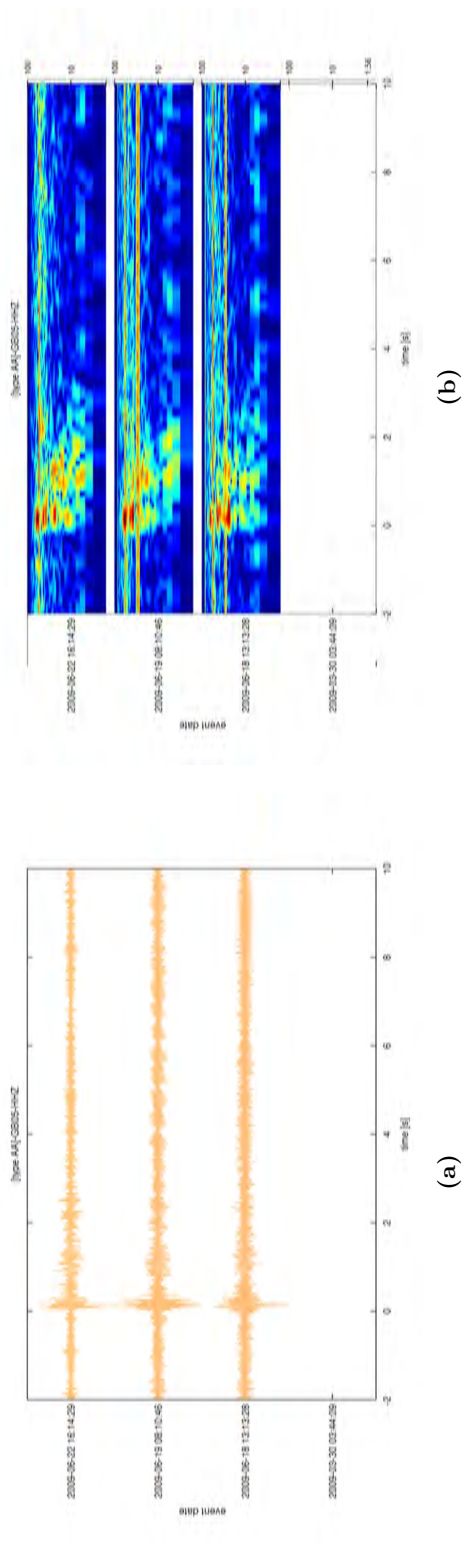


Figure B.11: Type AA - GB05 - HHZ. The seismograms are colored according to the event date in UTC (black: first; light brown: last). In the spectrogram, blue colors indicate low energy, red colors high energy. The units of the frequency scale on the right side of the seismograms is Hz.

B. SLOPE CANDIDATE EVENTS

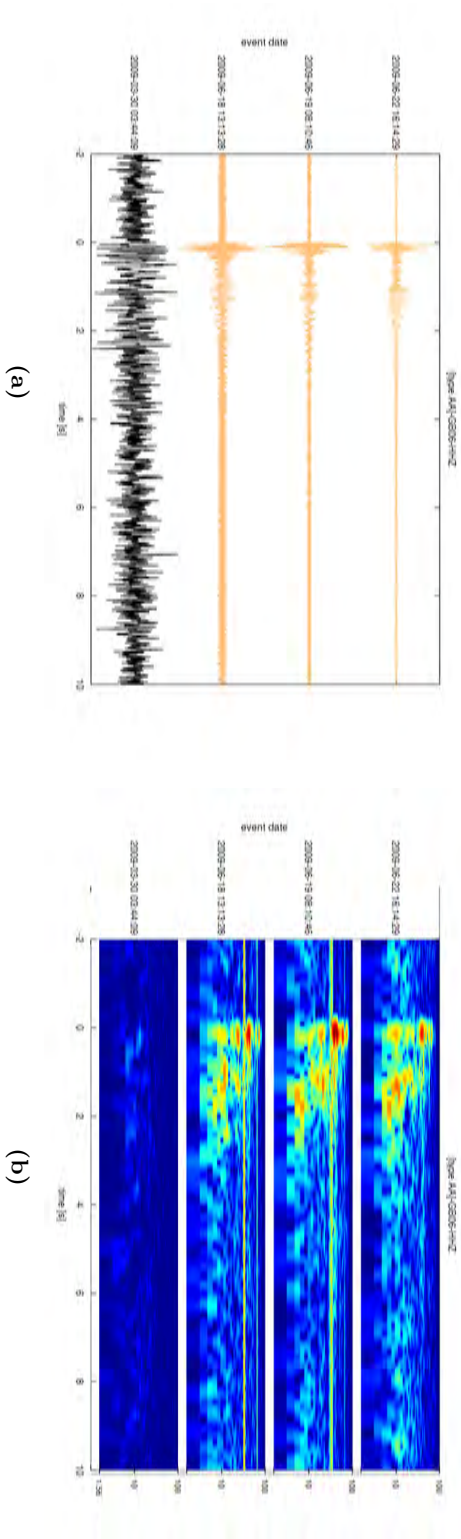
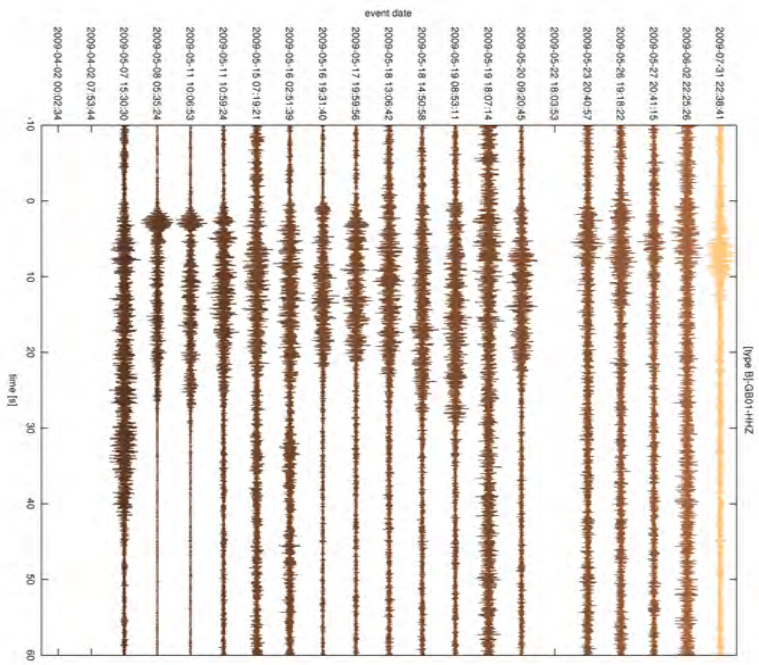


Figure B.12: Type AA - GB06 - HHZ. The seismograms are colored according to the event date in UTC (black: first; light brown: last). In the spectrogram, blue colors indicate low energy, red colors high energy. The units of the frequency scale on the right side of the seismograms is Hz.

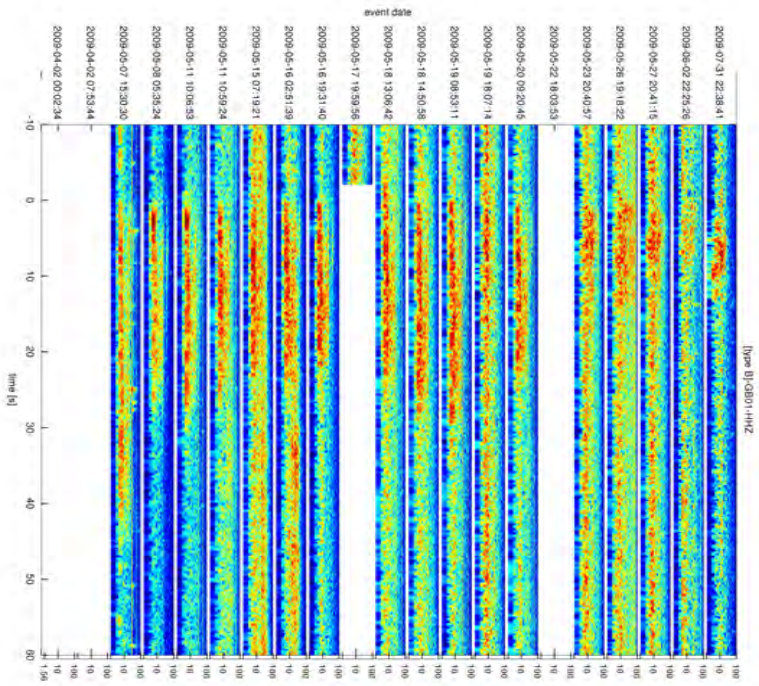
B.3 Type B

Type B events have an emergent onset and a long duration with a median of 24.1 seconds and an IQR of 11.8 seconds. The events have a low SNR (median = 2.4, IQR = 1.1) and are sometimes not visible in an unfiltered seismogram. Mostly, the events are not visible at the station GB02. Most of the energy is present in a low frequency band between 3 Hz and 10 Hz. Some of the events have energy in a second frequency band between 15 Hz and 25 Hz. All of the events show a similar frequency spectrum and a decreasing energy with time (see figure 7.4d). The later type B events (beginning with event number 14 in figure 7.4d) have a different spectrum than the events happening earlier.

B. SLOPE CANDIDATE EVENTS



(a)



(b)

Figure B.13: Type B - GB01 - HHZ. The seismograms are colored according to the event date in UTC (black: first; light brown: last). In the spectrogram, blue colors indicate low energy, red colors high energy. The units of the frequency scale on the right side of the seismograms is Hz.

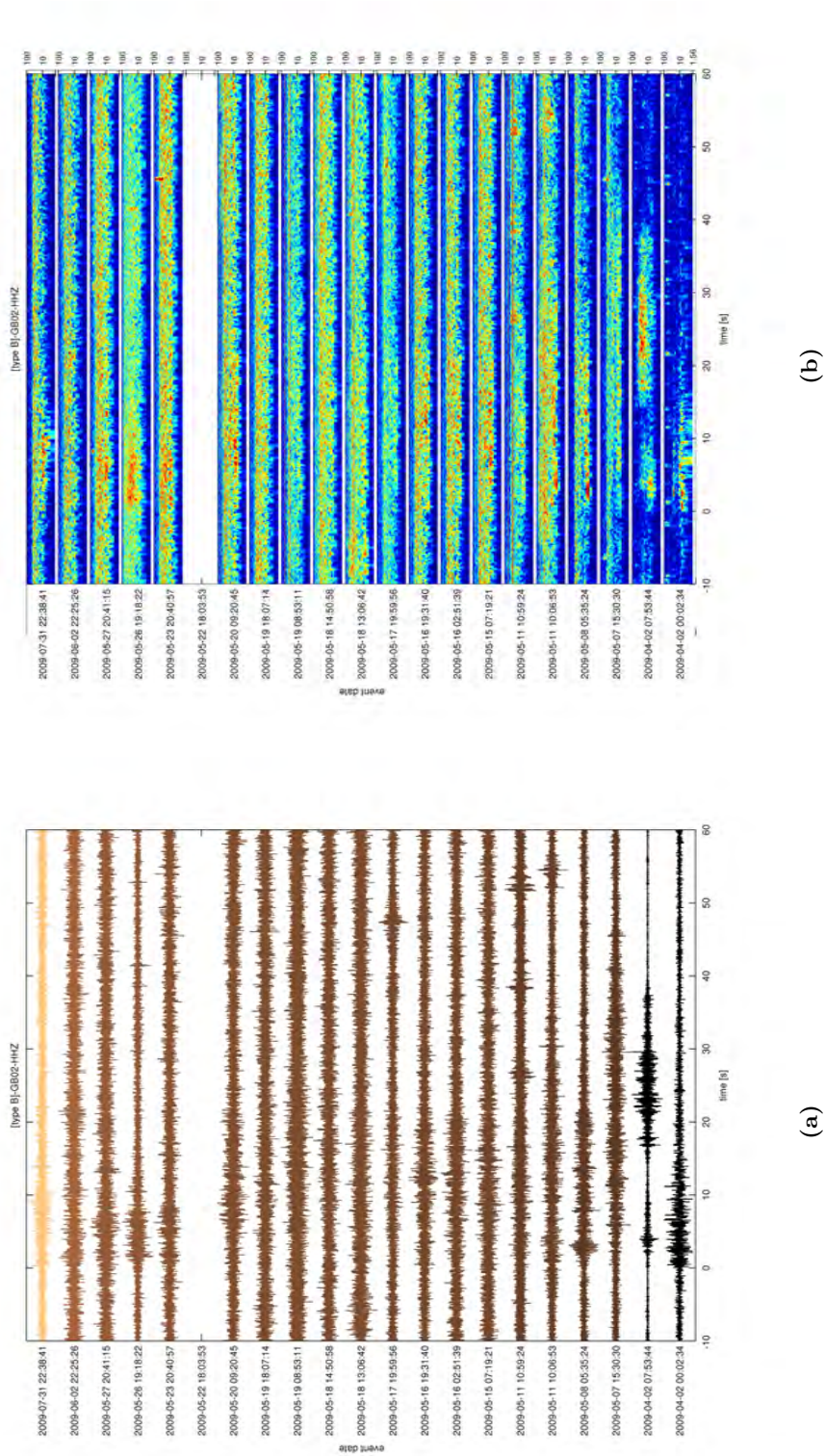
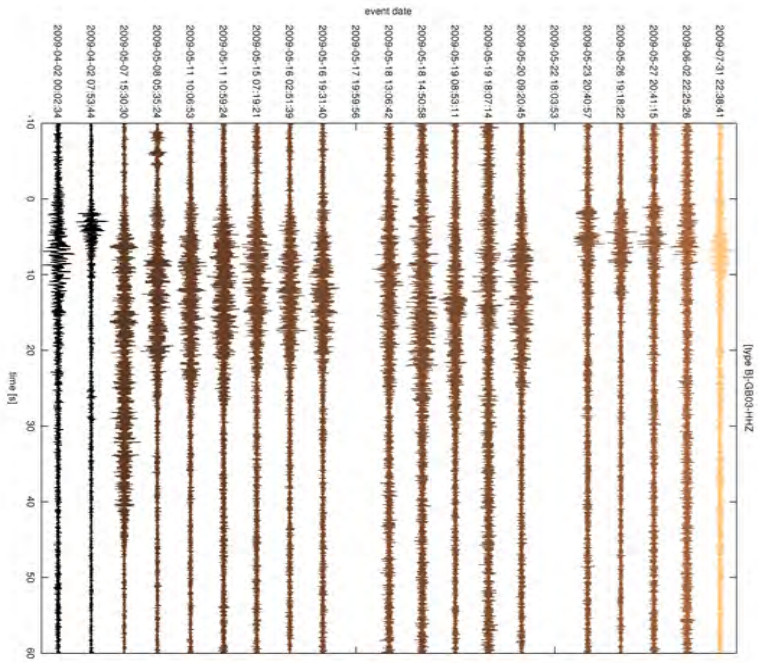
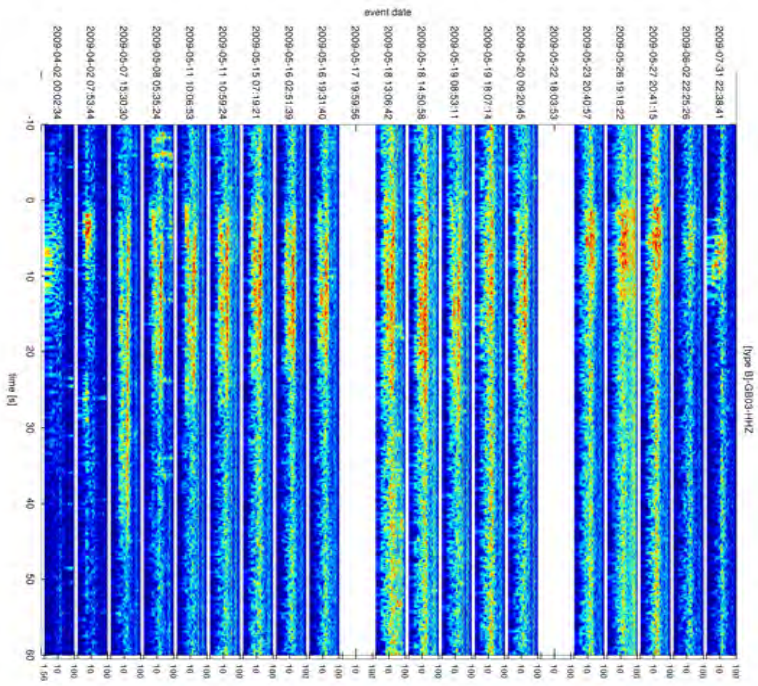


Figure B.14: Type B - GB02 -HHZ. The seismograms are colored according to the event date in UTC (black: first; light brown: last). In the spectrogram, blue colors indicate low energy, red colors indicate high energy. The units of the frequency scale on the right side of the spectrograms is Hz.

B. SLOPE CANDIDATE EVENTS

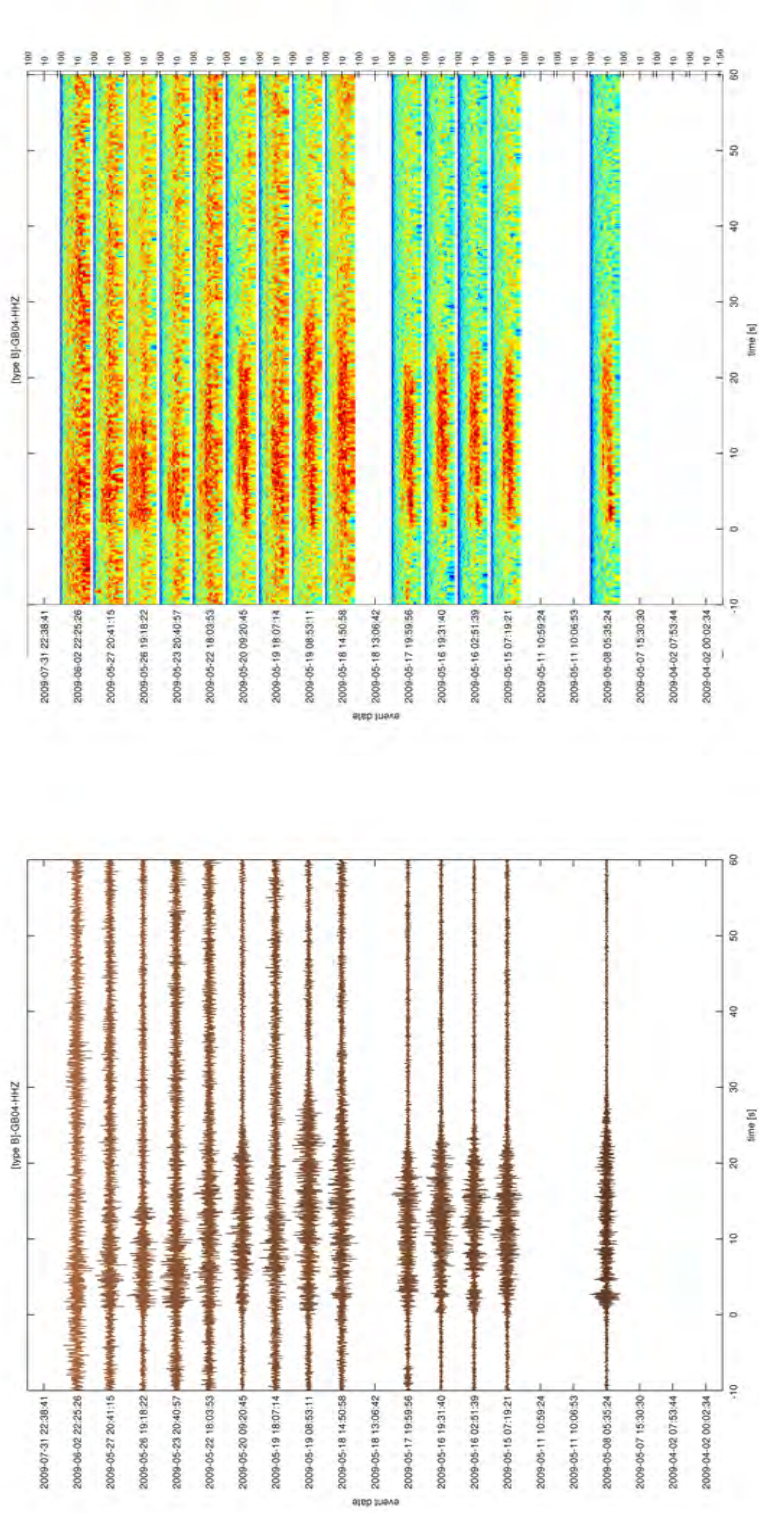


(a)



(b)

Figure B.15: Type B - GB03 -HHZ. The seismograms are colored according to the event date in UTC (black: first; light brown: last). In the spectrogram, blue colors indicate low energy, red colors high energy. The units of the frequency scale on the right side of the seismograms is Hz.

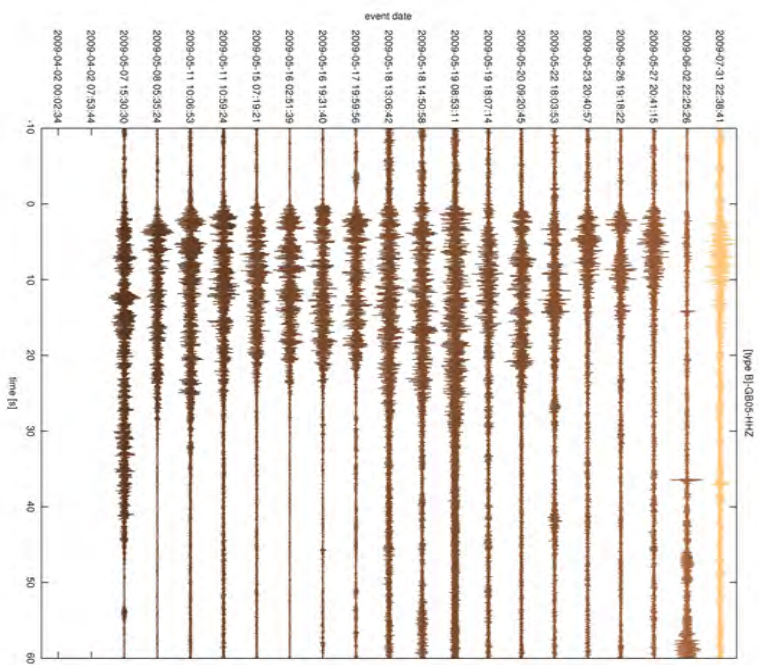


(a)

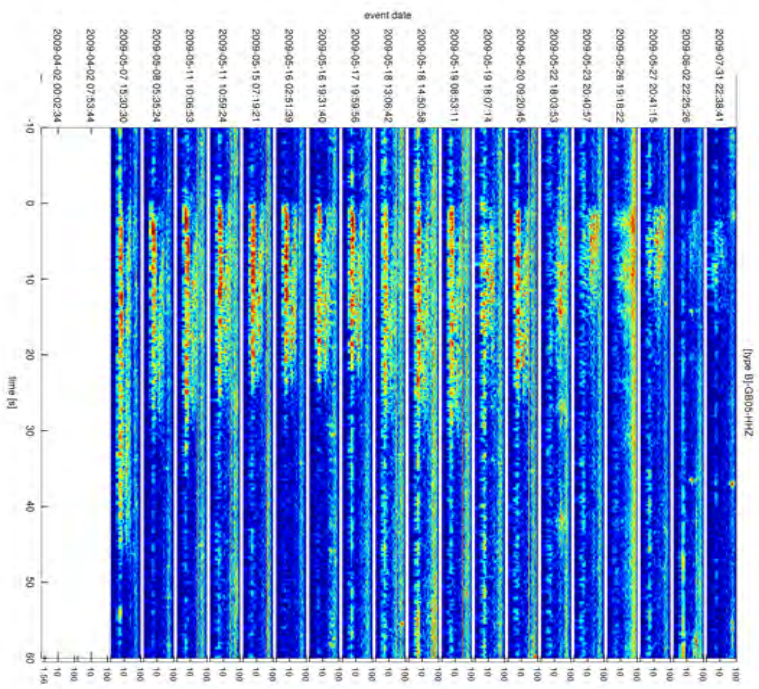
(b)

Figure B.16: Type B - GB04 - HHZ. The seismograms are colored according to the event date in UTC (black: first; light brown: last). In the spectrogram, blue colors indicate low energy, red colors indicate high energy. The units of the frequency scale on the right side of the seismograms is Hz.

B. SLOPE CANDIDATE EVENTS



(a)



(b)

Figure B.17: Type B - GB05 - HHZ. The seismograms are colored according to the event date in UTC (black: first; light brown: last). In the spectrogram, blue colors indicate low energy, red colors high energy. The units of the frequency scale on the right side of the seismograms is Hz.

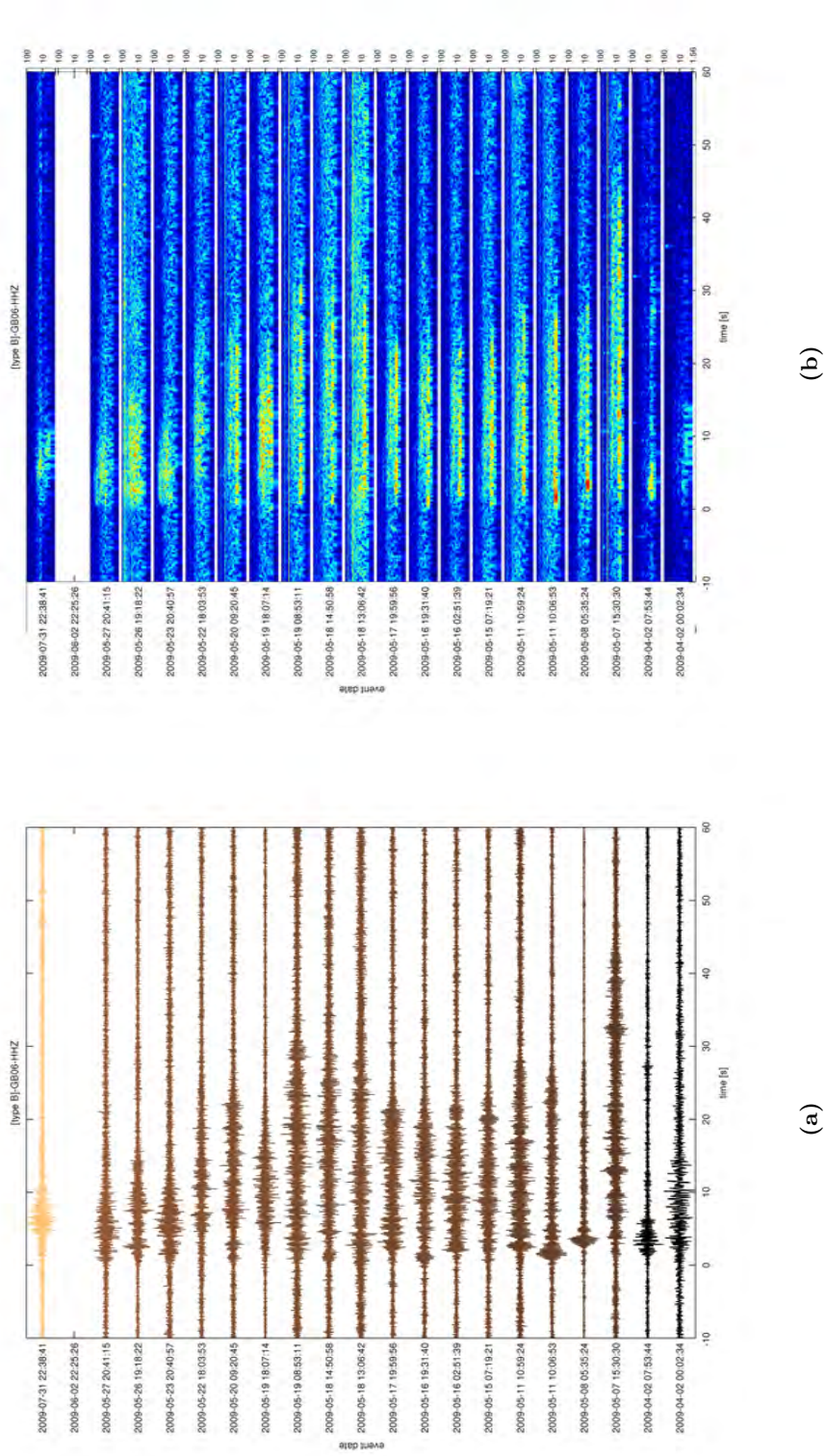
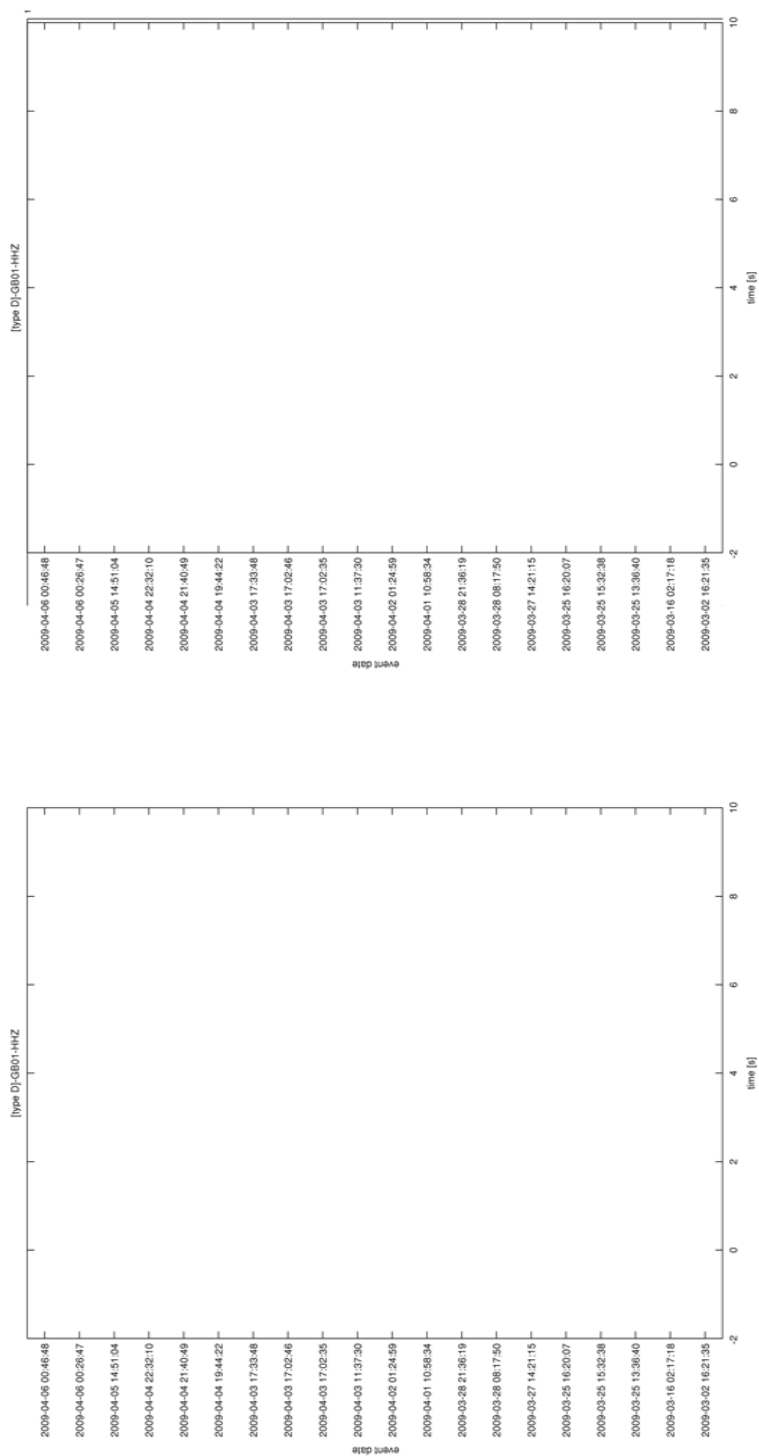


Figure B.18: Type B - GB06 - HHZ. The seismograms are colored according to the event date in UTC (black: first; light brown: last). In the spectrogram, blue colors indicate low energy, red colors indicate high energy. The units of the frequency scale on the right side of the spectrograms is Hz.

B. SLOPE CANDIDATE EVENTS

B.4 Type D

Type D events are short events with a weak first onset, that is sometimes hidden in the background noise. The median event length is 5.6 seconds (IQR = 5.6 s) and the median SNR is 3.4 (IQR = 3.8). The onset of the events shows frequencies above 10 Hz whereas the later part of the events is dominated by frequencies below 10 Hz. The separation between the high frequent onset and the low frequent ending of the events is clearly visible in the waveform. The low frequent part sometimes shows quite a monotone characteristic. Sometimes two or three successive type D events have been recorded.

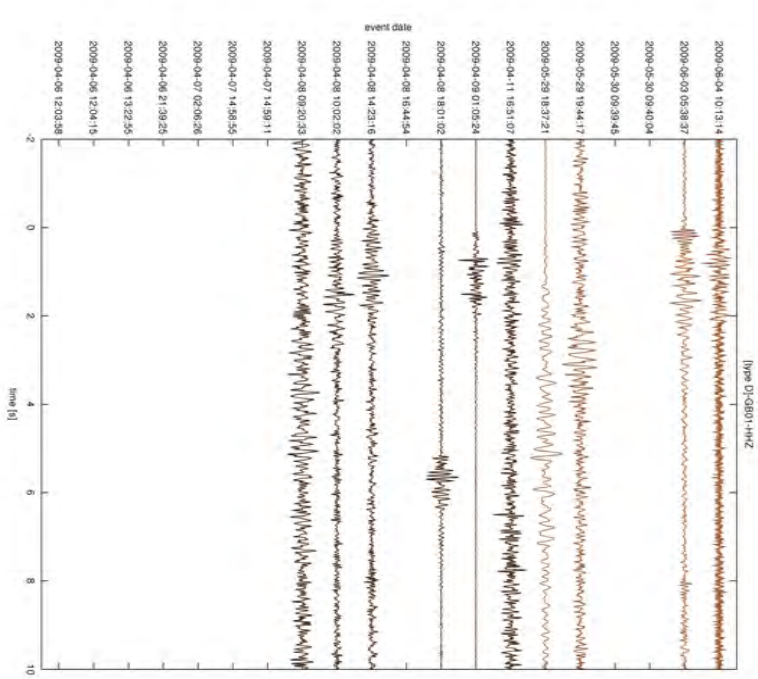


(a)

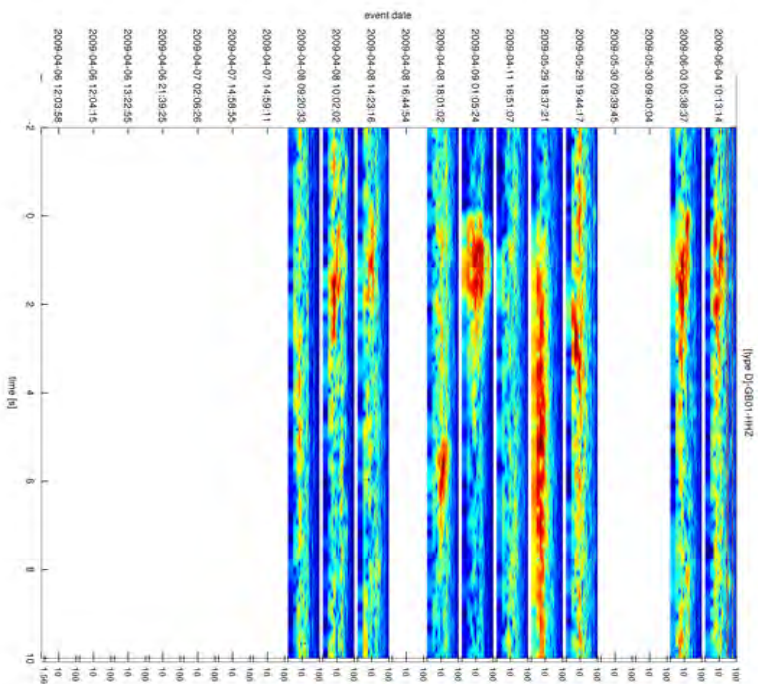
(b)

Figure B.19: Type D - GB01 - HHZ. The spectrograms are colored according to the event date in UTC (black: first; light brown: last). In the spectrogram, blue colors indicate low energy, red colors indicate high energy. The units of the frequency scale on the right side of the spectrograms is Hz.

B. SLOPE CANDIDATE EVENTS



(a)



(b)

Figure B.20: Type D - GB01 - HHZ. The seismograms are colored according to the event date in UTC (black: first; light brown: last). In the spectrogram, blue colors indicate low energy, red colors high energy. The units of the frequency scale on the right side of the seismograms is Hz.

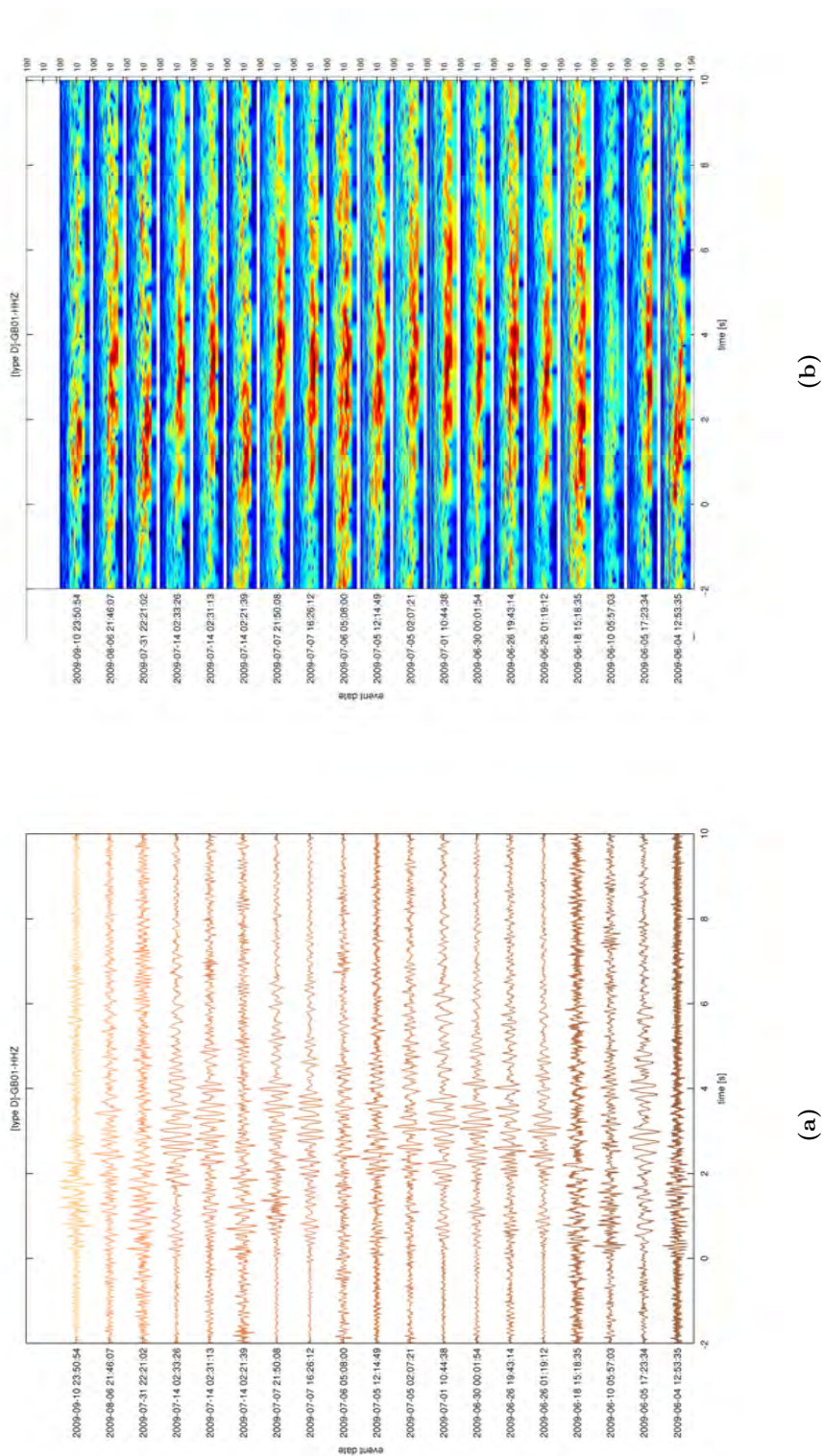
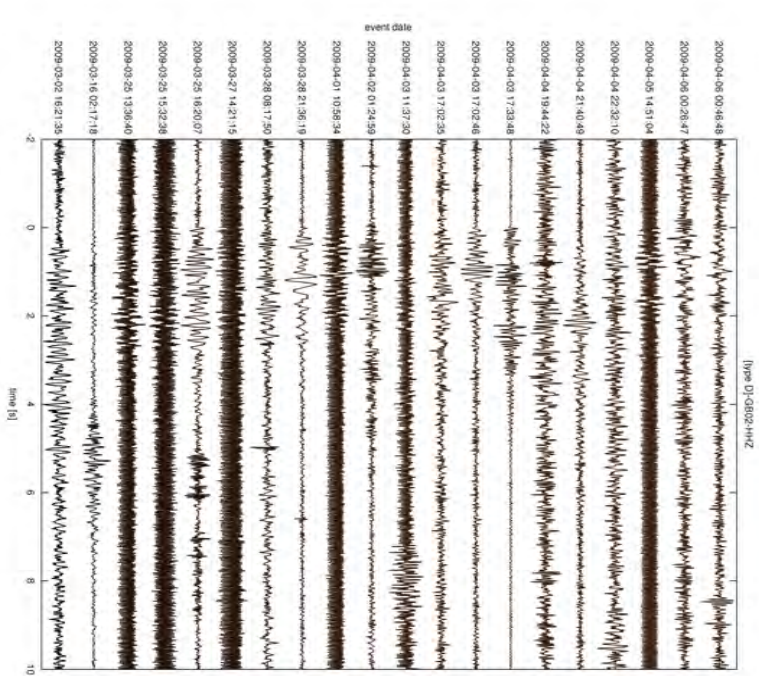
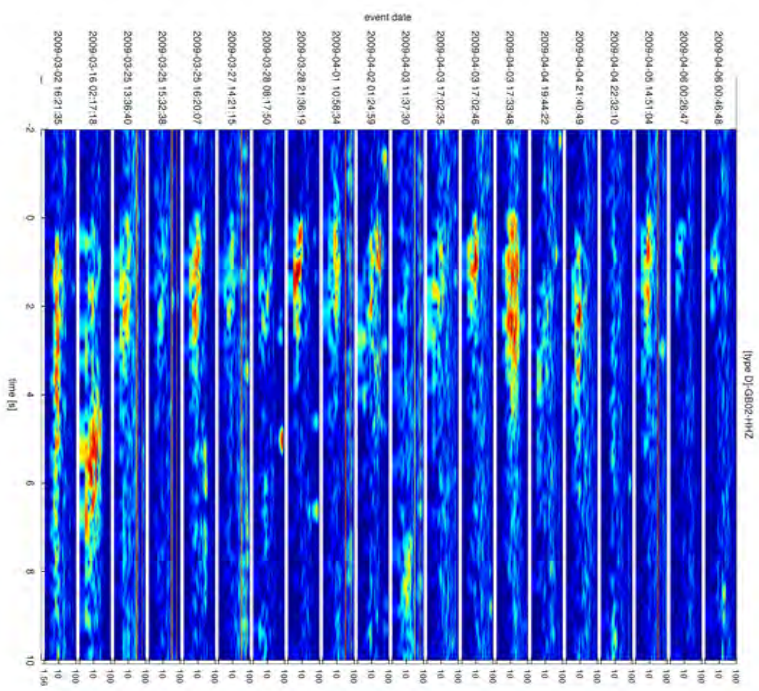


Figure B.21: Type D - GB01 - HHZ. The seismograms are colored according to the event date in UTC (black: first; light brown: last). In the spectrogram, blue colors indicate low energy, red colors high energy. The units of the frequency scale on the right side of the spectrograms is Hz.

B. SLOPE CANDIDATE EVENTS



(a)



(b)

Figure B.22: Type D - GB02 - HHZ. The seismograms are colored according to the event date in UTC (black: first; light brown: last). In the spectrogram, blue colors indicate low energy, red colors high energy. The units of the frequency scale on the right side of the seismograms is Hz.

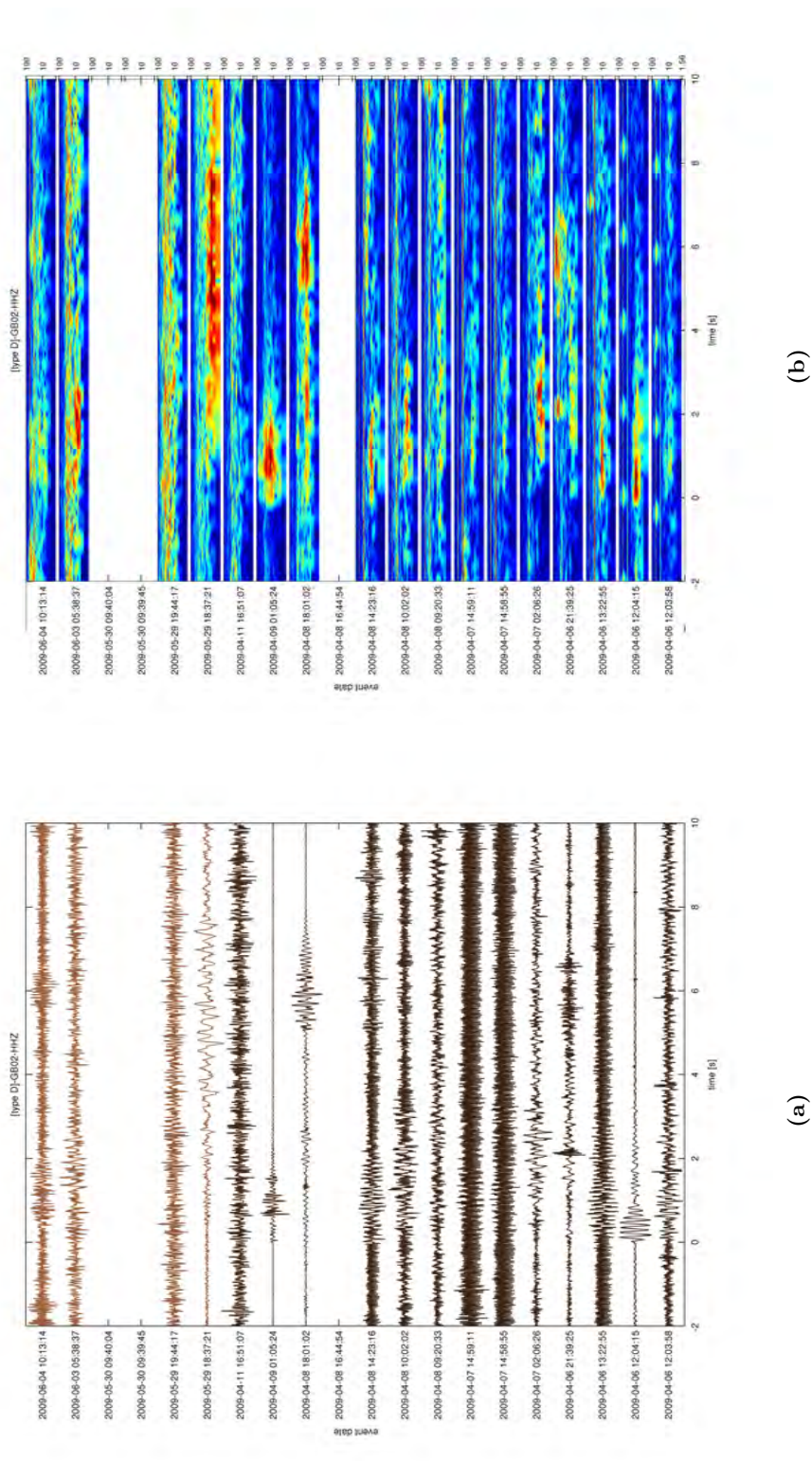
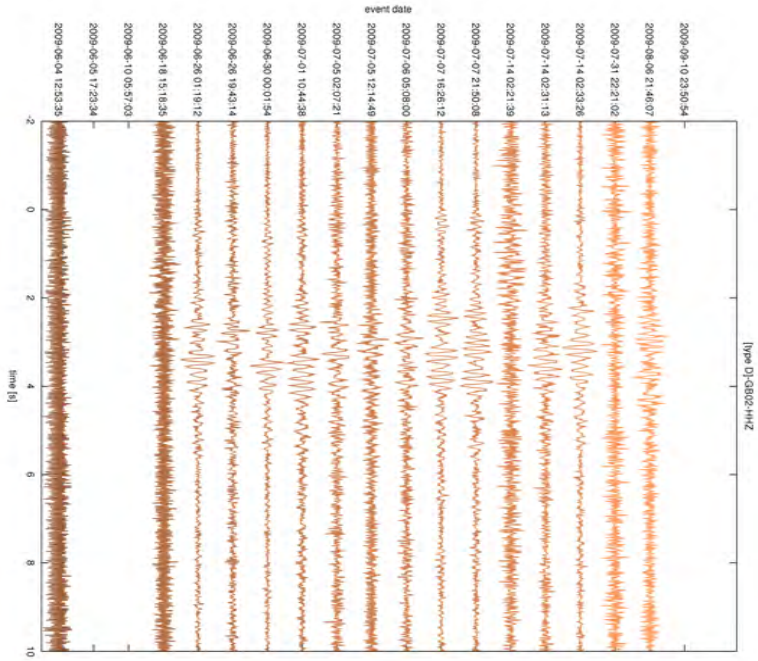
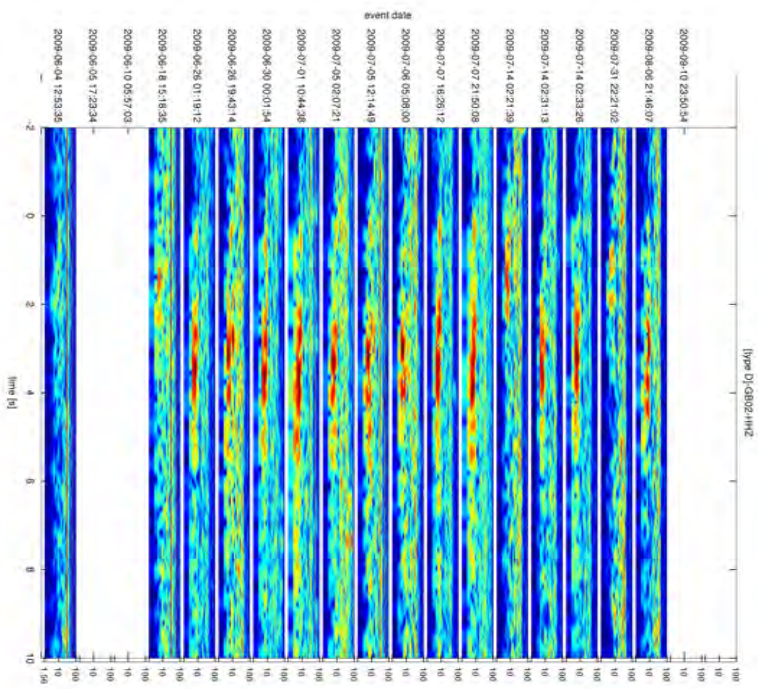


Figure B.23: Type D - GB02 - HHZ. The seismograms are colored according to the event date in UTC (black: first; light brown: last). In the spectrogram, blue colors indicate low energy, red colors indicate high energy. The units of the frequency scale on the right side of the spectrograms is Hz.

B. SLOPE CANDIDATE EVENTS

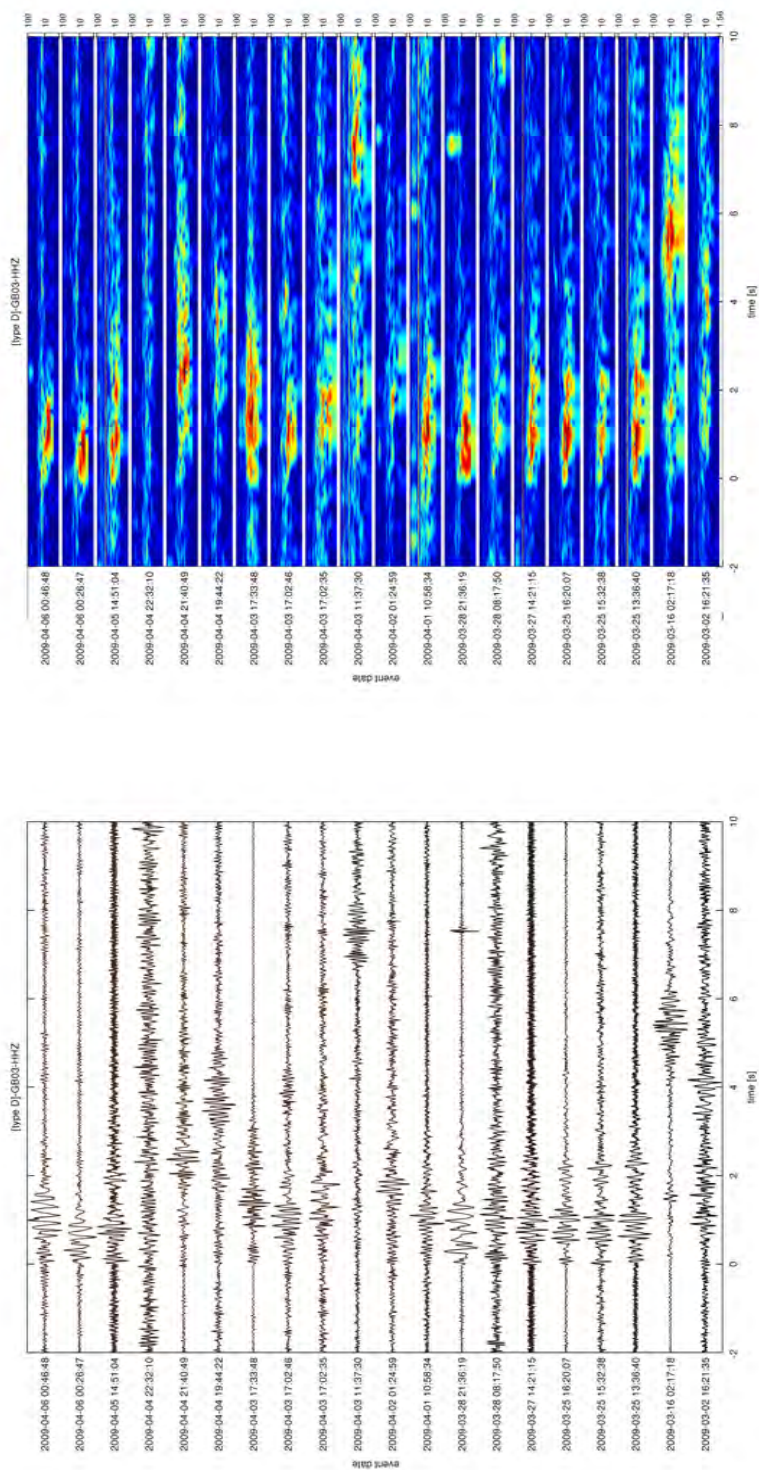


(a)



(b)

Figure B.24: Type D - GB02 - HHZ. The seismograms are colored according to the event date in UTC (black: first; light brown: last). In the spectrogram, blue colors indicate low energy, red colors high energy. The units of the frequency scale on the right side of the seismograms is Hz.

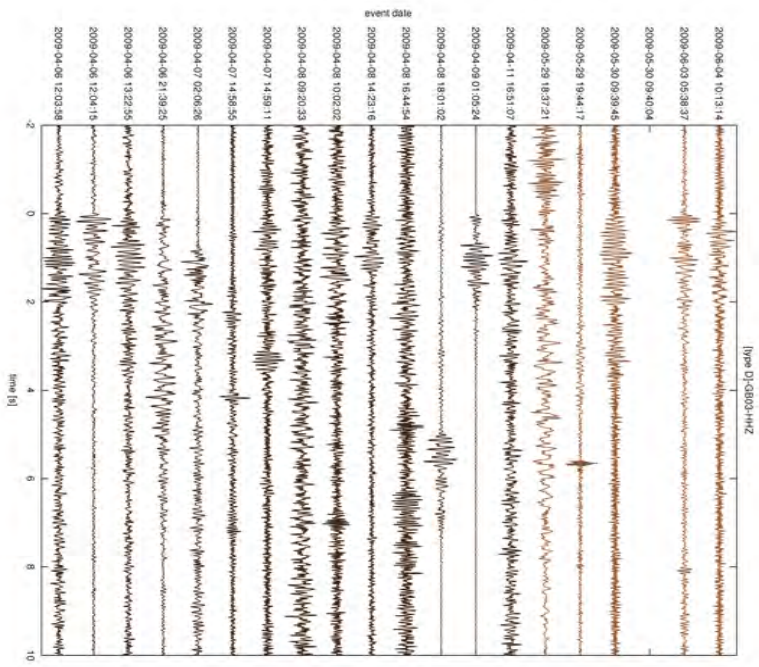


(b)

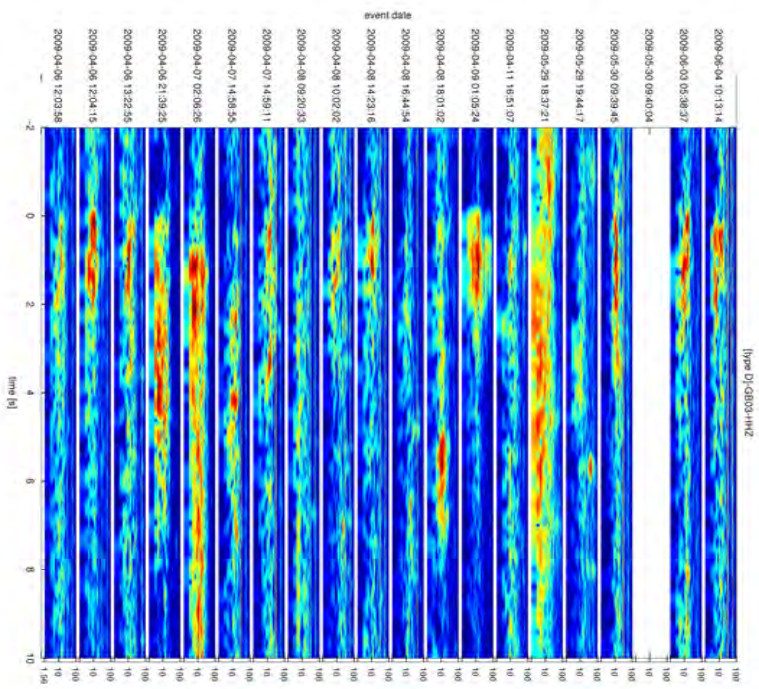
(a)

Figure B.25: Type D - GB03 - HHZ. The seismograms are colored according to the event date in UTC (black: first; light brown: last). In the spectrogram, blue colors indicate low energy, red colors indicate high energy. The units of the frequency scale on the right side of the spectrograms is Hz.

B. SLOPE CANDIDATE EVENTS

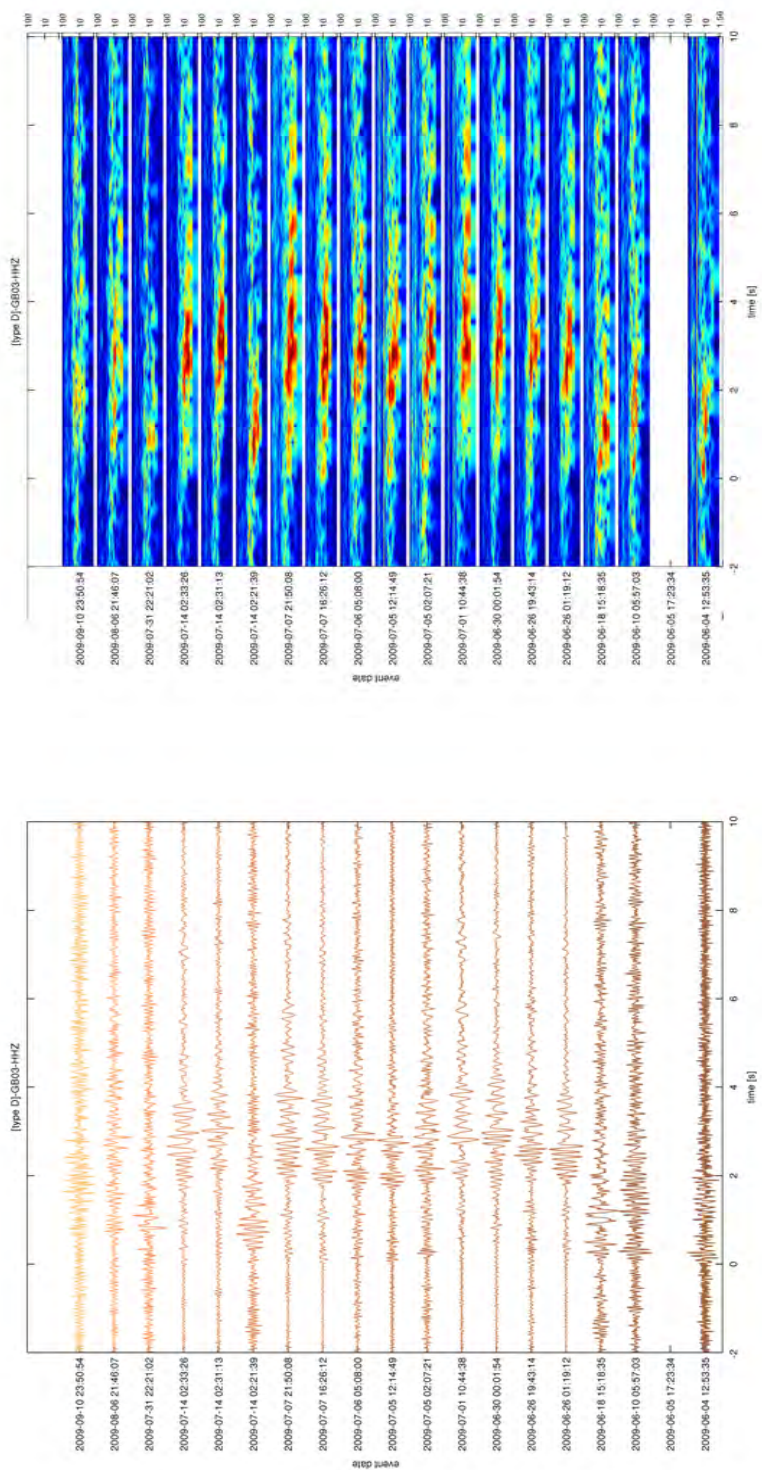


(a)



(b)

Figure B.26: Type D - GB03 - HHZ. The seismograms are colored according to the event date in UTC (black: first; light brown: last). In the spectrogram, blue colors indicate low energy, red colors high energy. The units of the frequency scale on the right side of the seismograms is Hz.

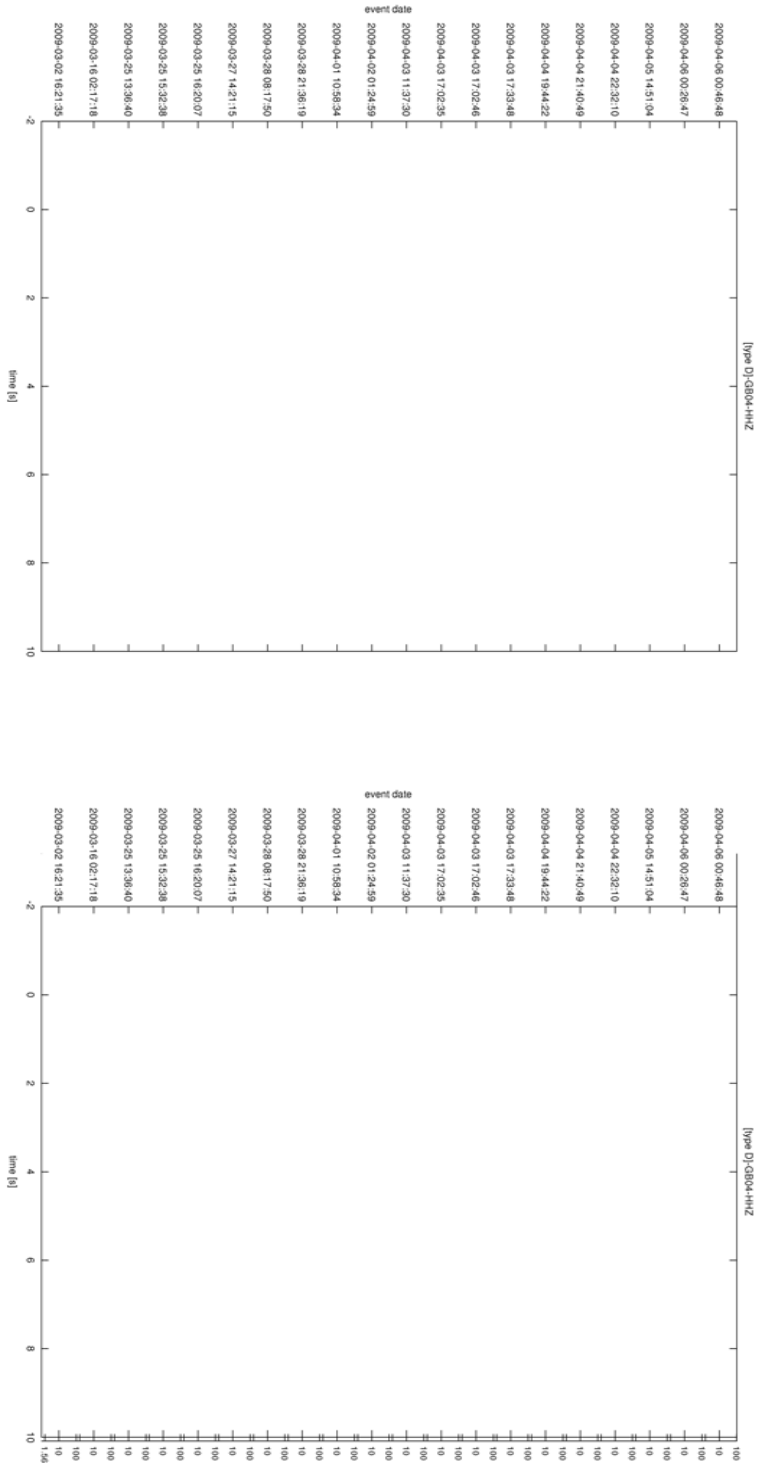


(b)

(a)

Figure B.27: Type D - GB03 - HHZ. The seismograms are colored according to the event date in UTC (black: first; light brown: last). In the spectrogram, blue colors indicate low energy, red colors high energy. The units of the frequency scale on the right side of the seismograms is Hz.

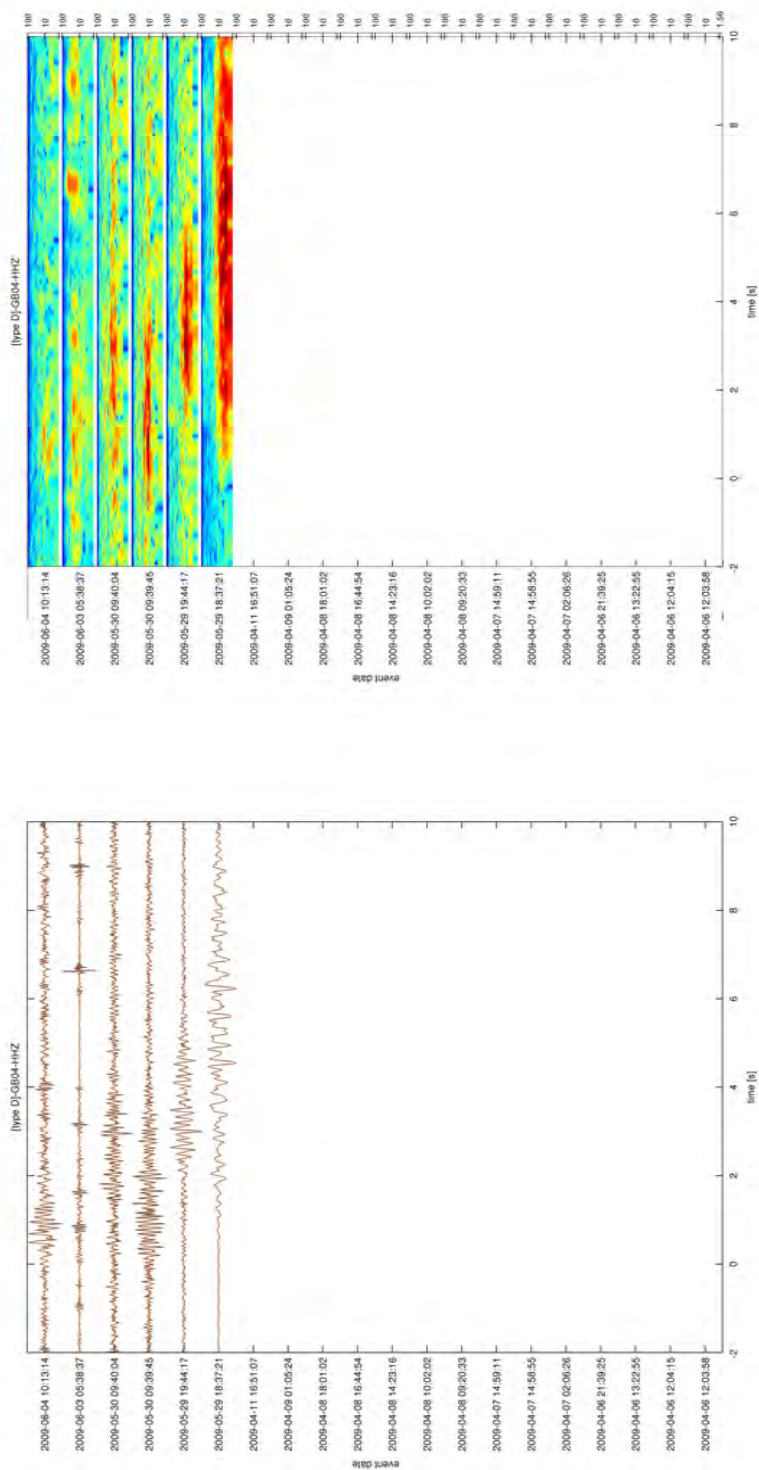
B. SLOPE CANDIDATE EVENTS



(a)

(b)

Figure B.28: Type D - GB04 - HHZ. The seismicograms are colored according to the event date in UTC (black: first; light brown: last). In the spectrogram, blue colors indicate low energy, red colors high energy. The units of the frequency scale on the right side of the seismicograms is Hz.

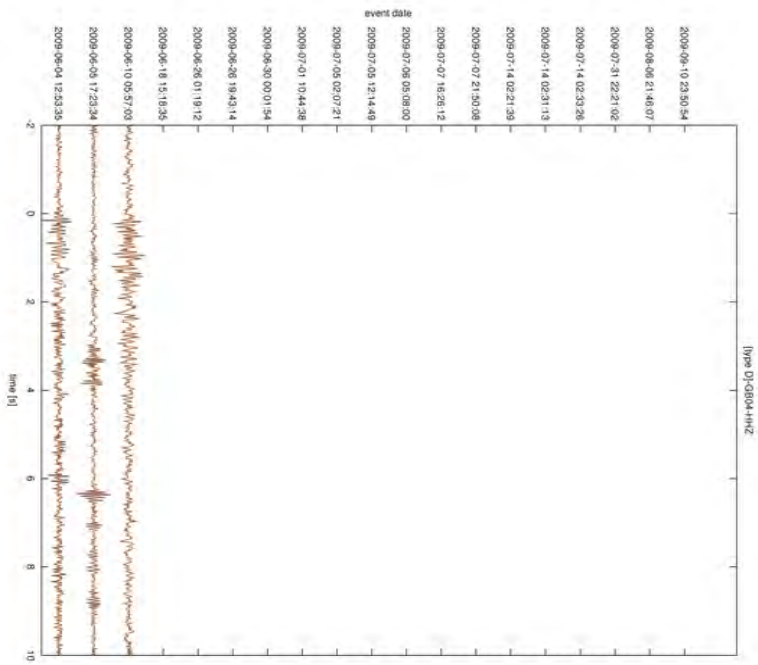


(b)

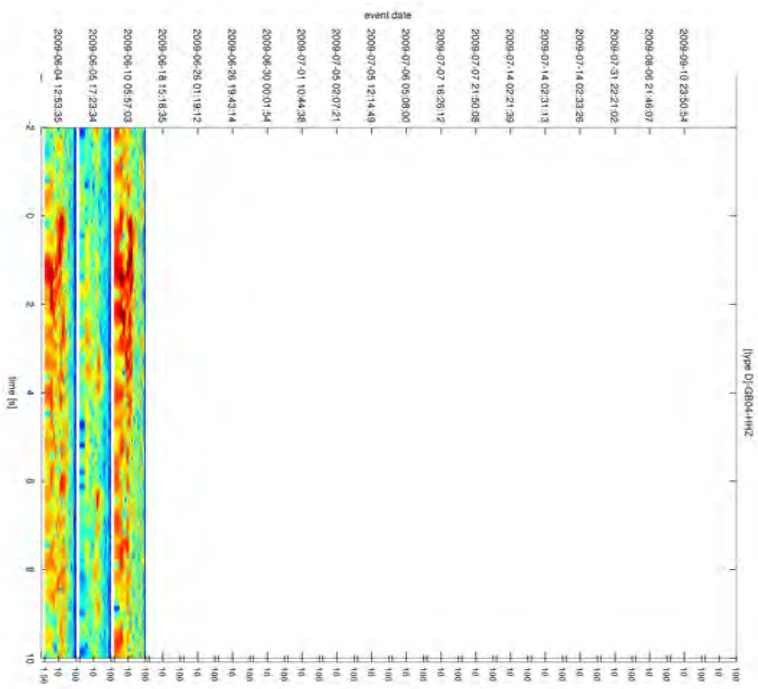
(a)

Figure B.29: Type D - GB04 - HHZ. The seismograms are colored according to the event date in UTC (black: first; light brown: last). In the spectrogram, blue colors indicate low energy, red colors high energy. The units of the frequency scale on the right side of the seismograms is Hz.

B. SLOPE CANDIDATE EVENTS

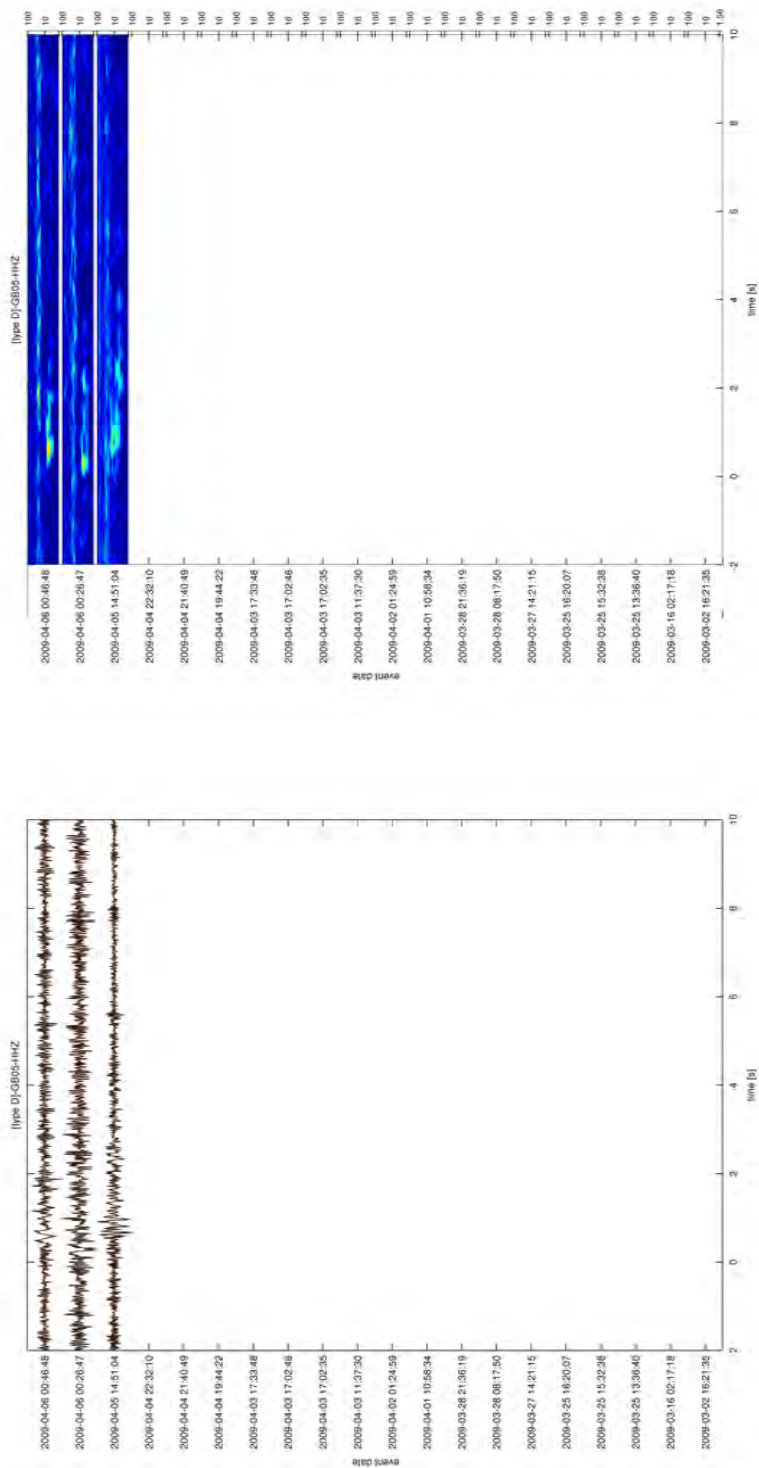


(a)



(b)

Figure B.30: Type D - GB04 - HHZ. The seismograms are colored according to the event date in UTC (black: first; light brown: last). In the spectrogram, blue colors indicate low energy, red colors high energy. The units of the frequency scale on the right side of the seismograms is Hz.

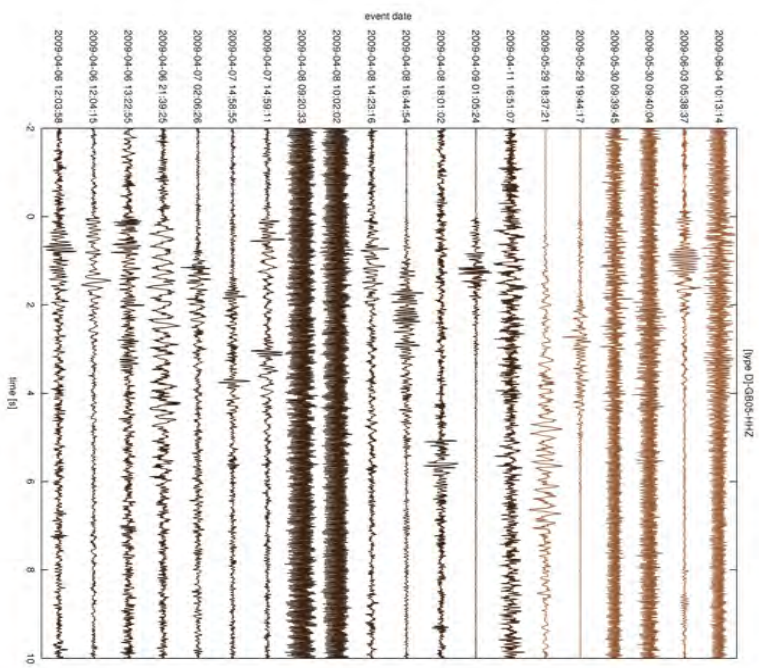


(a)

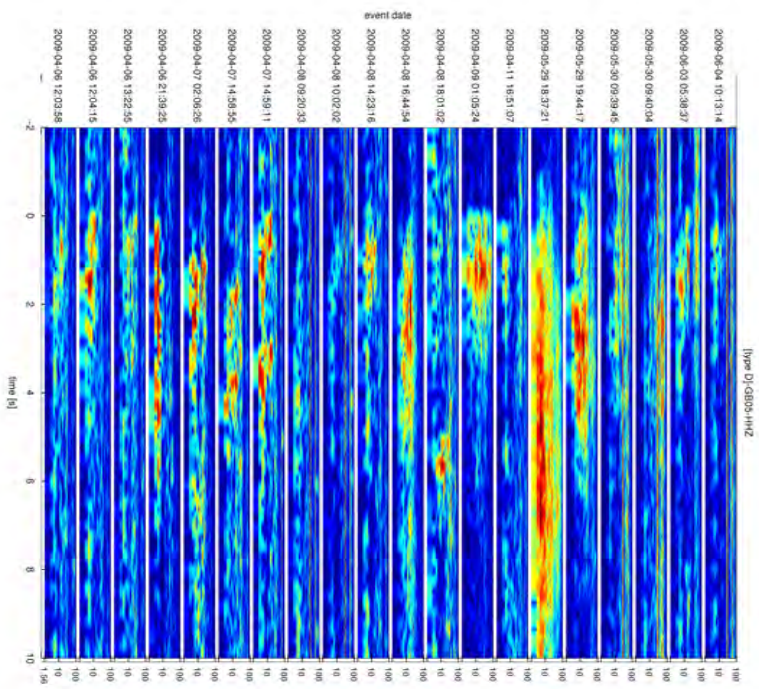
(b)

Figure B.31: Type D - GB05 -HHZ. The seismograms are colored according to the event date in UTC (black: first; light brown: last). In the spectrogram, blue colors indicate low energy, red colors high energy. The units of the frequency scale on the right side of the spectrograms is Hz.

B. SLOPE CANDIDATE EVENTS

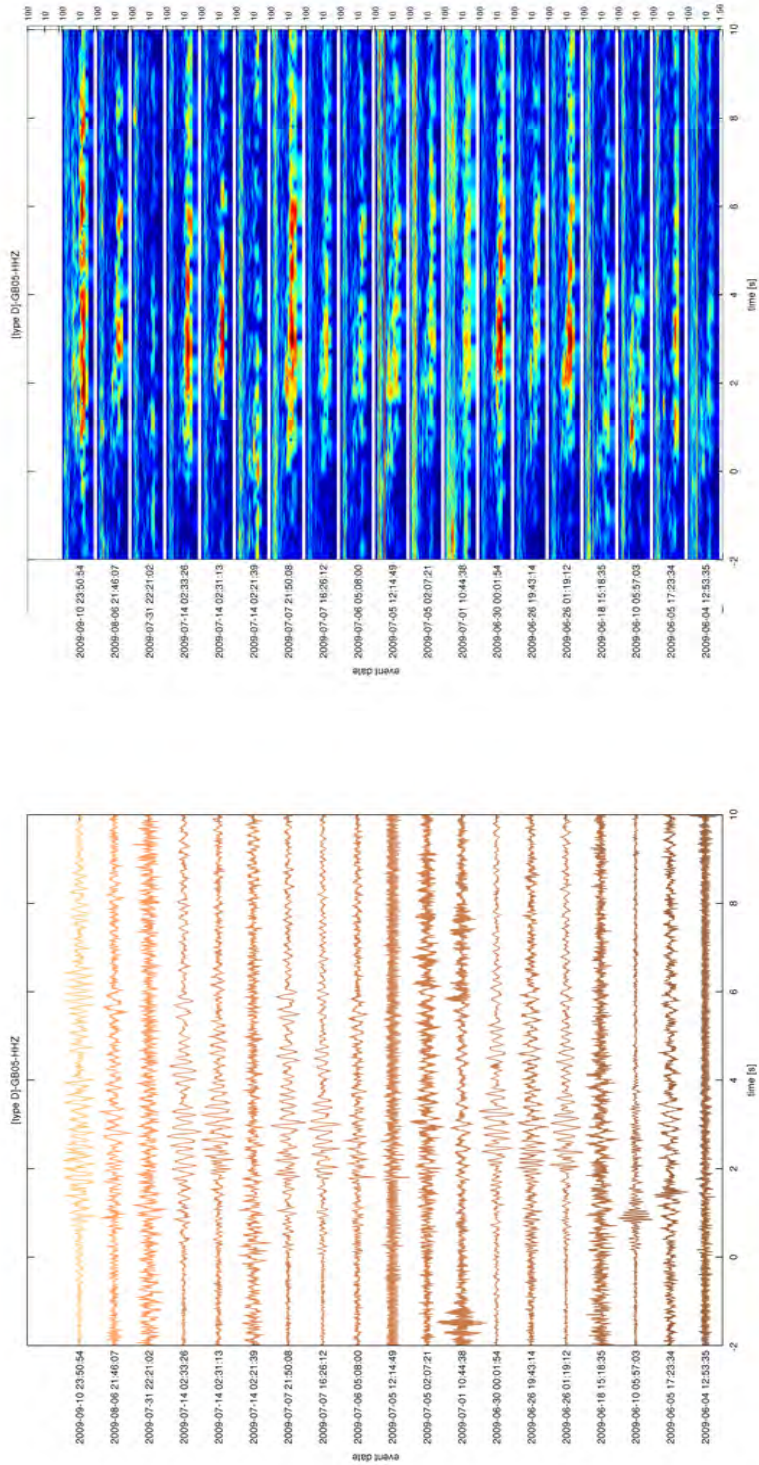


(a)



(b)

Figure B.32: Type D - GB05 - HHZ. The seismograms are colored according to the event date in UTC (black: first; light brown: last). In the spectrogram, blue colors indicate low energy, red colors high energy. The units of the frequency scale on the right side of the seismograms is Hz.

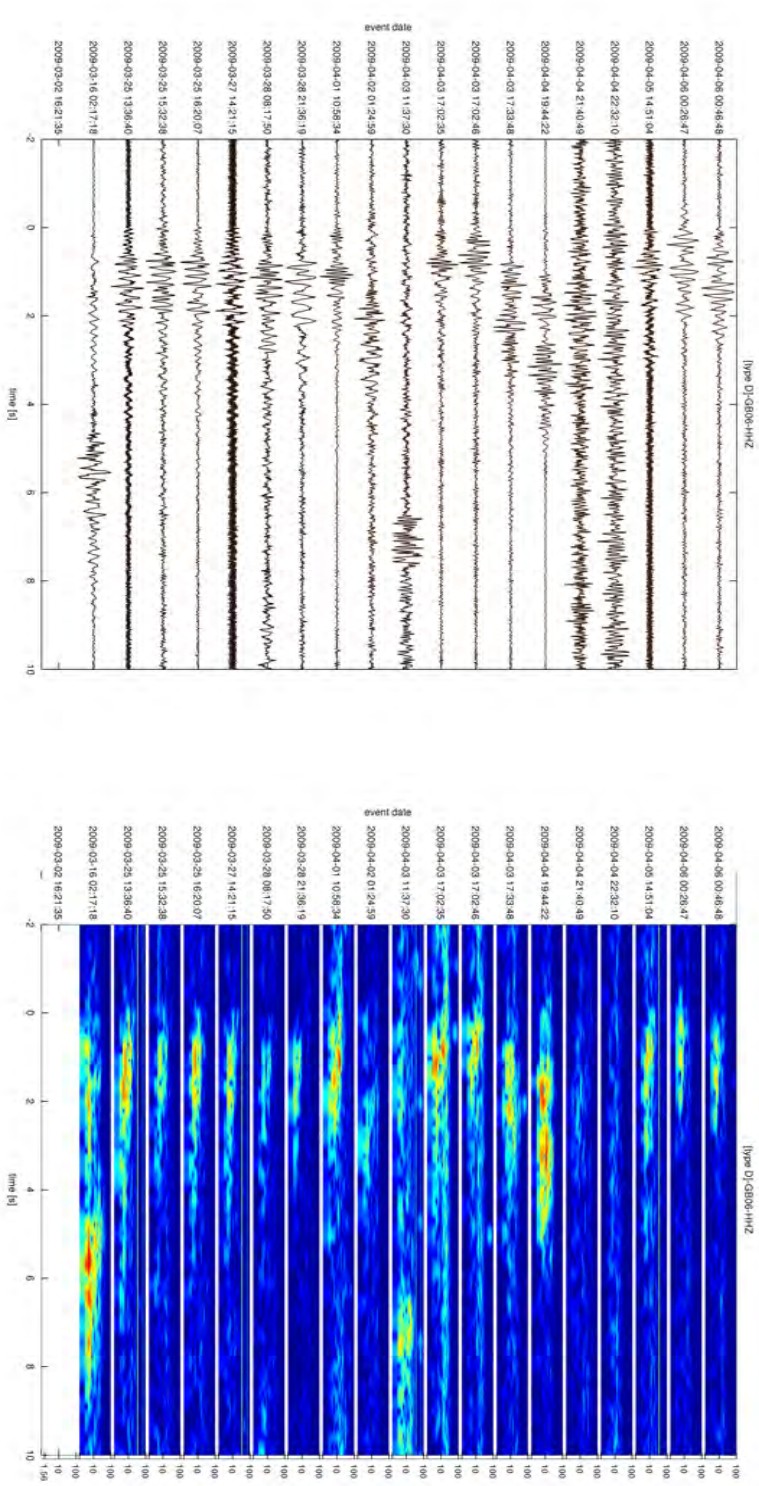


(b)

(a)

Figure B.33: Type D - GB05 - HHZ. The seismograms are colored according to the event date in UTC (black: first; light brown: last). In the spectrogram, blue colors indicate low energy, red colors high energy. The units of the frequency scale on the right side of the spectrograms is Hz.

B. SLOPE CANDIDATE EVENTS



(a)

(b)

Figure B.34: Type D - GB06 - HHZ. The seismograms are colored according to the event date in UTC (black: first; light brown: last). In the spectrogram, blue colors indicate low energy, red colors high energy. The units of the frequency scale on the right side of the seismograms is Hz.

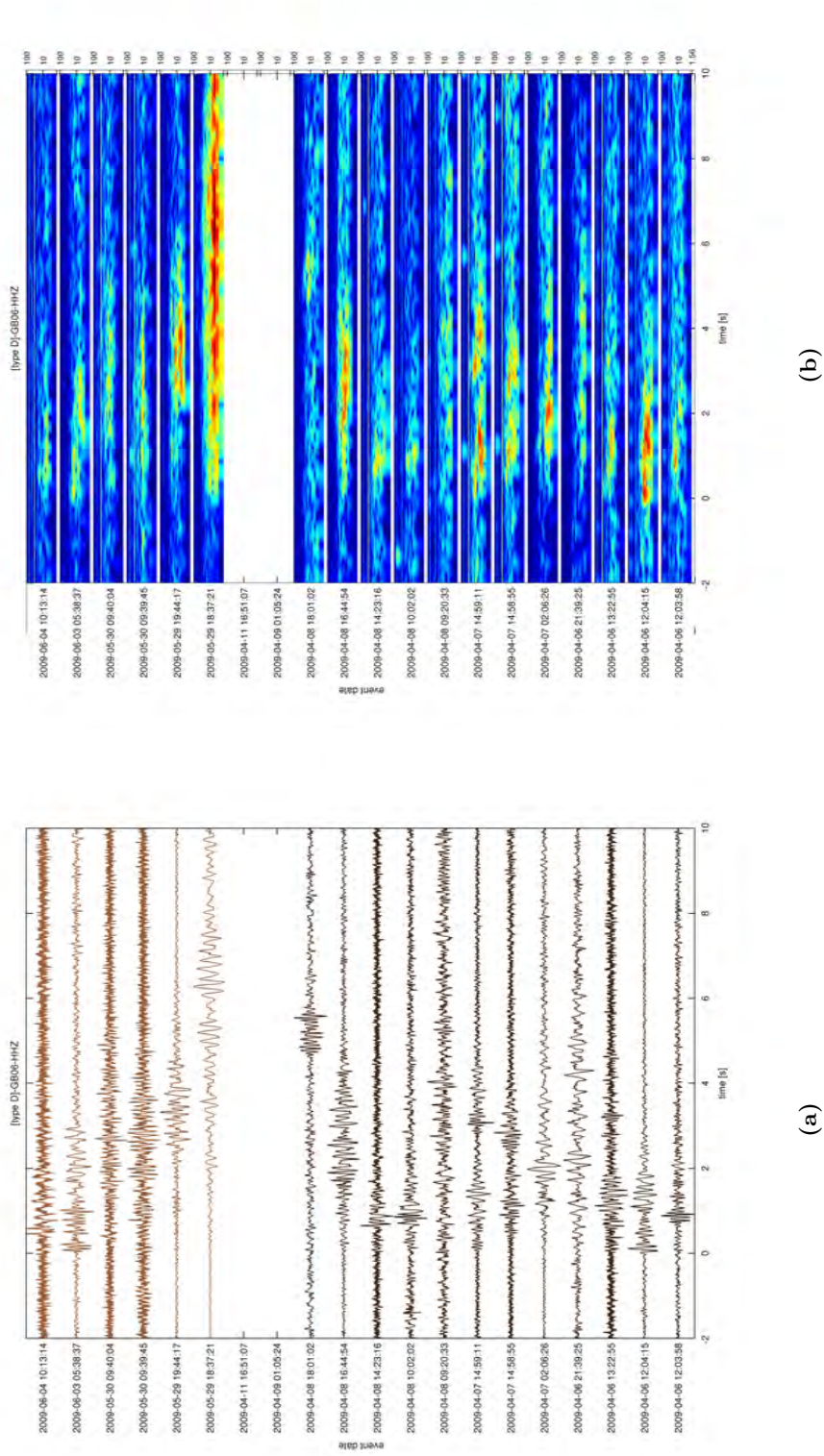
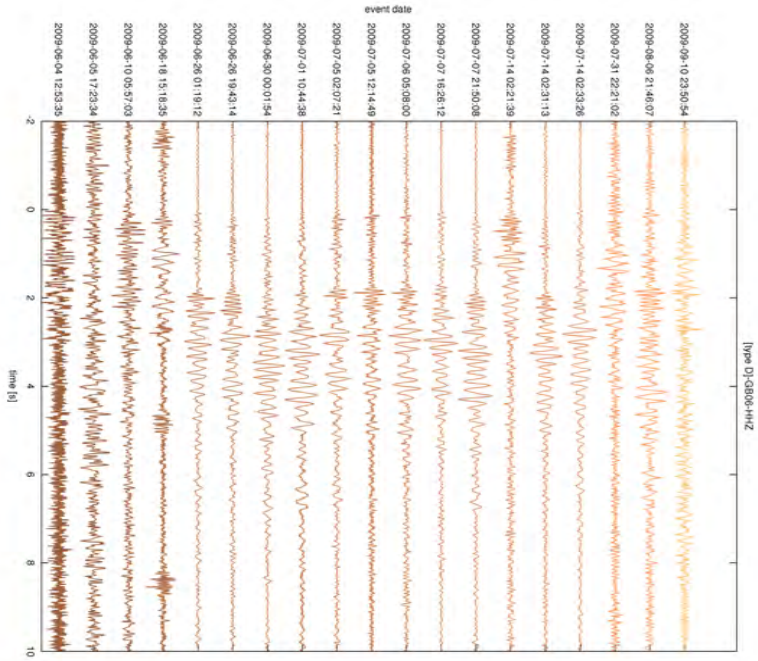
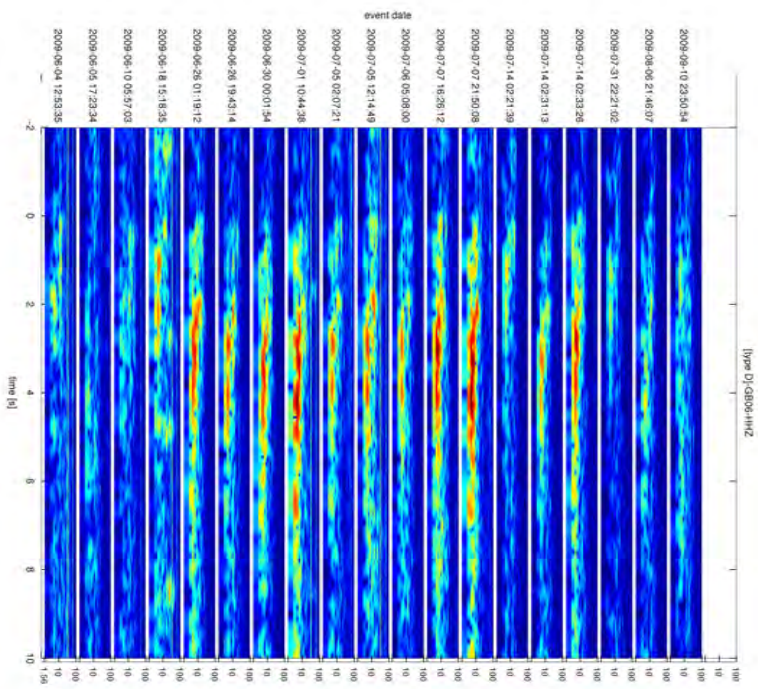


Figure B.35: Type D - GB06 -HHZ. The seismograms are colored according to the event date in UTC (black: first; light brown: last). In the spectrogram, blue colors indicate low energy, red colors high energy. The units of the frequency scale on the right side of the spectrograms is Hz.

B. SLOPE CANDIDATE EVENTS



(a)



(b)

Figure B.36: Type D - GB06 - HHZ. The seismograms are colored according to the event date in UTC (black: first; light brown: last). In the spectrogram, blue colors indicate low energy, red colors high energy. The units of the frequency scale on the right side of the seismograms is Hz.

B.5 Type rf

The type RF events have a long duration (median = 32.1 s, IQR = 38.3 s) and a SNR that varies strongly among the stations. The median SNR is 3.6 with an IQR of 32.3. It was possible to link one of these events to a rockfall happening on June 7, 2009 at 22:15:35 UTC (see figure 7.12). The waveform of the type RF events generally shows a series of short impulsive events with large amplitudes on one of the topmost stations GB05 and GB06. The amplitudes are attenuated strongly with distance and sometimes the waveform is not visible on the stations deployed at the toe of the slope. The daytime distribution of the events given in figure 7.7 shows, that the type RF events occurred mainly during the nighttime.

The observed rockfall with a known source location has also been used to verify the localization using NonLinLoc (see figure 7.13).

B. SLOPE CANDIDATE EVENTS

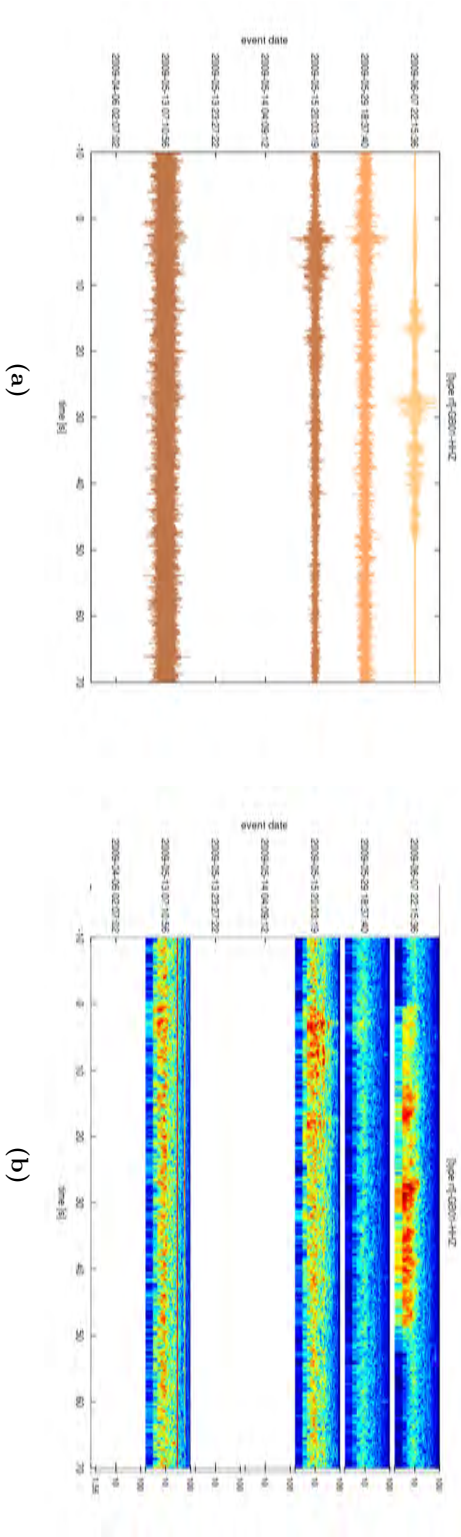


Figure B.37: Type rf - GB01 - HHZ. The seismograms are colored according to the event date in UTC (black: first; light brown: last). In the spectrogram, blue colors indicate low energy, red colors high energy. The units of the frequency scale on the right side of the spectrograms is Hz.

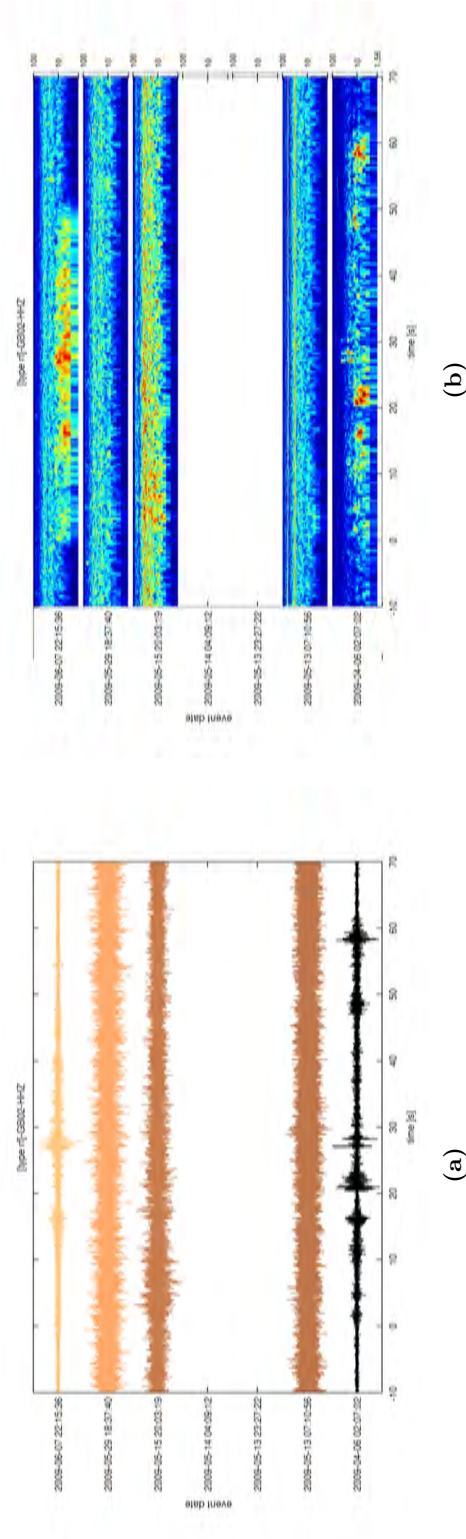


Figure B.38: Type rf - GB02 - HHZ. The seismograms are colored according to the event date in UTC (black: first; light brown: last). In the spectrogram, blue colors indicate low energy, red colors high energy. The units of the frequency scale on the right side of the seismograms is Hz.

B. SLOPE CANDIDATE EVENTS

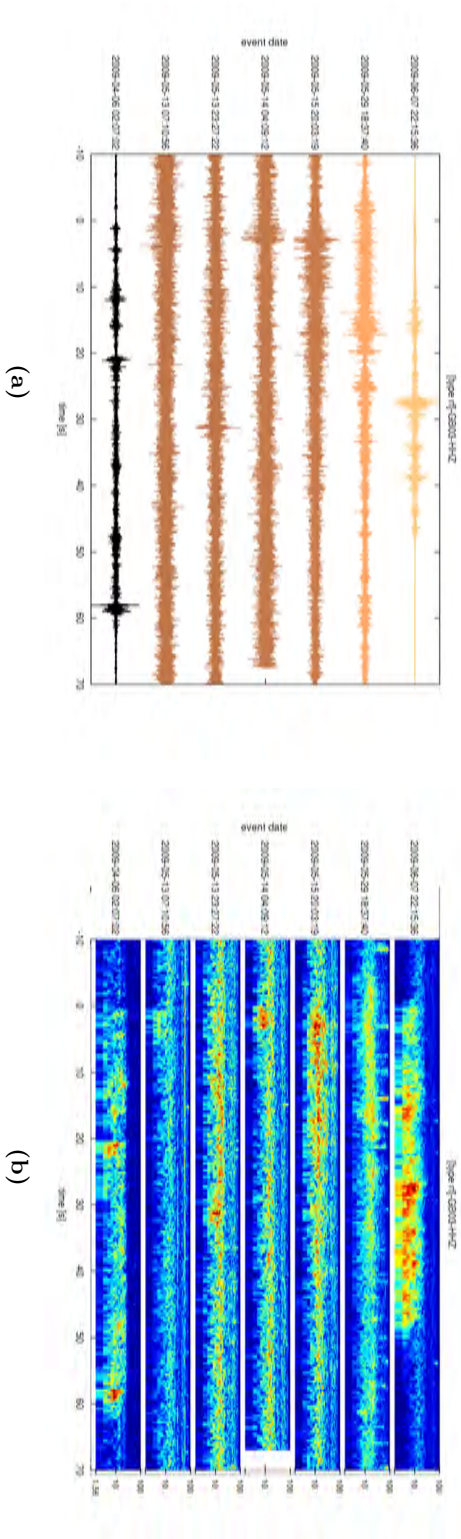


Figure B.39: Type rf - GB03 - HHZ. The seismograms are colored according to the event date in UTC (black: first; light brown: last). In the spectrogram, blue colors indicate low energy, red colors high energy. The units of the frequency scale on the right side of the seismograms is Hz.

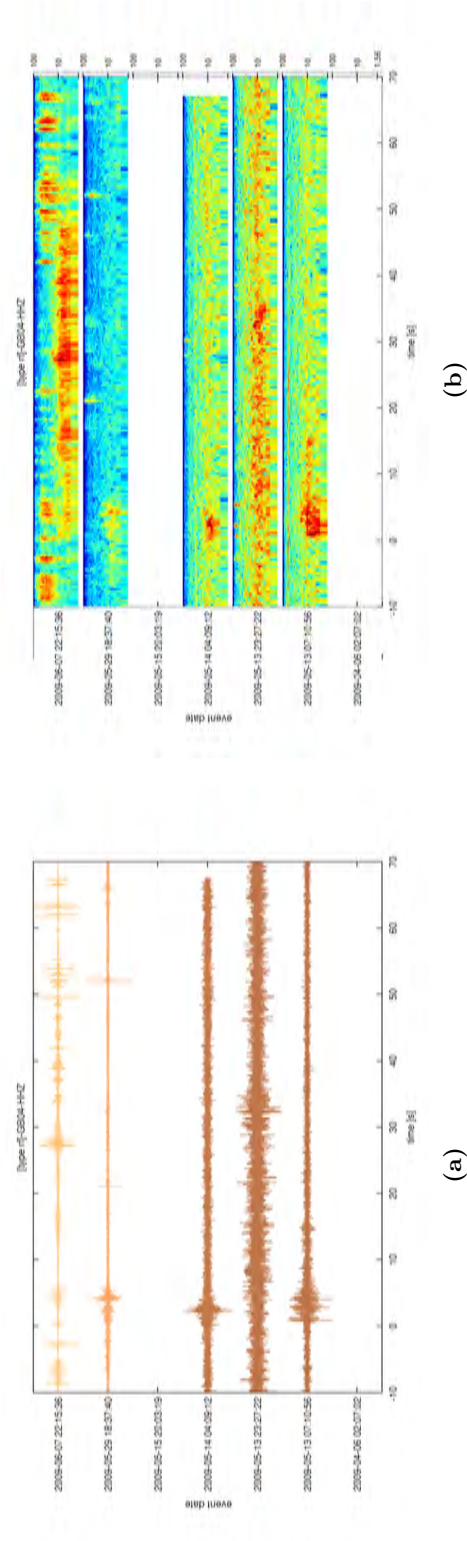


Figure B.40: Type rf - GB04 - HHZ. The seismograms are colored according to the event date in UTC (black: first; light brown: last). In the spectrogram, blue colors indicate low energy, red colors high energy. The units of the frequency scale on the right side of the seismograms is Hz.

B. SLOPE CANDIDATE EVENTS

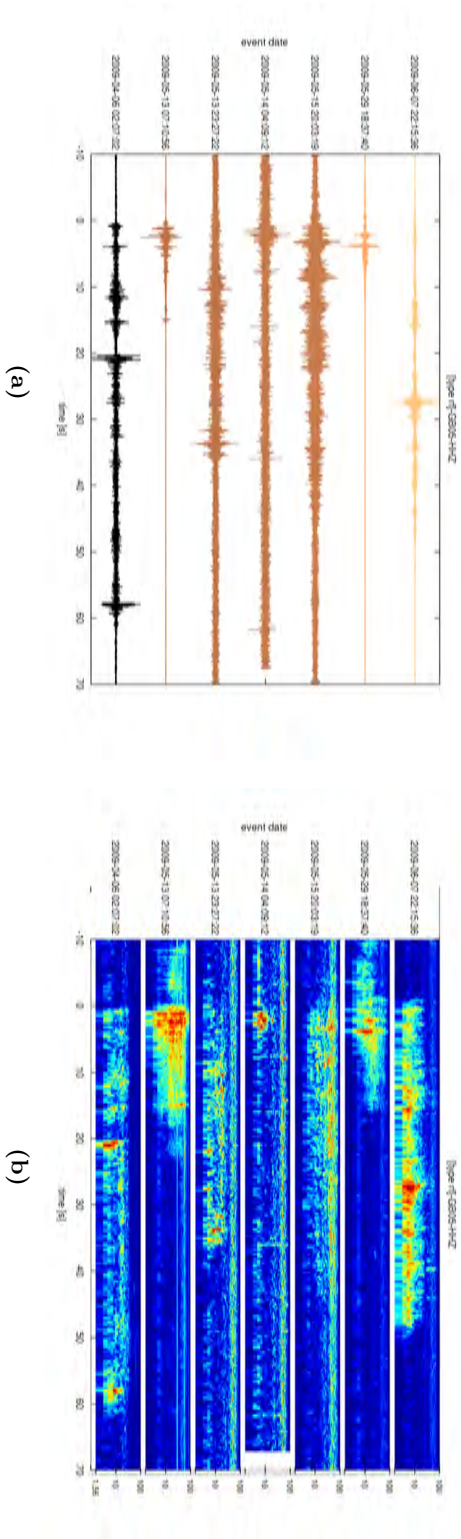


Figure B.41: Type rf - GB05 - HHZ. The seismograms are colored according to the event date in UTC (black: first; light brown: last). In the spectrogram, blue colors indicate low energy, red colors high energy. The units of the frequency scale on the right side of the spectrograms is Hz.

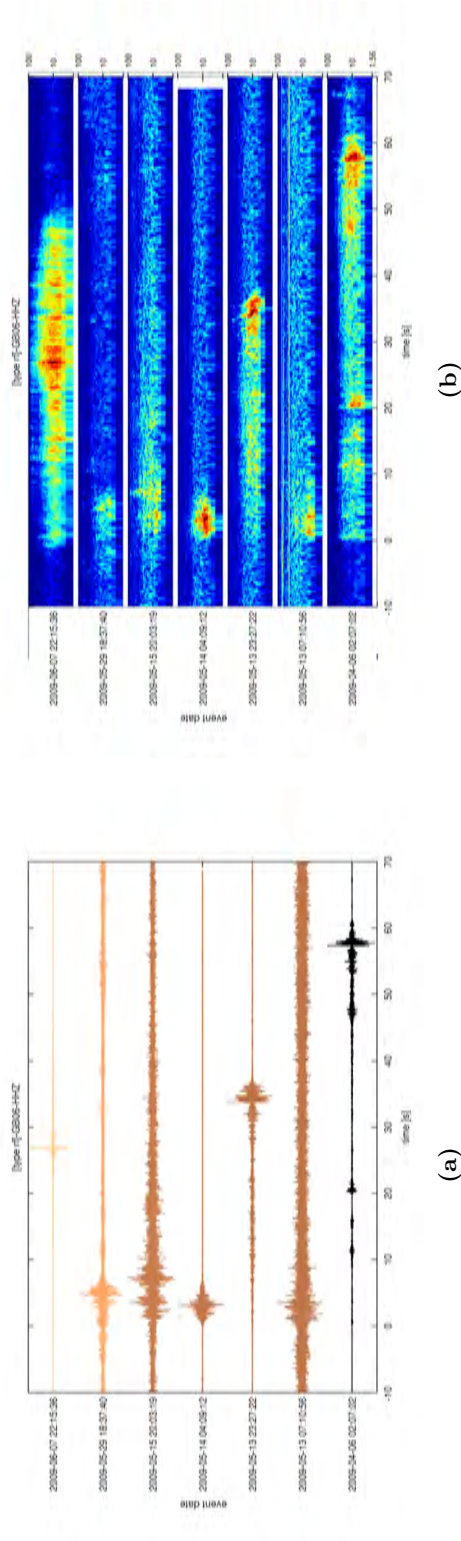
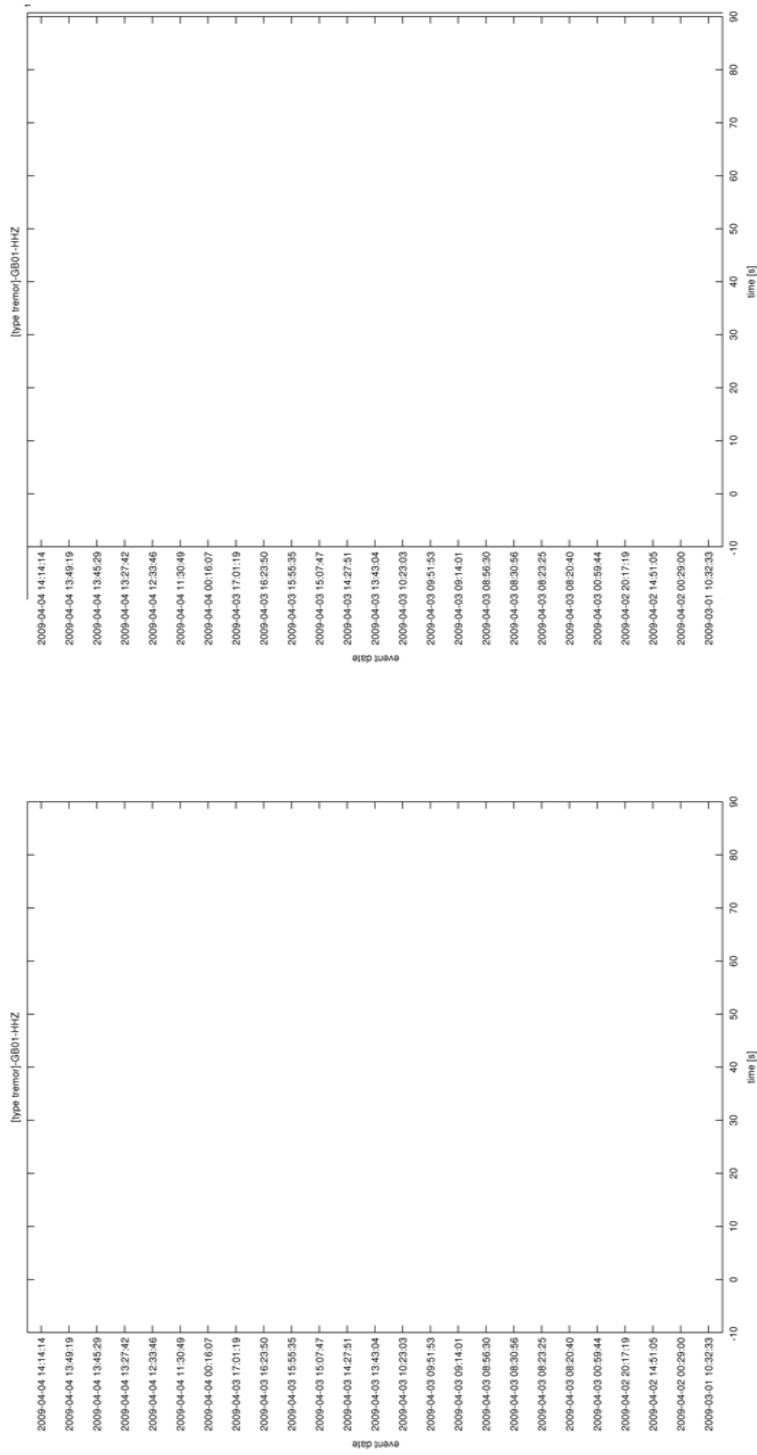


Figure B.42: Type rf - GB06 - HHZ. The seismograms are colored according to the event date in UTC (black; first; light brown; last). In the spectrogram, blue colors indicate low energy, red colors high energy. The units of the frequency scale on the right side of the seismograms is Hz.

B. SLOPE CANDIDATE EVENTS

B.6 Type tremor

The type tremor events have the longest duration (median = 50.4 s, IQR = 38.2 s) among the slope event types. The events have a high SNR (median = 4.9) with large variations (IQR = 11.5) among the individual events. The bandwidth of the events generally is quite broad with maximum frequencies of up to 100 Hz. The dominant energy is located in the frequency bands around 10 Hz. The waveform and time-frequency patterns correlate well among the individual stations and the amplitudes show noticeable attenuation over the seismic network. The main occurrence of the type tremor events is bound to a narrow time-span of 5 days from April 2, 2009 to April 6, 2009. 42 of the 49 tremor events occurred during this period.

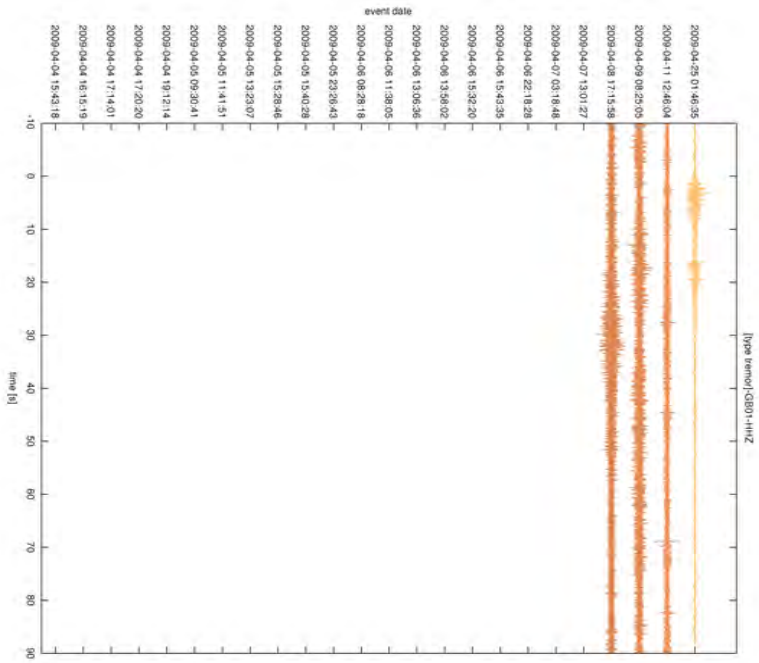


(a)

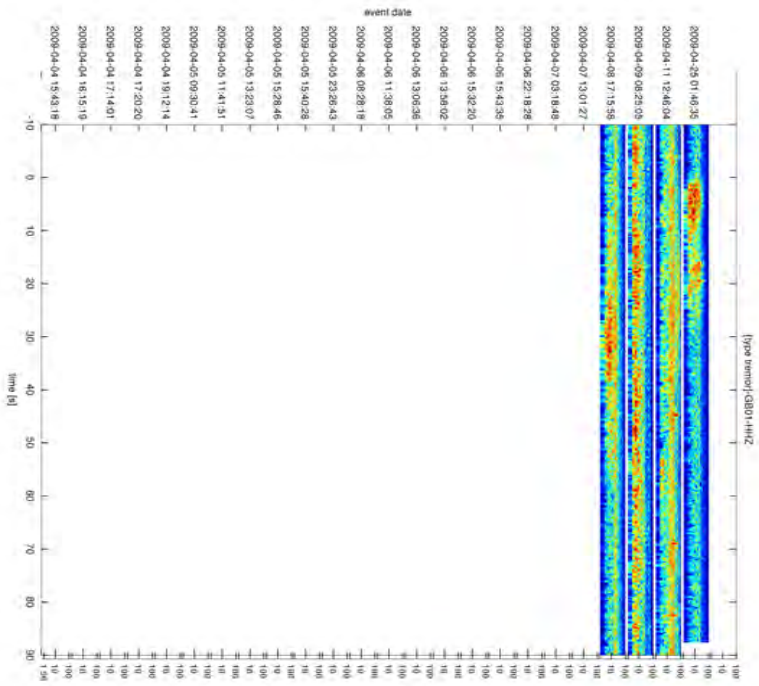
(b)

Figure B.43: Type tremor - GB01 - HHZ. The seismograms are colored according to the event date in UTC (black: first; light brown: last). In the spectrogram, blue colors indicate low energy, red colors high energy. The units of the frequency scale on the right side of the seismograms is Hz.

B. SLOPE CANDIDATE EVENTS

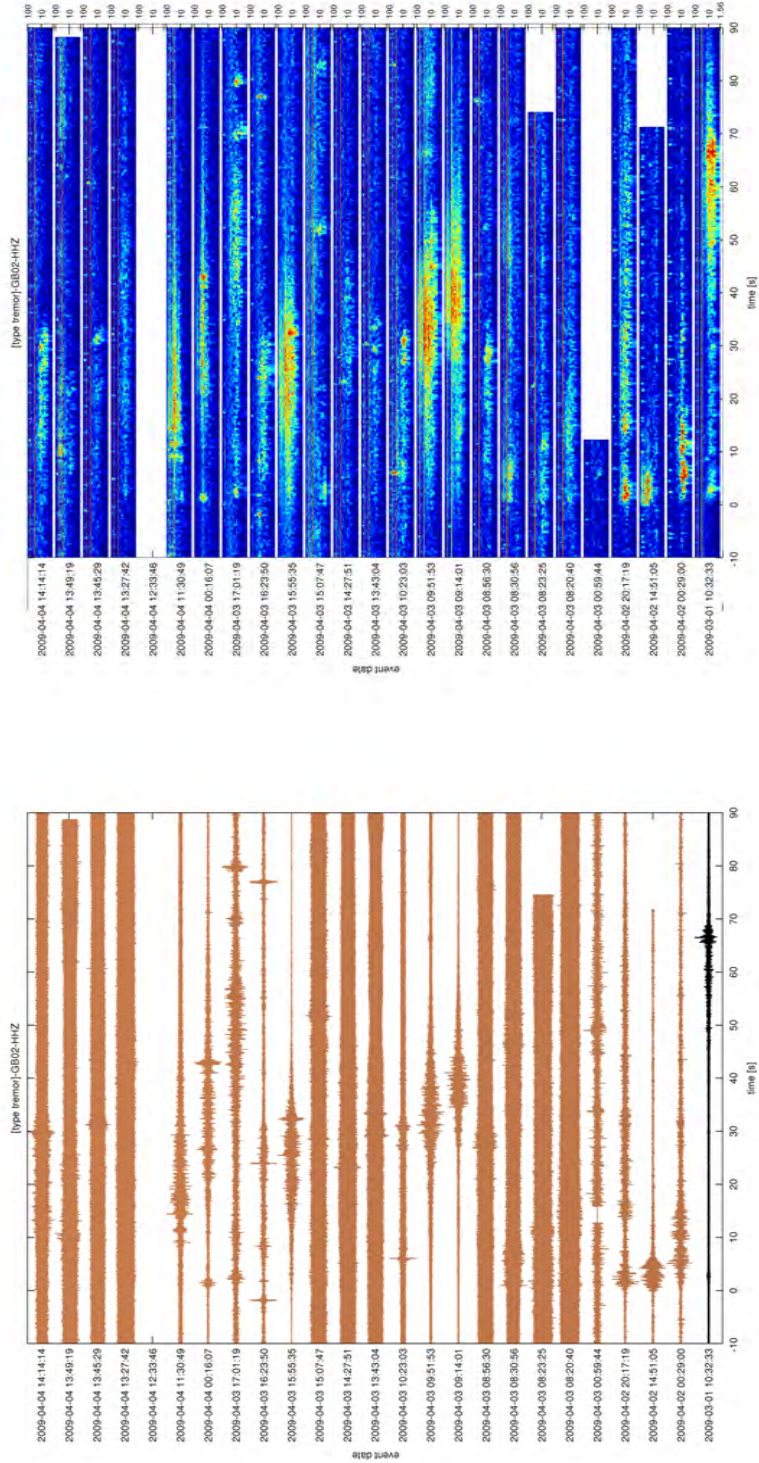


(a)



(b)

Figure B.44: Type tremor - GB01 - HHZ. The seismograms are colored according to the event date in UTC (black: first; light brown: last). In the spectrogram, blue colors indicate low energy, red colors high energy. The units of the frequency scale on the right side of the seismograms is Hz.

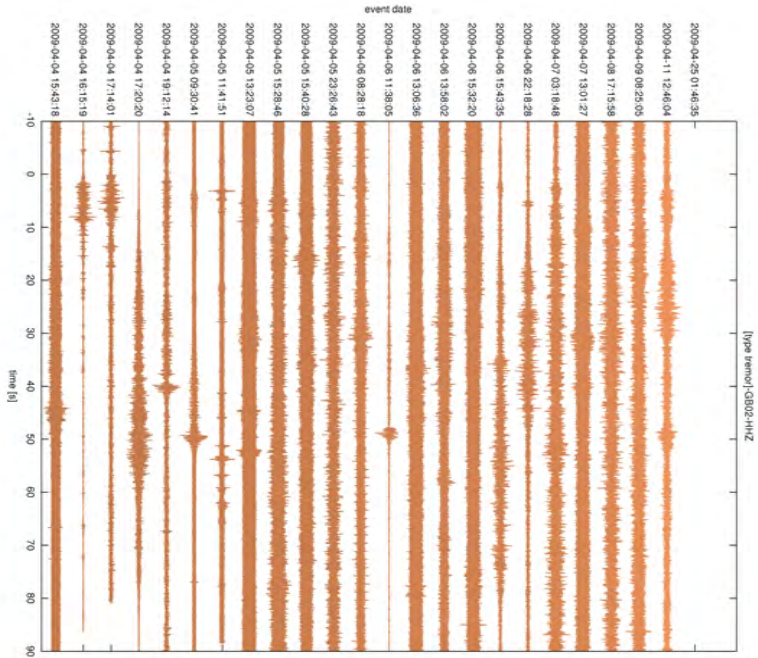


(a)

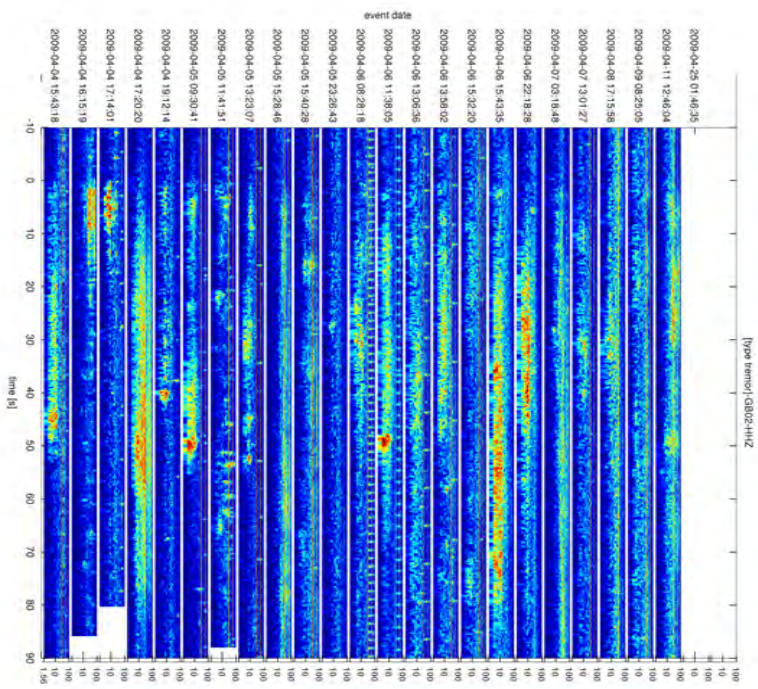
(b)

Figure B.45: Type tremor - GB02 -HHZ. The seismograms are colored according to the event date in UTC (black: first; light brown: last). In the spectrogram, blue colors indicate low energy, red colors high energy. The units of the frequency scale on the right side of the spectrograms is Hz.

B. SLOPE CANDIDATE EVENTS

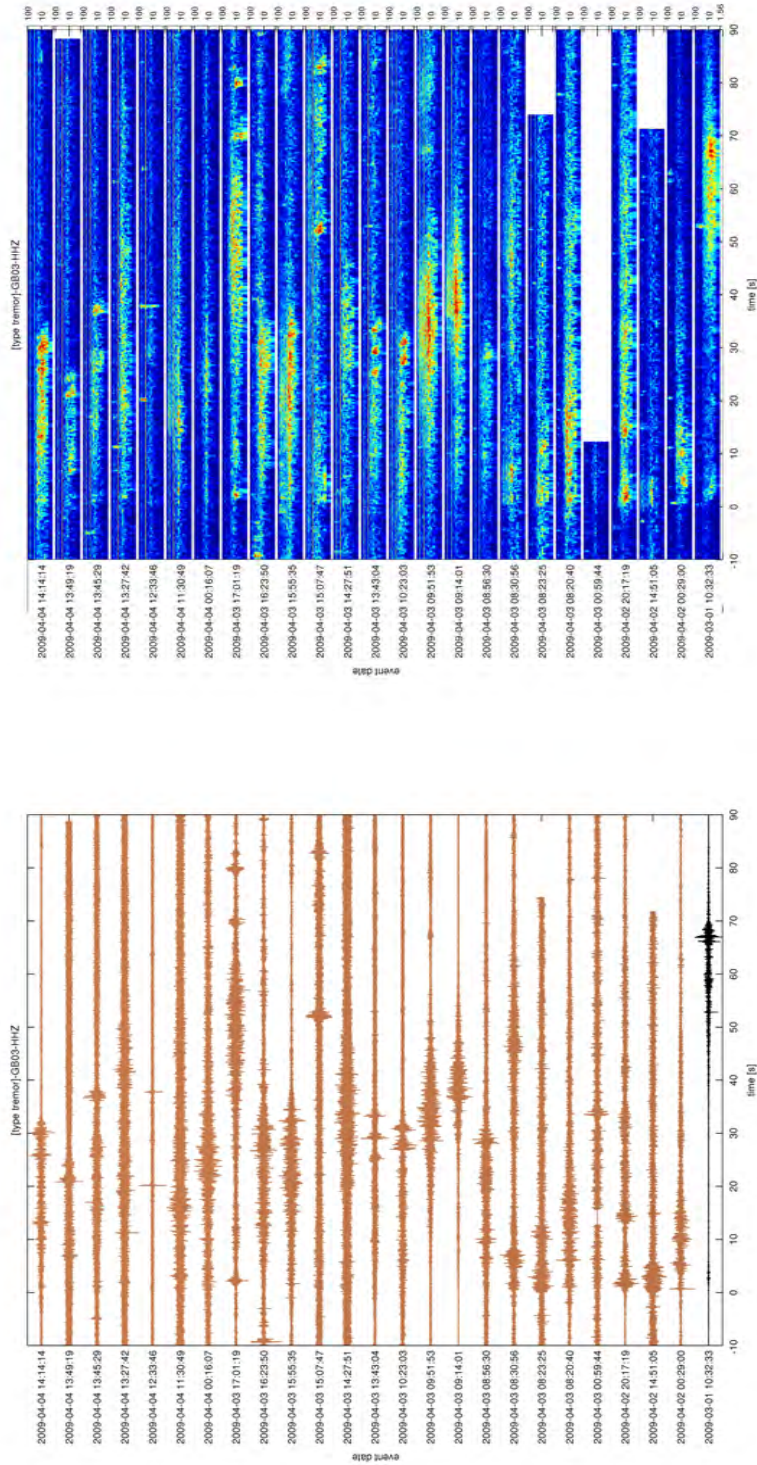


(a)



(b)

Figure B.46: Type tremor - GB02 -HHZ. The seismograms are colored according to the event date in UTC (black: first; light brown: last). In the spectrogram, blue colors indicate low energy, red colors high energy. The units of the frequency scale on the right side of the seismograms is Hz.

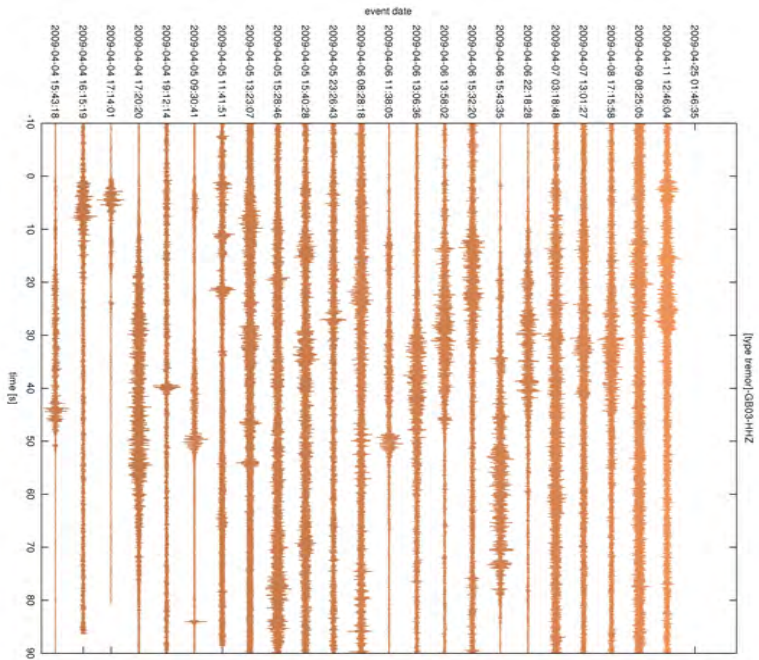


(a)

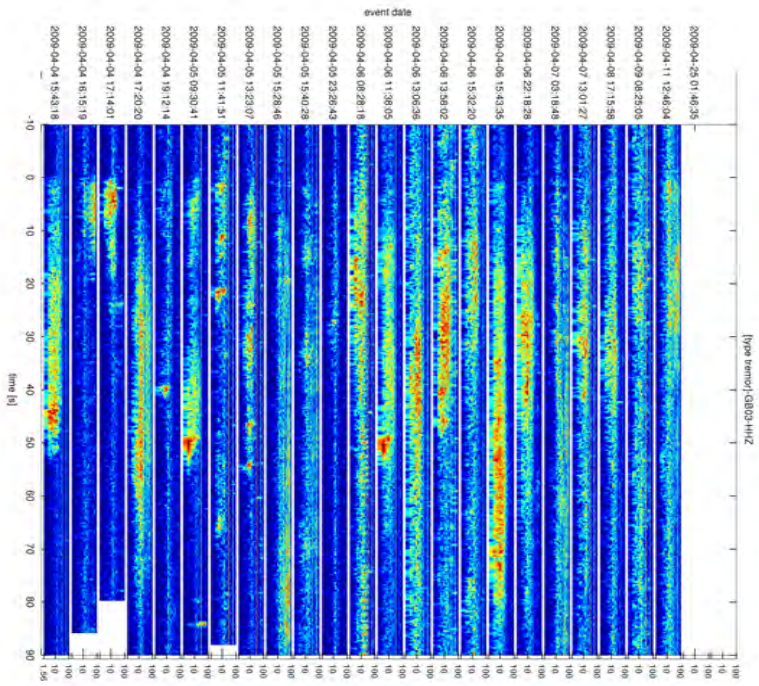
(b)

Figure B.47: Type tremor - GB03 -HHZ. The seismograms are colored according to the event date in UTC (black: first; light brown: last). In the spectrogram, blue colors indicate low energy, red colors high energy. The units of the frequency scale on the right side of the seismograms is Hz.

B. SLOPE CANDIDATE EVENTS

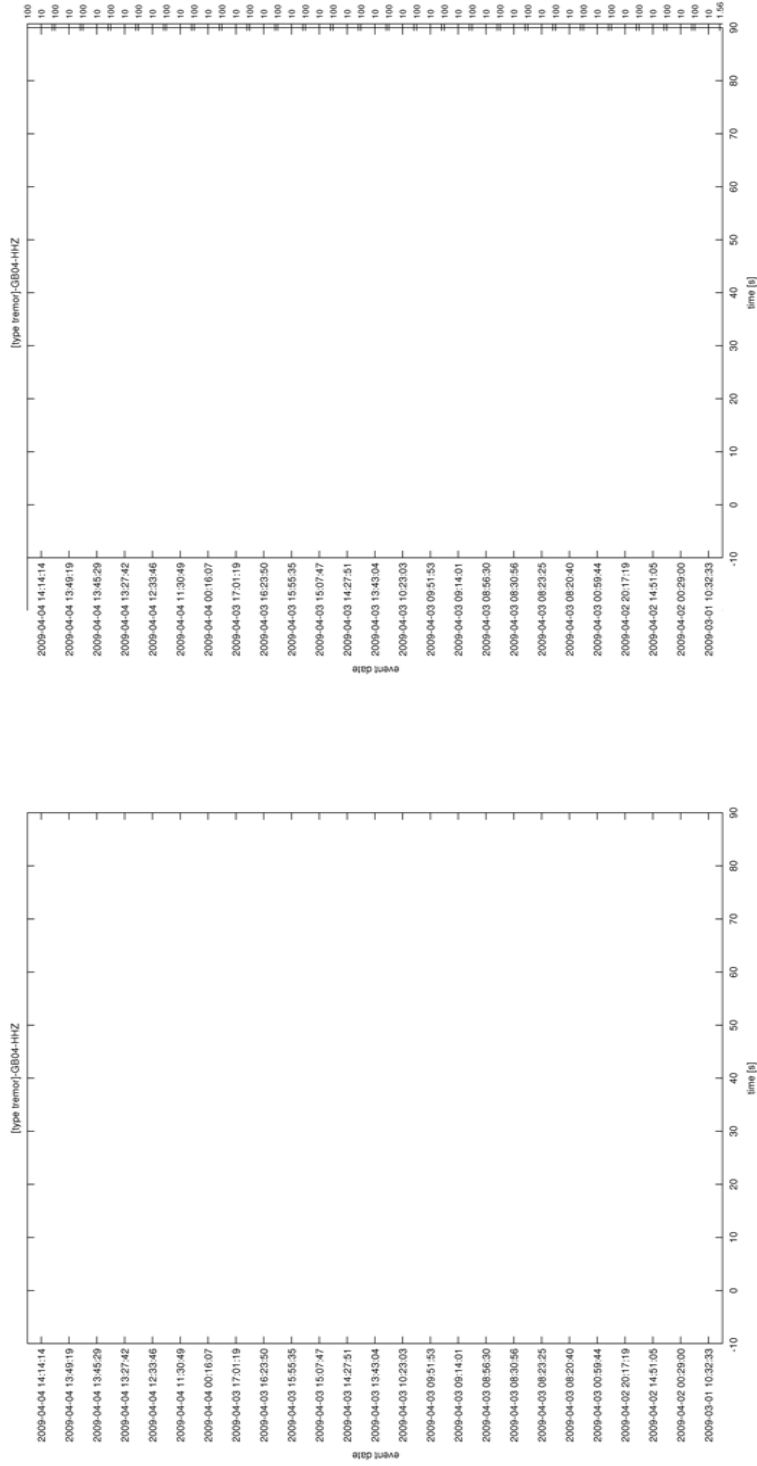


(a)



(b)

Figure B.48: Type tremor - GB03 -HHZ. The seismograms are colored according to the event date in UTC (black: first; light brown: last). In the spectrogram, blue colors indicate low energy, red colors high energy. The units of the frequency scale on the right side of the spectrograms is Hz.

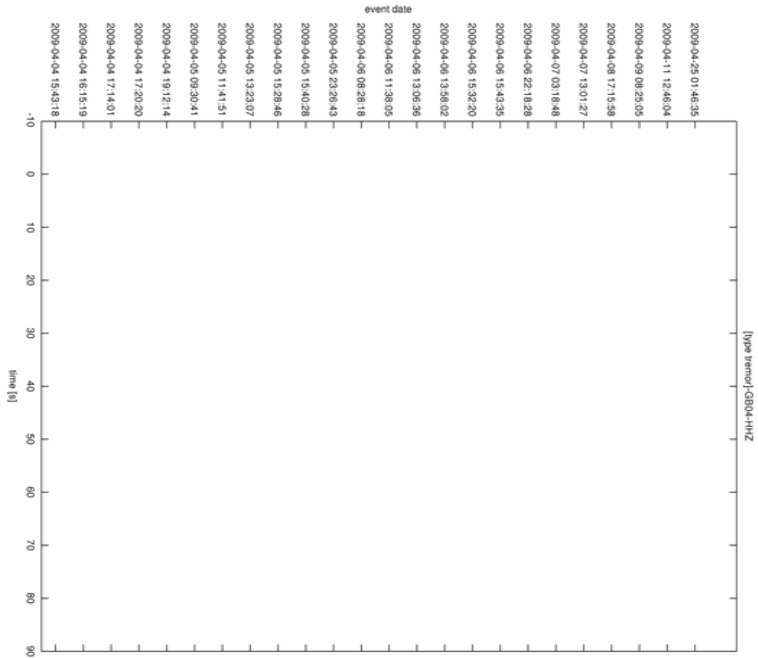


(a)

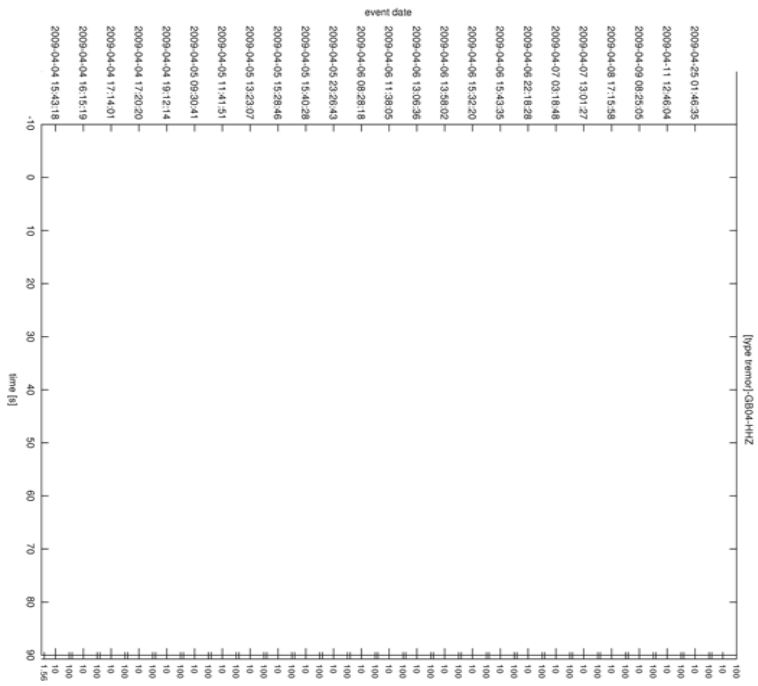
(b)

Figure B.49: Type tremor - GB04 -HHZ. The spectrograms are colored according to the event date in UTC (black: first; light brown: last). In the spectrogram, blue colors indicate low energy, red colors indicate high energy. The units of the frequency scale on the right side of the spectrograms is Hz.

B. SLOPE CANDIDATE EVENTS

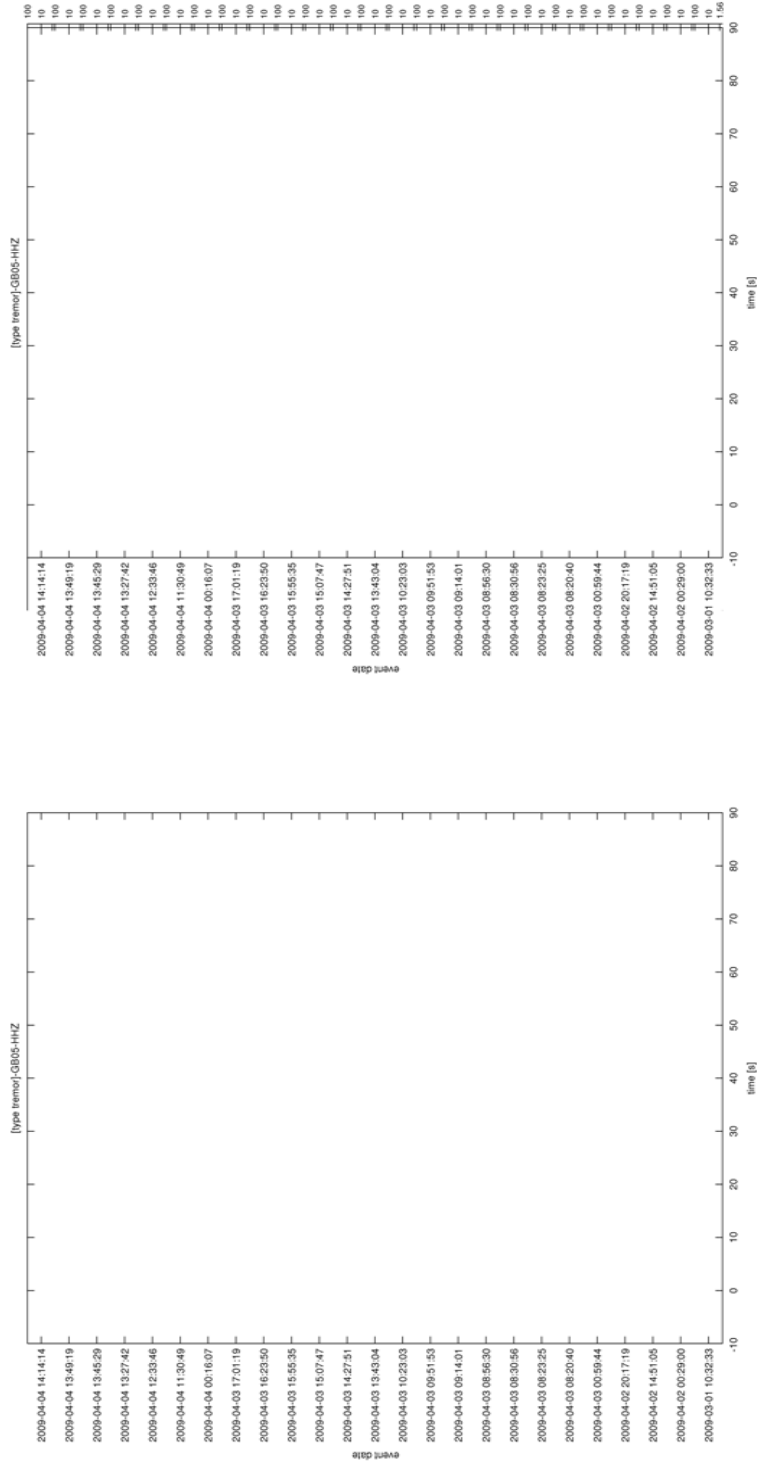


(a)



(b)

Figure B.50: Type tremor - GB04 -HHZ. The seismograms are colored according to the event date in UTC (black: first; light brown: last). In the spectrogram, blue colors indicate low energy, red colors high energy. The units of the frequency scale on the right side of the seismograms is Hz.

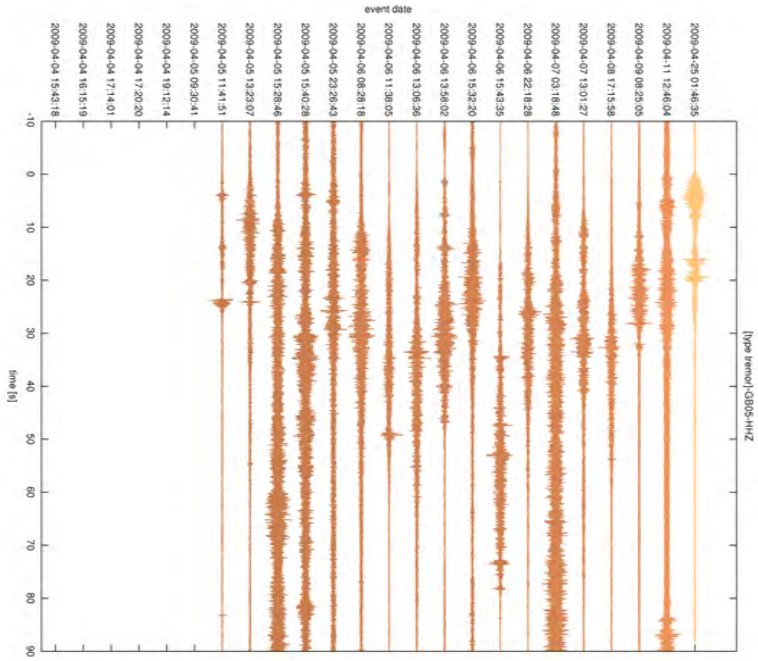


(a)

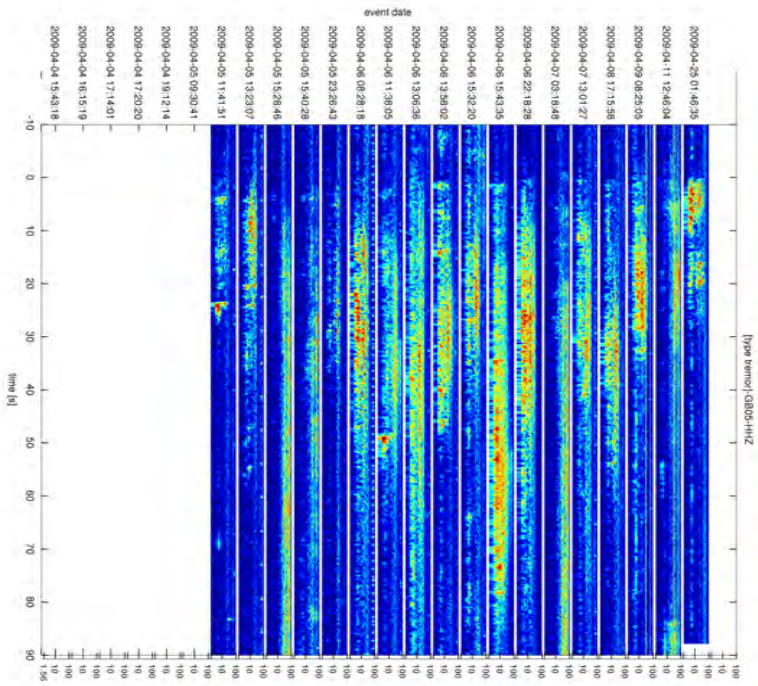
(b)

Figure B.51: Type tremor - GB05 -HHZ. The seismograms are colored according to the event date in UTC (black: first; light brown: last). In the spectrogram, blue colors indicate low energy, red colors high energy. The units of the frequency scale on the right side of the seismograms is Hz.

B. SLOPE CANDIDATE EVENTS

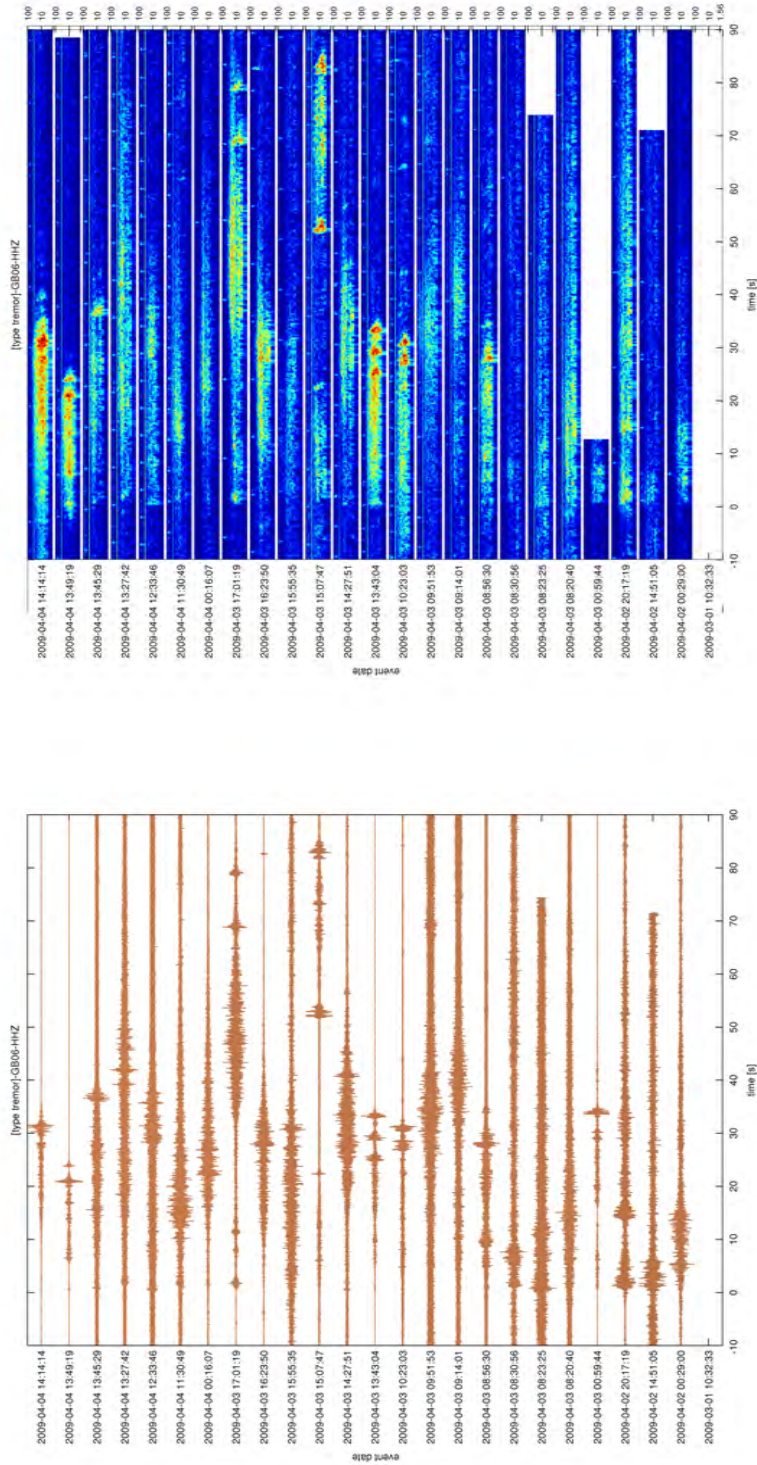


(a)



(b)

Figure B.52: Type tremor - GB05 -HHZ. The seismograms are colored according to the event date in UTC (black: first; light brown: last). In the spectrogram, blue colors indicate low energy, red colors high energy. The units of the frequency scale on the right side of the seismograms is Hz.

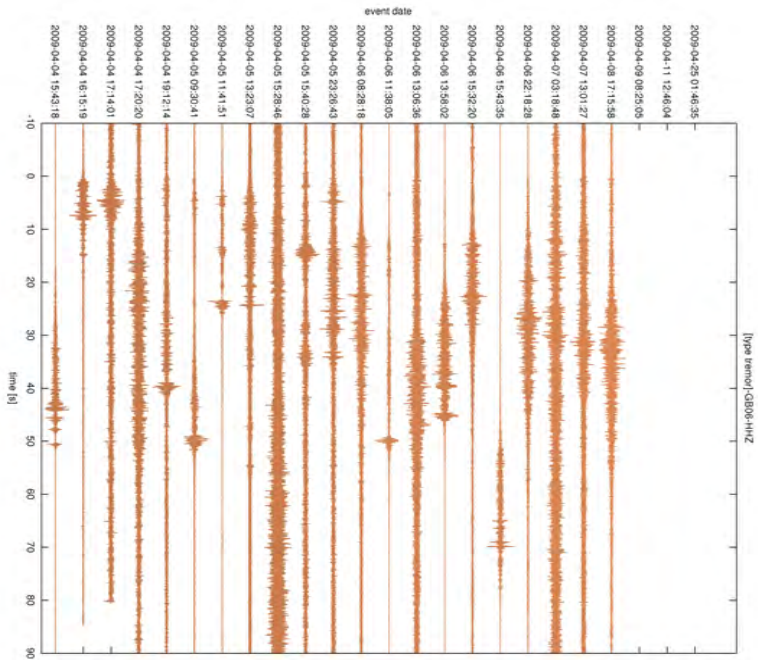


(a)

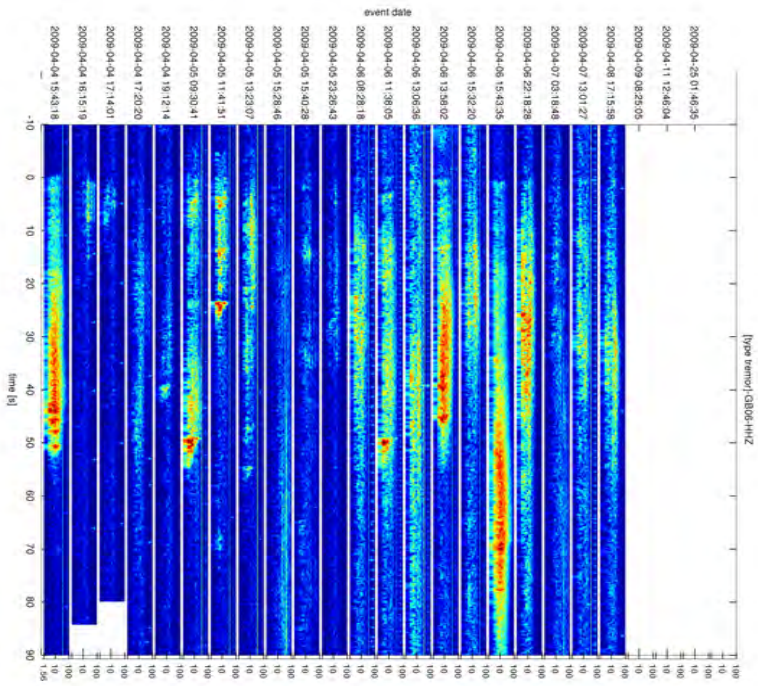
(b)

Figure B.53: Type tremor - GB06 -HHZ. The seismograms are colored according to the event date in UTC (black: first; light brown: last). In the spectrogram, blue colors indicate low energy, red colors high energy. The units of the frequency scale on the right side of the seismograms is Hz.

B. SLOPE CANDIDATE EVENTS



(a)



(b)

Figure B.54: Type tremor - GB06 -HHZ. The seismograms are colored according to the event date in UTC (black: first; light brown: last). In the spectrogram, blue colors indicate low energy, red colors high energy. The units of the frequency scale on the right side of the seismograms is Hz.

Résumé

Stefan Mertl

born June 1976 in Salzburg, Austria

www.stefanmertl.com

Education

- | | |
|-------------|--|
| 1994 – 2003 | Magister rer.nat. , Geophysics, University of Vienna. |
| 2002 – 2006 | fotoK , Artistic Photography, fotoK Vienna. |
| 1986 – 1994 | Secondary School , Bundesgymnasium Hallein. |
| 1982 – 1986 | Elementary School , Volksschule Kuchl. |

Professional Experience

- | | |
|----------------|--|
| 2012 – present | Managing Partner , Mertl Research GmbH, Vienna, Austria |
| 2011 – 2013 | Research Assistant , Vienna University of Technology, Institute of Geodesy and Geophysics, Vienna, Austria. |
| 2008 – 2011 | Research Associate , Vienna University of Technology, Institute of Geodesy and Geophysics, Vienna, Austria. |
| 2005 – 2006 | Junior Scientist , alpS – GmbH, Innsbruck, Austria. |
| 2003 – 2008 | Research Assistant , Vienna University of Technology, Institute of Geodesy and Geophysics, Vienna, Austria. |